UNIVERSITY OF SOUTHAMPTON

A Time-Resolved Incoherent Anti-Stokes Raman Spectroscopy Study of Optical Phonons in Single-Walled Carbon Nanotubes

by

John M. Nesbitt

A thesis submitted in partial fulfillment for the
degree of Doctor of Philosophy

in the
Faculty of Physical and Applied Sciences
School of Physics and Astronomy

December 2013

UNIVERSITY OF SOUTHAMPTON

ABSTRACT

FACULTY OF PHYSICAL AND APPLIED SCIENCES
SCHOOL OF PHYSICS AND ASTRONOMY

Doctor of Philosophy

by John M. Nesbitt

This thesis presents a time-resolved incoherent anti-Stokes Raman spectroscopy (TRIARS) study of the *D*- *G*- and *G*'-band phonon population dynamics in single-walled carbon nanotubes (SWCNTs). The purpose of this study is to explore the mechanisms which control the decay of non-equilibrium Γ-point and *K*-point phonon populations in SWCNTs, with the view of advancing our understanding of their electronic properties. Detailed resonance Raman spectroscopy (RRS) and TRIARS measurements have been carried out on a bundled SWCNT sample. Careful analysis of the RRS measurements shows that by carefully selecting the laser excitation energy used for the TRIARS measurements it is possible to study the phonon population dynamics of SWCNTs in two separate diameter ranges. The temperature dependence of the phonon population dynamics has been studied, in order to allow the anharmonic decay channels of the phonons to be explored through thermal activation. The results of the *G*-band TRIARS study support the existing notion that the main decay channel for *G*-band phonons is three-phonon anharmonic decay, and suggest that the lower energy daughter phonons have an energy of approximately 400 ± 100 cm^{-1}. Independent measurements of the G^+ and G^- intensity dynamics provide strong evidence that the anharmonic decay branches of the LO and TO Γ-point phonons in SWCNTs are not significantly affected by the splitting of the *G*-band due to curvature. These results also support the hypothesis that the decay rate of *G*-band phonons does not depend critically on SWCNT diameter. The *D*-band measurements provide the first experimentally determined values for the decay rate ($1/T_1$) of a non-equilibrium population of *K* phonons in SWCNTs, whilst a parallel investigation of *G*'-band TRIARS measurements provides valuable insight into how one should interpret TRIARS measurements of a two-phonon overtone Raman feature. The results of the *D*-band TRIARS study show that the decay rate of phonons, which can be represented close to the *K*-point in graphene, have a strong temperature dependence in the range $100 - 500$ K. This observation is consistent with a large decay channel towards low-energy (less than 150 cm^{-1}) acoustic phonon modes, which has been predicted in earlier theoretical work. A review of the existing ultrafast Raman measurements on SWCNTs is provided, and the implications of the results presented in this thesis are discussed.

Contents

List of Figures

List of Tables

Nomenclature

SWCNT	**S**ingle **W**alled **C**arbon **N**ano**T**ube
CVD	**C**hemical **V**apour **D**eposition
TRIARS	**T**ime-**R**esolved **I**ncoherent **A**nti-Stokes **R**aman **S**pectroscopy
CN-FET	**C**arbon **N**anotube **F**ield **E**ffect **T**ransistor
RRS	**R**esonance **R**aman **S**pectroscopy
RBM	**R**adial **B**reathing **M**ode
LCAO	**L**inear **C**ombination of **A**tomic **O**rbitals
DOS	**D**ensity **O**f **S**tates
vHs	**v**an **H**ove **s**ingularities
JDOS	**J**oint **D**ensity **O**f **S**tates
DR	**D**ouble **R**esonance
TWM	**TW**isting **M**ode
FWHM	**F**ull **W**idth **H**alf **M**aximum
E-Ph	**E**lectron-**Ph**onon
E-E	**E**lectron-**E**lectron
E-H	**E**lectron-**H**ole
H-H	**H**ole-**H**ole
Ph-Ph	**Ph**onon-**Ph**onon
CW	**C**ontinuous **W**ave
GTI	**G**ires **T**ournois **I**nterferometer
BRF	**B**i**R**efringent **F**ilter
KLM	**K**err **L**ens **M**ode-locking
Ti:Sa	**Ti**tanium **Sa**pphire
TPA	**T**wo-**P**hoton **A**bsorption
GaP	**Ga**llium **P**hosphide
LLTF	**L**aser **L**ine **T**unable **F**ilter
Si	**S**ilicon
CCD	**C**harged **C**oupled **D**evice
NIR	**N**ear **I**nfra**R**ed
UV	**U**ltra**V**iolet
VIS	**VIS**ible
HiPco	**Hi**gh **P**ressure **C**arbon **O**xygen Conversion

IPA	**I**so**P**ropyl **A**lcohol
SEM	**S**canning **E**lectron **M**icroscope
TEM	**T**ransmission **E**lectron **M**icroscope
AFM	**A**tomic **F**orce **M**icroscopy
PL	**P**hoto**L**uminescence
AC	**A**uto**C**orrelator
GaAs	**Ga**llium **A**r**S**enide
TB	**T**ight-**B**inding
IR	**I**nfra-**R**ed

Declaration of Authorship

I, John M. Nesbitt, declare that this thesis titled, 'A Time-Resolved Incoherent Anti-Stokes Raman Spectroscopy Study of Optical Phonons in Single-Walled Carbon Nanotubes' and the work presented in it are my own. I confirm that:

- This work was done wholly or mainly while in candidature for a research degree at this University.
- Where any part of this thesis has previously been submitted for a degree or any other qualification at this University or any other institution, this has been clearly stated.
- Where I have consulted the published work of others, this is always clearly attributed.
- Where I have quoted from the work of others, the source is always given. With the exception of such quotations, this thesis is entirely my own work.
- I have acknowledged all main sources of help.
- Where the thesis is based on work done by myself jointly with others, I have made clear exactly what was done by others and what I have contributed myself.

Signed:

Date: December 2013

List of Publications

1. John M. Nesbitt and David C. Smith, "Measurements of the Population Lifetime of D Band and G' Band Phonons in Single-Walled Carbon Nanotubes" *Nano Lett.*, 13, 416 – 422, 2013.

2. John M. Nesbitt and David C. Smith, "Separation of G^+ and G Phonon Population Dynamics in Semiconducting Single-Walled Carbon Nanotubes as a Function of Diameter and Temperature." *PRB*, 87, 195446, 2013.

3. John M. Nesbitt and David C. Smith, "A comprehensive study of phonon dynamics in semiconducting single-walled Carbon Nanotubes using time-resolved incoherent anti-Stokes Raman spectroscopy." In: *International Conference on the Science and Application of Nanotubes*, 24 – 29th June, 2012.

4. Cheng, Fei, George, Kathryn, Hector, Andrew L., Jura, Marek, Kroner, Anna, Levason, William, Nesbitt, John, Reid, Gillian, Smith, David C. and Wilson, James W, "Chemical vapor deposition of GaP and GaAs thin films from [^{n}Bu$_2$Ga(μ – E^tBu$_2$)$_2$Ga^{n}Bu$_2$] (E = P or As) and Ga(P^{t}Bu$_2$)$_3$" *Chem. Mater.*, 23, pp 5217 – 5222, 2011.

Acknowledgements

Some of the work in this thesis would not have been possible without the cooperation and support of a number of kind people. I hereby would like to acknowledge their valuable input.

First and foremost, I would like to express my sincere appreciation to my supervisor, Prof. David C. Smith, for his guidance, encouragement and continuous support throughout this research project. I am very grateful for his patience and for the invaluable help and advice he has given me over the years.

I would like to take the opportunity to thank Dr. Greg N. Ayre, who was immensely helpful in getting me up to speed in the laboratory. I owe him much for passing on his experience and knowledge and I wish him all the best in his future career.

I would like to express my gratitude to the workshop team for their engineering input. In particular, I would like to thank them for helping to improve the in-situ optical Raman microscope system, which has played a key role in the majority of measurements presented in this thesis. I would also like to thank Colin Miles and his team from keeping the Helium on tap.

Above all, I would like to thank my parents, Dyan and Kerry Nesbitt, and brother and sister, Gary and Sarah, for their unwavering support, guidance and love of so many years. Martyna also deserves a special mention for her emotional support and patience during the writing of this thesis.

To my Family

Chapter 1

Introduction

Amorphous carbon, graphite and diamond are three naturally occurring allotropes of carbon which have been known since antiquity. Over the centuries a number of applications have been discovered which make use of the properties of these materials. For example, graphite is a soft material which is often used as a lubricant and as the black material in the center of pencils, while diamond is the hardest known material and can be useful for mechanically engraving other hard materials [8]. The rarity of naturally occurring diamond combined with its resistance to being scratched has no doubt contributed to its suitability as one of the preferred gemstones. Although graphite and diamond are both pure carbon materials they exhibit contrasting mechanical properties because of their different structures; diamond consists of carbon atoms formed in a strong three-dimensional (3D) structure, while graphite consists of carbon atoms formed in two-dimensional (2D) layers, where the individual layers, known as graphene, are weakly held together by van-der-Waals forces.

In recent decades new forms of crystalline carbon have been discovered such as fullerenes [9], nanotubes [10] and isolated graphene [11]. These newer forms of carbon are referred to as low-dimensional carbon structures, or carbon nanostructures. Carbon nanostructures share a similar local structure, which consists of a 2D lattice of carbon atoms in a hexagonal arrangement. As a result, similar physics can be invoked to explain the electronic and vibrational properties of these materials [12, 13]. This has made carbon nanostructures attractive materials for studying the effects of low-dimensionality on the electronic and vibrational properties of a solid state system. In particular, the mechanical and electronic properties of carbon nanotubes have been extensively studied [14], leading to a wealth of understanding compared with other carbon nanomaterials.

Carbon nanotubes are novel materials that have been found to possess exceptional mechanical, thermal and electronic properties. For example, the tensile strength of carbon nanotubes can be more than 100 times that of steel [15], while the thermal conductivity is approximately 10 times that of copper [16]. Furthermore, carbon nanotubes can exhibit

semiconducting or metallic behaviour depending on their structure. These unique properties have led to a significant push in application development for carbon nanotubes, spanning several disciplines [17]. In the field of biomedicine, carbon nanotubes have been investigated as tools for drug delivery in cancer therapy [18–20], and as biosensors [21], while in the field in electrical engineering the superior electronic properties of carbon nanotubes and ability to choose between semiconducting and metallic behaviour offers the potential for developing a new generation of high performance electronics [17, 22].

1.1 Motivation

I begin my PhD at the University of Southampton in late 2009. At that time the research group acquired a Coherent Inc. Mira 900 Titanium sapphire laser system for use with an existing triple spectrometer Raman detection system. This highly reliable and stable laser source was ideal for performing resonance Raman spectroscopy (RRS) and time-resolved incoherent anti-Stokes Raman spectroscopy (TRIARS) experiments. The research group had previously been working on the mechanism of carbon nanotube formation by Chemical Vapour Deposition (CVD) and I was particularly interested in the electronic applications of carbon nanotubes after an inspiring final year undergraduate course on nanotechnology. This led me to review Raman spectroscopy studies on single-walled carbon nanotubes (SWCNTs) and ultimately to propose a PhD project based on measuring the ultrafast dynamics of Raman active phonon populations in SWCNTs using TRIARS.

In recent years SWCNTs have received considerable attention as novel electronic nanomaterials because of their short range ballistic transport properties [23, 24] and ability to carry high current densities [25, 26]. The realisation of SWCNT interconnects and field effect transistors (CN-FETs) [27, 28], proves SWCNTs to be promising materials for producing the active elements in a new generation of electronic devices. Studies have shown that SWCNTs boast a long mean-free path of approximately $0.5 - 0.8\mu$m for low-energy carriers [29], while for high-energy carriers a reduced mean-free path of approximately 0.3μm is observed [30, 31]. It has been shown that this reduction is due to strong coupling between high-energy electrons and optical phonons, particularly those phonons represented near the Γ- and K points in the Brillouin zone of graphene [30, 32–36]. These high-energy phonons are first- and second-order Raman active respectively [37], and are believed to predominantly decay through anharmonic processes into a pair, or possibly more, of lower energy phonons [6, 7, 38–40]. If these decay processes are not sufficiently rapid, a non-equilibrium optical phonon population can be generated. It has been proposed that electron-phonon scattering rates are enhanced by the build-up of a significant non-equilibrium population of the optical phonons, comparable to a phonon temperature of > 6000 K, which leads to stimulated scattering [33, 34]. These theoretical predictions suggest an optical phonon population lifetime of 5 ps. This has been

invoked to explain the current saturation and negative differential resistance which is observed in electrical transport experiments on suspended SWCNTs in a vacuum [16, 41]. Interestingly, increased currents have been observed for SWCNTs that are supported by substrates compared with those suspended in vacuum, which implies that tube-substrate interactions may assist the relaxation of optical phonons [6, 42, 43]. This suggests it may be possible to increase the carrier scattering length in SWCNTs up to the ultimate limit of ballistic transport [33]. Therefore, understanding the mechanisms behind Γ- and K-point phonon population decay represents an important step in application development for carbon nanotubes and towards improving the performance of SWCNT based electronic devices. The demand for such knowledge has led to a number of good quality studies on the ultrafast dynamics of Γ-point phonons in SWCNTs. However, our understanding is not yet complete as there are currently no direct measurements of the K-point phonon population dynamics due to the complexities of performing TRIARS experiments on second-order Raman features. Also and there is still some debate over certain assumptions and conclusions drawn from the existing ultrafast measurements of Γ-point phonons, which requires further clarification. In summary, the intention of this thesis is to explore the mechanisms which control the decay of non-equilibrium Γ-point and K-point phonon populations in SWCNTs, with the view of advancing our understanding of their electronic properties.

1.2 Organisation

Chapter 2 provides the reader with the basic theoretical background that is required to understand the work in this thesis. The geometric structure of SWCNTs is briefly summarised, followed by a discussion of the unique electronic and vibrational structures of SWCNTs. The theoretical aspects of Raman scattering that are relevant to the experiments in this thesis are discussed, including first- and second-order Raman scattering, RRS and time-resolved Raman spectroscopy. The chapter concludes with a description of the various scattering mechanisms which contribute to the ultrafast carrier and phonon dynamics which are discussed in the later chapters of this thesis.

Chapter 3 covers the experimental apparatus and techniques which are used throughout the work in this thesis. The first section of the chapter provides information on the general experimental apparatus which were used during the RRS and TRIARS experiments, including a discussion of the laser system, the Raman microscope and the detection system. The sample preparation method and sample environment control techniques are also discussed. The chapter concludes with a detailed discussion of how the RRS and TRIARS experiments were performed.

In Chapter 4 the RRS results are presented and discussed in relation to a set of clearly defined objectives. The first section provides details of the particular RRS experiments

that were performed. The analysis of the radial breathing mode (RBM) resonance measurements is presented first. This is followed by an investigation of the resonance behaviour of the D-band and G-band Raman features. A final section provides a summary of the chapter by stating the key conclusions that can be drawn from the results.

Chapter 5 presents a study of the dynamics of the G-band (Γ-point) phonon population measured using TRIARS. The chapter begins with a review of the existing ultrafast SWCNT G-band studies. This is followed by a description of the G-band TRIARS experiments that were performed for this study. The next section presents the results of the experiments. This is followed by a series of sections which are dedicated to the analysis and interpretation of the TRIARS data. The chapter concludes with a summary of the findings of the experiments.

Chapter, 6 presents a TRIARS study of the D- and G'-band Raman features of SWCNTs. The D-band TRIARS measurements are investigated first as they provide the first experimentally determined values for the decay rate ($1/T_1$) of a non-equilibrium population of D-band phonons in SWCNTs. This is followed by an investigation of G'-band TRIARS measurements, which are effectively TRIARS measurements performed on the overtone of the D-band.

Finally, Chapter 7 re-iterates and discusses the key conclusions that can be drawn from the study. The final chapter ends with suggestions for further work and a personal view of the future direction in this field.

Chapter 2

Theoretical Considerations

The unique structure of carbon nanotubes gives rise to remarkable mechanical, electronic and vibrational properties. These properties make them an ideal material for a range of technological applications, including CN-FETs and circuit interconnects [17, 44, 45]. In the past two decades Raman spectroscopy has proved to be a powerful tool for investigating the electronic and vibrational properties of carbon nanotubes, and its use is central to the work in this thesis. This chapter provides the basic theory that is required to understand and interpret the experimental results that are presented in the later chapters. If required, an exhaustive review of Raman scattering in carbon nanotubes, including an in-depth discussion of the theoretical considerations can be found in reference [37].

We begin this chapter by setting out the general notation used to describe the geometric structure of carbon nanotubes in terms of their 2D parent material graphene. We then discuss how the one-dimensional (1D) electronic and vibrational structures of carbon nanotubes can be obtained (to first-order) from the well-known 2D band structures of graphene. The theoretical aspects of Raman scattering that are relevant to the experiments in this thesis are discussed, including RRS, first- and second-order Raman scattering and time-resolved Raman spectroscopy. The chapter concludes with a brief discussion of the various scattering mechanisms which contribute to the ultrafast carrier and phonon dynamics reported in the later chapters of this thesis.

2.1 Single-Walled Carbon Nanotubes

Carbon has four valence electrons in its outer shell. In pure carbon materials, such as diamond and graphite, the neighbouring carbon atoms form covalent bonds by sharing electron pairs. In diamond, four σ bonds are created to form a strong 3D tetrahedral structure, where the orbitals of the carbon atoms undergo sp^3 hybridisation. In graphite,

the orbitals are sp^2 hybridised where three of the valence electrons form in-plane σ bonds, while the remaining one electron forms an out-of-plane π bond. This bonding tends to form 2D layers of carbon atoms in a strong hexagonal structure, where the individual layers, known as graphene, are held together by weak van-der-Waals forces generated by the out-of-plane π bonds. Although they are both made from carbon, the structural differences between diamond and graphite are profound; Graphite is considered a semi-metal, while diamond is an insulator with a band gap around 5.5eV.

2.1.1 Geometric Structure

Carbon nanotubes are another allotrope of carbon in which the carbon atoms are in a state of sp^2 hybridisation. Conveniently, a SWCNT can be visualised as a graphene sheet 'rolled-up' to form a seamless hollow cylinder with a wall one atom thick. SWCNTs usually have a large aspect ratio, with a diameter of approximately 1nm and length measured in microns. Disregarding length, a SWCNT can be completely described by its chiral vector $\vec{C}_\mathrm{h}$, which represents the circumference of the nanotube projected onto the 2D graphene sheet, and is defined as

$$\vec{C}_\mathrm{h} = n\vec{a_1} + m\vec{a_2}, \tag{2.1}$$

where n and m are integers, and $\vec{a_1}$ and $\vec{a_2}$ represent the unit vectors of the two-dimensional graphene lattice, shown in Figure 2.1.

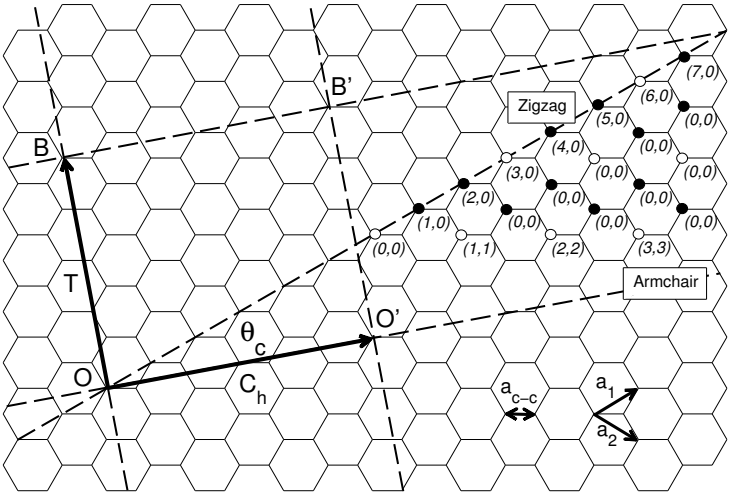

FIGURE 2.1: Projection of unrolled $(4, 2)$ nanotube on a graphene sheet showing chiral vector $\vec{C}_\mathrm{h}$, chiral angle θ_c, translational vector $\vec{T}$ (parallel to nanotube axis), unit vectors $\vec{a_1}$, $\vec{a_2}$, and C-C bond length a_{c-c}. The nanotube unit cell is defined by the rectangle OBB'O'. Open and solid circles denote semiconducting and metallic nanotubes respectively.

It follows that the diameter d_{t} of a nanotube can be written in terms of the integers (n, m) as

$$d_{\mathrm{t}} = C_{\mathrm{h}}/\pi = \sqrt{3}a_{C-C}\sqrt{n^2 + nm + m^2}/\pi, \tag{2.2}$$

where a_{c-c} is the C-C bond length in graphene (1.421 Å) and C_{h} is the chiral vector magnitude. The chiral vector runs perpendicular to the nanotube axis, and makes an angle θ_c with the unit vector $\vec{a_1}$. The chiral angle θ_c can also be written in terms of (n, m) as

$$\theta_c = tan^{-1}\left[\sqrt{3}m/(m + 2n)\right]. \tag{2.3}$$

In terms of chirality there are three classifications of carbon nanotubes; Armchair nanotubes for which $(n = m)$ and $\vec{\theta_c} = 30°$, zigzag nanotubes for which $(3n, 0)$ and $\vec{\theta_c} = 0°$, and chiral nanotubes where (n, m) and $0 < \vec{\theta_c} < 30°$ (see Figure 2.1).

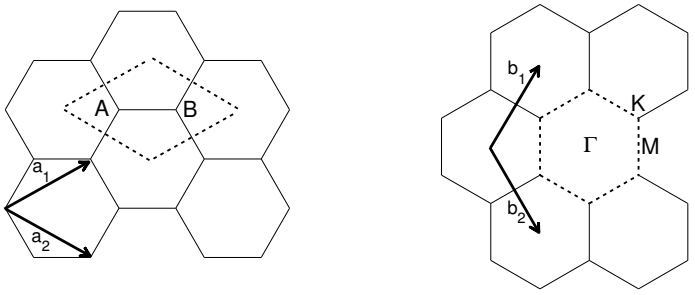

(a) (b)

FIGURE 2.2: Graphene (a) unit cell (dotted rhombus) containing two carbon atoms A and B, showing unit vectors $\vec{a_1}$ and $\vec{a_2}$ (b) Brillouin zone (dotted hexagon) showing reciprocal lattice vectors $\vec{b_1}$ and $\vec{b_2}$. High symmetry points of the Brillouin-zone Γ, K, and M are also shown.

The translational vector $\vec{T}$, shown in Figure 2.1, is determined by the shortest repeating distance in the direction of the nanotube axis. Therefore, in terms of the graphene lattice, the unit cell of a nanotube is given by a rectangle bounded by the chiral $\vec{C_{\mathrm{h}}}$ and translational $\vec{T}$ vectors (dotted rectangle in Figure 2.1). Figure 2.2 (a) shows the graphene unit cell as a dotted rhombus which contains two carbon atoms. The graphene unit cell is generally much smaller than the nanotube unit cell, and it can be shown geometrically that the number of graphene unit cells contained in a (n, m) nanotube unit cell can be expressed as

$$N = 2(n^2 + m^2 + nm)/d_r, \tag{2.4}$$

where d_r is the greatest common divisor of $(2n + m)$ and $(2m + n)$. Figure 2.2 (b) shows the reciprocal lattice and first Brillouin-zone (dotted hexagon) of graphene, where the

reciprocal lattice unit vectors $\vec{b_1}$ and $\vec{b_2}$ are constructed from the unit vectors $\vec{a_1}$ and $\vec{a_2}$ in real space using the standard definition $\vec{a_i} \cdot \vec{b_j} = 2\pi\delta_{i,j}$.

Although the details of the structure of SWCNTs provided in this section are sufficient to support the contents of this thesis, an exhaustive discussion of the structure of SWCNTS can be found in 'Carbon Nanotubes: Synthesis, Structure, Properties, and Applications' by M. Dresselhaus et al. [17].

2.1.2 Electronic Structure

Section 2.1.1 demonstrates that the local structure of a carbon nanotube is similar to that of graphene. In this section we discuss how the electronic band structure of carbon nanotube can be obtained (to first-order) from the well-known electronic band structure of graphene using a technique known as Brillouin zone-folding. Zone-folding is a well-established technique and has been used extensively to predict the electronic behaviour of SWCNTs [1, 46]. This section explains how confinement of the electron wave functions around the circumference of a nanotube leads to electronic states which can be considered a subset of those in graphene. Since the nanotube band structure will be derived from the band structure of graphene, we must first discuss how the graphene band structure may be calculated.

2.1.2.1 Electronic Structure of Graphene

In graphene the π electrons are close to the Fermi level and can be optically excited, while the σ electrons are far from the Fermi level so do not contribute to the optical processes reported in this work. Thus only the π electrons must be considered to determine the electronic structure. The two carbon atoms in the graphene unit cell lead to one valence band (π) and one conduction band (π*). Since the electrons will occupy their lowest energy states, the π band will be fully occupied while the π* band will be empty. In order to determine if graphene is metallic or semiconducting, the form of the conduction and valence bands can be calculated using the tight-binding model [47]. The tight-binding model assumes that the π electrons are tightly bound to the carbon atoms, and that the π electron wave function can be written as a linear combination of atomic orbitals (LCAO) as a Bloch wave. The tight-binding model applied to the π orbitals alone, can be used to predict the following energy dispersion $E(k)$ for graphene

$$E(k) = \frac{\pm\gamma_1|\alpha(k)|}{1 \pm \gamma_0|\alpha(k)|}, \tag{2.5}$$

$$|\alpha(K)| = \sqrt{1 + 4cos(\frac{\sqrt{3}a_{c-c}k_y}{2})cos(\frac{a_{c-c}k_x}{2}) + 4\cos^2(\frac{a_{c-c}k_x}{2})}, \tag{2.6}$$

where the parameters $\gamma_0 = 2.9$ eV and $\gamma_1 = 0.129$ eV can be obtained by fitting Equations 2.5 and 2.6 to experimental data [47]. Figure 2.3, shows the energy-momentum contours for the two-dimensional electronic band structure of graphene which has been plotted in the first Brillouin-zone using Equations 2.5 and 2.6. We can see that the band

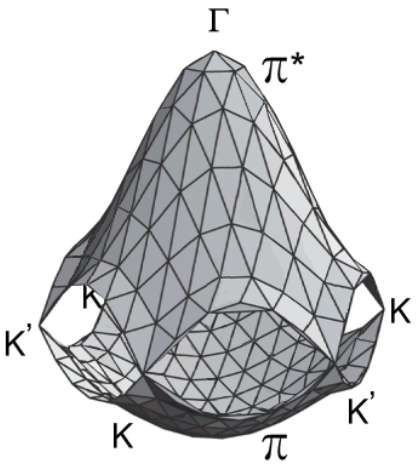

FIGURE 2.3: Two-dimensional electronic band structure of graphene plotted in the first Brillouin zone, calculated using tight-binding model (Equations 2.5 and 2.6). Adapted from [1].

structure consists of a π band and a π^* band, and that the maximum and minimum energies of these two bands can be found at the zone-center or Γ-point. The occupied π band touches the empty π^* band at six zone-edge points known as K-points. For this reason graphene is described as a semi-metal or zero-gap semiconductor.

2.1.2.2 Electronic Structure of Carbon Nanotubes

The local structure of a nanotube is similar to that of graphene, however, the unit cell of a carbon nanotube is much bigger, containing exactly N unit cells of graphene (see Equation 2.4). Thus we expect to find $2N$ electronic bands in carbon nanotubes i.e. one band from each carbon atom contained in the nanotube unit cell. To understand the nanotube band structure we begin with the electron wave functions in the two-dimensional graphene sheet, which can be expressed in Bloch wave form as

$$\psi(\vec{R}) = e^{i\vec{k}\cdot\vec{R}}u(\vec{R}), \tag{2.7}$$

where k is the electron wavevector and $u(\vec{R})$ is a function with the same periodicity as the lattice. If we ignore the curvature of the graphene sheet as it is rolled up to form the nanotube, the electron wave functions will be unchanged from those in graphene. However, due to the seamless nature of the nanotube structure, the electron wave functions must now obey periodic boundary conditions in the circumferential direction, which

require their wavevectors $\vec{k}$ to satisfy

$$\vec{k} \cdot \vec{C}_{\mathrm{h}} = 2\pi N, \tag{2.8}$$

where $N = 1, 2, ..., N-1, N$, while the wavevectors in the direction of the nanotube axis remain continuous (providing that the nanotube is sufficiently long). This set of allowed wavevectors can be represented as N parallel cutting lines in the Brillouin-zone of graphene. Figure 2.4 (a) shows the cutting lines for a $(4, 2)$ nanotube which are separated by the vector $\vec{K}_1$ and orientated parallel to the vector $\vec{K}_2$, where the reciprocal space vectors $\vec{K}_1$ and $\vec{K}_2$ have been derived from the real space vectors $\vec{C}_{\mathrm{h}}$ and $\vec{T}$ using the following relations

$$\vec{C}_{\mathrm{h}} \cdot \vec{K}_1 = \vec{T} \cdot \vec{K}_2 = 2\pi \quad \text{and} \quad \vec{C}_{\mathrm{h}} \cdot \vec{K}_2 = \vec{T} \cdot \vec{K}_1 = 0. \tag{2.9}$$

Note that the cutting line orientation is dependent on the chiral angle, while the cutting line separation is inversely proportional to the nanotube diameter.

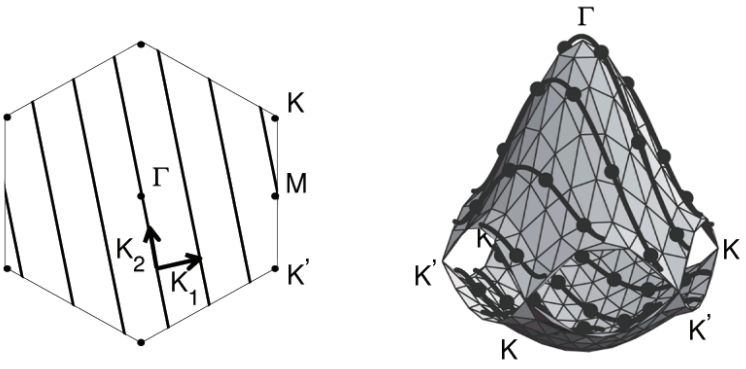

(a) (b)

FIGURE 2.4: (a) Cutting lines of a $(4, 2)$ nanotube shown in the first Brillouin-zone of graphene (*fully reduced representation*). (b) Fully reduced representation of cutting lines (*solid lines*) of $(4, 2)$ nanotube superimposed onto the band structure of graphene (from Figure 2.3) in the Brillouin-zone. *Black circles* show ends of cutting lines in fully extended representation (adapted from [1]).

In the Brillouin zone-folding scheme the electronic band structure of a nanotube is obtained by superimposing the cutting lines (allowed wavevectors) onto the electronic band structure of graphene in the first Brillouin zone. To demonstrate this, Figure 2.4 (b) shows the cutting lines from Figure 2.4 (a), superimposed onto the two-dimensional electronic band structure of graphene. The $E(k)$ points where the one-dimensional cutting lines intersect the two-dimensional surfaces are placed into the one-dimensional Brillouin zone of the nanotube. Figure 2.5 (a) shows the resulting $(4, 2)$ nanotube band structure. The total number of distinct sub-bands is less than $2N$ because a large

number of the sub-bands are doubly degenerate. Furthermore, the energy gap between the π and π^* bands in Figure 2.5 (a) predicts that the $(4, 2)$ nanotube will behave as a semiconductor. Remarkably, carbon nanotubes can be metallic or semiconducting, depending on whether or not their cutting lines intersect the K-point (Fermi-energy) in the 2D band structure of graphene. It is therefore useful to classify nanotubes according to

$$\mathrm{MOD}(2n + m, 3) = 0, 1, 2, \tag{2.10}$$

where a remainder of 0 denotes a MOD0 metallic nanotube, for which the cutting line crosses the K point, and a remainder of 1 or 2 denote MOD1 and MOD2 semiconducting nanotubes, for which the K point lies one-third or two-thirds the distance between consecutive cutting lines, as shown in Figure 2.5 (c). In reality, curvature effects create small band gaps in some MOD0 nanotubes, making them narrow-gap semiconductors. The tight-binding zone-folding approach fails to predict this phenomena because the curvature of the 2D graphene lattice is ignored. However, this effect is only significant for small diameter nanotubes and is not relevant to the results in this study.

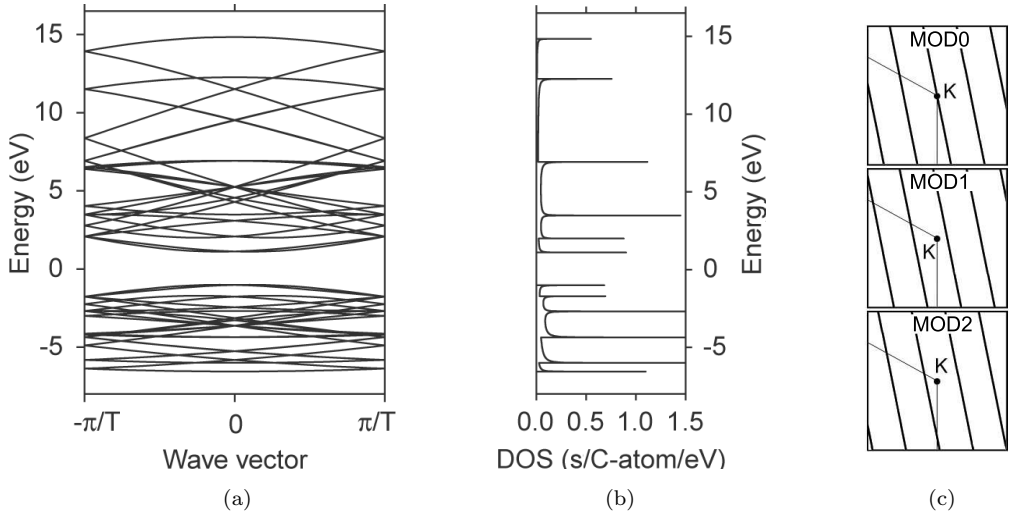

FIGURE 2.5: (a) Band diagram for $(4, 2)$ nanotube obtained from zone-folding in Figure 2.4 (b). (b) Density of eletronic states (DOS) calculated directly from (a). (c) The three possible configurations for cutting lines near the K-point which lead to metallic or semiconduting behaviour in carbon nanotubes. See main text for more details. Adapted from [1].

The 1D electronic density of states (DOS) are calculated by integrating along each band in Figure 2.5 (a). Figure 2.5 (b) shows the calculated DOS of the $(4, 2)$ example nanotube. The DOS consists of peaks known as van Hove singularities (vHs), which appear when the cutting lines in Figure 2.4 (b) are tangential to equal energy contours of the 2D band structure of graphene. As we will see, these vHs in the electronic DOS have a profound effect on the optical properties of SWCNTs [48].

2.1.2.3 Optical Transitions

In the Raman experiments reported in this thesis, electrons are optically excited from the π-band to the π^*-band near the K-points (Fermi-energy). At the energy of a vHs the optical absorption (and emission) rate increases by several orders of magnitude due to the increased number of available electron states [48]. This means that the inter-band optical transitions only occur between two vHs on the same cutting lines close to the K-point. For light polarised perpendicular to the nanotube axis the inter-band transitions are suppressed by the depolarisation effect, while for light polarised parallel to the nanotube axis, dipole selection rules only allow inter-band transitions on the same cutting line [13]. This means that the optical absorption (or emission) rate can be understood by considering the joint density of states (JDOS) [49]. The JDOS consists of one vHs for each vHs pair in the DOS between which an optical transition can occur. The vHs in the JDOS are labelled E_{ii} and are often plotted as a function of nanotube diameter in the so-called Kataura plot. Figure 2.6 shows a Kataura plot [48], where the E_{ii} have been calculated using the tight-binding zone-folding approach for nanotubes with diameters less than 3nm, where E_{11} and E_{22} are the first and second lowest energy transitions. The Kataura plot features distinct bands which are separated in energy and

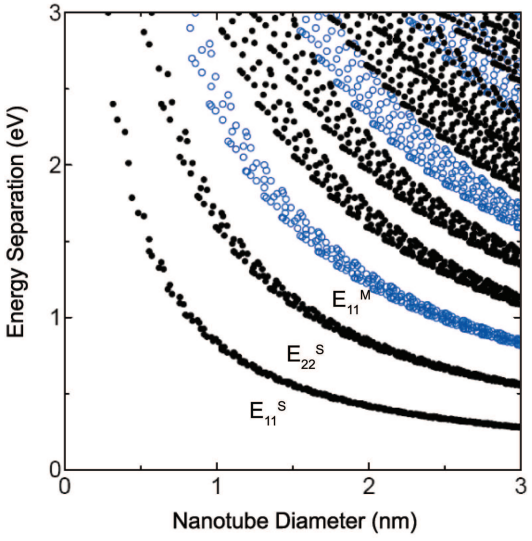

FIGURE 2.6: Kataura plot showing the transition energies E_{ii} as a function of nanotube diameter d_t for both semiconducting (black dots) and metallic (blue open circles) SWCNTs.

correspond to the different optical transitions (e.g. E_{11}, E_{22}...). The $1/d_t$ dependence for a particular E_{ii} comes from the fact that the separation of the cutting lines is inversely proportional to tube diameter d_t. Interestingly, the equal energy contours about the K-point in the graphene band structure are not circular, but instead form a trigonally warped shape with equal energy contours forming straight lines that connect the M

points in the graphene Brillouin-zone. This causes the vHs in the DOS to shift in energy depending on where the cutting line meets the equal energy contour, which ultimately depends on the cutting line orientation (or θ_c). This means that each (n, m) nanotube has a unique set of E_{ii}. The fact that the trigonal warping effect becomes more significant as we move away from K, explains why the width of the distinct bands in Figure 2.6 increases with increasing energy.

2.1.3 Phonon Structure

Phonons play a major role in the electronic and thermal properties of carbon nanotubes [17]. In Section 2.1.2 we discussed how the zone-folding technique could be used to approximate the 1D electronic structure of a nanotube from the 2D electronic structure of graphene. In a similar way, the 1D phonon structure of a carbon nanotube can be approximated by applying the zone-folding technique to the 2D phonon dispersion relations of graphene [13]. The graphene unit cell (see Figure 2.2 (a)), contains two carbon atoms, each with 6 degrees of freedom. This results in 6 phonon branches in the graphene dispersion relation, consisting of 3 acoustic and 3 optical modes. The frequency-momentum contours for the 6 phonon branches in graphene are shown as surfaces in Figure 2.7 (a). The 2D phonon dispersion relation in Figure 2.7 (a) has been calculated using a force constant model, however, the tight-binding method, or ab initio methods can also be used [1, 13]. Figure 2.7 (a) also shows the cutting lines for

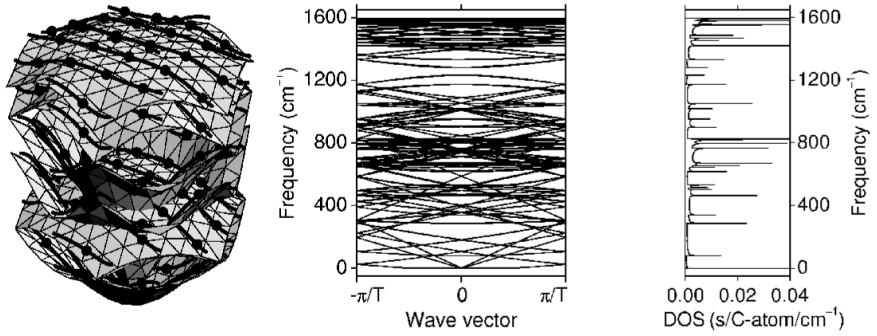

FIGURE 2.7: (a) Phonon dispersion relation of graphene, calculated by the force constant model. (b) The phonon dispersion relation for $(4, 2)$ nanotube obtained from zone-folding in (a). (c) Phonon DOS calculated from (b). Adapted from [1].

a $(4, 2)$ nanotube (Figure 2.4 (a)) superimposed onto the 2D phonon dispersion relation of graphene. The resulting 1D phonon dispersions and vibrational DOS for the $(4, 2)$ nanotube are shown in Figures 2.7 (b) and (c) respectively. There are 90 distinct phonon branches in the $(4, 2)$ nanotube, which is fewer than expected $(6N)$. This is due to a large number of degenerate modes. Note that the vibrational DOS consists of vHs similar to the electronic DOS.

As we have seen previously the zone-folding technique fails to predict the effects of curvature when graphene is rolled up to form a nanotube. In reality, the curvature of graphene causes coupling of the in-plane and out-of-plane modes. This effect gives rise to the twisting mode (TWM) where the carbon atoms vibrate in the circumferential direction and RBM where the carbon atoms vibrate in the radial direction.

2.1.4 Representing SWCNT Scattering Events in the Reciprocal Space of Graphene

It is common in the literature on SWCNT Raman spectroscopy to represent the scattering of an electron by a phonon by marking the initial and final states of the electron on to a diagram representing the graphene reciprocal space and to construct the wavevector of the phonon involved as the vector between the two states [1, 13, 30, 50]. Such a diagram is shown in Figure 2.8 (a), where q is the wavevector of the phonon involved in the scattering process.

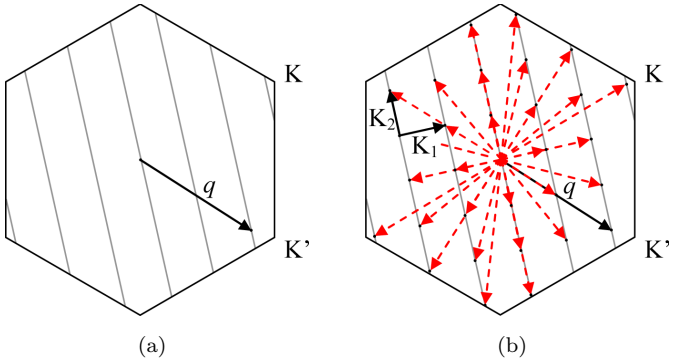

FIGURE 2.8: (a) Electron-phonon SWCNT scattering event represented in the 2D Brillioun-zone of graphene, showing the wavevector q of the phonon involved. (b) *Red arrows* represent phonons involved in Umklapp processes which can cause the transition shown in (a) (*black arrow*).

The formal implication that the wavevector of the phonon is the difference of the wavevector of the initial and final electronic states is that momentum conservation is the same in SWCNTs and graphene. This is clearly not the case. Firstly, momentum conservation in SWCNTs is associated with 1D momentum along the nanotube while momentum conservation in graphene is associated with 2D momentum in the plane. Secondly, Umklapp processes in each case are associated with quite different reciprocal lattice vectors [51]. In the case of SWCNTs, the reciprocal lattice 'vectors', $\vec{K_1}$ and $\vec{K_2}$, are associated with the chiral $\vec{C_h}$ and translation $\vec{T}$ vectors and will be much smaller than the reciprocal lattice vectors of graphene, $\vec{b_1}$ and $\vec{b_2}$. If only momentum conservation is taken into account then the phonons which can cause the transition shown in Figure 2.8 (a), represented in the graphene reciprocal space, are given in Figure 2.8 (b).

The reason why the representation of the scattering process shown in Figure 2.8 (a) is a good approximation is because;

(a) the actual electronic states in the SWCNTs are derived almost purely from the graphene states approximated by the cutting lines in the figure [1],

(b) high energy phonons, such as those responsible for the *G*- and *D*-band in SWCNT Raman spectra, are directly derived from graphene phonons (unlike the RBM for example),

(c) the phonon interaction (deformation potential) is reasonably local. Thus the matrix elements for the scattering of phonons in SWCNTs by phonons which are not the one shown in Figure 2.8 (a) are expected to be approximately zero.

It is convenient to use the graphene representation for all scattering events, however, it is important to consider when this might not be valid. The most obvious case would be RBM scattering events. The RBM is not simply derived from a graphene phonon and so cannot be represented on such a diagram. Another case might be electron-electron scattering. In this case whilst all the electronic states in SWCNTs are reasonably well approximated by pure graphene states, the non-local nature of the coulomb interaction could become a problem, allowing processes which involve scattering between cutting lines which do not appear to conserve momentum in the graphene representation.

2.2 Raman Spectroscopy of SWCNTs

Raman spectroscopy has proved to be one of the most useful tools for investigating the properties of SWCNTs and other carbon-based materials [2, 12, 52]. Figure 2.9 shows a typical SWCNT Raman spectra, which contains some unique features and some which are similar to those in the Raman spectra of graphene. There was initially much debate over the interpretation of SWCNT Raman spectra, however, thanks to the combined efforts of many researchers, we now know that the main features in the Raman spectra of SWCNTs can only be explained through a number of possible resonance Raman scattering processes [37]. Recently there have been many significant advances in this field, for example RRS has been used to achieve stable Raman signals from isolated carbon nanotubes [53], while a number of time-resolved Raman techniques have been used to probe phonon dynamics in semiconducting and metallic SWCNTs [6, 40, 54, 55]. Carbon nanotube Raman spectroscopy is a broad and complex subject which cannot be comprehensively covered here. Instead this section includes the details of SWCNT Raman spectroscopy which are required to understand the experimental techniques and result contained in this thesis. The theory of Raman scattering is treated in detail in reference [56], while a comprehensive review of Raman scattering in SWCNTs can be found in reference [37].

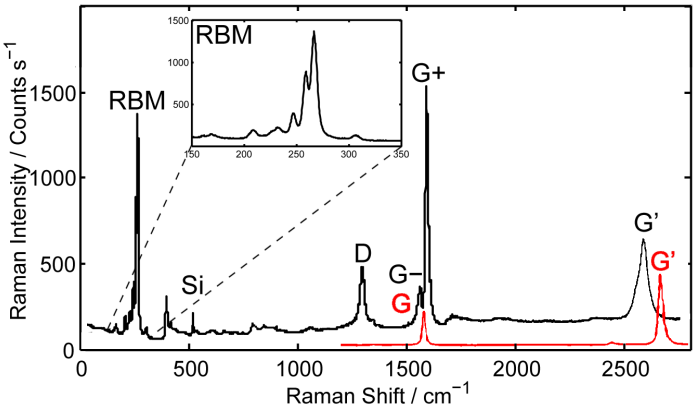

FIGURE 2.9: *Black* shows Raman spectra from bundled HiPco SWCNTs deposited on Si/SiO_2 taken with an excitation energy of 1.51eV. Inset shows zoom of RBM region. *Red* shows Raman spectra of graphene, taken from [2].

2.2.1 The Raman Effect

Raman scattering is a very weak optical process which involves the inelastic scattering of a photon. Many elementary excitations can be invloved in Raman scattering, however, in this study we are only concerned with Raman scattering involving phonons. Raman scattering involving a single phonon can be considered a three step process. (1) The first step involves the excitation of a real or virtual electron-hole pair by an incident photon of energy $\hbar\omega_{\mathrm{i}}$. (2) The electron or hole is then scattered by a phonon of energy $\hbar\omega_{\mathrm{ph}}$ through emission (Stokes scattering) or absorption (anti-Stokes scattering), which lowers or raises the energy of the electron-hole pair respectively. (3) In the final stage the electron-hole pair recombines, emitting an outgoing photon with its energy $\hbar\omega_{\mathrm{f}}$ shifted relative to that of the incoming photon by one phonon energy $\hbar\omega_{\mathrm{ph}}$. This energy shift is known as the Raman shift and is usually measured in relative wavenumbers (cm^{-1}).

The number of phonons which are emitted (or absorbed) in step (2) of the above process can be greater than one. The order of a particular scattering process is defined by the total number of scattering events (including elastic scattering from a defect) which take place. Raman spectra from SWCNTs contain a number of first-order and second-order Raman features, which can be understood by considering the resonance conditions in SWCNTs [37].

2.2.2 Resonance Raman Scattering

When any of the intermediate states in the scattering process are real electronic states, the Raman scattering rate is greatly enhanced. This phenomena is known as resonance Raman scattering (RRS) and can greatly increase Raman signals compared with non-resonance Raman scattering where all of the intermediate states are virtual states. For

any Raman scattering process there are at least two optical resonance conditions that are possible: (1) incoming resonance and (2) outgoing resonance. In the simple case of one-phonon Raman scattering these resonance conditions can be described by

$$\begin{aligned} E_{\mathrm{L}} &= \Delta E \quad \text{(Incoming resonance)} \\ E_{\mathrm{L}} &= \Delta E \pm \hbar\omega_{\mathrm{ph}} \quad \text{(Outgoing resonance)}, \end{aligned} \tag{2.11}$$

where $\mathrm{E_L} = \hbar\omega_{\mathrm{i}}$ is the laser excitation energy (incoming photon energy), ΔE is the energy separation of the initial and excited electronic states and $\hbar\omega_{\mathrm{ph}}$ is the energy of the phonon involved. In the case of two-phonon Raman scattering the outgoing resonance condition requires consideration of both phonons involved. Three important points to draw from Equation 2.11 are (1) that the incoming resonance condition is fixed for all Raman active modes for a particular SWCNT, (2) that the outgoing resonance condition is dependent on the energy of the phonon and (3) that the outgoing resonance conditions for Stokes and anti-Stokes scattering differ in energy by $2\hbar\omega_{\mathrm{ph}}$.

In the case of SWCNTs ΔE represents the allowed transition energies E_{ii} between two of the vHs in the electronic DOS (see Section 2.1.2.3). Although the JDOS are well-defined in energy (~ 0.04eV), a typical SWCNT resonance profile generally experiences additional broadening due to the finite lifetime of the intermediate electronic states. The singularity in the JDOS can cause significant enhancement of the Raman scattering rate. This is what makes it possible to obtain Raman spectra from a single isolated nanotube [53]. Since the E_{ii} resonance profiles are relatively well-defined in energy (~ 0.1eV) and because the E_{ii} possess a $1/d_{\mathrm{t}}$ dependence, resonant excitation can be used to study SWCNTs of a particular diameter range in a bundled SWCNT sample (see Figure 2.6) [37, 48, 52].

2.2.3 Non-Resonant Raman and Relation to IR Absorption

In the case that the incoming and outgoing photons are far from resonance with any of the intermediate states, all of the intermediate states give similar contributions to the scattering rate [56] and the matrix element which describes the Raman scattering process can be approximated by

$$|M| \propto \langle 0|\, \hat{\mathrm{H}}_{\mathrm{dipole}} \hat{\mathrm{H}}_{\mathrm{phonon}} \hat{\mathrm{H}}_{\mathrm{dipole}}\, |0\rangle, \tag{2.12}$$

where $\hat{\mathrm{H}}_{\mathrm{dipole}}$ and $\hat{\mathrm{H}}_{\mathrm{phonon}}$ are the electric dipole and election-phonon interaction Hamiltonians respectively. It is from this form of the Raman scattering matrix element that the selection rules and wavevector conservation are usually derived. The equivalent matrix element which describes the infra-red (IR) absorption process, where a photon is absorbed and phonon emitted, is given by

$$|M| \propto \langle 0| \hat{\mathrm{H}}_{\mathrm{dipole}} \hat{\mathrm{H}}_{\mathrm{phonon}} |0\rangle. \tag{2.13}$$

Equations 2.12 and 2.13 can also be represented by integrals of a function over all space. If inversion is a good symmetry of the system it follows that the integrand stays the same (+1 parity) or changes sign (−1 parity) under inversion. Importantly, it can be shown for +1 parity that it is possible for the integral over all space to result in a non-zero value, while for −1 parity the result of the integral is always zero.

All of the dipole matrix elements in equations 2.12 and 2.13 have −1 parity. This means that the Raman and IR processes are only allowed for +1 and −1 parity phonons respectively (see table 2.1). It is because of this difference in the selection rules that Raman scattering and IR absorption experiments provide partially complementary information.

Phonon Parity	Raman allowed	IR allowed
+1	Yes	No
−1	No	Yes

TABLE 2.1: Raman scattering and IR absorption selection rules.

While the selection rule described above tells us that phonons which are symmetric under inversion are 'Raman active', it does not tells us anything directly about the strength of the scattering process.

Group theory predicts that there are more symmetries in addition to inversion for SWCNTs [37], which means that the selection rules for IR absorption and Raman scattering are more complicated [57]. Furthermore, because it is only resonant Raman scattering which is experimentally observed for SWCNTs, the selection rules derived from equations 2.12 and 2.13 are not necessarily valid. A comprehensive treatment of symmetry and Raman scattering selection rules for SWCNTs can be found in references [37] and [57].

2.2.4 First-order Raman Scattering of RBM and *G*-band

First-order Raman scattering involves the scattering of a single phonon. Figure 2.10 shows the two possible third-order Feynman diagrams for this process which involve a phonon scattering with (a) an electron or (b) a hole. In this section we will focus mainly on electron scattering, however, one should be aware that a full description requires scattering from both carrier types to be considered. In both cases the vertices 1 and 3 represent the electron-hole excitation and recombination respectively, while vertex 2 represents the creation of a phonon. The scattering rate Γ for this process, calculated from third-order perturbation theory, is given by

$$\Gamma \propto |M|^2 \begin{cases} \delta(\omega_\mathrm{f} - \omega_\mathrm{i} + \omega_\mathrm{ph})(N_\mathrm{ph} + 1) & \text{Stokes} \\ \delta(\omega_\mathrm{f} - \omega_\mathrm{i} - \omega_\mathrm{ph})(N_\mathrm{ph}) & \text{anti-Stokes} \end{cases} \tag{2.14}$$

and

$$|M| = \sum_{k,l} \frac{\langle 0|\,\hat{\mathrm{H}}_3\,|l\rangle\,\langle l|\,\hat{\mathrm{H}}_2\,|k\rangle\,\langle k|\,\hat{\mathrm{H}}_1\,|0\rangle}{(\hbar\omega_l + i\gamma_l - \hbar\omega_\mathrm{f})(\hbar\omega_k + i\gamma_k - \hbar\omega_\mathrm{i})}, \tag{2.15}$$

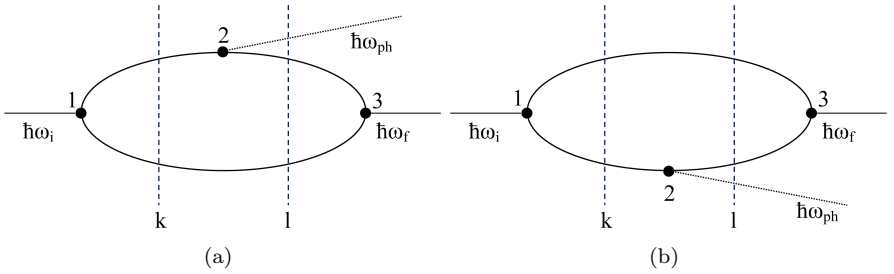

FIGURE 2.10: Third-order Feynman diagrams showing first-order Stokes Raman scattering of a phonon from (a) an electron and (b) a hole. The vertices 1 and 3 represent the electron-hole excitation and recombination respectively. Vertex 2 represents the creation of a phonon. The intermediate states are represented by *vertical dashed lines* and are labelled (k, l).

where $\hat{\mathrm{H}}_1$ and $\hat{\mathrm{H}}_3$ are the electric dipole Hamiltonians for the incident and scattered photons, $\hat{\mathrm{H}}_2$ is the Hamiltonian representing the electron-phonon interaction, $|k\rangle$ and $|l\rangle$ are the intermediate electron-hole pair states, $\hbar\omega_\mathrm{i}$ is the initial photon energy, ω_f is the scattered photon energy, ω_ph is the energy of the phonon invloved, γ_k and γ_l denote the broadening factor of the resonance due to the finite lifetime of the intermediate electronic states, and ω_k and ω_l are the energies of the intermediate electron-hole pair states. The delta functions in Equation 2.14 provide energy conservation and should be replaced with Lorentzian functions for phonons with finite lifetimes. N_ph is the phonon occupancy which can be calculated using Bose-Einstein statistics

$$N_\mathrm{ph} = \frac{1}{e^{\frac{\hbar\omega_\mathrm{ph}}{\mathrm{k_b}T}} - 1}, \tag{2.16}$$

where $\hbar\omega_\mathrm{ph}$ is the phonon energy, $\mathrm{k_b}$ is the Boltzmann constant and T is temperature. Equation 2.14 tells us that the Stokes scattering rate is proportional to $(N_\mathrm{ph}+1)$ while the anti-Stokes scattering rate is proportional to N_ph. This means that the rate of anti-Stokes scattering decreases with decreasing temperature. Some Raman spectroscopy studies have used the Stokes to anti-Stokes intensity ratio $I_\mathrm{S}/I_\mathrm{AS}$ as an internal temperature probe, however, one must be careful since there are other factors which can effect $I_\mathrm{S}/I_\mathrm{AS}$, such as resonance conditions.

Raman scattering processes are fundamentally the same in graphene and SWCNTs, however, the electron and phonon structures of a particular SWCNT are significantly different to those in graphene and therefore lead to different Raman spectra. Since it is more clear to visualise Raman scattering process in graphene, and because we do not deal with one specific type of SWCNT in this thesis, the illustrations provided are of scattering processes in graphene. These illustrations are then discussed in terms of Raman scattering in SWCNTs. Figure 2.11 shows the first-order (a) incoming and (b) outgoing resonance processes for Stokes Raman scattering where the crossed lines represent the approximately linear dispersion relation around the K-point of graphene. In order for the electron and hole to recombine, the wavevector of the initial and final

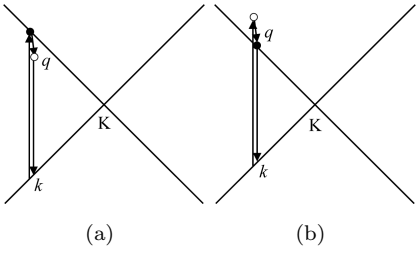

FIGURE 2.11: First-order resonance Raman processes showing (a) incident and (b) scattered resonance conditions. Equivalent anti-Stokes processes also exist. Real and virtual intermediate states are shown as *solid circles* and *open circles* respectively. The crossed lines represent the approximately linear dispersion relation near the K-point in graphene.

states should not differ by more than 2 times the photon wavevector. Since conservation of momentum requires

$$\mathrm{q_i} = \mathrm{q_f} \pm \mathrm{q_{ph}}, \tag{2.17}$$

and since the wavevector of an optical photon is very small, first order Raman scattering can only involve phonons for which q$\sim$ 0 (Γ-point phonons).

In SWCNTs there are many phonon modes at the Γ-point (see Figure 2.7), however, only a small number of these phonons are Raman active (see section 2.2.3). As predicted by group theory there are two zone-center phonons in SWCNTs which are Raman active. The first is the RBM which can be found in the frequency range $100 - 500\mathrm{cm}^{-1}$ for SWCNTs. The RBM is unique to nanotubes because it is due to all the carbon atoms moving in-phase in the radial direction (see Section 2.1.3). Each (n, m) SWCNT gives rise to one RBM in the form of a Lorentzian peak (isolated nanotubes) centred at a frequency of ω_{RBM}. The RBM frequency is inversely proportional to the SWCNT diameter and can be expressed as

$$\omega_{\mathrm{RBM}} = A/d_{\mathrm{t}} + B, \tag{2.18}$$

where A and B are parameters which depend on environmental effects such as the substrate material and tube-tube interactions [58]. Figure 2.9 shows various RBMs

obtained from a bundled HiPco SWCNT sample. The nanotube diameter distribution d_t and the electronic transition energies E_{ii} can be obtained from careful analysis of RBM RRS measurements, provided that the individual RBMs can be resolved. Furthermore, by comparing d_t and E_{ii} with calculated or empirical forms of the Kataura plot (Figure 2.6) one can accurately determine the (n,m) of an isolated SWCNT, or the diameter distribution of a bundled SWCNT sample [58–61].

The second first-order Raman feature in SWCNTs is known as the G-band. This feature is related to the tangential mode vibrations of the two carbon atoms in the graphene unit cell. In contrast to graphene, where the G-band can be found as a single Lorentzian peak at 1582cm^{-1}, the SWCNT G-band consists of many peaks distributed in the $1520-1595\text{cm}^{-1}$ range. The G-band consists of two main features, the G^+ band which can be found at 1592cm^{-1} and the G^- band at $\sim 1570\text{cm}^{-1}$ (shown in Figure 2.9). The G^+ band is due to vibrations along the nanotube axis (LO phonon) and so its frequency is not strongly dependent on SWCNT diameter, while the G^- band is due to vibrations in the circumferential direction of the SWCNT (TO phonon) and its frequency is strongly dependent on SWCNT diameter due to curvature effects. Furthermore, the lineshape of the G^- band is sensitive to whether the SWCNT is semiconducting or metallic. For semiconducting SWCNTs the G^- band exhibits a typical Lorentzian lineshape, while for metallic SWCNTs the G^- band exhibits an asymmetric Breit-Wigner-Fano (BWF) lineshape due to strong electron-phonon coupling [37, 62].

2.2.5 Second-order Raman Scattering of *D*-band and *G*'-band

There are two features in the Raman spectra of SWCNTs and graphene which are not predicted by group theory for first-order Raman scattering but have similar intensities to the RBM and G-band. These features are named the D-band and G'-band and they appear in the Raman spectra in the frequency range $1300-1400\text{cm}^{-1}$ and $2600-2800\text{cm}^{-1}$ respectively (Figure 2.9). There are several unique observations with regards the D- and G'-band features;

Observation 1 In graphene the D- and G'-band frequencies increase with increasing excitation energy.

Observation 2 In graphene the D-band can be well fitted with two Lorentzian functions of slightly different energy, while the G'-band requires only one Lorentzian to be fitted.

Observation 3 The G'-band frequency is approximately twice that of the D-band.

Observation 4 The intensity of D-band is proportional to the number of defects in a sample, while the G'-band has a similar intensity to the first-order G-band and is not defect dependent.

Observation 5 The D-band and G'-band linewidths are significantly broader for graphene than for isolated SWCNTs.

Observation 6 The G'-band Raman shift is slightly different for Stokes and anti-Stokes Raman scattering.

Each of these observations can be explained by the theory of second-order double-resonance (DR) Raman spectroscopy. In order to understand this, we will begin by looking at the simpler case of second-order DR Raman spectroscopy in graphene because it is from here that the phonons in SWCNT are derived. We will then discuss how the quantisation of the electron and phonon wavevectors in SWCNTs lead to more stringent DR scattering conditions.

Second-order Raman scattering involves two intermediate scattering events. These events can consist of either (1) one phonon and one elastic scattering event, or (2) two phonon scattering events where the two phonons can be the same (overtone mode) or different (combination mode). We will call these processes (1) one-phonon and (2) two-phonon second-order Raman scattering respectively. The fact that both electrons and holes can be involved, mean there are a total of 8 one-phonon second-order scattering processes and 4 two-phonon scattering processes. Figure 2.12 shows two forth-order Feynman diagrams representing (a) one-phonon and (b) two-phonon second-order Stokes Raman scattering involving electrons.

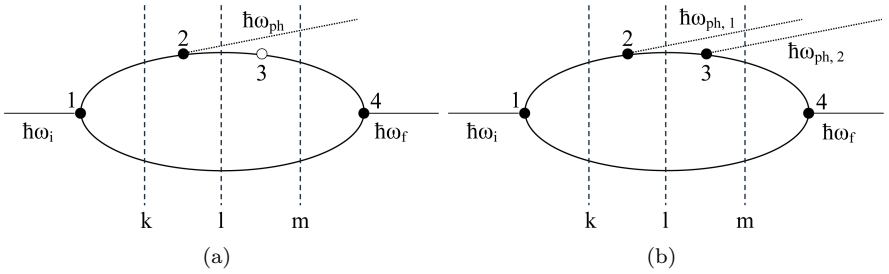

FIGURE 2.12: Forth-order Feynman diagrams showing (a) one-phonon and (b) two-phonon second-order Stokes Raman scattering processes. The vertices 1 and 4 represent the electron-hole excitation and recombination respectively. Vertex 2 and 3 represent the creation of a phonon (*solid circles*) or elestic scattering (*open circles*). The intermediate states are represented by *vertical dashed lines* and labelled (k, l, m).

The scattering rate Γ for these processes can be calculated from forth-order perturbation theory, where the matrix element describing the interactions is given by

$$|M| = \sum_{k,l,m} \frac{\langle 0|\,\hat{\mathrm{H}}_4\,|m\rangle\,\langle m|\,\hat{\mathrm{H}}_3\,|l\rangle\,\langle l|\,\hat{\mathrm{H}}_2\,|k\rangle\,\langle k|\,\hat{\mathrm{H}}_1\,|0\rangle}{(\hbar\omega_m + i\gamma_m - \hbar\omega_\mathrm{f})(\hbar\omega_l + i\gamma_l - \hbar\omega_\mathrm{i})(\hbar\omega_k + i\gamma_k - \hbar\omega_\mathrm{i})}, \tag{2.19}$$

where $\hat{\mathrm{H}}_1$ and $\hat{\mathrm{H}}_4$ are the electric dipole Hamiltonians for the incident and scattered photons, $\hat{\mathrm{H}}_2$ and $\hat{\mathrm{H}}_3$ are the Hamiltonian representing the two intermediate scattering events, $|k\rangle$ $|l\rangle$ and $|m\rangle$ are the intermediate electron-hole pair states, $\hbar\omega_{\mathrm{i}}$ is the initial photon energy, $\hbar\omega_{\mathrm{f}}$ is the scattered photon energy and ω_k and ω_l and ω_m are the energies of the three intermediate electron-hole pair states, and γ_k γ_l and γ_m denote the broadening factor of the resonance due to the finite lifetime of the intermediate electronic states.

In order for the electron and hole to recombine, we again require the initial and final states to differ by no more than 2 times the photon wavevector. In second-order Raman scattering this is achieved by two equal and opposite scattering wavevectors, q and $-$q, which return the electron to its original state. For this reason second-order Raman scattering can involve (q$\neq$ 0) phonons.

When two of the three intermediate states in the second-order Raman scattering process are real electronic states, the scattering rate becomes significantly enhanced. This is known as DR second-order Raman scattering. Figures 2.13 (a)-(d) show 4 one-phonon second-order DR Stokes Raman scattering events. The crossing lines in these figures represent the approximately linear dispersion relation around the K-point (K'-point) in graphene, while the real and virtual intermediate states are shown as solid and open circles respectively. Since the K and K' points in graphene are in-equivalent, both intra-valley and inter-valley scattering q vectors are allowed. In each case there is (1) an incoming or outgoing resonance and (2) one resonance involving the intermediate state k+q. The equal energy lines about the K-point can be approximated as circles centred on the K-point. Therefore, as depicted in Figures 2.14 (a) and (b), the possible q vectors (measured from the Γ-point) exist within a circle of radius $\sim$ 2k centred on the Γ or K point for intra-valley and inter-valley scattering respectively. In the phonon dispersion relation of graphene shown in Figure 2.15 (a) there is only one phonon branch whose energy, close to the K-point, matches the observed D-band frequency ($\sim$ 1300cm^{-1}). Thus we can assign the D-band to the inter-valley scattering of electrons by phonons around the K-point. The dispersive behaviour ($d\omega/dE_{\mathrm{L}} = 53\mathrm{cm}^{-1}/\mathrm{eV}$) of the D-band in graphene now becomes simple to explain [63]. Turning to Figure 2.13 (b), as the excitation energy increases the initial state k moves away from the K-point due to the linear dispersion E(k). This means that the q wave vector must also increase order to satisfy the DR condition. Furthermore, for any particular laser energy both incoming and outgoing resonance processes (Figures 2.13 (b) and (c)) can both be satisfied. This is the reason why the D-band can be fitted with two Lorentzian.

We now turn to the G'-band which has approximately twice the D-band frequency and double the dispersion. This observation can be explained by two-phonon second-order DR Raman scattering. Figures 2.13 (e)-(f) show 2 two-phonon second-order intra-band and inter-band DR Raman scattering events. In this case, two opposite momentum inter-valley scattering phonons around the K-point with energy $\sim$ 1300cm^{-1} combine,

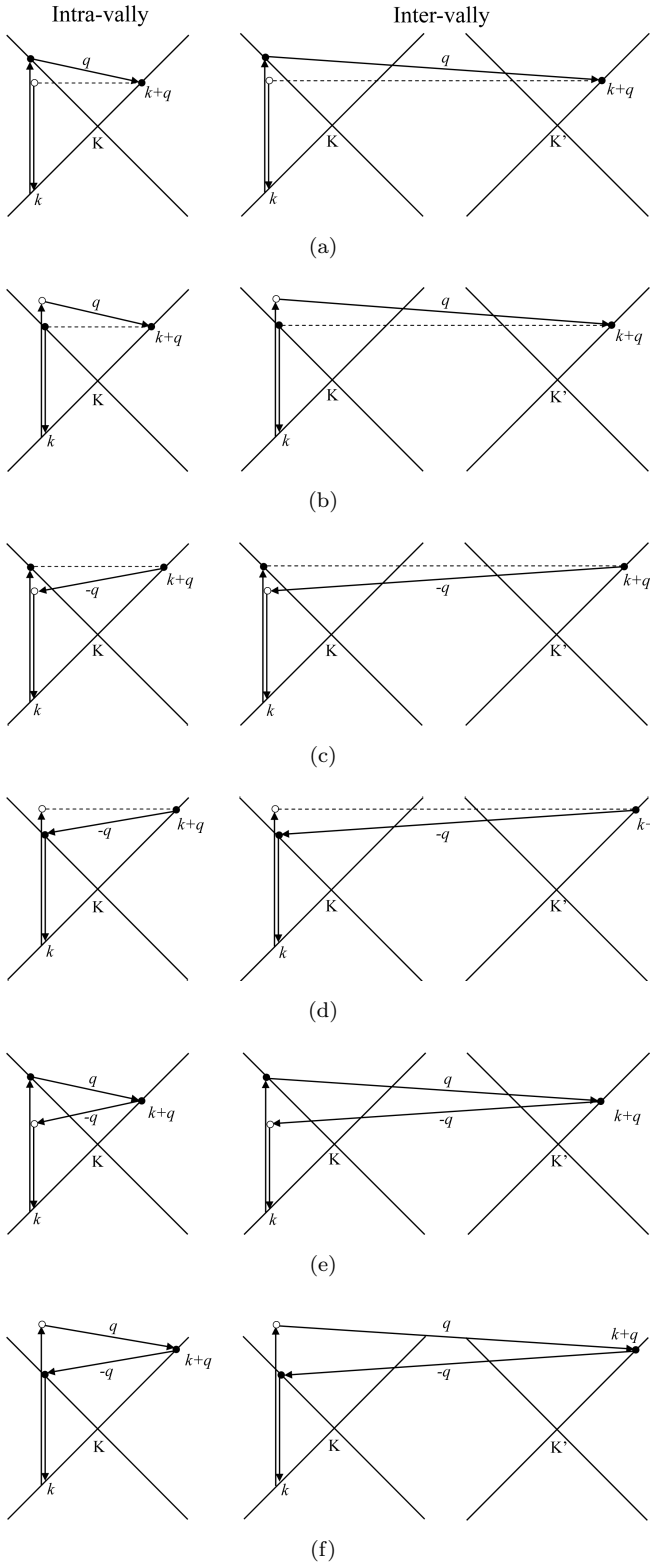

FIGURE 2.13: Second-order (a)-(d) one-phonon and (e)-(f) two-phonon double resonance Raman Stokes processes, showing intra-valley (left) and inter-valley (right) scattering processes. Equivalent anti-Stokes processes also exist. Real and virtual intermediate states are shown as *solid circles* and *open circles* respectively. The crossed lines represent the approximately linear dispersion relation near the K-point (and inequivalent K'-point) in graphene.

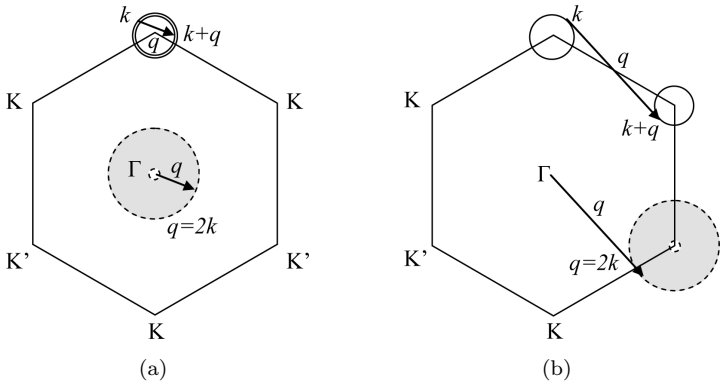

FIGURE 2.14: 2D Brillouin-zone of graphene showing possible q vectors for (a) intra-valley and (b) inter-valley scattering near the K-point. Equal energy contours are approximated as circles centred on the K-points. Possible q vectors lie within *shaded circles* as measured from the Γ-point.

giving rise to a Raman feature at $\sim 2600\text{cm}^{-1}$. This means that the G'-band can be considered an overtone of the D-band, probing similar phonons. Unlike one-phonon second-order Raman scattering, two-phonon Raman scattering does not require elastic scattering from a defect. This explains why the intensity of D-band is proportional to the number of defects in a sample, while the G'-band intensity is not defect dependent (observation 4).

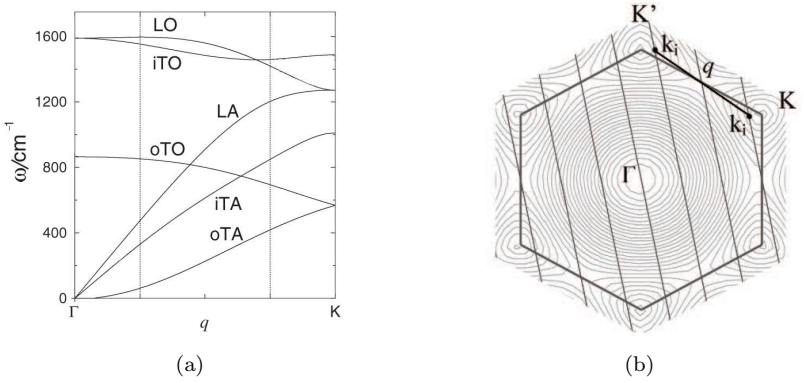

FIGURE 2.15: (a) Phonon dispersion relations for graphene showing the 6 phonon branches, adapted from [3]. (b) 2D Brillouin-zone of graphene showing cutting lines of a $(4, 2)$ SWCNT. k_i represent vHs points where the equal energy contours are tangential to the cutting lines giving rise to vHs in the electron DOS.

In the case of SWCNTs, the real electronic states are at points, k_i, where the equal energy contours of the 2D graphene dispersion relation are tangential to the cutting lines i.e where there is a vHs in the electron DOS (see Figure 2.15 (b)). This means that the D-band and G'-band features from SWCNTs are significantly enhanced when the initial (or final) state k and scattered state k+q are close to k_i points. This has two consequences which are relevant to the interpretation of the second-order Raman features in our experiments; (1) The incoming (or outgoing) resonance condition produces a discreet

resonance profile for each (n, m) SWCNT, similar those observed for RBMs. (2) Only DR Raman processes for which the two resonant states are close to the same energy i.e. those represented in Figures 2.13 (b) and (c), experience significant enhancement. This results in a narrower range of phonons contributing to the D-band and G'-band in SWCNT and explains why the second-order DR features in SWCNT Raman spectra exhibit narrower linewidths to those in graphene Raman spectra (observation 5). Using the same reasoning, two-phonon DR Raman scattering should be much weaker than one-phonon DR Raman scattering in SWCNT because it is not possible for the intermediate states to be the same energy (Figures 2.13 (e) and (f)). However, the G'-band intensity is generally much greater than the D-band intensity in SWCNT Raman spectra (see Figure 2.9). This observation suggests the electron-phonon interaction is much stronger than the interaction involving elastic scattering from a defect.

In addition to the possible Stokes processes that are shown in Figure 2.13, there exists an identical set of anti-Stokes processes which can be represented by reversing the processes (all of the arrows) in the figures. For a particular excitation energy, the DR condition in two-phonon Raman scattering processes (Figures 2.13 (e) and (f)), will select a smaller q scattering phonon for Stokes scattering than anti-Stokes scattering, due to the dispersion E(k) about K. This explains why the G'-band Raman shift is slightly different for Stokes and anti-Stokes scattering (observation 6).

2.2.6 Summary of Active Modes in SWCNTs and Graphene

In addition to the Raman features discussed in this section, there are a plethora of overtones and combination modes which give rise to a number of weak DR Raman features is SWCNTs. A comprehensive list of these features and details of their origin can be found in [37]. Table 2.2 summarises the Raman features from SWCNT and graphene which are relevant to this study. Details include; name, frequency, scattering process (where SR stands for single resonance and DR stands for double resonance), and dispersion $d\omega/dE_{\mathrm{L}}$ with laser energy E_{L}.

Name	$\omega(\mathrm{cm}^{-1})$	Resonance	$d\omega/dE_{\mathrm{L}}$	Description
RBM	$A/d_{\mathrm{t}} + B$	SR	0	Unique to nanotubes
Si	520	NA	0	TO mode Silicon Substrate
D	~ 1350	DR1	53	LO mode, Inter-vally
G^{-}	~ 1570	SR	0	Zone-center TO
G-band	1582	SR	0	Graphene only
G^{+}	1592	SR	0	Zone-center LO
G'	~ 2700	DR2	106	Overtone of D-mode

Table 2.2: Details of Raman active phonons in SWCNTs and graphene which are relevant to this study.

2.3 Linewidth of Raman Features

In addition to the spectral width of the excitation laser beam, there are several mechanisms that can contribute to the linewidth of SWCNT Raman features. These include (1) intrinsic contributions which can be separated into (a) contributions which broaden individual modes, such as phonon-phonon and electron-phonon interactions and (b) multiple mode coupling caused by the resonance Raman scattering processes, and (2) extrinsic effects (which are generally inhomogeneous) such as defects, deformations, tube-tube and tube-substrate interactions [64, 65]. Inhomogeneous broadening contributions can be *minimised* by taking SWCNT Raman measurements at the single nanotube level [65], however, it can still be difficult or even impossible to identify or separate out the individual contributions to the Raman linewidth [65].

In the case that inhomogeneous linewidth broadening and multiple mode coupling are negligible (i.e when the linewidth of the Raman feature represents the natural linewidth), the Raman linewidth Γ is determined by the total dephasing time T_2 of the phonon, and can be calculated in units of cm^{-1} by ($\Gamma = 1/\pi c T_2$). The total dephasing time T_2 is dependent on the pure dephasing time, τ_{ph}, and phonon population lifetime T_1 according to

$$2/T_2 = 2/\tau_{\mathrm{ph}} + 1/T_1. \tag{2.20}$$

This means that linewidth studies can only provide limited information on the phonon dynamics, even when the Raman linewidth is a good measure of T_2. There have been many studies which make estimates of optical phonon lifetimes in SWCNT using the full-width-half-maximum (FWHM) of the Raman lineshape Γ [34, 66]. However, these studies rely on the assumption that the mechanisms contributing to the Raman linewidth are known, and can only provide a lower-bound estimate of the phonon population lifetime T_1. If we wish to present the phonon dynamics of SWCNTs in detail, T_1 and T_2 must be independently measured through other means, such as time-resolved Raman spectroscopy techniques.

2.4 Time-Resolved Raman Spectroscopy

Time-resolved Raman spectroscopy allows the dynamics of Raman active phonons to be measured directly. There are two fundamental approaches to time-resolved Raman spectroscopy, (1) the coherent approach, which usually measures the total dephasing dynamics T_2 and (2) the incoherent approach which measures the phonon population dynamics T_1. There are two experimental techniques which have been used for coherent and incoherent SWCNT phonon dynamics studies, these techniques are known as

time-resolved coherent anti-Stoke Raman spectroscopy (TRCARS) and time-resolved incoherent anti-Stoke Raman spectroscopy or TRIARS. In this section the basic principles of TRCARS and TRIARS are discussed, and a summary of previous coherent and incoherent time-resolved Raman studies of phonon dynamics in SWCNTs is provided.

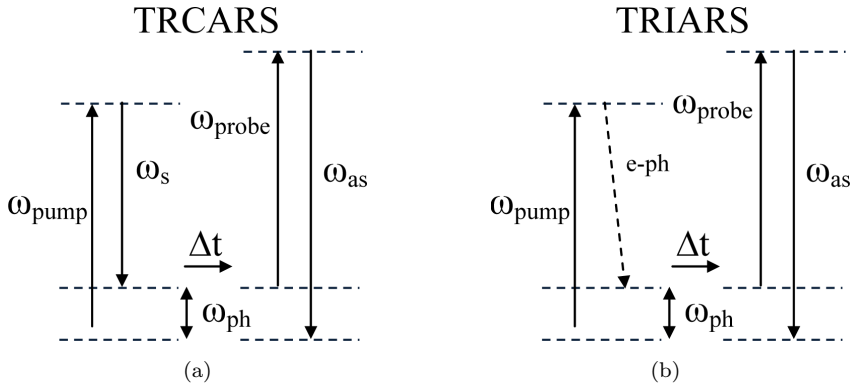

FIGURE 2.16: (a) TRCARS schematic showing transitions (see text for details). (b) TRIARS schematic showing transitions (see text for details).

In a typical TRCARS experiment (see Figure 2.16) (a) a pump pulse and Stokes pulse simultaneously arrive at the sample. The pump pulse with energy $\hbar\omega_{\text{pump}}$ excites the system from the ground state to a real or virtual state, while the Stokes pulse with energy $\hbar\omega_{\text{s}} = \hbar\omega_{\text{pump}} - \hbar\omega_{\text{ph}}$ stimulates Stokes scattering, generating a coherent superposition of phonons of energy $\hbar\omega_{\text{ph}}$, which is effectively a sound wave. After a time delay Δt a probe pulse of energy $\hbar\omega_{\text{as}}$ provides an anti-Stokes Raman signal whose intensity is proportional to the amplitude of the coherent phonon superposition. Monitoring the anti-Stokes Raman signal intensity as a function of pump-probe delay allows the total dephasing dynamics T_2 to be measured. In the case of a simple TRCARS experiment, it has been shown that the measured lifetime contains both homogeneous and inhomogeneous contributions and can be a measure of free induction decay [54, 67, 68], which is comparable to line-shape analysis in the frequency domain (discussed in Section 2.3). Raman echo is another coherent time-resolved Raman technique, which can determine the extent of inhomogeneous broadening under certain experimental conditions [68, 69]. In a typical Raman echo experiment the system is coherently excited by a set of pump pulses in a similar manner to a TRCARS experiment. A second re-phasing pulse (π-pulse) introduced at time, t, then reverses the dephasing process. At a time $2t$ a probe pulse detects the amount of coherence through the anti-Stokes Raman signal intensity. There have been no reported Raman echo experiments carried out on SWCNTs, most probably due to the complex experimental setup, however one should be aware that the technique exists.

In a typical TRIARS experiment (see Figure 2.16) (b) a pump pulse photo-excites electron-hole pairs with excess energy in the sample. These electron-hole pairs then rapidly cool through carrier-phonon interactions, generating an incoherent non-equilibrium

phonon population in the process. A time delayed, Δt, probe pulse then provides an anti-Stokes Raman signal whose intensity is proportional to the phonon population. In this case, monitoring the anti-Stokes Raman signal as a function of pump-probe delay allows the population lifetime, T_1, to be measured.

The first time-resolved Raman study of SWCNTs was reported in 2008 by Song et al. [55]. In this study, an elaborate two-colour TRIARS approach was used to excite isolated $(6, 5)$ SWCNTs via their E_{11} transition and probe via their E_{22} transition. A room temperature lifetime of 1.1 ± 0.2ps was obtained for the G-band phonon population, which was comparable with estimates obtained from spontaneous Raman linewidth studies. This work encouraged two subsequent TRIARS studies [6, 40] and one TRCARS study of G-mode phonon dynamics in SWCNTs [54]. These studies are reviewed in detail in Chapter 5.

In this thesis, a co-polarised degenerate TRIARS approach has been developed to measure population lifetimes of the G, D and G'-band phonons in the temperature range of 4 to 600K. The major advantage of a degenerate TRIARS experiment is that both the pump and probe pulses can be tuned to the same E_{ii}, which maximises the TRIARS signal. A full description of this technique, including a discussion of the advantages and disadvantages are given in Section 3.3.

2.5 Ultrafast Electron and Phonon Dynamics in SWCNTs

Electron and phonon dynamics in SWCNTs have been extensively studied in recent years, not least because they provide insight into electron-electron (e-e), electron-phonon (e-ph), and phonon-phonon (ph-ph) interactions, which play a fundamental role in Raman scattering processes [70, 71], carrier transport [30, 33, 34] and heat conductivity [16, 72].

In bulk inorganic semiconductors, e-e, e-ph, and ph-ph interactions are, in general, well understood and are treated in a number of textbooks including 'Introductory Solid State Physics' written by H.P.Myers [51] and 'Quantum processes in Semiconductors' written by B.K.Ridley [73]. Meanwhile, in low-dimensional systems, such as SWCNTs and graphene, the confinement of electrons and phonons complicates the situation, and this has led to conflicting experimental and theoretical results [74–77]. It is beyond the scope of this thesis to understand all of the possible mechanisms which play a role in electron and phonon dynamics in SWCNTs. Instead, this section provides details of the scattering mechanisms which are thought to be most important to understanding the phonon population dynamics reported in Chapters 5 and 6. The section concludes with discussions on how the G-band (Γ-point) and D- and G'-band (K-point) phonon populations may be generated during the TRIARS experiments in this thesis.

2.5.1 Carrier-Carrier Scattering in SWCNTs

Carrier-carrier scattering events are governed by the electrostatic interaction between charged particles (the Coulomb interaction) and are responsible for randomly redistributing energy and momentum among photoexcited carriers while conserving energy and momentum in the total carrier population [78]. In general e-e and h-h scattering tends to thermalise the electron and hole distributions, while e-h scattering tends to bring the two distributions to a common temperature. Carrier-carrier scattering can be responsible for both intra- and inter-sub-band processes. A detailed discussion of carrier-carrier scattering rates in bulk semiconductors can be found in Ref [73].

For $1D$ systems it is common to see a significant enhancement in the carrier-carrier scattering rate, which can be explained by spatial confinement and reduced effectiveness in screening [79]. It is understood that a hot photoexcited carrier population in SWCNTs will thermalise via the e-e interaction on a time-scale of approximately 30 fs [80, 81], which results in an electronic system with a well-defined temperature that is above the lattice temperature.

Multiple carrier scattering processes, such as Auger recombination, can be invoked to explain the promotion of electrons to energy states much higher than the population of photo-excited electrons. Auger recombination involves exciton-exciton annihilation where the resulting energy is transferred to other charge carriers [79, 82, 83].

2.5.2 Carrier-Phonon Scattering

Carrier-phonon scattering events in carbon nanotubes are due to the deformation-potential interaction [84]. Electron-phonon (e-ph) scattering is responsible for both intra- and inter-sub-band and intra- and inter-valley scattering processes, which play a fundamental role in Raman scattering in SWCNTs [37]. e-ph scattering is also responsible for the strong coupling between high-energy electrons and optical phonons [32, 35, 36], which limits high-field transport in SWCNTs.

Although the timescale of e-ph scattering events in SWCNTs are not known, they are believed to be on the order of tens of femtoseconds. For example, after E_{22} photoexcitation of a particular species of SWCNTs, the electrons and holes in the E_{22} sub-band are expected to relax to the fundamental band edge via various e-ph scattering processes, with strong coupling expected for optical phonons which can be represented near the Γ and K points in the graphene Brillouin-zone [33, 34, 36], and this process has been observed to occur in less than 100 fs [80, 85].

2.5.3 Anharmonic Phonon Scattering

There are a number of good textbooks and publications which provided a mathematical treatment for anharmonic phonon-phonon scattering in crystals [86–88]. This section is intended to give a brief overview of this topic and summarise the important points which are relevant to the interpretation of the results in Chapters 5 and 6. Within the harmonic approximation phonons do not interact and have an infinite lifetime. However, when one includes higher order terms in the expansion of the crystal potential, phonon-phonon (anharmonic) interactions are possible. In perturbation theory, the crystal potential can be expanded to increasing order terms which describe three, four, five ... phonon anharmonic interactions respectively. The strength of anharmonic interactions decreases rapidly as the number of phonons involved in the process increases. This means that in general, three-phonon process, where one phonon decays to produce two phonons or visa-versa, are the most common anharmonic interactions. It can be shown [86, 87] that the decay rate for a phonon with wavevector $\vec{q'}$ for three-phonon anharmonic scattering is given by

$$\begin{aligned}\Gamma_{ph-ph}(\vec{q'},i) \propto \sum_{\vec{q},i_1,i_2} |V_3 \begin{pmatrix} \vec{q'} & \vec{q} & -\vec{q} \\ i & i_1 & i_2 \end{pmatrix}|^2 \\ \times \{[1+n(\vec{q},i_1)+n(-\vec{q},i_2)] \times \delta(\omega(\vec{q'})-\omega(\vec{q},i_1)-\omega(-\vec{q},i_2)) \\ + 2[n(\vec{q},i_1)-n(-\vec{q},i_2)] \times \delta(\omega(\vec{q'})+\omega(\vec{q},i_1)-\omega(-\vec{q},i_2))\}, \end{aligned} \quad (2.21)$$

where the matrix element V_3 is proportional to the third derivative of the inter-atomic displacement, n are the occupation numbers of the phonons calculated from Bose-Einstein statistics ($n = [1/exp(\hbar\omega_{q,i}/k_BT) - 1]^{-1}$), the δ functions are necessary in order to satisfy energy and momentum conservation and the sum is performed over all possible phonon branches i_1 and i_2. The first term in Equation 2.21 describes the down-conversion three-phonon process, where a parent phonon decays into two lower-energy daughter phonons, while the second term describes the up-conversion process, where two phonons scatter to create a single higher-energy phonon. Only the first term is believed to be important in our measurements since the up-conversion process requires a significant number of higher energy states to scatter into, and the optical phonons that are measured are effectively the highest energy phonons in the system [37, 40].

The fact that the decay rate is dependent on the phonon occupation numbers, which in turn are dependent on the sample temperature, can be interpreted as the thermal activation of decay channels. Assuming that the optical phonon population decay rates measured in this thesis are dominated by three-phonon anharmonic decay processes, equation 2.21 tells us that temperature dependence of the decay rate will follow $\Gamma(T) = \Gamma_0[1 + n(E_1,T) + n(E_2,T)]$.

2.5.4 Generation of *G*-band Phonons in a TRIARS Experiment

During the G-band TRIARS experiments in Chapter 5, the laser excitation energies are directly resonant with the E_{22} optical transitions of various semiconducting SWCNTs species. The results from these TRIARS experiments indicate that a non-equilibrium population of Γ-point ($q \sim 0$) phonons is generated on a rapid (< 200 fs) timescale, before decaying freely through various anharmonic processes.

To consider how these phonons may be generated we turn to Figure 2.17 which shows a schematic representation of the E_{11} and E_{22} sub-bands in a semiconducting SWCNT. To begin the process, an incoming laser pulse with an average photon energy approximately equal to the E_{22} optical transition energy ($\hbar\omega_{\mathrm{L}} \sim E_{22}$) generates photoexcited electrons at the lowest point on the E_{22} sub-band, indicated as point A in figure 2.17. Femtosecond transient absorption and fluorescence measurements have shown that these electrons relax to the fundamental band edge (point C) in less than 100 fs [80, 85]. In order to emit a G-band $q \sim 0$ phonon an electron must scatter between two allowed states which have approximately the same momentum but a difference in energy of one G-band phonon energy ($\hbar\omega_G = 0.20$ eV). Therefore, it is proposed that the G-band phonons are generated high up in the fundamental sub-band, indicated as point B in figure 2.17. Both e-e and e-ph scattering events are likely to contribute to the inter sub-band scattering of electrons from the point A to point B.

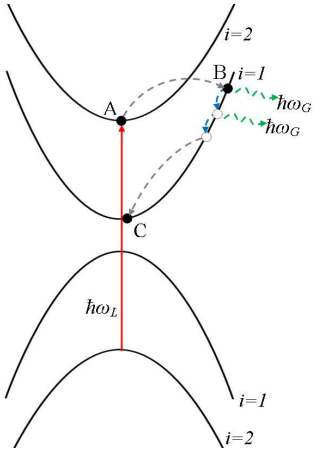

FIGURE 2.17: A schematic representation of the E_{11} and E_{22} sub-bands in a semiconducting SWCNTs, showing the possible processes which lead to the generation of G-band ($q = 0$) phonons after E_{22} optical absorption. It is believed that G-band phonons are generated by the relaxation of electrons high up in the E_{22} sub-band.

After possibly generating a number of G-band phonons, an electron high up in the fundamental band will eventually relax to the fundamental band edge (point C). One implication of this process is that once all of the electrons arrive at the fundamental band edge, they are unlikely to interact with G-band phonons due to the flat nature of the dispersion and because of energy and momentum conservation. The fact that all of the E_{22} photoexcited electrons are expected to arrive at the fundamental band

edge (point C) in less than 100 fs suggests that a G-band phonon population will be rapidly generated and then allowed to decay freely without further interaction from the electrons, assuming that the above process is dominant in phonon generation.

2.5.5 Generation of D-band Phonons in a TRIARS Experiment

The D- and G'-band TRIARS experiments in Chapter 6 were performed for the same SWCNT sample and for the same excitation conditions as the G-band TRIARS measurements in Chapter 5. The results from these TRIARS experiments indicate that a non-equilibrium population of D- and G'-band phonons is also being generated in the resonant SWCNTs, on a timescale less than 200fs, before decaying freely through various anharmonic (and possibly other) decay processes. The phonons responsible for the D- and G'-band features in the experiments, as predicted by double resonance Raman theory (see Section 2.2.5), are phonons which can be represented close to the K-point in the graphene Brillouin-zone as vectors which join two vHs in the electronic DOS, as depicted in Figure 2.18 (a).

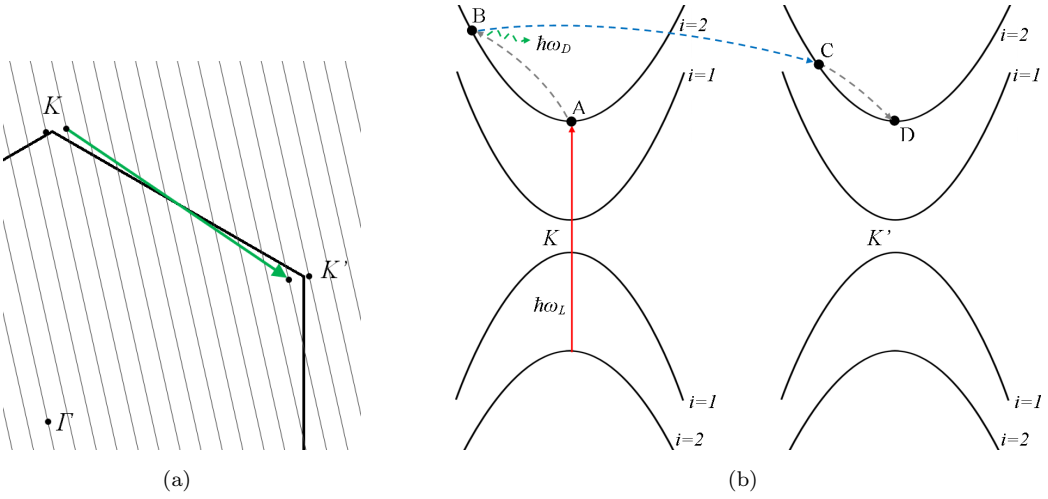

FIGURE 2.18: (a) Schematic representation of the D- and G'-band phonons probed by the TRIARS experiments in this thesis. (b) A schematic representation of the E_{11} and E_{22} sub-bands in a semiconducting SWCNTs at the non-equivalent K points, showing the possible processes which lead to the generation of D and G'-band (K) phonons after E_{22} optical absorption. It is believed that the phonons are generated by the intervalley relaxation of electrons high up in the E_{11} and E_{22} sub-bands.

To consider how the K phonons may be generated we turn to Figure 2.18 (b) which shows a schematic representation of the E_{11} and E_{22} sub-bands in a semiconducting SWCNTs at the non-equivalent K points. Again an incoming laser pulse with an average photon energy approximately equal to the E_{22} optical transition energy ($\hbar\omega_{\mathrm{L}} \sim E_{22}$) generates photoexcited electrons at the lowest point on the E_{22} sub-band, indicated as point A in figure 2.18. As discussed in Section 2.5.4 these electrons are observed to relax to the fundamental band edge in less than 100 fs. In order to emit a phonon close to the

K-point an electron must undergo intervalley scattering between the two real states at non-equivalent K points. Due to energy and momentum conservation it is proposed that this predominantly occurs for electrons which are high up in the sub-bands where the dispersion is steep. This could obviously occur following inter sub-band scattering of the photoexcited electrons to a point high up in the E_{11} sub-band, or, as shown in Figure 2.18, could occur following intra sub-band scattering of electrons to a point high up in the E_{22} sub-band. More importantly, once the electrons relax to the fundamental band edge, which occurs in less than 200 fs, they will be far less likely to generate K phonons. This suggests that the D- and G'-band phonon population will be rapidly generated and then allowed to decay freely without further interaction from the electrons, assuming that the above process is dominant in phonon generation.

2.5.6 Excitonic Effects

Recent work suggests that light absorption in SWCNTs results in strongly-correlated electron-hole states known as excitons [89–93]. The binding energies of these excitons, which can be probed by excitation spectroscopy [89], are measured to be on the order of 400 meV (for 0.8 nm diameter SWCNTs). Since there is still some debate as to whether excitonic effects play a significant role in SWCNT RRS, and because the (n, m) assignments presented in Section 4.2.4 are consistent with the known diameter distribution of the sample and in reasonable agreement with the optical resonances predicted by the simpler model based only on the vHs and JDOS, excitonic effects are not considered in this work. It is apparent that further experimental work will be required to settle the debate. Whatever the outcome, it is not expected to have a significant impact on the conclusions reached in Chapter 4, or effect the experimental results in Chapters 5 and 6.

Chapter 3

Experimental Apparatus and Techniques

In this chapter, the experimental apparatus and techniques which are used throughout this work are discussed. The experiments in this thesis are based on two techniques, continuous-wave (CW) RRS and ultrafast TRIARS. The first section of this chapter contains information on the general experimental apparatus and techniques which were used for the experiments, including a discussion of the laser system, the Raman microscope and the detection system. The ability to carry out measurements on SWCNTs in the temperature range 4-600K was crucial for studying the scattering mechanisms which govern the phonon dynamics. Therefore, a discussion is provided on the apparatus and techniques which were used to control the sample environment. A section has also been dedicated to sample preparation. The chapter concludes with detailed discussions on how the RRS and TRIARS experiments were performed.

3.1 General Experimental Apparatus and Techniques

This section provides details on the general experimental apparatus and techniques which are relevant to the CW RRS and ultrafast TRIARS experiments. Wherever possible, the key specifications of the individual components are provided to assist any reader who is attempting to replicate the experiments.

3.1.1 Laser System

The light source used in the experiments is a Coherent Mira 900-P Titanium Sapphire ($Ti:Al_2O_3$) solid-state laser which is pumped by a Coherent Verdi V-8 frequency-doubled diode-pumped single mode 532nm laser. This laser system allows simple switching between CW and mode-locked operation which is ideal for performing both RRS and TRIARS experiments. The basic theory of mode-locking and the propagation of laser pulses are treated in many textbooks [94, 95] and will not be included here. This section includes a detailed description of the laser system used and discussions on the techniques used to characterise, monitor, and filter the laser output.

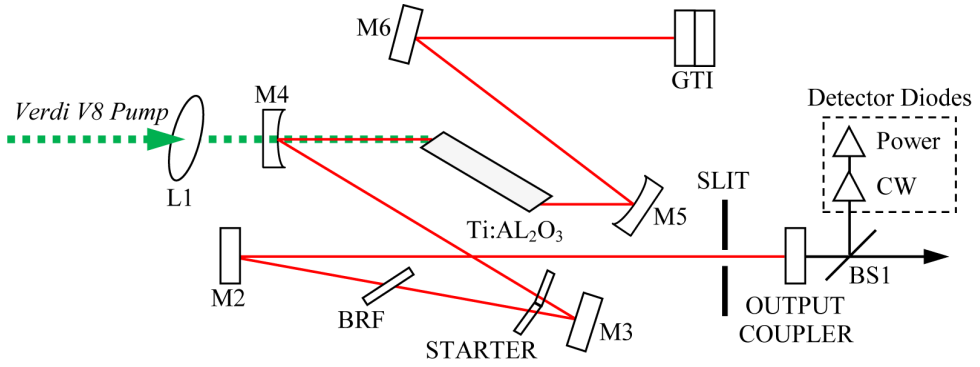

FIGURE 3.1: Schematic of Coherent Mira 900-P Ti:Sa laser cavity showing Gires-Tournois interferometer (GTI), gain medium ($Ti:Al_2O_3$), birefringent filter (BRF) and other various components (see main text for more details).

The Mira 900-P laser cavity is illustrated in Figure 3.1. The pump beam (*green*) enters the cavity thorough a mirror (M4) after passing through a lens (L1) which focuses the 532nm beam onto the $Ti:Al_2O_3$ crystal where it is strongly absorbed. To produce ultrafast pulses from the broad emission spectrum of the $Ti:Al_2O_3$ crystal, the Mira 900 cavity design uses a passive mode-locking technique known as Kerr lens mode-locking (KLM) [96]. The Kerr effect causes the refractive index of the gain medium to be modified when the field intensity is sufficiently high. This causes a lensing effect, which results in a smaller beam size for mode-locked pulses than for the CW light. When the slit prior to the output coupler is fully open the cavity operates in CW mode, however, when the slit is narrowed to clip the wider CW beam, the CW mode experiences higher loss than the pulsed mode. The Mira becomes mode-locked when the CW loss reaches the lasing threshold for the CW mode. The Gires-Tournois interferometer (GTI) provides a negative group-velocity-dispersion (GVD) to correct for the positive GVD inside the cavity, which would otherwise cause broadening of the ultrafast pulses. The angle of a birefringent filter (BRF) can be tuned to select the narrow band of modes supported by cavity. The BRF provides almost continuous wavelength tuning in the 700-980nm range, which is ideal for RRS measurements on SWCNTs. The emission spectrum of the $Ti:Al_2O_3$ crystal and the performance of the various optical elements in the system both contribute to an output power profile which peaks in the center of the operational range

(approximately 800nm), and drops-off rapidly at the long and short wavelength limits, as shown in Figure 3.2. It can be difficult to achieve stable mode-locking of the Ti:Sa at certain wavelengths because of absorption caused by the presence of water vapour and oxygen in the laser cavity. To manage this problem the Mira 900-P laser cavity was always purged with a continuous flow of dry nitrogen during mode-locking operation.

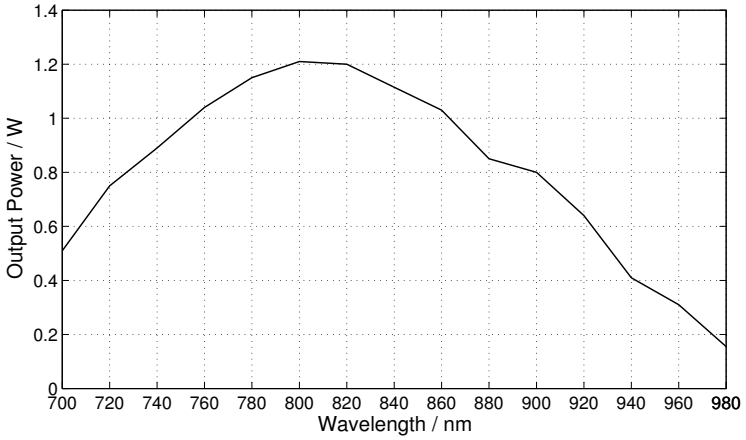

FIGURE 3.2: Power output of Mira 900-P laser system. Measured in CW mode across the entire operational range of the system.

Specification	Mira 900-P
Power Output	See Figure 3.2
Tuning Range	700-980nm
Pulse duration	$\sim$ 1.9ps (optimised)
Repetition Rate	76 MHz
Noise	$< 0.1\%$
Stability	$< 3\%$
Beam Diameter	$\sim$ 0.8mm
Divergence	1.7mrad
Spatial Mode	TEM_{00}
Polarisation	Horizontal

TABLE 3.1: Laser system specifications relevant to CW and mode-locked operation.

There are several advantages to using this laser system for ultrafast TRIARS measurements on SWCNTs. Firstly, the Mira output contains low noise ($< 0.1\%$ intensity fluctuations) due to the inherently stable single-frequency Verdi-V8 pump laser. The commercial Mira-900 laser also features a CW detector, humidity sensor, automatic starter and a computer monitoring β-lock mode, which all contribute to a system with superior long term stability ($< 3\%$ intensity drift). Specifications of the Mira 900-P system are given in Table 3.1. The duration of picosecond pulses produced by the Mira-900 could be reduced (to an extent) by manually adjusting a bias voltage supplied to the GTI while monitoring the pulses produced in real-time. This functionality was particularly important for setting up TRIARS experiments, where the temporal and spectral resolution of the experiments is limited by the duration and spectral width of the laser pulses.

3.1.1.1 Monitoring the Laser Source

The output spectrum of the Ti:Sa was monitored in real-time using an Ocean Optics HR4000 high-resolution spectrometer. The HR4000 spectrometer is based on a symmetrical crossed Czerny-Turner design with fixed diffraction grating and CCD (3648 pixels), and has a spectral resolution of 0.25nm/px. The output power of the Ti:Sa was monitored using a Spectra-Physics 407A thermopile power detector, which has a power range of $<$ 5mW to 20W and a calibration accuracy of $\pm 1\%$ for 1W at 800nm. Both of these tools were valuable for aligning and tuning the wavelength of the laser cavity. For more accurate spectral measurements, i.e. during Raman experiments, the laser source was scattered into the TriVista triple spectrometer (see Section 3.1.3), which was capable of providing a maximum spectral resolution of 0.012nm/px. At lower powers levels, and where precise measurements of the beam power was required, a Newport 2832-C power meter and 818-IR low power attenuated detector were used. The 2832-C power meter has an internal calibration for the spectral response of the 818-IR detector in order to produce reliable readings for the wavelengths being measured. The CW component of the laser output was monitored by a diode in the Ti:Sa laser head. To measure the ultrafast laser pulse durations in real-time an intensity autocorrelator was built (see Section 3.1.1.2).

3.1.1.2 Temporal Characterisation of Pulses

The duration of the ultrafast laser pulses were measured using an intensity autocorrelator [97]. The autocorrelator was based on a two-arm collinear design, and the autocorrelation signal was provided by the non-linear two-photon absorption (TPA) of a gallium phosphide (GaP) photodiode. In one of the arms of the autocorrelator, a mirror was mounted on a loudspeaker which was driven at approximately 50Hz with sufficient amplitude to provide the temporal overlap of the pulses. The time axis was calibrated by introducing a delay into one of the arms of the autocorrelator in increments of 1ps using a high precision translational stage. Figure 3.3 (a) shows a typical calibration measurement for a pulse generated by the Mira 900 laser at a wavelength of 820nm. Figure 3.3 (b) shows two calibrated and normalised autocorrelation measurements, one obtained shortly after mode-locking the laser (*black line*) and one obtained after minimising the pulse duration by supplying a small positive bias voltage to the GTI (*red line*).

To extract the pulse duration from the autocorrelation measurements in Figure 3.3 (b) some assumptions have to be made as to the exact temporal shape of the pulses. A reasonable fit to the autocorrelation shape was a Gaussian function. For an autocorrelation pulse of this shape the deconvolution factor is 0.707. This means that the pulse intensity FWHM is 0.707 times the intensity autocorrelation FWHM [97]. The pulse durations in Figure 3.3 (b), are 3.92ps and 2.10ps respectively. This demonstrates the extent to which the pulse durations could be tuned using the GTI bias voltage (see Section 3.1.1).

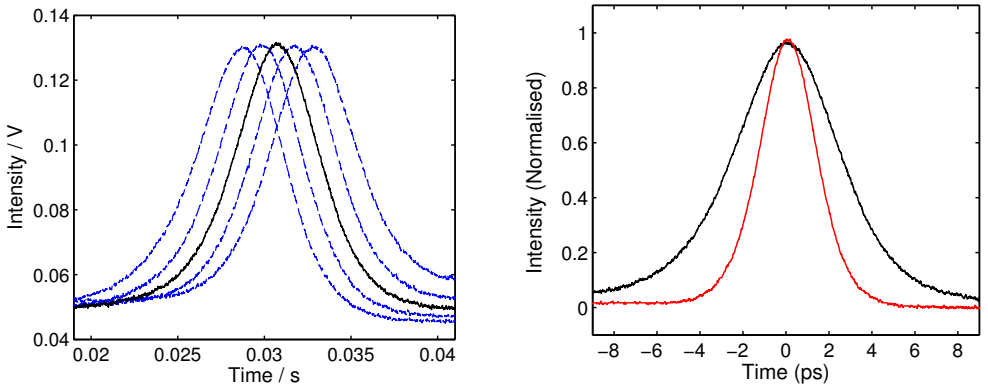

(a) (b)

FIGURE 3.3: (a) Non-calibrated intensity autocorrelation (*solid black line*) and calibration measurements (*broken blue lines*) taken after introducing a delay into one of the arms of the autocorrelator in increments of 1ps. (b) Calibrated and normalised autocorrelation measurements obtained shortly after mode-locking the laser (*black line*) and after minimising the pulse duration by supplying a small positive bias voltage to the GTI (*red line*).

3.1.1.3 Filtering the Laser Source

It was necessary to spectrally filter the light from the laser source to ensure that unwanted broadband fluorescence produced in the Ti:Sa laser system would not enter the Raman microscope or detector system. The laser source was filtered using a Photon Etc. laser line tunable filter (LLTF) during CW operation and a Laserspec LLTF during mode-locked operation. The specifications of these bandpass filters are given in Table 3.2.

Filter	Photon Etc. LLTF	Laserspec LLTF
Spectral Range (nm)	$715 - 1000$	$420 - 995$
Bandwidth (nm)	< 0.4	~ 1.0
Suppression @ 50cm^{-1}	ND4	ND3

TABLE 3.2: Specifications of Photon Etc. LLTF and Laserspec LLFT spectral filters.

The < 0.4nm FWHM bandwidth of the Photon Etc. LLTF was ideal for filtering the laser output in CW operation, and provided high out-of-band rejection, allowing CW Raman measurements to be obtained within 20cm^{-1} of the laser line. However, during mode-locking the bandwidth of this filter was generally shorter than the spectral width of the laser pulses (~ 0.4nm), which resulted in unwanted pulse broadening. The Laserspec LLTF had sufficient bandwidth to pass the ~ 2ps pulses without causing significant pulse broadening. The dispersive behaviour of the filters was investigated using the intensity autocorrelator (see Section 3.1.1.2).

3.1.2 Raman Microscope

The Raman measurements in this thesis were performed using a custom built Raman microscope with a back-scattering configuration. In this configuration the Raman microscope delivers the laser light to the sample whilst also collecting and collimating the back-scattered Raman light for detection. This design is known for its superior stability, and has been used in a wide number of TRIARS and RRS studies [40, 55, 58, 61]. In addition to the Raman microscope, an in-situ optical microscope was built to provide real-time imaging of the sample and the laser focal spot. This was a valuable tool for monitoring the region of the sample which was being probed and for assisting with the spatial and temporal overlapping of pump and probe beams during the TRIARS experiments.

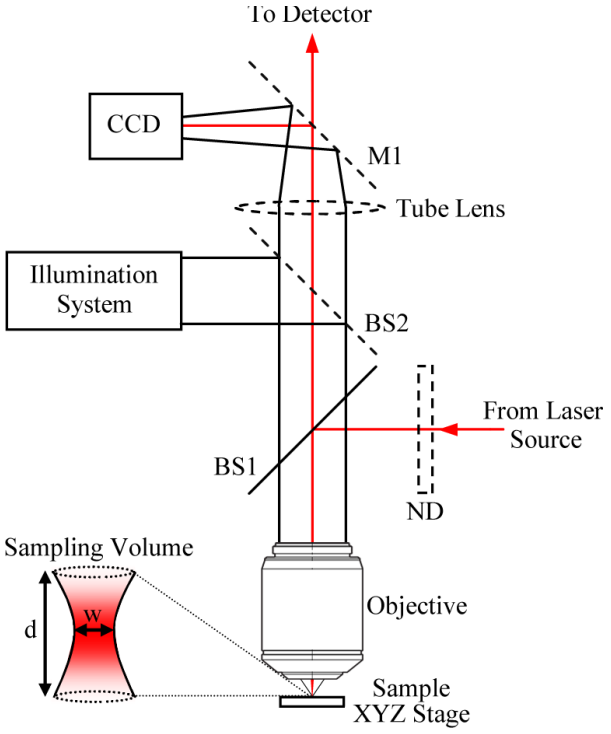

FIGURE 3.4: Schematic of the combined Raman microscope and in-situ optical microscope system. Dashed lines indicate removable optics which allow switching between Raman microscope operation and in-situ optical microscope operation.

Figure 3.4 shows a schematic of the Raman microscope and in-situ optical microscope system. The microscope has two modes of operation (1) Raman microscope operation and (2) optical microscope operation. The microscope was designed in such a way that certain optical components (shown as dashed symbols in figure 3.4) could be easily removed and replaced without disturbing the Raman microscope alignment when switching between the two modes of operation. During Raman microscope operation, the laser beam enters the Raman microscope and is reflected from an ultra-thin 50 : 50 beamsplitter (BS1). The beam is then brought to a focus by a LMPLan-IR 50x objective with a numerical aperture of 0.55, focal distance of 3.6mm and working distance of

6.0mm. The focused beam results in a sampling volume (see Figure 3.4), which has a waist (spot size) w where the energy density is at its greatest, and depth d defined by the point where there is no longer any appreciable Raman scattering. The focal spot diameter was approximated by recording the power transmitted through a 1μm pinhole which was translated horizontally across the beam at the beam waist, while the focal depth was approximated by recording the intensity of the 520cm^{-1} Raman feature from a Si substrate as a function of distance between the focal plane and substrate i.e as a function of defocusing. For the wavelengths used in the experiments the focal spot diameter and focal depth were measured to be approximately 1μm ($1/e^2$ radii) and 2μm respectively. The sample was mounted on an XYZ translational stage for spatial (XY) Raman measurements and focusing (Z) of the Raman microscope. Raman and Rayleigh scattered photons which are back-scattered into the objective are collimated into the detection system (see Section 3.1.3). During optical microscope operation the intensity of the laser beam was reduced by passing the beam through an absorptive neutral density filter (ND) with a transmission of 0.01% before the beam entered the Raman microscope. A typical illumination system containing an aperture stop and field stop was constructed to illuminate the sample via a second broadband 50 : 50 beamsplitter (BS2). A Zeiss tube lens was placed at the correct distance to form an image of the infinity corrected objective focal plane on a Chameleon CMLN-1352M CCD camera via a mirror (M1). One important feature of the microscope setup was that the interchangeable optics did not disturb the laser position on sample.

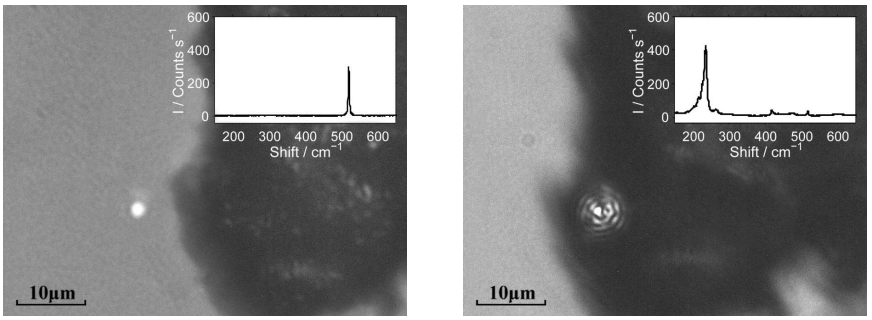

(a) (b)

FIGURE 3.5: Microscope images of a bundled SWCNTs aggregate (*dark region*) deposited onto an Si/SiO_2 substrate, showing the focused laser spot positioned (a) on the Si/SiO_2 substrate and (b) on the bundled nanotube aggregate. Insets show the Raman spectra that were obtained in each case.

Figure 3.5 (a) shows an image of a bundled SWCNTs aggregate (*dark regio*n) deposited onto an Si/SiO_2 substrate, obtained using the in-situ optical microscope. The scale of the image on the CCD detector was calibrated using the translation stage on which the sample was mounted. The bright circle in the center of the image shows the focal spot (approximately 1μm diameter) of the laser beam focused onto the Si substrate. Figure 3.5 (b) shows the image obtained when the sample was translated horizontally 10μm so that the focal spot was positioned to the SWCNT bundles. After focusing the laser

spot onto the Si/SiO_2 substrate and translating the sample so that the focal spot was positioned in the region of the bundled SWCNTs, the sampling region was translated by half of the focal depth (1μm) in the z direction (away from the substrate), so that the sampling volume contained predominantly bundled SWCNTs. The Raman spectra obtained for the focal spot positions are shown in the inset of each figure. Figure 3.5 (a) (inset) shows a single peak at $520cm^{-1}$ which is attributed to the TO mode of Si, while Figure 3.5 (b) (inset) shows a range of peaks corresponding to the RBMs of different SWCNTs in resonance with the excitation energy of the laser.

3.1.3 Raman Detection System

The detection system must be able to measure a very small quantity of Raman scattered light amongst a large quantity of Rayleigh scattered light with similar wavelength. The system chosen was a computer controlled Princeton Instruments TriVista triple spectrometer and Roper Scientific PyLoN LN/400BR nitrogen cooled deep depletion CCD detector. This section provides details of the detector system including its configuration and specifications. Information is also provided on the technique used to calibrate and correct for the spectral response of the detection system.

The TriVista triple spectrometer consists of three stages, as shown in Figure 3.6. Each stage has the same Czerny-tuner design featuring an entrance slit, a collimating mirror, an interchangeable triple grating turret, a focusing mirror and an exit slit (or CCD detector for stage 3). In order to separate the small quantity of Raman scattered light from the large quantity of Rayleigh scattered light the triple spectrometer was configured in subtractive mode, which gives the best stray-light rejection. In this mode the scattered light enters the first stage through an input lens and entrance slit S1. The input lens is adjusted to fill the entire aperture of the first collimating mirror before the light is dispersed by the grating G1. Slit S2 then acts as a bandpass filter, only allowing through a selected portion of the spectrum. The grating G2 recombines all the dispersed light and re-focuses it into the middle of the slit S3. Grating G3 then disperses the selected band of light onto the CCD detector. In this configuration gratings G1 and G2 must be the same so that their dispersive actions precisely cancel each other. The spectral resolution in this configuration is entirely defined by the spectral resolution of the third stage which depends on the width of slit S3, the grating G3 groove density, and the focal length of the stage.

The diffraction gratings selected for stages 1 and 2 have a groove density 900g/mm and a linear dispersion of 1.93nm/mm @ 800nm (center of measurement range). The efficiency of this grating as a function of wavelength for surface (s) and planar (p) polarised incident light is shown in Figure 3.7 (a). Depending on the laser wavelength, the input polarisation, and the required resolution, one of two possible gratings could be chosen for stage three; either 1500g/mm or 1800g/mm, which provide linear dispersions of

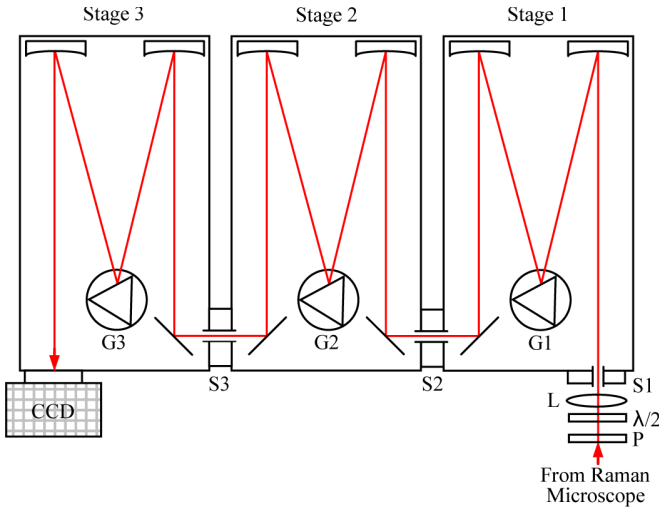

FIGURE 3.6: Detector system diagram. Red line shows approximate light path.

0.63nm/mm and 1.43nm/mm respectively @ 800nm. These gratings exhibit significantly different efficiency functions to the 900g/mm efficiency function shown in Figure 3.7. In order to maximise CCD coverage and optimise stray light rejection, slightly different system configurations were used when selecting the 1500g/mm and 1800g/mm gratings. These configurations are given in Table 3.3.

Configuration	9_9_15_subtractive	9_9_18_subtractive
Stage 1		
Entrance slit (S1) μm	$30-70$	$30-70$
Bandpass nm	White	White
Grating g/mm (G1)	900	900
Linear dispersion nm/mm	1.93	1.93
Stage 2		
Entrance slit (S2) mm	10	23
Bandpass nm	19.3	44.39
Grating (G2) g/mm	900	900
Linear dispersion nm/mm	1.93	1.93
Stage 3		
Entrance slit (S3) μm	$30-70$	$30-70$
Bandpass nm	18.74	42.54
Grating (G3) g/mm	1500	1800
Linear dispersion nm/mm	1.43	0.63
CCD Coverage mm	26.8mm (Full)	26.8mm (Full)
Pixel resolution cm^{-1}/px	0.22	0.50

TABLE 3.3: Configurations used for TriVista triple spectrometer including CCD Coverage and pixel resolution.

Most Raman measurements were performed in the $0.7-1.2\mu$m range. For this reason the choice of CCD detector was primarily based on near-infrared (NIR) optimisation. CCD detection at NIR wavelengths can be quite challenging for two reasons (1) the silicon that CCDs are made of becomes transparent at $\sim 1\mu$m which reduces the quantum

efficiency of the device and (2) spectra taken in the NIR suffer from thermal noise in comparison to those taken in the UV-VIS range. The nitrogen cooled deep depletion CCD detector utilises a thicker and higher resistivity epitaxial layer, which allows the potential wells to penetrate deeper into the silicon and minimizes the distance in which the charge generated by photons can diffuse without being counted as a signal. Nitrogen cooling is required to reduce the higher dark current which is present in this type of CCD device. Figure 3.7 (b) shows the quantum efficiency of the LN/400BR CCD detector as a function of wavelength.

The efficiencies of the various optical components and the CCD detector all combine to give the total spectral response of the detector system. Figures 3.7 (a) and (b) suggest that there will be a significant variation in the spectral response of the combined system in the 400-1200nm operational range. It is particularly important that any variation in the spectral response is corrected for during RRS measurements, since the laser energy is tuned over a large wavelength range.

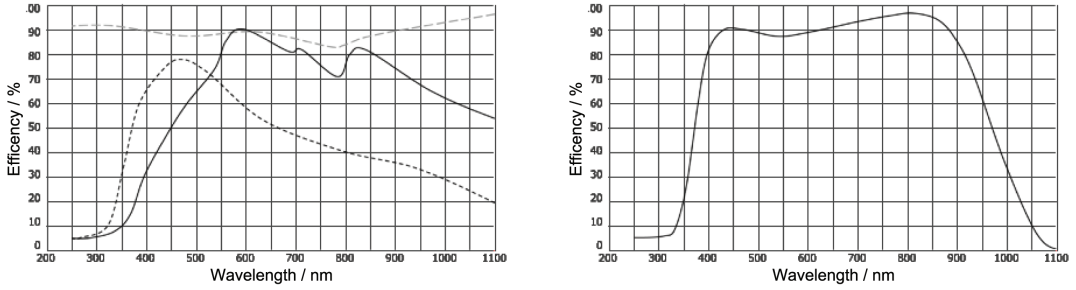

(a) (b)

FIGURE 3.7: (a) Shows efficiency as a function of wavelength of for 900g/mm grating for p-polarised light (solid black line) s-polarised light (dashed black line). Grey dashed line shows efficiency of silver coated mirrors. (b) Quantum efficiency of Roper Scientific PyLoN LN/400BR nitrogen cooled deep depletion CCD detector.

To calibrate the spectral response of the detector system the following technique was used. Firstly, the spectral output of a pre-calibrated Ocean Optics LS-1-CAL-INT-220 tungsten halogen light source was measured using the detector system. The output of the light source was collimated and passed through a linear polariser which was set to achieve either s-polarised or p-polarised incidence with the vertically mounted gratings in the detector system. Spectra were collected in 5nm increments across the entire operational wavelength range of the detector system for both 9_9_15_subtractive and 9_9_18_subtractive configurations and for both s-incidence and p-incidence. The spectral output measured by the detector system was then compared with the calibration data obtained from the Ocean Optics calibration service. Details regarding Ocean Optics calibration procedure can be found in Reference [98]. A Matlab function was created (see Appendix A Matlab Code 1) to calculate the efficiency correction factors from the data obtained by the detector and the calibration data. In this function the calibration data is represented by a continuous standard black body model which gives a good fit to

the discreet calibration data when using a least squares fitting algorithm. This function produces two 1340xN matrices, one containing the wavelengths and one containing the correction factors corresponding to each of the 1340 pixels across the CCD detector and N spectra taken in 5nm increments. Appendix B contains the efficiency functions calculated for both 9_9_15_subtractive and 9_9_18_subtractive configurations for both s-polarised and p-polarised light.

To correct the raw Raman spectra for the spectral response of the detector system a second Matlab function was created (see Appendix A Matlab Code 2). If the Raman spectrum being corrected shares its center wavelength with one of the calibration measurements the function simply looks up the correction factors from the relevant column in the correction matrix, however if it does not, a linear interpolation technique is used to calculate the approximate correction factor from the two columns with center wavelengths either side of the center wavelength of spectrum being corrected. This interpolation technique was a good approximation because the correction factor for a specific pixel varied linearly between two spectra taken 5nm apart.

3.1.4 Sample Environment

To measure the temperature dependence of the phonon dynamics, it is necessary to vary the temperature of the bundled SWCNT sample in the range 4-600K whilst maintaining optical access to the sample from the Raman microscope. Furthermore, it is crucial that each measurement is performed at the same location on the sample to avoid measuring spatial variations in the dynamics which could possibly be caused by a variation in the SWCNT local environment. This was achieved using a helium flow Oxford Instruments Microstat for measurements in the temperature range 4-294K and Linkam THMS600E hot stage for measurements in the temperature range 150-600K.

Figure 3.8 (a) shows the experimental setup for the helium flow Oxford Instruments Microstat (A). A compact Oerlikon PT70F turbo pump (B) was connected to the Microstat to provide a constant vacuum of $\sim 10^{-6}$mbar inside the sample chamber. The Microstat has a 0.5mm thick sapphire window which provides optical access to the chamber. The sample was mounted on a silver cold finger which was thermally anchored to the tip of a heat exchanger. A syphon was used to link a helium storage dewar (C) to the cryostat. The cryostat exhaust line was connected to a helium gas flow controller and a small gas flow pump, which was used to control the flow of helium to the heat exchanger. Temperatures below 4.2K were achieved by lowering the pressure in the heat exchanger using a needle valve on the syphon. A three point calibrated rhodium iron temperature sensor was mounted on the heat exchanger. For temperature measurements between 4K and 292K an Oxford Instruments ITC502 temperature controller would automatically supply and monitor a current to a heating element which was in thermal contact with the heat exchanger. This setup had a temperature stability of < 0.1K. The thermal

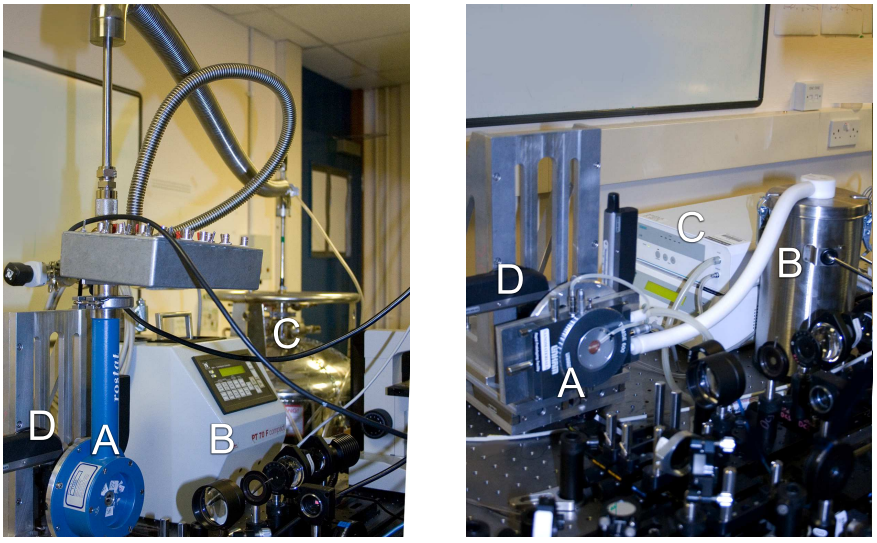

(a) (b)

FIGURE 3.8: Images of sample enviroment control systems, showing (a) helium flow Oxford Intruments Microstat and (b) Linkam THMS600E hot stage. See main text for more details.

expansion of the cold finger was measured to be approximately $0.1\mu\text{mK}^{-1}$. This means that it was necessary to track the spot position on the sample when varying temperature using the in-situ optical microscope (see Section 3.1.2). Measurements were not taken until the sample environment had sufficiently stabilised.

The Linkam THMS600E hot stage experimental setup is shown in Figure 3.8 (b). The sample was mounted inside the hot stage (A) on a silver heating block positioned in the center of a nitrogen purged chamber, where a 0.17mm fused quartz window provided optical access to the sample. A liquid nitrogen filled dewar (B) was connected to the hot stage through a stainless steel cooling tube which directly injected the coolant into the silver block. The coolant exhaust was redirected to purge the sample chamber and the external face of the optical window. For measurements below room temperature a Linkam LNP94/2 pump (C) was used to automatically control coolant flow through the heating block. The temperature of the heating block was measured by a 100ohm platinum resistor sensor. For measurements above room temperature a Linkam TMS 94 temperature controller automatically supplied and monitored a current to a heating element inside the heating block. This setup had a temperature stability of < 0.1K. In order to allow focusing of the Raman microscope and spatial Raman measurements, both sample environments were mounted on an XYZ translation stage (D) fitted with Newport LTA series precision motorized actuators, which have an incremental motion of 0.1μm.

3.1.5 Sample Preparation and Details

SWCNT Raman studies are usually best performed at the single nanotube level where inhomogeneous broadening of the Raman features are minimised [65]. However, performing TRIARS measurements at the single nanotube level would be a significant challenge because it would be difficult to achieve a sufficiently stable TRIARS signal. This is believed to be the reason why there are currently no reports of TRIARS measurements at the single nanotube level. It has been shown that this problem can be overcome by performing TRIARS measurements on bundled SWCNTs [6, 40, 55], where the anti-Stokes Raman signal represents the response from an ensemble of SWCNTs, which reside in the sampling volume and are in resonance with the laser excitation energy. There were two key requirements of the SWCNT sample used for the work in this thesis; (1) that a stable TRIARS signal could be achieved over a long time period, in the temperature range $4-600$K, and (2) that SWCNTs in two separate diameter ranges could be studied under similar environmental conditions. Both of these requirements could be met by using a single bundled SWCNT sample.

The SWCNT sample was produced from commercially obtained (Carbon Nanotechnologies) nanotubes, which were synthesised by the HiPco process. The nanotubes came with only standard purification, which produced bundled semiconducting and metallic SWCNTs with diameters in the range $0.8-2.0$nm. Details of these SWCNTs which may be useful to the discussion have been provided in Appendix C. To produce the sample the nanotubes were suspended in IPA by sonication (see Figure 3.9 (a)), and subsequently deposited onto an oxide coated (200nm) silicon substrate (Si/SiO_2) to form an optically thick film of bundled HiPco SWCNT. Figure 3.9 (b) presents an SEM image of the sample showing the typical formation of bundled nanotube ropes which are held together by van-der-Waals forces.

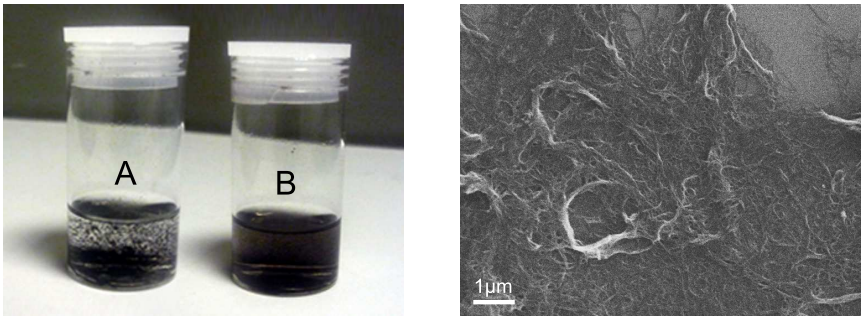

(a) (b)

FIGURE 3.9: (a) IPA SWCNT solution (A) before and (B) after 6 minutes sonication. (b) SEM image of bundled HiPco SWCNT sample (the substrate can be seen in the top right corner). White scale bar represents 1μm.

The most important factor in the choice of the underlying substrate was fluorescence, which is typically observed as a broad background signal in the Raman spectra. Fluorescence can be responsible for offsetting the baseline and reducing the signal to noise ratio in Raman measurements. Si/SiO_2 produces minimal fluorescence in the range $0.7 - 1.0\mu$m range, and thus provides an ideal material for the underlying sample substrate.

3.1.6 Localised Laser Heating

The average laser power used during the RRS and TRIARS experiments is 5mW. Because of the small focal spot size it is possible that the sampling region could be heated to a temperature well-above the heat exchange temperature due to localised laser heating. If this happens this would mean the temperature sensors would give incorrect readings for the sample temperature, which would be lower than the actual temperature within the sampling volume. Conveniently, the Stokes to anti-Stokes intensity ratio can be used as a tool for probing the temperature of the sampling region using the following expression

$$I_{\mathrm{AS}}/I_{\mathrm{S}} = \frac{(\omega_{\mathrm{L}} + \omega_{\mathrm{ph}})^4}{(\omega_{\mathrm{L}} - \omega_{\mathrm{ph}})^4}[exp(\hbar\omega_{\mathrm{ph}}/k_B T) - 1]^{-1}, \tag{3.1}$$

where I_{AS} and I_{S} are the anti-Stokes and Stokes Raman intensities ω_{L} is the laser frequency, ω_{ph} is the frequency of the phonon involved in the Raman scattering [13, 99]. Incoming and outgoing resonance conditions for Stokes and anti-Stokes scattering will also affect the $I_{\mathrm{AS}}/I_{\mathrm{S}}$ ratio. This means that the above expression can only be used to obtain the local sample temperature, T, during non-resonant Raman scattering. For this reason the local temperature was investigated through the non-resonance $520\mathrm{cm}^{-1}$ Si Raman feature.

Figure 3.10 shows the temperature of heat exchange plotted against the local sample temperature which has been determined from Equation 3.1 and the $I_{\mathrm{AS}}/I_{\mathrm{S}}$ ratio of the $520\mathrm{cm}^{-1}$ Si Raman feature. The measurements were performed with CW laser light with an average power of 5mW. The results suggest a small and constant ($\sim$ 20K) increase in the local sample temperature compared with the heat exchange temperature. Reducing the laser power by one order of magnitude (see *blue data point* in Figure 3.10) did not cause the local sample temperature, as determined by $I_{\mathrm{AS}}/I_{\mathrm{S}}$, to tend towards the heat exchange temperature as one would expect. The measured constant difference between the temperature of the heat exchange and the temperature determined from the I_{AS}/I_S ratio is too small to have any significant impact on the conclusions drawn from the temperature dependent measurements in this thesis. For this reason, the heat exchange temperature is taken as the sample temperature throughout the experiments.

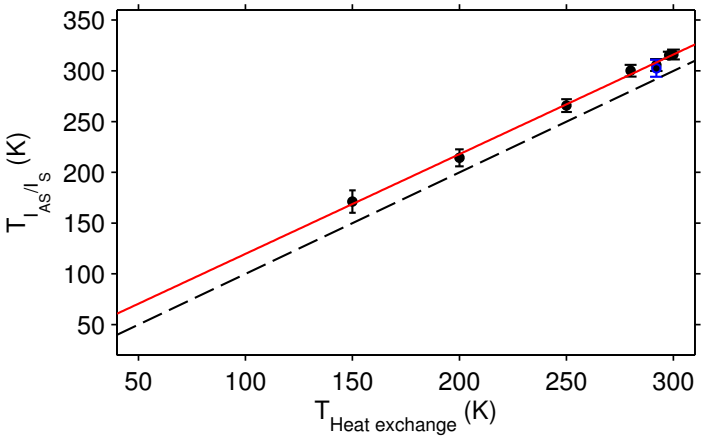

FIGURE 3.10: Localised laser heating. Plot shows temperature of heat exchange against the local temperature which has been determined from Equation 3.1 and the I_{AS}/I_S ratio of the 520cm^{-1} Si Raman feature. Measurements were performed for CW laser light with an average power of 5mW. Also shown is a linear fit to the data points (*solid red line*) and the temperature of the heat exchange (*broken black line*). The blue data point at $T = 292K$ represents a measurement taken for a laser power of (0.5mW).

3.2 Resonance Raman Spectroscopy

The setup used for the RRS experiments is shown in Figure 3.11. A Coherent Mira 900-P Ti:Sa laser source provided continuous tuning of the output wavelength between $700 - 980$nm, with an average power output of approximately 1W (see Section 3.1.1). During RRS measurements the laser system was operated in CW mode to produce a well-defined output wavelength with a spectral width of < 0.2nm. Any unwanted fluorescence produced in the laser system was removed by filtering the laser output with a Photon Etc. LLTF with a band-pass of < 0.4nm (see Section 3.1.1.3). The beam was then passed through a half-wave plate followed by a vertical polariser. The beam was reflected from a $50:50$ beamsplitter into the Raman microscope (see Section 3.1.2 for more details), where it was focused onto the sample using a LMPLan-IR 50X microscope objective, producing a focal a spot size of approximately 1μm ($1/e^2$ radii). The laser power was measured at the sample position using a Newport 2832-C power meter and 818-IR low power attenuated detector (see Section 3.1.1.1). The laser-damage threshold of the bundled SWCNT sample was measured to be approximately 5×10^6W/cm^{-1} i.e 50mW on a 1μm^2 focal spot. This is similar to the damage threshold observed by others [100–102], and can be explained by the high thermal conductivity and temperature stability of SWCNTs [103]. To ensure the long term stability of the measurements, the laser power was held at 5mW at the sample position i.e. one order of magnitude less than the laser-damage threshold. As the wavelength of the laser system was varied the LLTF band-pass was re-centred on the laser wavelength and the half-wave plate was adjusted to ensure a constant power ($< 1\%$ variation) and maintain vertical polarisation at the sample. In order to calibrate the detector system for measuring in Raman shift, the laser wavelength had to be determined. This was done by scattering the laser light into the

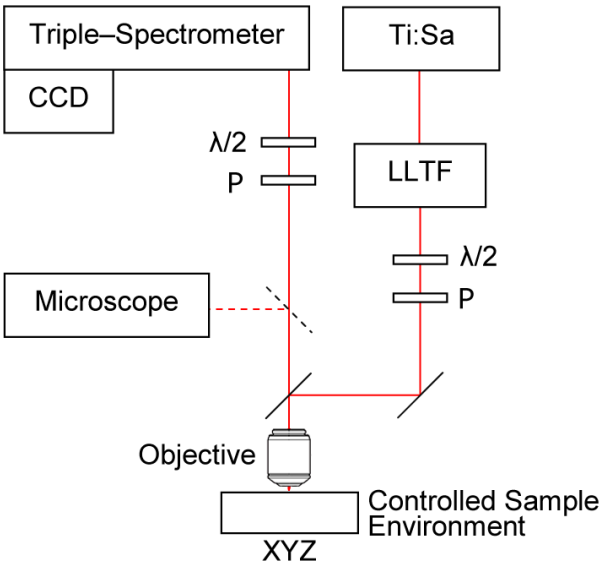

FIGURE 3.11: Schematic of RRS experimental setup showing Ti:Sa laser system, LLTF, half-wave plates ($\lambda/2$), polarisers (P), objective, in-situ optical microscope, triple spectrometer, and CCD detector. Removable optics are represented by *dashed lines*.

detector system and measuring the peak wavelength. Due to the finite width of the CW laser line and the CCD pixel resolution, the uncertainty in the calibrated Raman shift was $\pm 0.44\text{cm}^{-1}$. The sample was mounted in an Oxford Instruments Microstat in vacuum (approximately 10^{-6}mbar), so that the sample temperature could be varied in the range $4 - 292$K (see Section 3.1.4 for more details). The Microstat was mounted on a high resolution (0.1μm) XYZ translation stage so that the bundled SWCNT sample could be positioned in the Raman microscope sampling volume. The back-scattered Raman light was collected and collimated by the Raman microscope, before being passed to the detector system. Before entering the detector, the back-scattered light was analysed by a vertical linear polariser. For RRS measurements in the $700 - 980$nm range, the optimum configuration for the detector system was a subtractive double band-pass filter (900 gr/mm) followed by a dispersive stage (1500 gr/mm) for p-polarised light (see Section 3.1.3). To ensure optimum throughput the back-scattered light was passed through a half-wave plate and rotated by $\pi/2$ at the input of the detector to establish p-polarisation at grating incidence. All of the recorded spectra were corrected to account for the wavelength dependent efficiency of the detection system, as discussed in Section 3.1.3.

RRS measurements were performed by recording the Raman spectra, of a particular Raman feature, as a function of laser wavelength (excitation energy). The incremental steps in wavelength were chosen dynamically to compliment the form of the resonance profiles being measured. A small amount of beam steering caused by the LLTF filter was corrected for using two adjacent steering correction mirrors positioned immediately after the LLTF filter, which were used to maximise the Raman signal measured by the detector. To monitor the stability of the experiment the laser wavelength was returned

to its initial value to check that there was no significant change in the measured signal intensity during the experiment. Stability was not found to be an issue during RRS measurements. The in-situ optical microscope was used to monitor and record the position of the focal spot on the sample during the measurements. RRS measurements were taken at several locations on the sample. The repeatability of the RRS measurements was monitored by returning the focal spot to the same position on the sample and comparing spectra with those obtained previously at the same location. In some cases, RRS measurements were performed at room temperature ($T = 292$K) and low temperature ($T = 4$K) on the same location of the sample. This was achieved by giving the Microstat and sample sufficient time to stabilise (approximately one hour) after cooling, before using the in-situ optical microscope to re-position the focal spot to within the spot diameter. The repeatability of the RRS measurements is demonstrated in the RRS results presented in Chapter 4.

3.3 Time-Resolved Incoherent Anti-Stokes Raman Spectroscopy

The time-resolved Raman experiments reported in this thesis are based on TRIARS. This technique is used to determine the population lifetime, T_1, of the Raman active phonons (see Section 2.4) in SWCNTs. It is understood that the optical phonons decay into lower-energy 'secondary' phonons through anharmonic ph-ph interactions (see Section 2.5.3). This means that the phonon decay rate ($1/T_1$) is dependent on the population of the secondary phonons, and through thermal activation, sample temperature (see Section 2.5.3). Thus by measuring the decay rate of the phonon population as a function of sample temperature we are able to investigate the energy of the secondary phonons contributing to the measured phonon decay rate.

In 1980 von der Linde et al. performed the first TRIARS study of bulk GaAs [104]. Since then TRIARS has proved very useful for investigating dynamics in bulk semiconductors. However, when TRIARS is used to study phonon population dynamics in low-dimensional systems, such as SWCNTs, there are additional experimental implications which must be considered. During a TRIARS experiment it is usually necessary to separate the pump signal from the probe signal so that the full phonon population dynamics can be obtained [104–106]. The simplest method used to separate the pump signal from the probe signal is by polarisation, i.e setting orthogonal polarisation states for the pump and probe beams and placing a polarisation analyser prior to the detector. However, for SWCNTs the polarisation of the absorbed and scattered light is favoured parallel to the nanotube axis [13], meaning polarisation cannot be used to distinguish between the pump and probe signals. Another method used to distinguish between the pump and probe signals is by colour, i.e. using different energies $\hbar\omega_{\mathrm{L}}$ for the pump and probe beams and placing a suitable dichroic mirror prior to the detector. However, due

to the 1D electronic structure in SWCNTs, only optical transitions with energy close to E_{ii} are allowed (see Section 2.1.2.3). This means that the separate energies of the pump and probe pulses must both be close in energy to the E_{ii} of the same SWCNT if a sufficient TRIARS signal is to be achieved. This generally means that SWCNT TRIARS requires an elaborate (often unstable) experimental setup that is capable of generating pump and probe pulses with independently tunable energies, for example a Ti:Sa laser and optical parametric generator. Nevertheless, there have been a number of SWCNT TRIARS studies reported which successfully use this approach [6, 40, 55]. These studies are reviewed in detail at the beginning of Chapter 5.

The TRIARS experiments reported in this thesis are based on a co-polarised degenerate pump-probe technique. This technique has been developed to overcome the difficulties of performing a two-colour TRIARS experiment on SWCNTs and has the added advantage that both pump and probe beams can be tuned to the peak of the same resonance, which maximises the TRIARS signal. The rest of this section is dedicated to describing in detail the co-polarised degenerate TRIARS experiment and discussing its advantages and disadvantages over the more standard two-colour TRIARS approach.

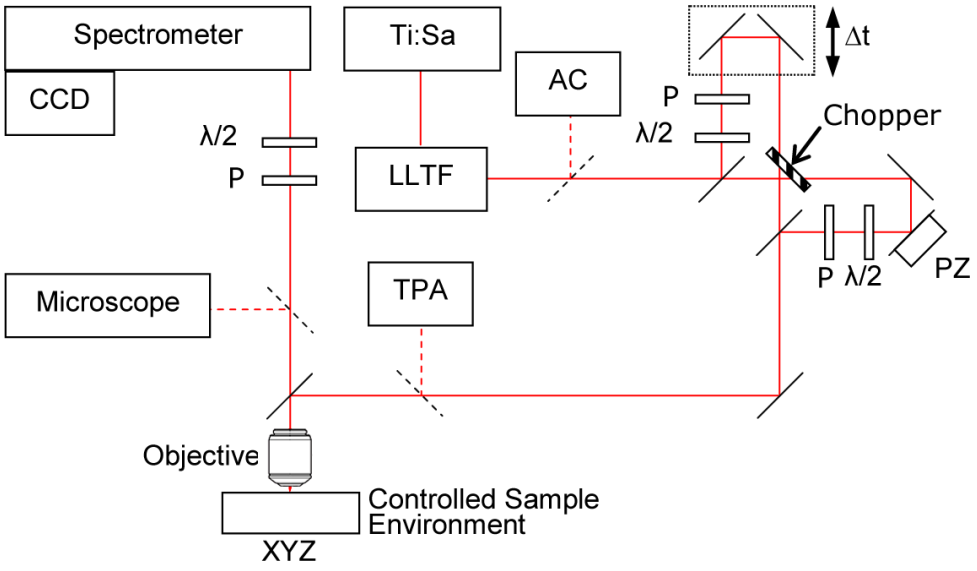

FIGURE 3.12: Schematic of TRIARS experimental setup showing Ti:Sa laser system, LLTF, intensity autocorrelator (AC), half-wave plates ($\lambda/2$), polarisers (P), computer controlled delay line (Δt), mechanical chopper, piezo mounted mirror (PZ), in-situ TPA cross-correlation detector, objective, in-situ optical microscope, spectrometer, and CCD detector. Removable optics are represented by *dashed lines*.

The setup used for the co-polarised degenerate TRIARS experiment is shown in Figure 3.12. The Coherent Mira 900-P Ti:Sa laser source was mode-locked to produce approximately 2ps pulses with a spectral width of approximately 6cm^{-1} (FWHM). For more information regarding the mode-locking operation of the Ti:Sa laser system see Section 3.1.1. To remove unwanted fluorescence produced in the laser system the output of the

laser source was filtered with a Laserspec LLTF with a band-pass of approximately 1nm (see Section 3.1.1.3). An intensity autocorrelator (AC) was used to monitor the pulse durations immediately after the TLLF. To produce identical pump and probe pulses the laser beam was split into two beams of equal power by a 50:50 beam splitter. The first beam was passed through a half-wave plate and linear polariser (power and polarisation control optics), while the second beam was sent through a computer controlled variable delay line Δt and an identical set of polarisation and power control optics. The two beams were recombined at a second 50:50 beam splitter to form a single beam consisting of pairs of equal intensity pulses with controllable delay. The collinear beams were reflected from a 50 : 50 beamsplitter into the Raman microscope (see Section 3.1.2 for more details), where they were focused onto the sample using a LMPLan-IR 50x microscope objective. The focal a spot size was measured to be approximately 1μm ($1/e^2$ radii). The TRIARS measurements were performed for a range of sample temperatures, between 4K and 600K. The sample was mounted in a helium flow Oxford Instruments Microstat for measurements in the temperature range 4-294K and Linkam THMS600E hot stage for measurements in the temperature range 150-600K. The method used to ensure that measurements were performed on the same location of the sample was the same method used during RRS experiments (see Section 3.2).

This co-polarised degenerate TRIARS approach has two disadvantages over the more standard two-colour TRIARS experiment. The first is that the collinear beams result in strong interference effects at the combining beam splitter. These were effectively removed to within better than 98% by introducing a piezo driven mirror (PZ) into one of the optical paths. The piezo stack was driven by a triangular wave function which rapidly varied the length of one of the optical paths by a number of whole wavelengths, so that on the timescale of a Raman measurement the interference effects were effectively averaged to zero. The second disadvantage is that the measured dynamics is effectively the dynamics which would be measured in a standard TRIARS experiment added to a reflection of itself in zero delay. At first, it might appear this would make it impossible to determine the rising edge dynamics, however, this is not the case if reasonable assumptions and careful fitting of the dynamics are used (see Section 5.4) and Appendix D.

A slow scanning in-situ two-photon absorption (TPA) cross-correlator (GaP photodiode) was used to measure the cross-correlation of the pump and probe pulses before they entered the Raman microscope. During a cross-correlation measurement the pump and probe beams were modulated with a frequency ratio of 5/3 by a dual frequency optical chopper blade. A Stanford Research SR830 Lock-in Amplifier was used to monitor the response signal from the TPA detector at the second-harmonic of the chopper frequency. This was to ensure that the recorded response of the TPA detector was dependent on both the pump pulse and probe pulse incidence. Figure 3.13 shows typical pulse cross-correlations obtained with the in-situ cross-correlator with the piezo switched off (*black*)

and on (*red*). The cross-correlations made with the in-situ cross-correlator were checked against measurements using another TPA detector at the sample position, which gave identical results (within the accuracy of the measurement). The major advantage of the degenerate, co-polarised, co-linear geometry is that both pump and probe can be tuned to the peak of the same resonance, maximising the TRIARS signal. In addition, it requires a less complex and more stable experimental setup than a two-colour pump-probe system.

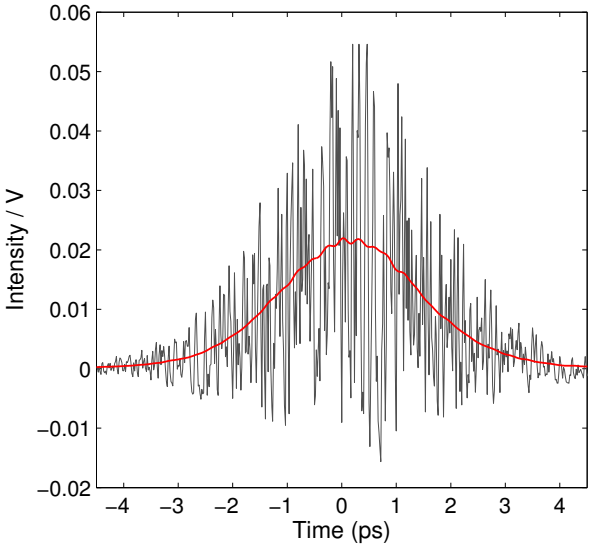

FIGURE 3.13: Typical pulse cross-correlations obtained with the in-situ cross-correlator, showing (*black*) the interference of the pulses when the piezo was switched off, and (*red*) the interference effects effectively averaged out when the piezo stack driver was switched on.

The cross-correlation measurement was recorded and fitted with a Gaussian function to locate the position of zero delay in the pump-probe delay line. This allowed the zero delay position to be determined to within ±0.03ps. When the pump-probe delay was zero and the piezo driver was switched off, the interference of the pump and probe focal spots, observed through the in-situ optical microscope, was utilised to achieved spatial overlap of pump and probe beams at the sample position. The Raman microscope and detector system were configured and calibrated using the same approach described for RRS measurements in Section 3.2.

We have already discussed that the anti-Stokes Raman signal intensity is proportional to the population of phonons, and that recording the anti-Stokes Raman signal as a function of pump-probe delay is what allows the phonon population dynamics to be studied. However, to accurately measure the phonon population dynamics a number of anti-Stokes measurements were taken. Firstly, anti-Stokes Raman spectra were recorded for the pump beam alone and probe beam alone, as the sum of these two spectra provides a measure of the background phonon population. Next, the anti-Stokes Raman signal intensity was monitored as the pump-probe delay was increased, until the anti-Stokes

Raman signal intensity was equal to that of the background phonon population, i.e. where there was no measurable pump excitation. A pump-probe delay of 25ps was found to be sufficient for a background signal in all of the TRIARS experiments. The anti-Stokes Raman spectra were then recorded as a function of pump-probe delay by an automated LabView program which controlled the delay line and CCD detector. The values of pump-probe delay at which spectra were taken were chosen to compliment the fitting technique (discussed in Section 5.4), and were always symmetric in their values about zero delay. The weak nature of anti-Stokes Raman scattering meant that typical CCD integration times were 30 seconds. This translates into a typical TRIARS experiment time of 1 hour. In order to monitor the stability of the experiment and account for any random variations or drift in the signal, a background measurement was recorded every third measurement. Pump-probe cross-correlation measurements were made before and after every TRIARS experiment, and the data was discarded if the cross-correlation (FWHM) had varied by greater than 100fs.

Chapter 4

Resonance Raman Spectroscopy of Bundled SWCNTs

The well-defined optical transition energies in SWCNTs (see Section 2.1.2.3) make them ideal candidates for RRS studies. RRS can be a useful tool, not just for providing insight into the electronic structure of SWCNTs [107, 108], and determining the diameter distribution in a bundled SWCNT sample [58, 59, 109], but also for selectively studying SWCNTs of a particular type through resonant excitation [6, 40, 54, 55, 65, 110, 111]. In this thesis RRS is used as a tool to characterise the bundled HiPco SWCNT sample, and to determine which SWCNT species are contributing to the intensity of the D-band and G-band Raman features for a particular excitation energy E_{L}. This work is necessary so that SWCNTs of a particular type (or diameter) can be selectively studied during the TRIARS experiments. The specific objectives which were set for the RRS experiments in this thesis are listed below;

Objective 1 to characterise the bundled SWCNT sample by determining the optical transition energies and the (n, m) indices of the SWCNT species that are resonant in the operational energy range of the laser system,

Objective 2 to establish which SWCNTs are contributing to the intensity of the D-band and G-band Raman features for a particular excitation energy,

Objective 3 to identify at least two excitation energies which could be used during the TRIARS experiments to study the phonon dynamics of SWCNTs in different diameter ranges, i.e. to identify excitation energies for which the Raman signal is attributed to the response of SWCNT in different diameter ranges,

Objective 4 to investigate the effect of temperature on the optical transition energies, E_{ii}, to determine if the excitation energy will need to be varied during the temperature dependent TRIARS experiments.

In this chapter, the RRS results are presented and discussed in relation to the objectives outlined above. The first section provides details of the specific RRS experiments that were performed. The analysis of the RBM resonance measurements is presented first because (1) it allows the (n, m) indices of the resonant SWCNTs to be determined and (2) it can reveal more information than the D-band and G-band resonance measurements due to the fact that RBMs from different SWCNTs can be spectrally resolved and the fact that the incoming and outgoing RBM resonances can be treated as a single resonance profile. This is followed by an investigation into the excitation laser energy E_{L} dependence of the D-band and G-band Raman features. A final section provides a summary of the chapter by stating conclusions that can be drawn from the results.

4.1 Experimental Details

RRS experiments were performed by carefully recording Raman spectra as a function of laser excitation energy E_{L}, so that the E_{L} dependence of the Raman intensity, shift and linewidth (FWHM) of a particular Raman feature can be studied. To achieve the objectives outlined above several RRS experiments were performed on the same bundled SWCNT sample that is used for the TRIARS experiments in Chapters 5 and 6. This section provides an overview of the individual RRS experiments that were performed, while a detailed discussion of the experimental apparatus and techniques used for the RRS measurements can be found in Section 3.2.

In order to achieve objectives 1 and 2 RRS measurements were recorded for the RBM, D-band and G-band features for both Stokes and anti-Stokes scattering and for two locations on the sample. The RRS measurements were taken over the full operational range of the system to maximise the number of resonant SWCNTs, and therefore, maximise the potential of achieving objective 3. To satisfy objective 4, RRS measurements were taken at both room temperature ($T = 292$ K) and low temperature ($T = 4$ K) at the same location on the sample.

There are two clarifications to make regarding the RRS experiments. Firstly, the efficiency of the detector system was significantly reduced at wavelengths above 1050 nm (see Section 3.1.3). This meant that there was an upper-limit in the excitation wavelength that could be used to obtain Stokes Raman spectra, furthermore, this upper-limit was dependent on the frequency of the Raman feature being recorded. The Stokes detection limits of the RBM, D-band, G-band, and G'-band, were approximately 1020 nm, 910 nm , 886 nm and 800 nm respectively. In practice, this meant that D-band and G-band Raman signal detection was severely hindered in the long wavelength limit of the RRS measurements and that the Stokes G'-band RRS signal was not obtainable. Secondly, the anti-Stokes Raman spectra could not be obtained for low temperature

measurements because there were no excited states available to contribute to the anti-Stokes Raman scattering process. The time taken to complete a single RRS experiment was several hours. During this time it was not uncommon to observe variations in the Raman signal intensity. These intensity variations were caused by (1) a long-term drift ($< 2\mu$m) in the sampling region due to small changes in the laboratory temperature, and (2) damage to the SWCNTs in the sampling region caused by incident laser radiation. Furthermore, experiments performed at non-ambient temperatures were more likely to experience a significant drift in the position of the sampling region. Two comparable sampling regions were carefully chosen to minimise long-term variations in the Raman signal intensity. The criteria for a viable sampling region was (1) that the Raman signal would vary by less than 10% within a 10μm square centred on the sampling region, which indicated a region of uniform SWCNT density and (2) that the Raman signal would vary by less than 5% over a period of 5 hours, which indicated that the bundled SWCNT film was in good thermal contact with the substrate and was therefore less likely to experience laser damage. Two sampling regions were selected to provide a stable Raman signal throughout the duration of the RRS and TRIARS experiments. We will refer to these two sampling regions as 'sampling region A' and 'sampling region B'.

4.2 Analysis of RBM Resonance Measurements

The Raman spectra of bundled SWCNTs contain contributions from nanotubes that are present in the sampling region and resonant with the excitation laser energy. In this case, analysis of the RBM is much simpler than analysis of D-band and G-band because (1) the RBM frequency, ω_{RBM}, is dependent on tube diameter d_t (see Equation 2.18), meaning that the RBM features from different species of SWCNT can, in most cases, be spectrally resolved, and (2) the incoming and outgoing resonance conditions for an RBM differ in energy by much less than the width (FWHM) of the individual resonance profiles, and therefore can be treated as a single 'combined' resonance profile. Furthermore, analysis of the RBM data is particularly useful because it can be used to determine the (n, m) structural indices of the SWCNT species that are in resonance. Figures 4.1 through to 4.4 present an overview of the RBM spectra that were recorded in each of the RRS measurements. Figures 4.1 and 4.2 show Stokes and anti-Stokes RBM spectra obtained for a total of 36 different laser energies at sampling region A, while Figures 4.3 and 4.4 show Stokes resonance spectra obtained for room temperature ($T = 292$ K) and low temperature ($T = 4$ K) taken at sampling region B for a total of 86 and 10 laser energies respectively. Each of the anti-Stokes RBM features in figure 4.2 has a corresponding Stokes RBM feature in figure 4.1, with the latter appearing red shifted relative to the former (see section 4.2.2). A fitting procedure was carefully used to model each of the Raman spectra to obtain the Raman intensity, shift and linewidth (FWHM) of each of the RBMs as a function of excitation laser energy E_{L}.

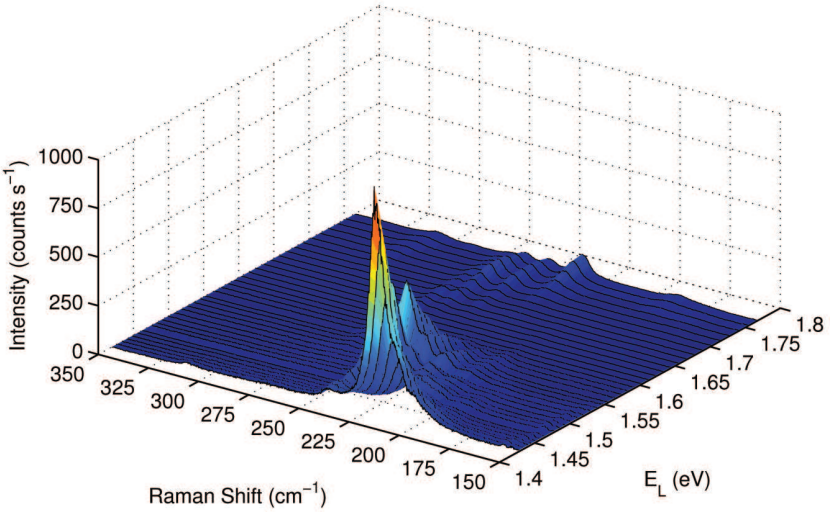

FIGURE 4.1: A 3D plot showing an overview of the Stokes RBM RRS measurements of the bundled HiPco SWCNT sample, taken at room temperature ($T = 292$K) and at sampling region A. The wavelength was varied in ~ 5 nm increments and a total of 36 laser lines were used.

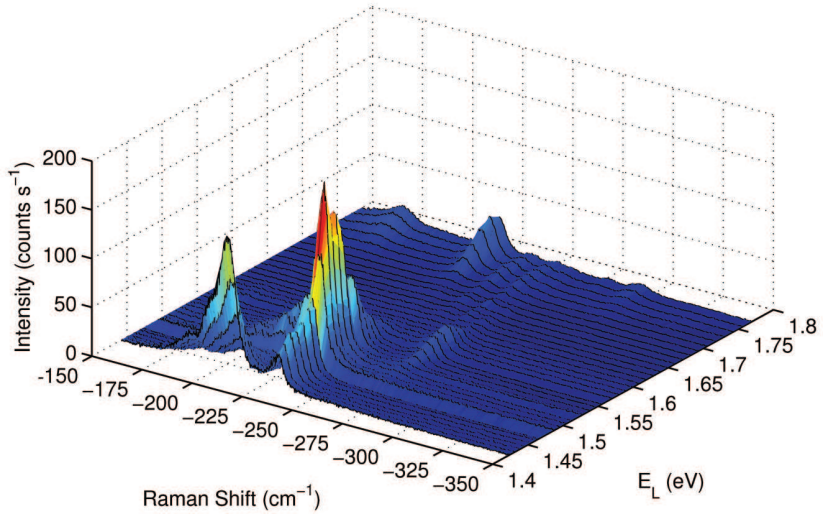

FIGURE 4.2: A 3D plot showing an overview of the anti-Stokes RBM RRS measurements of the bundled HiPco SWCNT sample, taken at room temperature ($T = 292$K) and at sampling region A. The wavelength was varied in ~ 5 nm increments and a total of 36 laser lines were used.

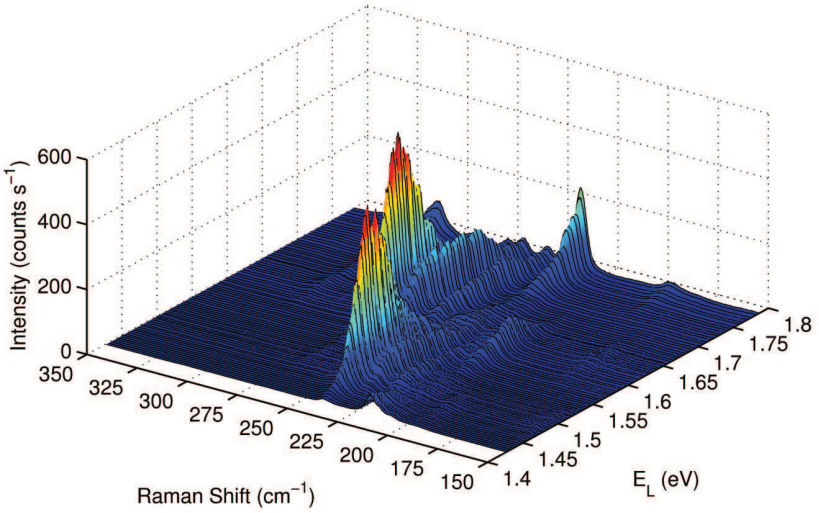

FIGURE 4.3: A 3D plot showing an overview of the Stokes RBM RRS measurements of the bundled HiPco SWCNT sample, taken at room temperature ($T = 292$K) and at sampling region B. The wavelength was varied in ~ 2 nm increments and a total of 86 laser lines were used.

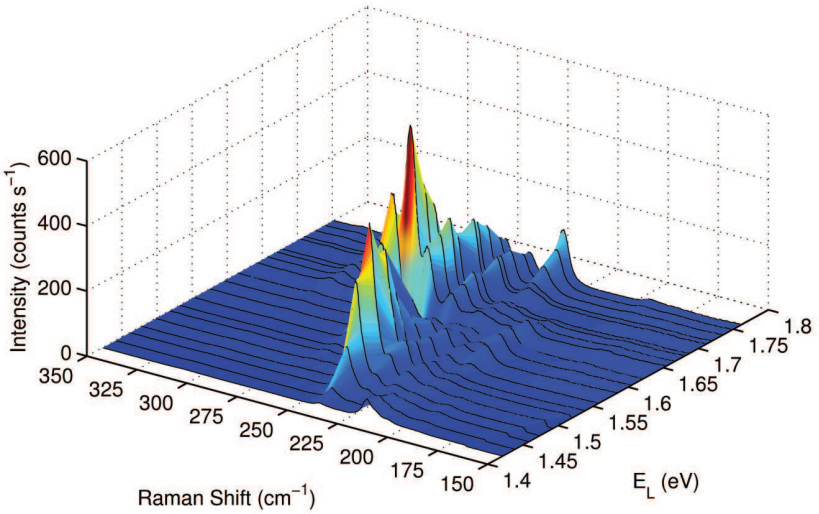

FIGURE 4.4: A 3D plot showing an overview of the Stokes RBM RRS measurements of the bundled HiPco SWCNT sample, taken at low temperature ($T = 4$K) and at sampling region B. The wavelength was varied in ~ 10 nm increments and a total of 10 laser lines were used.

4.2.1 Fitting Procedure

This section discusses the fitting procedure that was used to determine the Raman intensity, shift (ω_{RBM}) and linewidth FWHM (Γ_{RBM}) of the individual RBM features in the Raman spectra. It has been shown for an isolated SWCNT that the RBM lineshape fits well to a simple Lorentzian function with a spectral width (FWHM) of approximately $3\mathrm{cm}^{-1}$ [100]. However, in bundled SWCNTs the RBM feature can experience inhomogeneous broadening and exhibit more complex line shapes associated with tube-tube interactions [37, 112]. In addition, instrumental broadening is to be expected due to the limiting resolution of the detection system which incorporates system aberrations, diffraction effects, slit broadening, pixel resolution and the finite width of the laser line. This broadening factor was estimated experimentally by observing the width of the CW laser line as measured by the detection system, which was approximately $3\mathrm{cm}^{-1}$ FWHM. In spite of these facts, all of the RBM features fitted sufficiently well to simple Lorentzian functions, indicating that the effect of bundling on the RBM lineshape was weak and that instrumental broadening had little or no effect on the measured Raman line shapes.

The fitting procedure used was based on a linear least squares regression algorithm. The fitting function used to model the experimental RBM spectra was based on the sum of a linear polynomial and n Lorentzian functions, and can be summarised by Equation 4.1

$$f(x, p_0, p_1, a_1, b_1, c_1, \ldots, a_n, b_n, c_n) = (p_1 x + p_0) + \sum_{i=1}^{n} a_i \frac{{b_i}^2}{(x - c_i)^2 + {b_i}^2}, \tag{4.1}$$

where n is the number of resolvable RBM features in the spectra, p_0 and p_1 are the fitting parameters which govern the form of the linear polynomial, and a_i, b_i and c_i are the fitting parameters which represent the Raman intensity, linewidth/2 (FWHM) and shift of each of the Lorentzian features that are included. In summary, the purpose of the linear polynomial is to model the linear broadband background, while the sum of Lorentzian functions models the n RBM features that are present in the spectra.

The Matlab function which was created to control the fitting procedure is provided in Appendix A Matlab Code 3. This function requires the initial values and constraints of the fitting parameters to be specified manually, and returns the best fit parameters along with their 95% confidence bounds. Figure 4.5 shows a typical result of this fitting function applied to an RBM spectrum obtained at an excitation energy of 1.63eV at room temperature on sampling region B. It is clear from the form of the residuals that the experimental lineshape of the RBM features are not exact Lorentzians, which can be easily explained by the points outlined above. However, the Lorentzian line shapes provide a sufficiently good fit to determine the properties of the individual RBM

features. The fitting parameters obtained from the fit in Figure 4.5, along with their 95% confidence intervals, are presented in Table 4.1.

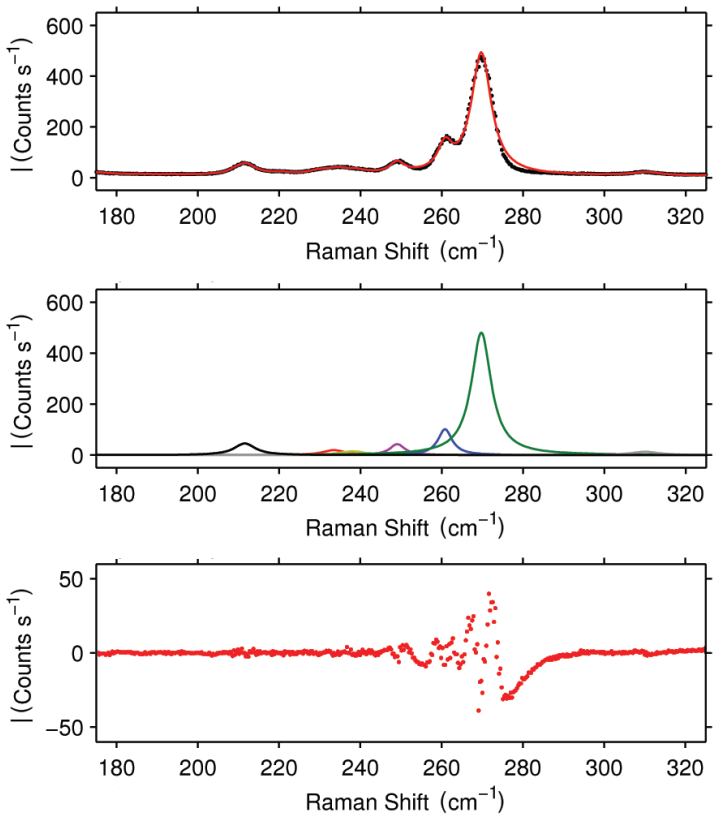

FIGURE 4.5: RBM fitting procedure. *Top*: shows the fit (*solid red line*) to an experimental RBM spectrum (*black dots*) taken for $E_{\mathrm{L}} = 1.63$eV at $T = 292$K and at sampling region B. *Middle*: shows Lorentzian components which make up the fit. *Bottom*: shows the fitting residuals.

c_i [Shift (cm^{-1})]	a_i [Intensity (counts s^{-1})]	$2b_i$ [Γ_{RBM} FWHM (cm^{-1})]
211.4 ± 0.1	45.7 ± 0.3	6.2 ± 0.6
233.5 ± 0.5	19.4 ± 0.5	6.6 ± 1.0
238.1 ± 0.3	14.9 ± 0.6	7.2 ± 1.2
249.0 ± 0.1	43.0 ± 0.2	6.4 ± 0.6
260.0 ± 0.1	101.6 ± 0.1	6.2 ± 0.4
267.3 ± 0.1	480.5 ± 0.1	6.0 ± 0.2
310.0 ± 0.4	13.0 ± 0.6	6.0 ± 0.8

TABLE 4.1: Lorentzian (RBM) fitting parameters obtained from the fit in Figure 4.5. Background fitting parameters; $p_0 = 14.1462$ and $p_1 = -0.0234$.

To determine the E_{L} dependence of the RBM intensity, shift, and linewidth (FWHM) the fitting function described above was applied to all of the RBM Raman spectra obtained in each of the RRS experiments. Figure 4.6 shows several example fits to the spectra taken for different E_{L} in the range $1.5 - 1.7$eV for measurements taken at room temperature ($T = 292$K) and at sampling region B.

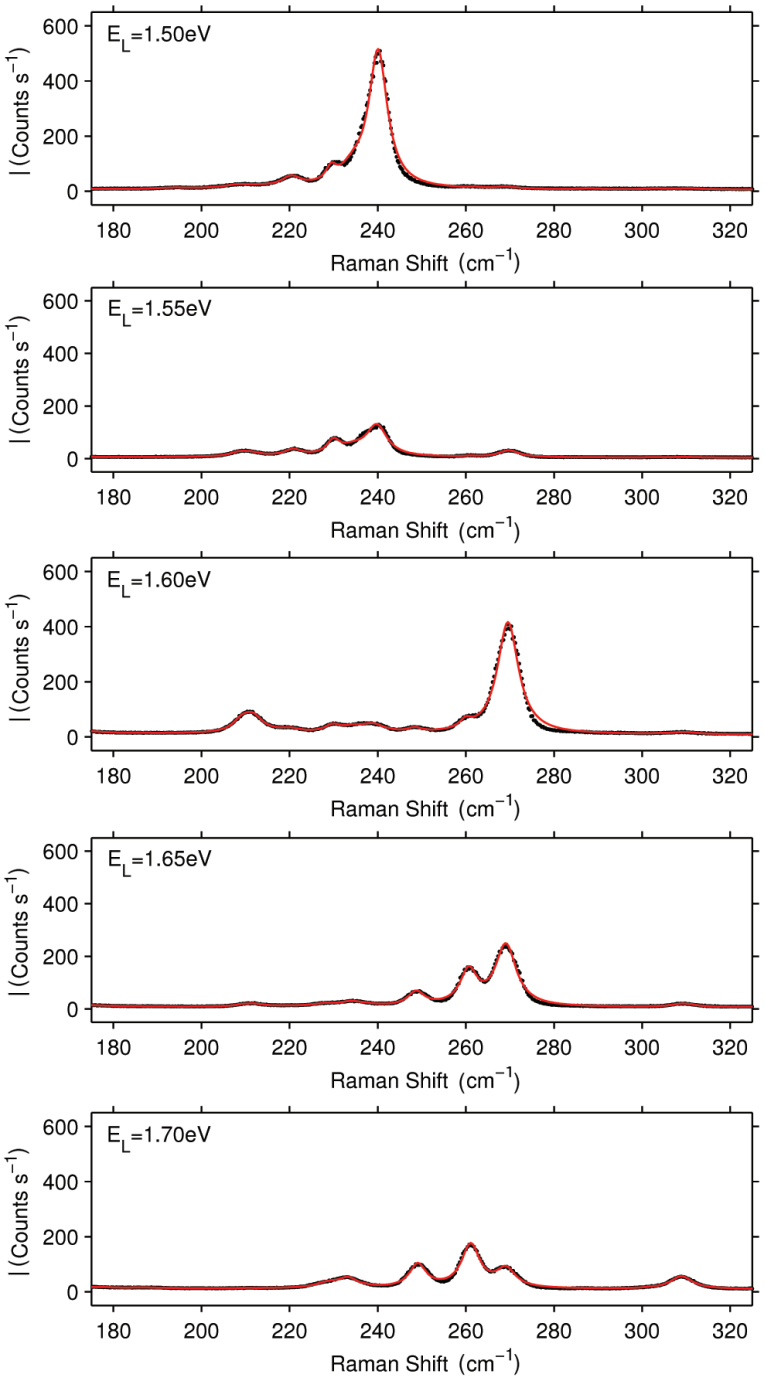

FIGURE 4.6: Example fits (*solid red line*) to experimental RBM spectra (*black dots*) taken for different E_{L} in the range $1.5 - 1.7$ eV. Measurements were taken at room temperature ($T = 292$K) and at sampling region B. Each of the RBM features that are present in the spectra are from SWCNT species that have resonances close to E_{L}.

4.2.2 Stokes and anti-Stokes Resonance Conditions

We know from the theory of resonant Raman scattering (see Section 2.2.2) that for a single Raman active mode there are both incoming and outgoing resonance conditions for Stokes and anti-Stokes scattering, and that while the energy of the incoming resonance is the same for Stokes and anti-Stokes scattering, determined by the optical transitions of a SWCNT (E_{ii}), the energy of the outgoing resonance occurs one phonon energy $\hbar\omega_{\mathrm{ph}}$ higher (Stokes) or lower (anti-Stokes) than the energy of the incoming resonance. Taking $\omega_{\mathrm{RBM}} = 200\mathrm{cm}^{-1}$ to be a typical RBM frequency, this means that the incoming and outgoing RBM resonances will differ in energy by approximately 0.025eV. We know that these resonance profiles experience an energy broadening of approximately 0.05eV due to the JDOS and the lifetime of the intermediate scattering states [49]. This means that we can expect the incoming and outgoing RBM resonance profiles to overlap to create a single combined resonance profile.

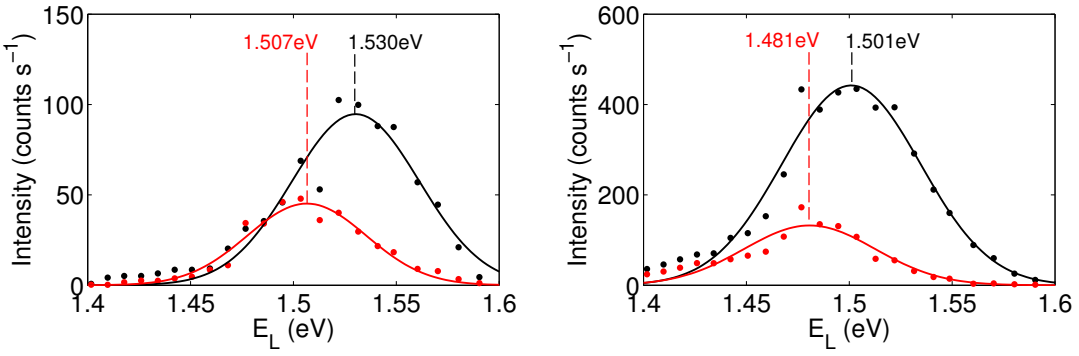

(a) (b)

FIGURE 4.7: Stokes (*Black*) and anti-Stokes (*Red*) RBM intensities as a function of excitation energy E_{L} for (a) $\omega_{\mathrm{RBM}} = 228\mathrm{cm}^{-1}$ and (b) $\omega_{\mathrm{RBM}} = 238\mathrm{cm}^{-1}$, taken at room temperature (T= 292K) and at sampling region A. The 'combined resonance profiles' have been fitted by single Gaussian functions. The center energies of these Gaussian functions are provided in the figures.

Figures 4.7 (a) and (b) show the Stokes and anti-Stokes intensity profiles for RBM features with $\omega_{\mathrm{RBM}} = 228\mathrm{cm}^{-1}$ and $\omega_{\mathrm{RBM}} = 238\mathrm{cm}^{-1}$ respectively. Each of the intensity profiles has been fitted with a single Gaussian function to determine the center energy and width (FWHM) of the resonance. The width of the intensity profiles were measured to be approximately 0.08eV. The center energies of the Stokes and anti-Stokes resonances (indicated in the figures), are to within experimental error, separated by one phonon energy $\hbar\omega_{\mathrm{ph}}$. Assuming that the incoming and outgoing resonances contribute equally to the combined resonance profiles, these observations are consistent with the theory of resonance Raman scattering and support the assumption that the optical transition energies, E_{ii}, can be approximated by subtracting $\hbar\omega_{\mathrm{ph}}/2$ from the center energy of the Stokes RBM resonance profile.

4.2.3 Inhomogeneity of the bundled SWCNT sample

In these experiments it is assumed that the Raman signal is the response from an ensemble of different SWCNTs species that reside in the Raman microscope sampling volume and are in resonance with E_{L}. In all of the experiments the Raman signal intensity was found to be independent of the incident polarisation angle. This supports the assumption that the SWCNTs are randomly orientated throughout the sample and that there are a large number of SWCNT contributing to the Raman signal. Meanwhile, RRS measurements taken at sampling regions A and B reveal some significant differences in their spectra. Figures 4.8 (a) and (b) show the RBM intensity as a function of E_{L} for all RBMs that could be fitted for measurements obtained from sampling regions A and B respectively. Comparing figures (a) and (b) it is immediately clear that there are different SWCNT distributions at sampling regions A and B. For example, the SWCNT responsible for the $\omega_{\mathrm{RBM}} = 267\mathrm{cm}^{-1}$ mode (indicated by dark green), can be found in sampling region B but not in sampling region A. Comparing the resonant Raman scatting intensities of a particular RBM obtained from sampling regions A and B can be used to determine the relative densities of a particular SWCNT species contained within the two sampling volumes, however, it is not possible to determine the relative densities of different species of SWCNTs by directly comparing the resonant Raman scatting intensities of their RBMs. This is because the matrix elements representing the e-phonon and electron-photon interactions influence the Raman intensity and can vary with SWCNT type [113, 114]. To do this, one would need to take into account the effect of the matrix elements involved [114].

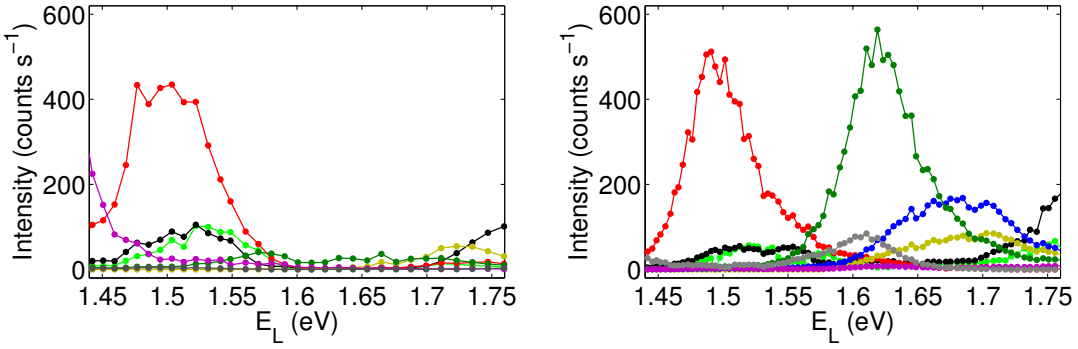

FIGURE 4.8: Plots showing the RBM intensity as a function of excitation energy, E_{L}, for measurements performed at (a) sampling region A and (b) sampling region B. Both measurements were performed at room temperature ($T = 292\mathrm{K}$). Plots show all RBMs that were obtained from the fitting procedure described in Section 4.2.1. Colour scheme: *grey* $\omega_{\mathrm{RBM}} = 211\mathrm{cm}^{-1}$ *purple* $\omega_{\mathrm{RBM}} = 213\mathrm{cm}^{-1}$ *light green* $\omega_{\mathrm{RBM}} = 228\mathrm{cm}^{-1}$ *black* $\omega_{\mathrm{RBM}} = 234\mathrm{cm}^{-1}$ *red* $\omega_{\mathrm{RBM}} = 238\mathrm{cm}^{-1}$ *yellow* $\omega_{\mathrm{RBM}} = 249\mathrm{cm}^{-1}$ *blue* $\omega_{\mathrm{RBM}} = 260\mathrm{cm}^{-1}$ *dark green* $\omega_{\mathrm{RBM}} = 267\mathrm{cm}^{-1}$.

In conclusion, the sample exhibits a significant degree of inhomogeneity which must be considered when performing Raman measurements. To be consistent, all future RRS and

TRIARS experiments are performed at sampling region B, which was found to contain a greater variety of resonant SWCNT species.

4.2.4 Nanotube (n, m) Assignment

There are a range of techniques that can provide information on the structural properties of SWCNTs. Microscopy techniques such as scanning electron microscopy (SEM), transmission electron microscopy (TEM), and atomic force microscopy (AFM), are powerful tools for determining the structural properties of SWCNTs, but these techniques can often be time consuming and lead to sample damage due to their invasive nature [115]. In contrast, spectroscopy techniques such as photoluminescence (PL) spectroscopy and Raman spectroscopy can provide rapid and less invasive tools for determining the (n, m) structural indices of SWCNTs [116, 117]. There have been a large number of studies demonstrating the use of Raman spectroscopy for this purpose [58–60, 117–121]. The majority of these studies are based on a graphical comparison of the relationship between the RBM frequencies, ω_{RBM}, and the theoretical Kataura plot (see Section 2.1.2.3). One (usually negative) aspect of Raman spectroscopy is that it can only be used to determine the structural properties of SWCNT that are resonant. This means that many laser sources are usually required to fully characterise a bundled SWCNT sample. However, this makes Raman spectroscopy particularly useful for determining the (n, m) structural indices of SWCNTs in this study because it is only the SWCNTs that are resonant (and contributing to the signal) which we wish to identify.

The (n, m) assignment procedure used in this thesis was adapted from a technique developed by Cheng et al. [58], with the additional advantage of using experimentally determined values of the optical transition energies, E_{22}, that were obtained for some of the SWCNT species. To begin the assignment process, high resolution spectra were obtain for two excitation energies, 1.51eV and 1.63eV, where according to Figure 4.8 (b), the two spectra are dominated by a response from different SWCNT species. To determine the Raman intensity, shift and linewidth (FWHM) of all RBMs present, the spectra were fitted using the technique discussed in Section 4.2.1. Figure 4.9 presents the fits and measured RBM frequencies, ω_{RBM}, for the spectra taken at (a) 1.51eV and (b) 1.63eV. It should be noted that the fitting procedure was performed with the minimum number of Lorentzian functions possible and without constraints on the linewidth parameters. This was to avoid over interpretation of the Raman spectra. Table 4.2 shows the fitting parameters obtained from the fits shown in Figures 4.9 (a) and (b), where the intensities are given as the ratio of the RBM intensity to the sum total of the RBM intensities, $\mathrm{I_{RBM}/I_{Total}}$, so that the modes which dominate the RBM spectra can be easily identified.

We know from Equation 2.18 that ω_{RBM} is inversely proportional to the SWCNT diameter d_t, and that d_t can be calculated from the structural indices, (n, m), according

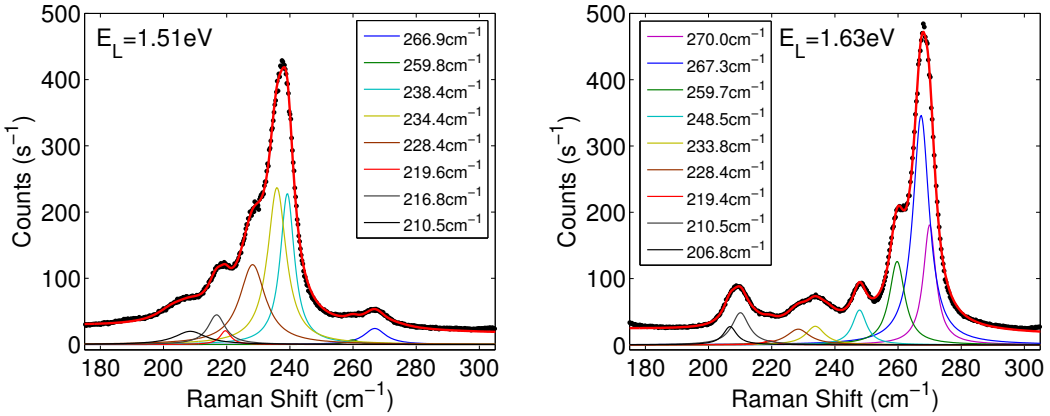

(a) (b)

FIGURE 4.9: Shows the fit (*solid red line*) to the experimental RBM spectra (*black dots*) taken for (a) $E_{\mathrm{L}} = 1.51$eV and (b) $E_{\mathrm{L}} = 1.63$eV. Measurements were performed at room temperature ($T = 292$K) and at sampling region B. Also shown are the individual Lorentzian functions which make up the fit and their corresponding ω_{RBM} values obtained from the c_i fitting parameter.

to Equation 2.2. Unfortunately, it is not possible to determine the SWCNT structural indices directly from ω_{RBM} because the A and B coefficients in Equation 2.18 can vary significantly due to sample conditions such as the diameter distribution, SWCNT growth methods, and the substrate material. A complete table of experimentally reported values for the A and B coefficients can be found in ref [58]. To work around this problem the greatest possible diameter range was calculated from the range of ω_{RBM} in Table

E_{L}	c_i [ω_{RBM} (cm^{-1})]	$2b_i$ [Γ_{RBM} FWHM (cm^{-1})]	$\mathrm{I_{RBM}/I_{Total}}$
1.51eV	210.5	11.0	0.0276
821nm	216.8	7.2	0.0621
	219.6	5.6	0.0289
	228.4	7.9	0.1672
	234.4	6.4	0.3283
	238.4	5.8	0.3161
	259.8	5.6	0.0097
	266.9	8.6	0.0336
1.63eV	206.8	5.4	0.0319
761nm	210.5	5.8	0.0563
	219.4	7.8	0.0072
	228.4	6.0	0.0275
	233.8	6.2	0.0325
	248.5	6.6	0.0610
	259.7	6.0	0.1461
	267.3	6.4	0.4019
	270.0	5.4	0.2104

TABLE 4.2: Fitting parameter values, obtained from the fits shown in Figures 4.9 (a) and (b).

4.2 using Equation 2.18 and the extreme values of A and B from the literature [58]. This diameter range was then plotted on the theoretical Kataura plot along with the excitation laser energy E_{L} to identify the (n, m) indices of all of the potential SWCNT candidates, as shown in Figure 4.10 for $E_{\mathrm{L}} = 1.63\mathrm{eV}$. Note that the E_{ii} in the Kataura plot are only an approximation, calculated using the nearest-neighbour tight binding (TB) model, and that empirically obtained Kataura plots have also been shown to depend on the environmental conditions of the sample [4]. For this reason, all SWCNTs within the greatest possible diameter range and within 0.25eV of the excitation energy were treated as potential SWCNT candidates. It is clear from Figure 4.10 that all of the SWCNT candidates exist in the E_{22} semiconducting branch of the Kataura plot.

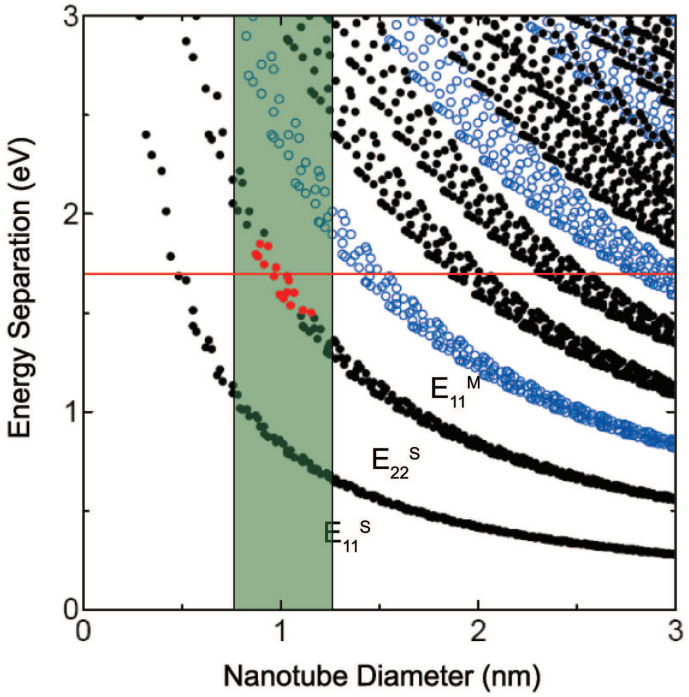

FIGURE 4.10: Kataura plot showing the optical transition energies E_{ii} as a function of nanotube diameter d_t for both semiconducting (*black dots*) and metallic (*blue open circles*) SWCNTs. Calculated using tight-binding model ($\gamma_0 = 2.9$ eV). The *horizontal red line* indicates $E_{\mathrm{L}} = 1.63\mathrm{eV}$, while the greatest possible diameter range for SWCNT candidates is indicated by the *shaded region* between the two *vertical black lines*.

The potential d_t values identified from Figure 4.10 were plotted $(1/d_t)$ against the experimental ω_{RBM} for all (n, m) assignments which were possible. This included multiple (n, m) assignments for a single ω_{RBM}. Assuming the relationship suggested by Equation 2.2, a linear fit was then applied to obtain the best fit to all of the potential assignments. The same fit was then re-applied only to those points representing unambiguous assignments, or the assignments which were closest to the linear fit, as shown in Figure 4.11 (a) for $E_{\mathrm{L}} = 1.63\mathrm{eV}$. The (n, m) assignments for both excitation laser energies ($E_{\mathrm{L}} = 1.51\mathrm{eV}$ and $E_{\mathrm{L}} = 1.63\mathrm{eV}$) are presented in Table 4.3, along with the refined A and

B fitting parameters. Note that the experimentally obtained coefficients are consistent with those obtained in other studies [58].

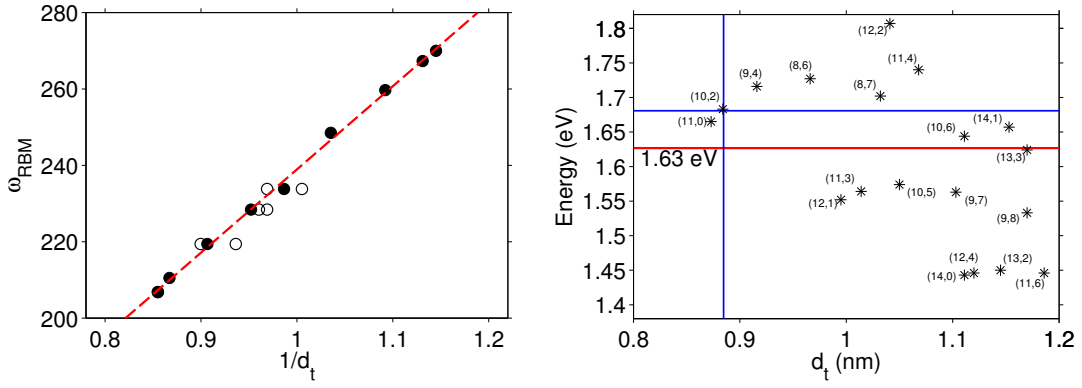

(a) (b)

FIGURE 4.11: (a) Potential SWCNT diameters d_t plotted $(1/d_t)$ against the experimental ω_{RBM} for all (n, m) assignments which were possible. The filled circles indicate unambiguous assignments, or the assignments which were closest to the regression (*red broken line*) and used to refine the A and B parameters. $A = 217.8 \pm 5.1\mathrm{cm}^{-1}\mathrm{nm}$ and $B = 21.1 \pm 5.1\ \mathrm{cm}^{-1}$. (b) Experimentally determined Kataura plot taken from [4]. Horizontal red line indicates $E_{\mathrm{L}} = 1.63\mathrm{eV}$. *Horizontal* and *vertical blue lines* indicate the experimentally determined E_{22} and the assigned SWCNT diameter d_t for the $\omega_{RBM} = 266.9\mathrm{cm}^{-1}$ RBM.

E_{L}	ω_{RBM} (cm^{-1})	d_t (nm)	Assignment	A $(\mathrm{cm}^{-1}\mathrm{nm})$ and B (cm^{-1})
1.51eV	210.5	1.1532	$(14, 1)$	$A = 215.2 \pm 6.5$
821nm	216.8	1.1115	$(14, 0)$	$B = 23.4 \pm 6.5$
	219.6	1.1029	$(9, 7)$	
	228.4	1.0502	$(10, 5)$	
	234.4	1.0136	$(11, 3)$	
	238.4	0.9948	$(12, 1)$	
	259.8	0.9156	$(9, 4)$	
	266.9	0.8841	$(10, 2)$	
1.63eV	206.8	1.1695	$(13, 3)$	$A = 217.8 \pm 5.1$
761nm	210.5	1.1532	$(14, 1)$	$B = 21.1 \pm 5.1$
	219.4	1.1029	$(9, 7)$	
	228.4	1.0502	$(10, 5)$	
	233.8	1.0136	$(11, 3)$	
	248.5	0.9658	$(8, 6)$	
	259.7	0.9156	$(9, 4)$	
	267.3	0.8841	$(10, 2)$	
	270.0	0.8733	$(11, 0)$	

TABLE 4.3: Identified ω_{RBM} and (n, m) assignments for $E_{\mathrm{L}} = 1.51\mathrm{eV}$ and $E_{\mathrm{L}} = 1.63\mathrm{eV}$. SWCNT diameters d_t and refined A and B coefficients are also given.

To make use of the experimentally determined E_{22} values, obtained from the Stokes resonance profiles in Figure 4.8, the structural (n, m) assignments in Table 4.3 were

compared with previously proposed (n, m) assignments based on PL measurements carried out by Weisman et al. [4]. To demonstrate this, Figure 4.11 (b) shows an empirical version of the Kataura plot which was plotted from Weisman's measurements. Overlaid on the plot are *horizontal* and *vertical blue lines* which indicate the SWCNT diameter d_t that was assigned to the $\omega_{RBM} = 266.9\text{cm}^{-1}$ RBM and the experimentally determined E_{22} value for the $\omega_{RBM} = 266.9\text{cm}^{-1}$ mode respectively. Weisman's measurements were made on SWCNTs in aqueous surfactant suspension, therefore, we can expect a level of disagreement with the optical transition energy E_{22} obtained from the bundled SWCNT sample. Even so, the interception of the two *blue lines* in Figure 4.11 (b) indicates that the (n, m)=$(10, 2)$ assignment for the $\omega_{RBM} = 266.9\text{cm}^{-1}$ RBM is in agreement with the assignment proposed by Weisman. Furthermore, for all experimental E_{22} values that were available, the assignments in Table 4.3 were found to be in agreement with Weismans previously proposed (n, m) assignments. In conclusion, for sampling region B, the excitation laser energies $E_\text{L} = 1.51\text{eV}$ and $E_\text{L} = 1.63\text{eV}$ have strong incoming resonances with SWCNT species in different diameter ranges. Drawing on the information contained in Tables 4.2 and 4.3, for $E_\text{L} = 1.51\text{eV}$, the majority (approximately 90%) of the Raman signal is due to a response from SWCNT species in the diameter range $0.99 - 1.11\text{nm}$, while for $E_\text{L} = 1.63\text{eV}$, the majority (approximately 82%) of the Raman signal is due to SWCNTs in the diameter range $0.87 - 0.97\text{nm}$.

4.2.5 Temperature Dependence of Optical Transition Energies

A TRIARS experiment specifically probes SWCNT species with optical transition energies E_{ii} close to the excitation laser energy E_L. In order to measure the temperature dependence of the phonon dynamics, the TRIARS experiments reported in this thesis are performed for sample temperatures in the range $T = 4 - 600\text{K}$. However, the measured E_{ii} and nanotube (n, m) assignments made in Section 4.2.4 are based on RRS measurements performed at room temperature ($T = 292\text{K}$). In theory, if the optical transition energies E_{ii} vary significantly with temperature, the same TRIARS experiment performed for different sample temperatures could probe the dynamics of different SWCNT species. It follows that it may be necessary to tune the laser energy as the sample temperature is varied so that the TRIARS experiment continues to probe the same SWCNT species.

There have been two notable studies on the temperature dependence of the optical transition energies E_{ii} in SWCNTs. The first study, carried out by Fantini et al. on bundled HiPco SWCNT, found that the E_{22} energies are red shifted for MOD1 SWCNT and blue shifted for MOD2 SWCNTs (see Section 2.1.2.2) [107]. The typical E_{22} redshifts in this study were measured to be in the range 20-140meV when varying the power density from 0.1 to $2.5\text{mW}/\mu\text{m}^2$ as a means of varying the local sample temperature. In a second study, carried out by Cronin et al. on SWCNT freely suspended in air across

a quartz trench, the optical transition energies were found to down shift in energy by as much as 50meV/140K [108]. The observed temperature dependence of E_{ii} in these studies has been attributed to a combination of effects, including e-ph coupling, thermal expansion of the lattice, and tube-tube interactions [107, 108]. More importantly, it is clear from these studies that the temperature dependence of E_{ii} must be considered before conducting TRIARS experiments for different sample temperatures.

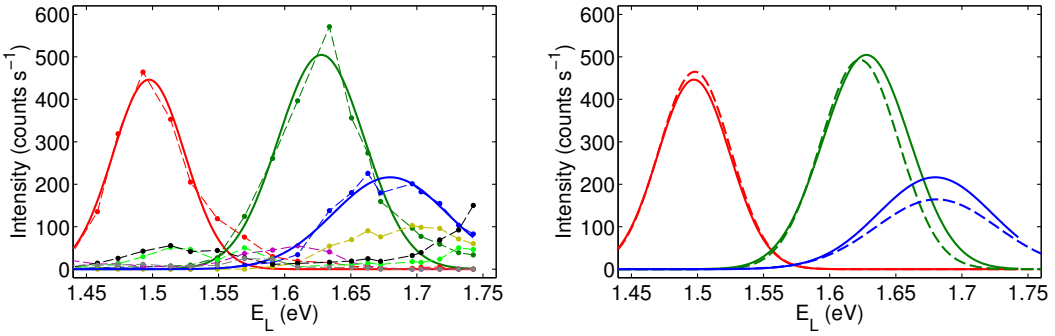

FIGURE 4.12: Temperature dependence of the optical transition energies, E_{ii}. (a) Shows RBM intensity as a function of excitation energy, E_{L}, for measurements performed at low temperature ($T = 4$K) at sampling region B. For clarity the coloured dash lines connect consecutive data points. Example Gaussian fits (*solid curves*) are shown for three of the RBM resonance profiles. (b) Shows the fitted resonance profiles for $T = 292$K (*broken curve*) and $T = 4$K (*solid line*). Colour scheme: *grey* $\omega_{\mathrm{RBM}} = 211\mathrm{cm}^{-1}$ *purple* $\omega_{\mathrm{RBM}} = 213\mathrm{cm}^{-1}$ *light green* $\omega_{\mathrm{RBM}} = 228\mathrm{cm}^{-1}$ *black* $\omega_{\mathrm{RBM}} = 234\mathrm{cm}^{-1}$ *red* $\omega_{\mathrm{RBM}} = 238\mathrm{cm}^{-1}$ *yellow* $\omega_{\mathrm{RBM}} = 249\mathrm{cm}^{-1}$ *blue* $\omega_{\mathrm{RBM}} = 260\mathrm{cm}^{-1}$ *dark green* $\omega_{\mathrm{RBM}} = 267\mathrm{cm}^{-1}$.

Figure 4.12 (a) shows the RBM intensity as a function of excitation energy, E_{L}, for measurements performed at low temperature ($T = 4$K). These measurements were taken at sampling region B, and can therefore be directly compared with the results presented in Figure 4.8 (b). Each of the RBM resonance profiles were fitted with Gaussian functions but for the purpose of illustration only three of these fits are shown in Figure 4.12 (a). For the same three RBMs, Figure 4.12 (b) compares the Gaussian functions which were fitted to the experimental RBM resonance profiles obtained for $T = 292$K (*broken line*) and $T = 4$K (*solid line*). From this comparison it is tempting to suggest that the E_{ii} associated with the $\omega_{\mathrm{RBM}} = 238\mathrm{cm}^{-1}$ RBM exhibits little or no temperature dependence, while the other two RBMs experience a slight upshift and downshift (approximately 5meV) in their E_{ii}. However, within the resolution of the experiment ($\pm$10meV) there is no measurable temperature dependence of E_{ii}. In conclusion, RRS measurements taken at room temperature ($T = 292$K) and low temperature ($T = 4$K) suggest that there is no significant temperature dependence of E_{ii} when compared with the energy width of the resonance profiles, which means that it will not be necessary to tune the laser excitation energy E_{L} during TRIARS measurements.

4.3 Analysis of *D*-band and *G*-band Resonance Measurements

Analysis of D-band and G-band resonance measurements is carried out in a similar manor to the analysis of the RBM resonance measurements in Section 4.2. However, unlike the RBMs, the D- and G-band contributions from different SWCNTs are spectrally overlapped, and generally cannot be resolved. A further complication is introduced because the difference in energy between the incoming and outgoing resonance conditions is much greater than the individual resonance widths. Fortunately, the interpretation of the D- and G-band resonance profiles can be assisted by knowing the optical transition energies, E_{ii}, which can be determined from the RBM resonance intensity profiles (Section 4.2).

Careful analysis of the G-band, including the G^+ and G^- components, can be a useful tool for SWCNT characterisation. For example, it is possible to determine whether a resonant or isolated SWCNT is semiconducting of metallic through lineshape analysis (see Section 2.2.4), and to determine the SWCNT diameter, d_t, though the G^- frequency, ω_{G^-} [5, 122]. Meanwhile, for measurements of bundled SWCNTs, the dispersive nature of the D-band can reveal when the spectrum is dominated by a particular species of SWCNT through Raman shift and linewidth analysis.

Figures 4.13 and 4.14 present an overview of the D- and G-band spectra, recorded at room temperature ($T = 292$K) and at sampling region B. Similar measurements were also taken at low temperature ($T = 4$K) and at sampling region A.

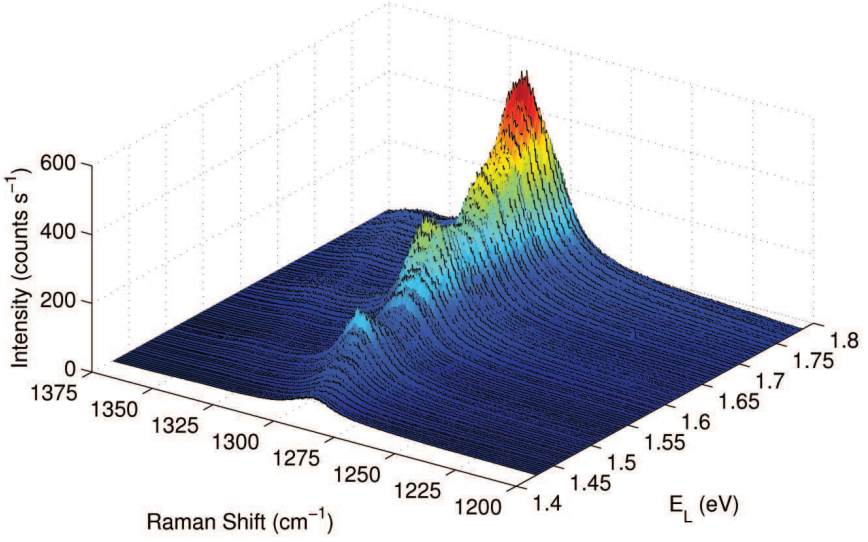

FIGURE 4.13: A 3D plot showing an overview of the Stokes D-band RRS measurement, taken at room temperature ($T = 292$K) and at sampling region B. The wavelength was varied in ~ 2 nm increments and a total of 86 laser lines were used.

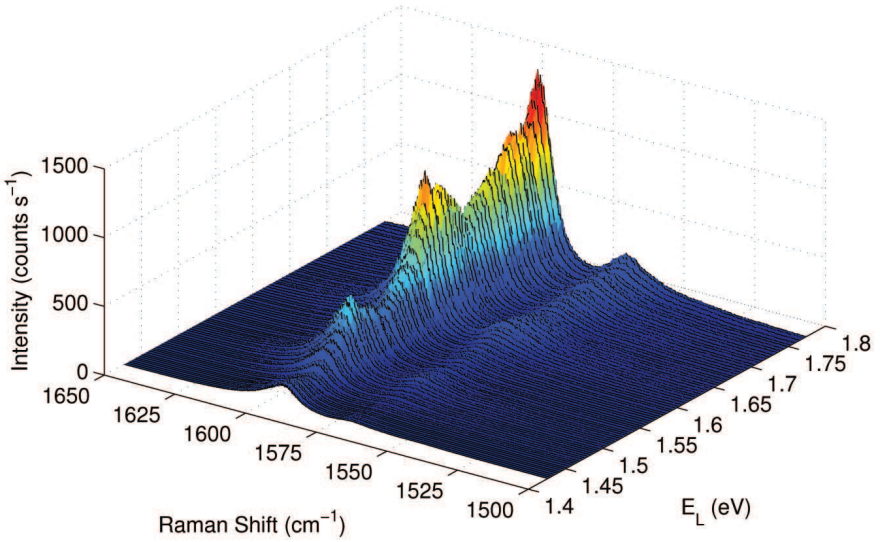

FIGURE 4.14: A 3D plot showing an overview of the Stokes G-band RRS measurements, taken at room temperature ($T = 292$K) and at sampling region B. The wavelength was varied in ~ 2 nm increments and a total of 86 laser lines were used.

This section begins with a description of the fitting procedures used to obtain the Raman intensity, shift and linewidth (FWHM) of the D- and G-band Raman features. This is followed by an interpretation of the E_{L} dependence of the D- and G-band Raman intensity, the E_{L} dependence of the D-band shift (ω_D) and linewidth (Γ_D) and the E_{L} dependence of the G-band shift ($\omega_{G^{\pm}}$).

4.3.1 Fitting Procedures

This section discusses the fitting procedures that are used to determine the Raman intensity, shift and linewidth FWHM of the D- and G-band features as a function of laser excitation energy, E_{L}. Apart from the particular fitting functions that are used, the procedures for fitting the D- and G-band are similar to the RBM fitting procedure described in Section 4.2.1, i.e. they are based on a linear least squares regression algorithm and use similar Matlab functions (see Appendix A Matlab Code 3) to control the regression and return the fitting parameters and 95% confidence bounds. The G- and D-band fitting functions are selected by considering the theory of first and second order Raman scattering, taking into account the inhomogeneous broadening that is expected for measurements performed on bundled SWCNTs, and by reviewing the fitting techniques used in other studies. There is not sufficient room to discuss in detail the scattering mechanisms which govern the characteristics of the D- and G-band Raman features here, however, an in-depth discussion of the Raman scattering mechanisms responsible for the D- and G-band features can be found in Sections 2.2.5 and 2.2.4 respectively.

4.3.1.1 *D*-band Fitting Procedure

In the ideal case of an isolated SWCNT, with limited inhomogeneous broadening, the theory of DR Raman scattering tells us that the D-band can be well fitted with two Lorentzian functions of slightly different frequency, ω_D [37, 100]. Therefore, the fitting function that was used to model the D-band was based on the sum of a linear polynomial and two Lorentzian functions, and can be summarised by Equation 4.2

$$f(x, p_0, p_1, a_1, b_1, c_1, a_2, b_2, c_2) = (p_1 x + p_0) + \sum_{i=1}^{2} a_i \frac{{b_i}^2}{(x - c_i)^2 + {b_i}^2} \tag{4.2}$$

where, p_0 and p_1 are the fitting parameters which govern the form of the linear polynomial, and a_i, b_i and c_i are the fitting parameters which represent the Raman intensity, linewidth/2 (FWHM) and shift of the two Lorentzian functions that are included. The linear polynomial is included to model the linear broadband background, while the two Lorentzian functions model the Raman active modes which make up the D-band. Figure 4.15 shows a typical result of this fitting function applied to a room temperature ($T = 292$K) D-band spectrum obtained for $E_{\mathrm{L}} = 1.51$eV and from sampling region B.

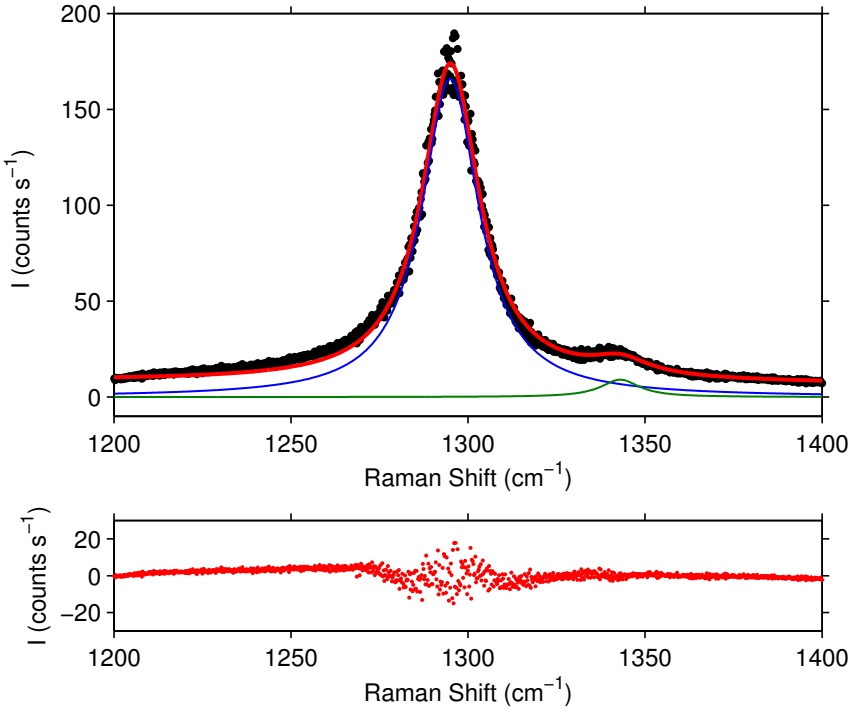

FIGURE 4.15: *Top:* Plot showing the fit (*solid red line*) to the D-band experimental Raman spectra (*black dots*) taken for $E_{\mathrm{L}} = 1.51$eV, at room temperature ($T = 292$K), and at sampling region B. Also shown are the Lorentzian functions which have been determined by the least squares fitting procedure. *Bottom:* Shows the residuals of the fit.

c_i [ω_D (cm^{-1})]	a_i [I (counts s^{-1})]	$2b_i$ [(Γ_D) FWHM (cm^{-1})]
1295 ± 0.5	165.7 ± 1.0	19.8 ± 0.2
1343 ± 1.0	9.059 ± 1.2	13.2 ± 2.8

TABLE 4.4: Lorentzian (D-band) fitting parameters obtained from the fit in Figure 4.15.

It is clear from the form of the residuals that the experimental lineshape of the D-band features are not exact Lorentzians, which can be explained by inhomogeneous broadening and bundling effects. However, the Lorentzian line shapes provide a sufficiently good fit to determine the Raman intensity, shift and width of the two main D-band features. The fitting parameters obtained from the fit in Figure 4.15, along with their 95% confidence bounds, are presented in Table 4.4. The more intense of the two D-band features, $\omega_D = 1295\text{cm}^{-1}$, is likely to be the response of those SWCNT species which are most resonant for $E_{\text{L}} = 1.51\text{eV}$. However, one cannot be sure if the less intense D-band feature, $\omega_D = 1295\text{cm}^{-1}$, is due to the same SWCNT species, as predicted by the theory of second-order Raman scattering, or due to a small population of large diameter SWCNT species in the sample [5, 48]. For this reason, future analysis of the D-band is confined to examining the fitting parameter associated with the dominant D-band feature. It is important to note that the Raman intensity, shift and linewidth obtained from this fitting procedure are those of a D-band feature which is a sum of different D-band features originating from different SWCNT species in resonance with E_{L}.

4.3.1.2 *G*-band Fitting Procedure

The G-band generally consists of two main features, the G^+ feature which can be found at approximately 1592cm^{-1} and the G^- feature which can be found at approximately 1570cm^{-1}. In the case of an isolated semiconducting SWCNT, with limited inhomogeneous broadening, it has been demonstrated that the G-band can be well fitted by two Lorentzian functions which represent the G^+ and G^- bands [123]. However, for bundled SWCNTs, it has been shown that the two main features can each require between one and four Lorentzian functions of slightly different frequency to be well fitted [37, 123, 124].

After careful consideration two fitting functions were attempted for the G-band. The first function, which we will name the 'detailed fitting function', was based on fitting three Lorentzians to each of the two main Raman features (6 Lorentzians in total), which was the maximum number of Lorentzian pairs which could be added without risking over interpretation of the Raman spectra. The second fitting function, which we will name the 'simple fitting function', was based on fitting one Lorentzian function to each of the two main Raman features (2 Lorentzians in total). This fit assumes that the G-band signal is from a single type of SWCNT with limited inhomogeneous broadening. Both

of these fitting functions included a linear polynomial to model the linear broadband background.

Figure 4.16 shows a typical result of the 'detailed fitting function' applied to a G-band spectrum obtained for $E_{\mathrm{L}} = 1.51\mathrm{eV}$ at room temperature and on sampling region B. The fact that three Lorentzians provide a good fit to the G^- band indicates that the Raman signal is dominated by the response of semiconducting SWCNT species, which is entirely consistent with the (n, m) assignments made in Section 4.2.4. Another important observation is that there is no evidence of the strong $1582\mathrm{cm}^{-1}$ G-band feature seen in graphene and graphite [2, 125]. Whilst the SWCNTs came with only 'standard purification', this suggests that the bundled SWCNTs are of high purity, and means that all of the observed features are explicable as coming from SWCNTs.

The fitting parameters obtained from the fit in Figure 4.16, along with their 95% confidence intervals, are presented in Table 4.5. The inset in Figure 4.16 shows a result of the 'simple fitting function' applied to the same G-band spectrum. The fitting parameters obtained from this model are provided in Table 4.5.

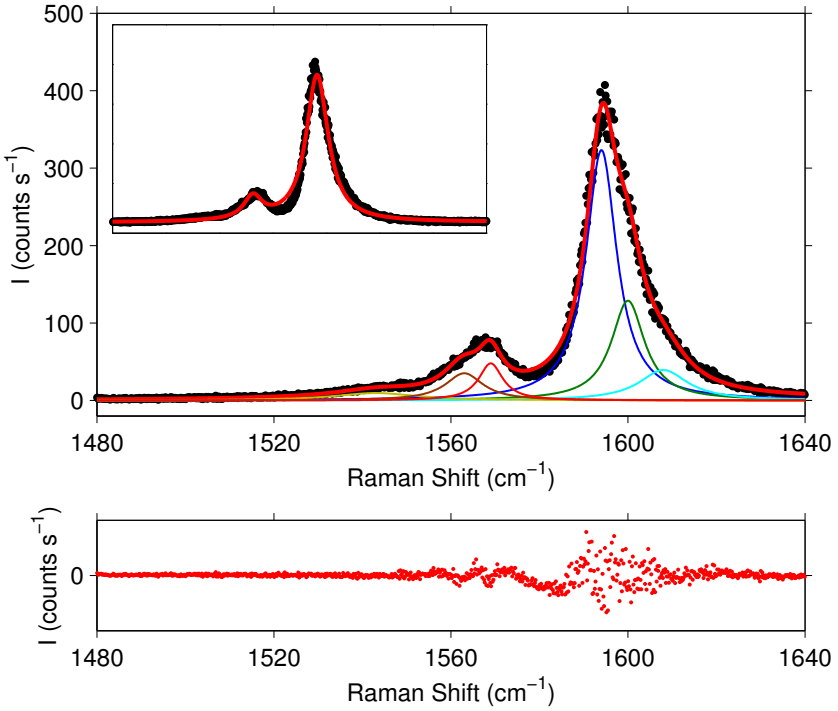

FIGURE 4.16: *Top:* Plot showing a result of applying the 'detailed fitting function' (*solid red line*) to the experimental G-band Raman spectra (*black dots*) taken for $E_{\mathrm{L}} = 1.51\mathrm{eV}$ at room temperature ($T = 292\mathrm{K}$) and at sampling region B. Also shown are the 6 Lorentzian functions which have been determined by the fitting procedure. *Bottom:* Shows the residuals of the fit. *Inset:* Shows the result of applying the 'simple fitting function' to the same experimental data. See main text for more information on the fitting functions used.

Model	c_i [ω_G (cm^{-1})]	a_i [I (counts s^{-1})]	$2b_i$ [Γ_G FWHM (cm^{-1})]	Feature
Detailed	1543 ± 3	9.6 ± 1.8	23.0 ± 8.4	G^-
	1563 ± 1	35.2 ± 7.0	10.4 ± 3.0	G^-
	1569 ± 2	47.9 ± 9.1	6.6 ± 1.4	G^-
	1594 ± 1	323.3 ± 9.2	8.4 ± 0.2	G^+
	1600 ± 2	128.8 ± 15.5	9.2 ± 1.4	G^+
	1608 ± 3	39.3 ± 10.2	13.4 ± 2.0	G^+
Simple	1566 ± 1	57.6 ± 4.2	10.4 ± 1.2	G^-
	1596 ± 1	369.9 ± 3.8	12.6 ± 0.2	G^+

TABLE 4.5: Lorentzian (G-band) fitting parameters obtained from the fitting in Figure 4.16. Results are presented for the 'detailed fitting function' and 'simple fitting function'.

It would not be reasonable to assume that the 'detailed fitting function' is able to resolve the contributions from different species of SWCNT. In fact, fits to the Raman spectra for each of the laser energies provided evidence to the contrary. Meanwhile, it can be shown from the values given in Table 4.5 that the 'simple fitting function' provides one Raman shift and intensity for each of the G^+ and G^- bands, which can be interpreted as a weighted average of the contributions from the different species of SWCNT that are resonant. The rest of this section focuses on the interpretation of the fitting parameters obtained from the 'simple fitting function', as this function provides sufficiently clear results without risking over interpretation of the Raman spectra.

4.3.2 E_{L} dependence of the D- and G-band Raman Intensity

In a TRIARS experiment the time-dependent component of the signal is dominated by a response from SWCNT species that absorb a significant amount of the incident laser radiation and satisfy a resonance condition for anti-Stokes Raman scattering. This means that we are only concerned with the SWCNT species for which the incoming resonance condition is satisfied i.e. $E_{\mathrm{L}} \sim E_{ii}$. However, it is useful to know which SWCNT species contribute to the time-independent component of the TRIARS signal as this can allow one to extract useful information on the fractional increase in the pumped to non-pumped phonon population [126] (see Appendix D).

Figure 4.17 shows the E_{L} dependence of (a) the D-band intensity and (b) the G-band intensity (G^+ and G^- bands), obtained at room temperature ($T = 292$K) and at sampling region B. Also indicated on the figure are the incoming and outgoing resonances of the $(12, 1)$ SWCNT and the incoming resonance of the $(10, 2)$ SWCNT species. The D- and G-band intensities were obtained from the fitting procedures described in Section 4.3.1, thus the D- and G-band intensity profiles shown in Figure 4.17 are interpreted as a sum of intensity profiles from many species of SWCNT. In both cases we see a strong enhancement in the intensity of the Raman signal at the incoming resonance energies. This suggests that both the D-band and G-band Raman signals are dominated by the

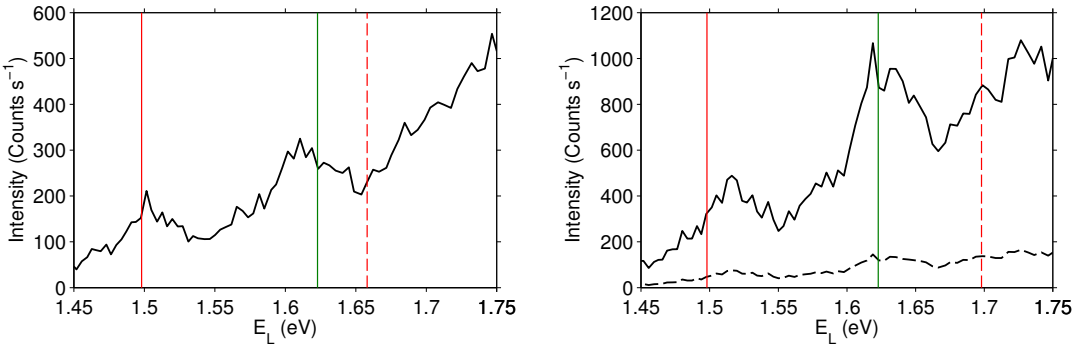

(a) (b)

FIGURE 4.17: Plots showing (a) D-band intensity (*solid black line*) as a function of E_{L}, and (b) G^+ (*solid black line*) and G^- band (*broken black line*) intensities as a function of E_{L}. Measurements were performed at room temperature ($T = 292$K) at sampling region B. Also indicated are the incoming (*solid coloured line*) and outgoing (*broken coloured line*) resonance energies for the $(12,1)$ $\omega_{\mathrm{RBM}} = 238\mathrm{cm}^{-1}$ *red* and $(10,2)$ $\omega_{\mathrm{RBM}} = 267\mathrm{cm}^{-1}$ *dark green* SWCNT species.

same species of SWCNT that dominate the RBM signal at those energies. Similar Raman intensity contributions are expected for the outgoing resonance energy of the $(12,1)$ SWCNT (*dashed line*). Whilst there is a possible increase in the G-band intensity at the $(12,1)$ outgoing resonance energy, there is no evidence of an increase in the D-band intensity due to the $(12,1)$ outgoing resonance. This suggests that the scattering rate for outgoing resonance may be lower than that for the incoming resonance; however, one must be careful not to over interpret the D- and G-band resonance intensity profiles because the incoming and outgoing resonances of the individual SWCNT species cannot be separated out.

4.3.3 E_{L} dependence of the D-band Shift and Linewidth

In graphene, the D-band frequency, ω_D, has been shown to have a strong linear dependence on the excitation laser energy, E_{L}, with a dispersion of approximately $53\mathrm{cm}^{-1}/\mathrm{eV}$ [17, 37]. The origin of this dispersive behaviour has already been discussed in Section 2.2.5. Meanwhile, there have been a number of investigations of the dispersive nature of the D-band in both bundled and isolated SWCNT samples, with some notable differences in their observations [17, 127–129]. Firstly, the D-band frequency in bundled SWCNT is consistently $\sim 20\mathrm{cm}^{-1}$ lower, compared with graphene and isolated SWCNT, and exhibits and oscillatory behaviour as the laser energy E_{L} is varied [127]. Secondly, for isolated SWCNTs and for a given E_{L}, the D-band frequency is measured to be different for different SWCNTs species [128, 129]. It has been concluded from these studies that the D-band spectra observed for a bundled SWCNT sample is a sum of the different D-band signals originating from different (n,m) SWCNT species [17]. Thus, for the E_{L} where a single type of SWCNT dominates the Raman spectra one would expect the

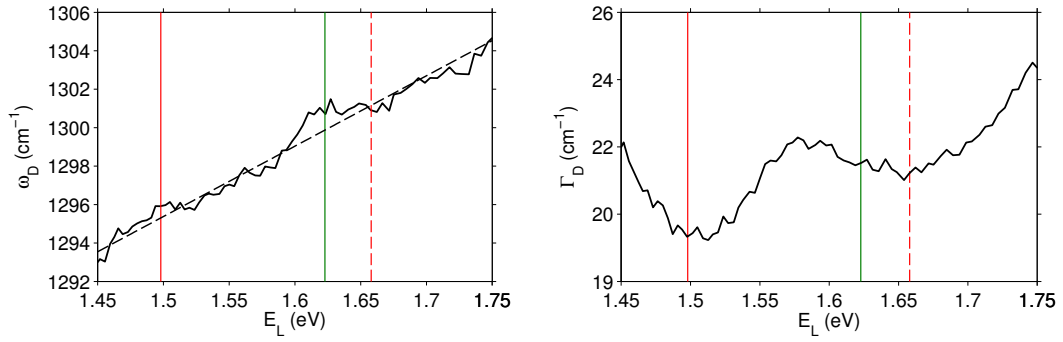

(a) (b)

FIGURE 4.18: Plots showing (a) ω_D (*solid black line*) as a function of E_{L}, and (b) Γ_D as a function of E_{L}. Measurements were performed at room temperature (T= 292K) at sampling region B. Also indicated are the incoming (*solid coloured line*) and outgoing (*broken coloured line*) resonance energies for the (12,1) $\omega_{\mathrm{RBM}} = 238\mathrm{cm}^{-1}$ *red* and (10,2) $\omega_{\mathrm{RBM}} = 267\mathrm{cm}^{-1}$ *dark green* SWCNT species.

frequency, ω_D, as determined by the fitting procedure described in Section 4.3.1, to tend to the frequency of that particular SWCNT, and the Raman linewidth, Γ_D, to tend to the linewidth expected for an isolated SWCNT.

Figures 4.18 (a) and (b) present the E_{L} dependence of ω_D and Γ_D respectively, as determined by fitting the spectra obtained at room temperature ($T = 292\mathrm{K}$) and at sampling region B. The incoming and outgoing resonance energies of the SWCNT species which have the most intense RBM signals ($(12,1)$ and $(10,2)$) are indicated in the figures. A linear E_{L} dependence of ω_D is observed with a measured dependence of $\omega_D = 1241 + 37E_{\mathrm{L}}$. On closer examination the measured dispersion of the D-band becomes relatively flat in the energy ranges $1.49 - 1.54\mathrm{eV}$ and $1.60 - 1.68\mathrm{eV}$. These flat regions coincide with the incoming resonance energies of the two dominant SWCNTs. This strongly supports the notion that different SWCNT species dominate the D-band Raman spectra for laser energies 1.51eV and 1.63eV, and that the SWCNT species are those assigned in Section 4.2.4. Meanwhile, Figure 4.18 (b) shows a narrowing of the linewidth Γ_D as E_{L} tends towards the incoming resonance energies of the two dominant SWCNTs. This provides additional evidence that a limited number of SWCNT species dominate the D-band Raman spectra for laser energies 1.51eV and 1.63eV.

4.3.4 E_{L} dependence of G-band Shift

G-band measurements on isolated SWCNTs have shown that the frequency of the G^+ band, ω_{G^+}, is independent of nanotube diameter d_t, while the frequency of the G^- band, ω_{G^-}, is strongly dependent on d_t and whether the SWCNT is metallic or semiconducting [5]. The d_t dependence of ω_{G^+} and ω_{G^-} is shown in Figure 4.19 (a) [5]. The strong diameter dependence of ω_{G^-} and the fact the ω_{G^+} exhibits essentially no dependence on d_t originates from the fact that the G^+ mode is related to carbon atom vibrations

along the SWCNT axis, while the G^- mode is related to carbon atom vibrations along the circumferential direction of the SWCNT (see Section 2.2.4).

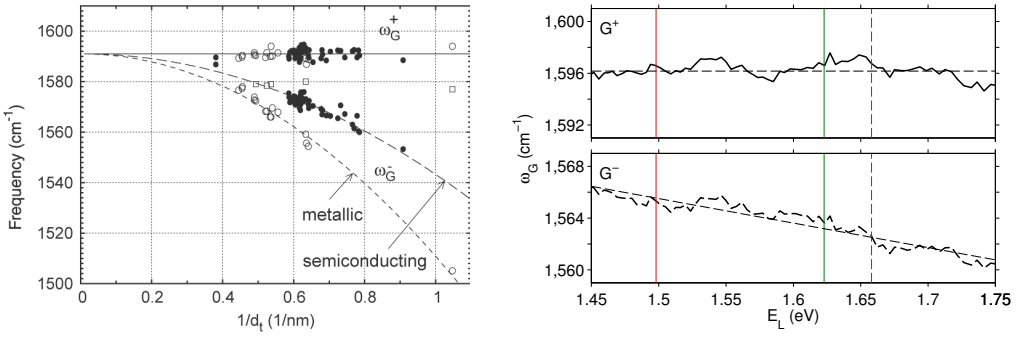

(a) (b)

FIGURE 4.19: (a) Plot showing the d_t dependence of ω_{G^+} and ω_{G^-} for both metallic and semiconducting SWCNTs. Taken from ref [5]. (b) Plots showing ω_{G^+} (*solid black line*) and ω_{G^-} (*broken black line*) as a function of E_{L}. Measurements were performed at room temperature ($T = 292$K) at sampling region B. Also indicated are the incoming (*solid coloured line*) and outgoing (*broken coloured line*) resonance energies for the $(12, 1)$ $\omega_{\mathrm{RBM}} = 238\mathrm{cm}^{-1}$ *red* and $(10, 2)$ $\omega_{\mathrm{RBM}} = 267\mathrm{cm}^{-1}$ *dark green* SWCNT species.

One would expect ω_{G^-}, as determined by the 'simple fitting procedure' described in Section 4.3.1, to tend to the ω_{G^-} of the SWCNT which dominates the G-band spectra. Figure 4.19 (b) shows the E_{L} dependence of ω_{G^+} and ω_{G^-}, obtained at room temperature ($T = 292$K) and at sampling region B. It is clear from the figure that ω_{G^+} is essentially independent of d_t while ω_{G^-} decreases with increasing E_{L}. This behaviour supports the assumption that the majority of the G-band Raman signal is due to a response from SWCNT species in the diameter range $0.99 - 1.11$nm for $E_{\mathrm{L}} = 1.51$eV and $0.87 - 0.97$ for $E_{\mathrm{L}} = 1.63$eV.

4.4 Conclusions

Using a technique based on a graphical comparison of the relationship between experimentally determined ω_{RBM} and E_{22} and the Kataura plot, structural (n, m) assignments have been made for all of the SWCNT species which are resonant in the energy range of the experimental system. These structural assignments have been shown to be in agreement with previously proposed (n, m) assignments based on PL measurements, carried out by Weisman et al. [4]. The sample was found to exhibit a significant degree of inhomogeneity, which must be considered when performing Raman measurements. As a result it was decided that all future TRIARS measurements would be performed at sampling region B, which contains a greater variety of resonant SWCNT species. Careful analysis of the RBM resonance measurements shows that for $E_{\mathrm{L}} = 1.51$eV the majority of the Raman signal is due to a response from SWCNT species in the diameter range $0.99 - 1.11$nm, while for $E_{\mathrm{L}} = 1.63$eV the majority of the Raman signal is

due to SWCNT species in the diameter range $0.87 - 0.97$nm. Analysis of the D- and G-band resonance measurements, including investigations of the E_{L} dependence of ω_D, Γ_D and ω_{G^-} is consistent with the findings from RBM analysis. The E_{L} dependence of the D- and G-band intensity suggests that the scattering rate for outgoing resonance is lower than that for the incoming resonance for the D- and G-bands, however, this result cannot be confirmed due to the fact that the incoming and outgoing D- and G-band resonances of the individual SWCNT species cannot be separated out.

These findings suggest that TRIARS measurements performed for excitation energies $E_{\mathrm{L}} = 1.51$eV and $E_{\mathrm{L}} = 1.63$eV will predominantly probe the phonon dynamics of SWCNT species in different diameter ranges. Furthermore, RRS measurements taken at room temperature ($T = 292$K) and low temperature ($T = 4$K) suggest that there is no significant temperature dependence of E_{ii} when compared with the energy width of the resonances. This means that during TRIARS measurements it will not be necessary to tune the laser energy E_{L} when varying the sample temperature.

Chapter 5

A Study of the *G*-band Phonon Population Dynamics

This chapter presents a study of the dynamics of the G-band (Γ-point) phonon population measured using TRIARS. The study has been undertaken to improve our understanding of G-band phonon decay in SWCNTs, which is believed to be a limiting factor of high-field transport (see Chapter 1), and includes the results from over 70 independent TRIARS experiments. The publication which covers this work can be found in Ref [130] and in the Publications section in this thesis. The chapter begins with a review of the existing ultrafast SWCNT G-band studies. This is followed by the details of the specific TRIARS experiments that are performed in this study. The next section presents the results of the TRIARS experiments. This is followed by two sections which are dedicated to the analysis and interpretation of the TRIARS data. The chapter concludes with a summary of the findings of the experiments.

5.1 Review of Ultrafast SWCNT *G*-band Studies

In certain cases, studies of the Raman linewidth and its dependence on temperature can indirectly probe the phonon dynamics in SWCNTs [65, 131, 132]. However, these measurements can only provide a lower limit on the phonon population lifetime since the Raman linewidth can include contributions from inhomogeneous broadening and pure dephasing (see Section 2.3). Quick analysis of the G-band phonon linewidths presented in Table 4.5, and those reported for isolated SWCNTs [65], suggest a lower limit of approximately 0.7ps for the G-band phonon population lifetime, T_1, which is much less than has been theoretically predicted [34].

In recent years, ultrafast studies of G-band phonons in SWCNTs have been carried out using time-resolved Raman spectroscopy techniques, which offer the ability to measure

the phonon dynamics more directly (see Section 2.4). TRIARS is particularly useful for probing the phonon population lifetime, T_1, whilst TRCARS can provide a measure of the total dephasing time T_2 and is often a measure of free induction decay which is comparable to line-shape analysis in the frequency domain. These two techniques, along with careful linewidth studies, can provide complimentary information for studying the phonon dynamics. For example, Lee et al. [54] were able to exclude artefacts which arise from the comparison of dynamics measured under different sample conditions, and under different measurement schemes, by performing sequential TRIARS and TRCARS measurements on the same SWCNT sample in order to measure $T_2/2$ and T_1. Using this technique, Lee et al. were able to study the pure dephasing time $\tau_{\mathrm{ph}}/2$ (see Equation 2.20), which provides information on the elastic scattering of phonons in SWCNTs.

In this thesis we are primarily concerned with the mechanisms that are important to the decay of the non-equilibrium phonon population, which can be studied through TRIARS alone. The TRIARS experiments presented in this chapter build on a number of recent G-band TRIARS studies. The first of which was reported in 2008 by Song et al. [55]. Using an excitation laser energy of 1.55 eV, Song et al. measured a room temperature G-band optical phonon population lifetime of $T_1 = 1.1$ ps for dispersed semiconducting $(6, 5)$ SWCNTs. The SWCNTs in Song's study were suspended in D_2O with sodium dodecylbenzene sulfonate or sodium cholate as a surfactant. Song et al. successfully demonstrated the power of TRIARS as a tool for probing the dynamics of Raman active phonons in SWCNTs and paved the way for others to adopt the technique. In a separate study by Kang et al. [6], the room temperature G-band phonon lifetime in bundled semiconducting, and bundled metallic SWCNTs were measured to be $T_1 = 1.2$ ps, and $T_1 = 0.9$ ps, respectively. For both semiconducting and metallic SWCNTs, Kang observed a G-band phonon lifetime which was inversely proportional to temperature; scaling as approximately $1/T$ in the $300 - 450$ K range, as shown in Figure 5.1. In Kang's measurements, an excitation laser energy of 1.58 eV was used to excite the E_{22} transition of $0.85 < d_t < 1.2$ nm semi-conducting SWCNTs in a bundled HiPco sample in one experiment, and excite the E_{11} transition of $1.35 < d_t < 1.6$ nm metallic SWCNTs in a bundled arc-discharged sample in another experiment. In both cases the bundled SWCNTs were deposited on sapphire substrates. Both Song and Kang observed no significant variation in G-band phonon lifetime when varying the pump fluence by more than two orders of magnitude (see inset in Figure 5.1). Song and Kangs' studies provide strong evidence that the decay of G-band phonons must occur through the generation of lower-energy phonons, i.e., through three phonon anharmonic coupling processes [6, 55]. More recently, Chatzakis et al. [40] obtained a room temperature G-band phonon lifetime of $T_1 = 1.11$ ps, and demonstrated that the temperature dependence of the phonon population decay rate $(1/T_1)$ can be well described by the anharmonic decay of the G-band phonons into two lower energy daughter phonons. In this study, bundled HiPco SWCNTs were deposited on a fused-quartz substrate and excited with an energy of 1.55 eV. This simultaneously excited the E_{11} transition of $1.1 < d_t < 1.2$ nm semiconducting

SWCNTs and the E_{22} transition of $d_t \sim 1.7$ nm metallic SWCNTs. Consequently, the G-band phonon decay rates obtained in Chatzakis' study reflect the response from an ensemble of semiconducting and metallic SWCNTs. When comparing the anharmonic decay of G-band phonons in SWCNTs and graphene Chatzakis measured a large energy difference between the predicted daughter phonon pairs. This behaviour was presumed to be caused by the addition of decay channels from modes that are unique to SWCNTs, such as anharmonic decay with the RBM as one of the two daughter phonons. Whilst it is likely that RBMs are providing an additional decay channel for the G-band phonons [133], Chatzakis' study does not provide sufficient evidence to support this presumption because of the limited number of temperature dependent data points.

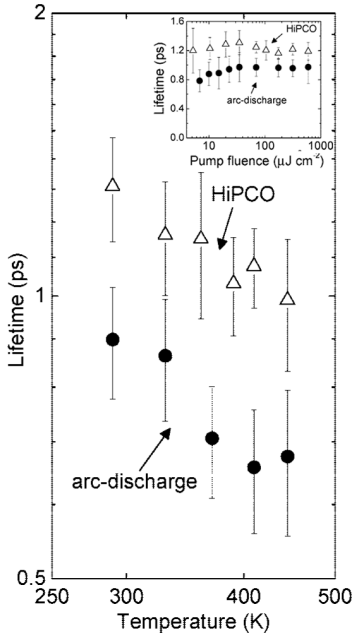

FIGURE 5.1: Lifetimes of Γ-point optical phonons in HiPCO (*open triangles*) and arc-discharge nanotubes (*filled circles*) as function of sample temperature at a pump fluence of 35μJ cm^{-2}. Upper inset shows the phonon lifetimes as a function of pump fluence at room temperature. Taken from [6].

The three TRIARS studies that have been discussed are based on measurements performed on different species of SWCNTs under various environmental conditions. The good agreement of the room temperature G-band phonon lifetimes obtained from these separate studies has led to the conclusion that the G-band phonon decay rate in SWCNTs does not depend critically on the local environment or on SWCNT structural parameters [6, 40]. However, Kang observed a significant difference in the decay rate of semiconducting and metallic SWCNTs under 'similar' environmental conditions, which may indicate a significant dependence on SWCNT structural parameters. It is believed an investigation that would allow one to exclusively study the G-band phonon decay rate in semiconducting (or metallic) SWCNT in different diameter ranges whilst under the same environmental conditions would clarify this situation. Another possible origin of this observation comes from the splitting of the graphene G-band in SWCNTs

(see Section 2.2.4). Whilst formally not the same, the LO and TO phonons at the Γ-point ($q = 0$) in graphene are effectively the same modes and have the same energy (1582cm^{-1}). This implies that the LO and TO phonons, which are responsible for the G-band in graphene, are likely to share the same anharmonic decay branches [7]. However, in SWCNTs the LO and TO phonons have different energies due to the curvature of the lattice (see Section 2.2.4). It is unlikely that such a small change in the energy of the LO and TO phonons would significantly alter their anharmonic decay branches, however, it is difficult to say for sure without obtaining empirical evidence. None of the existing G-band TRIARS studies are able to separately resolve the G^+ and G^- band phonon dynamics because of the significant bandwidth of the ultrafast pulses that are used [6, 40, 55]. Instead, these studies make the assumption that the TRIARS signal is dominated by the G^+ band. Whilst it is true for semiconducting SWCNTs that the G^+ band dominates the equilibrium Raman spectrum, this is often not the case for metallic SWCNTs [134]. Furthermore, there is no guarantee that the non-equilibrium populations probed in TRIARS experiments follow the equilibrium Raman spectra in either metallic or semiconducting tubes [37]. Finally, in semi-conducting SWCNTs the G^+ band is attributed to the LO phonon while in metallic SWCNTs the same feature is attributed to the TO phonon [71, 135, 136], and it is understood that the high-energy electrons couple more strongly to LO than TO phonons [34]. Therefore, being able to separately resolve the dynamics of the G^+ and G^- band phonons is an important next step in understanding the dynamics of these phonons and their influence on the electronic transport properties of SWCNTs.

5.2 Experimental Details

This section briefly discusses the details of the G-band TRIARS experiments that are reported in this chapter. Unlike the existing TRIARS studies which use colour as a means of separating pump and probe [6, 40, 55], the TRIARS experiments presented in this chapter are based on a co-polarised degenerate pump-probe technique. A detailed description of the experimental apparatus and techniques used for these measurements can be found in Section 3.3.

To ensure that a stable signal was achieved and that the conclusions reached in Section 4.4 remain valid, the G-band TRIARS experiments were performed at sampling region B on the same bundled SWCNT sample used for RRS investigation in Chapter 4, with an average power of 5mW for the individual pump and probe beams. TRIARS experiments were performed for two laser excitation energies, 1.51 eV and 1.63 eV, so that the G-band phonon dynamics could be independently measured for SWCNT species in the diameter ranges $0.99 - 1.11\text{nm}$ and $0.87 - 0.97\text{nm}$, while under the same environmental conditions. For each laser excitation energy, TRIARS measurements were performed as a function of sample temperature in the range $T = 4 - 600$ K, in order to investigate the

anharmonic decay channels of the G-band phonons through thermal activation. To make it possible to separately resolve the G^+ and G^- band dynamics, pulse durations were carefully selected to strike a sensible balance between temporal and spectral resolution. Finally, a select number of TRIARS measurements were performed with both pump and probe beams at half-power (2.5mW). This was to make sure that no significant transient sample heating was occurring (see Section 3.1.6), and to determine if there were any non-linear contributions to the G-band phonon population dynamics.

5.3 *G*-Band TRIARS Measurements

At the beginning of each TRIARS experiment the anti-Stokes Raman spectra were recorded for the pump beam alone and probe beam alone by blocking each beam in turn. For a single pulsed beam, the measured intensity of the anti-Stokes G-band feature was much greater than expected for thermal equilibrium. For example at 4K a significant anti-Stokes G-band signal was observed for pulsed light, while for the same average power in CW mode there was no measurable signal. This effect was also observed by Kang et al. [6], and can be explained by self-scattering of the $\sim$ 2 ps pulses, i.e. phonons generated at the beginning of the pulse scatter with photons near the end of the pulse. This observation is important to the TRIARS results for two reasons. Firstly, it provides evidence that the generation of G-band phonons is rapid while the population decay is slow enough to allow a non-equilibrium phonon population to be generated. Secondly, it means that the sum of the anti-Stokes Raman spectra obtained from the pump beam alone and probe beam alone does not represent the thermal equilibrium phonon population because phonons are already being generated and scattered within each pulse. By measuring the G-band phonon dynamics as a function of laser power, it has been shown in this study, and others [6, 55], that the G-band phonon lifetime does not depend significantly on the phonon occupation. This means that the dynamics of the non-equilibrium phonon population generated by one laser pulse is likely to be independent of the dynamics of the non-equilibrium population generated by the other laser pulse, and that the self-scattering intensity is not dependent on pump-probe delay. To avoid confusion, we will refer to the sum of the individual pump and probe anti-Stokes G-band intensities as the 'background' phonon population.

To accurately measure the dynamics of the phonon population it was necessary to record the anti-Stokes Raman intensity as a function of pump-probe delay. First, with both pump and probe beams incident on the sample, the anti-Stokes Raman signal intensity was monitored as the pump-probe delay was increased until the anti-Stokes Raman signal intensity was equal to that of the background phonon population, i.e. where there was no measurable pump excitation; a pump-probe delay of 10ps was sufficient for the background phonon population to be reached, however, to be sure the background spectra were recorded at 25ps in all of the TRIARS experiments. Figure 5.2 (a) compares

the background spectra obtained for a pump-probe delay of 25ps (*red*) with the sum of the spectra obtained from the pump beam alone and the probe beam alone (*black*). To measure the temporal evolution of the anti-Stokes Raman signal a total of 61 spectra were recorded for pump-probe delays in the range 20ps to −20ps. The data points were symmetric about zero delay but were not equally spread because they were mostly populated where the fitting procedure (see Section 5.4) was most sensitive to the points. After every third spectra was recorded a 25ps background spectra was also recorded so

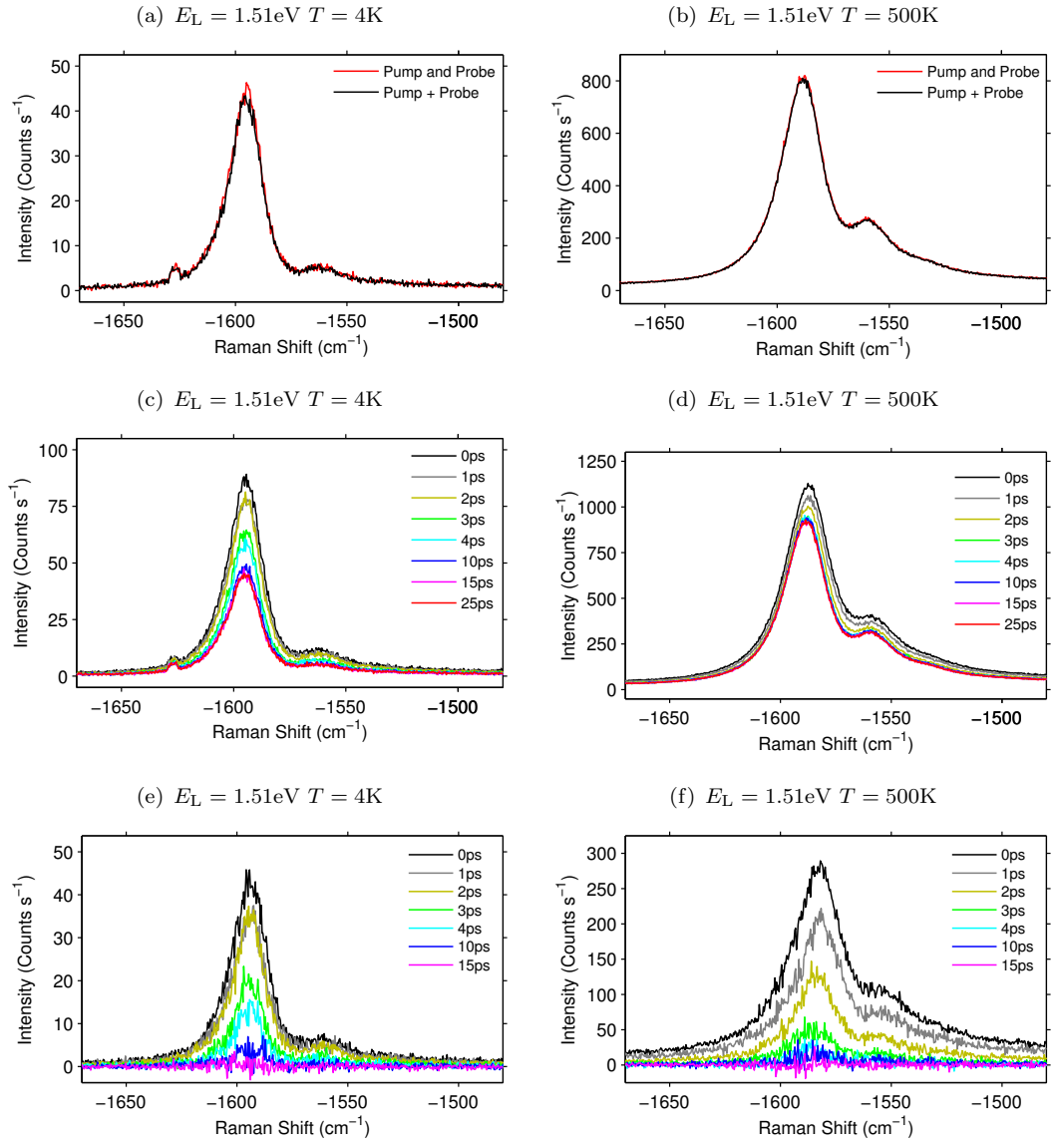

FIGURE 5.2: Representative sample of results for $E_L = 1.51$eV TRIARS measurements. *Top row:* Plots comparing the background spectra obtained for a pump-probe delay of 25ps (*red*) with the spectra obtained by summing the pump beam alone and probe beam alone (*black*) for (a) $T = 4$K and (b) $T = 500$K. *Middle row:* Plots showing a selection of anti-Stokes spectra that were obtained for various pump-probe delays for (c) $T = 4$K and (d) $T = 500$K. *Bottom row:* (e) and (f) show subtracted spectra that were obtained by subtracting the 25 ps background spectra from the spectra shown in (c) and (d) respectively.

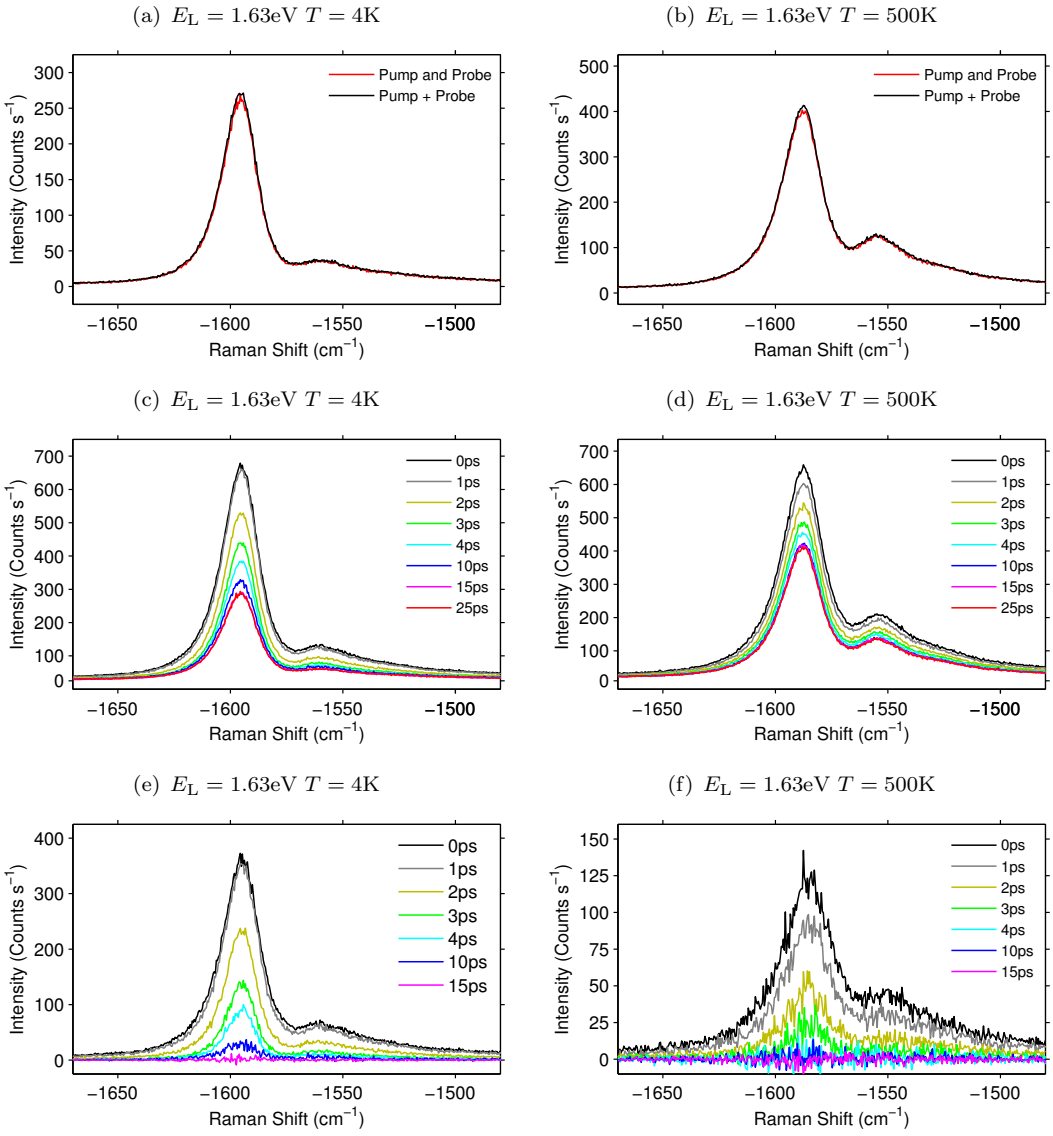

FIGURE 5.3: Representative sample of results for $E_L = 1.63$eV TRIARS measurements. *Top row:* Plots comparing the background spectra obtained for a pump-probe delay of 25ps (*red*) with the spectra obtained by summing the pump beam alone and probe beam alone (*black*) for (a) $T = 4$K and (b) $T = 500$K. *Middle row:* Plots showing a selection of anti-Stokes spectra that were obtained for various pump-probe delays for (c) $T = 4$K and (d) $T = 500$K. *Bottom row:* (e) and (f) show subtracted spectra that were obtained by subtracting the 25ps background spectra from the spectra shown in (c) and (d) respectively.

that the stability of the experiment and drift in the Raman signal could be monitored. Figure 5.2 (c) shows a selection of anti-Stokes G-band Raman spectra that were obtained for various pump-probe delays in a low temperature ($T = 4$K) $E_L = 1.51$eV TRIARS experiment. It is clear from these spectra that the anti-Stokes G-band intensity increases with decreasing pump-probe delay. Figure 5.2 (e) shows the subtracted spectra that were obtained by subtracting the nearest corresponding background spectra from each of the spectra shown in Figure 5.2 (c). The dynamics of the G-band intensity in the

subtracted spectra is interpreted as being the phonon population dynamics convolved with the instrumental response of the pump-probe system (pulse cross-correlation), as discussed in Appendix D. Note that the artefact at approximately -1625cm^{-1} in Figures 5.2 (a) and (c) is not present in the subtracted spectra. This artefact was likely to be generated by trapped charge in the deep depletion CCD detector.

In order to exemplify the large number of G-band TRIARS experiments that were performed, Figures 5.2 (a)-(f) and 5.3 (a)-(f) present a representative sample of background spectra, anti-Stokes spectra as a function of pump-probe delay, and subtracted spectra, for TRIARS measurements taken at the low temperature limit (4K) and towards the high temperature limit (500K), for both excitation laser energies, $E_{\text{L}} = 1.51\text{eV}$ and $E_{\text{L}} = 1.63\text{eV}$.

5.3.1 Resolving the G^+ and G^- Band Intensity Dynamics

To resolve the dynamics of the G^+ and G^- band phonons it was necessary to be able to independently determine the intensities of the G^+ and G^- bands in the subtracted spectra. This was achieved by fitting the subtracted spectra with the simple G-band fitting function (described in Section 4.3.1.2). This fitting function consists of a sum of two Lorentzian functions and a linear background. Example fits to the subtracted spectra are shown in Figure 5.4 (a) and (b) for $E_{\text{L}} = 1.63\text{eV}$ and $T = 4\text{K}$ and $T = 500\text{K}$ respectively. Lower limits were placed on the fitting parameters representing the Lorentzian linewidths to prevent the fitting algorithm from narrowing the linewidth to fit the experimental noise in the low signal limit. The fitting parameters were used to extract the Raman intensity, shift, and linewidth (FWHM) for both the G^+ and G^- bands. Next, to check that the G^+ and G^- band intensities could be independently determined, all of the fitting parameters were fixed except those controlling the Lorentzian which represented the G^- band. In turn, the fit was then re-applied with the amplitude of the Lorentzian representing the G^+ band forced to its upper and lower 95% confidence limits. When this was done no significant (less than 0.2%) variation in the fitted G^- intensity was observed, which indicated that the G^+ and G^- band intensities could be independently determined.

Figures 5.4 (c)-(f) show the intensity as a function of pump-probe delay for the G^+ band (*closed circles*) and G^--band (*open circles*) obtained from fitting the spectra in Figures 5.4 (a) and (b). Also shown are the pump-probe cross-correlations (*broken lines*) obtained during the TRIARS measurements. Note that the intensities of the pump-probe cross-correlations have been scaled for illustrative purposes. Similarly, the Raman shift as a function of pump-probe delay for the G^+ and G^--bands, obtained from fitting the spectra in Figures 5.4 (a) and (b), are shown in (g) and (h). A quick comparison between the intensity dynamics and the cross-correlations in figures (c) and (d) demonstrates that the dynamics are clearly temporally resolvable but occur on a

(a) $E_{\mathrm{L}} = 1.63\mathrm{eV}$ $T = 4\mathrm{K}$ (b) $E_{\mathrm{L}} = 1.63\mathrm{eV}$ $T = 500\mathrm{K}$

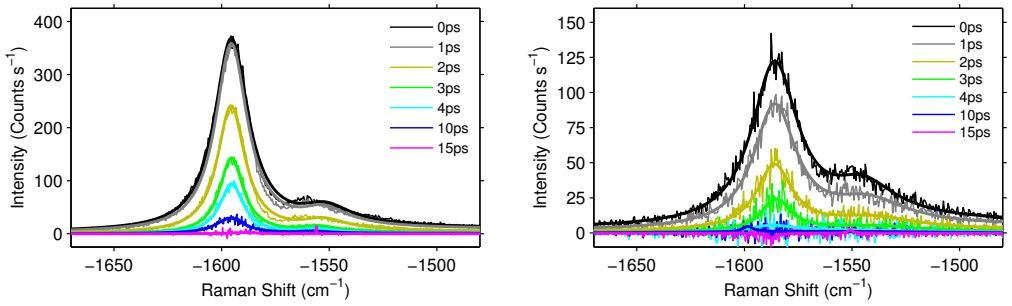

(c) $E_{\mathrm{L}} = 1.63\mathrm{eV}$ $T = 4\mathrm{K}$ (d) $E_{\mathrm{L}} = 1.63\mathrm{eV}$ $T = 500\mathrm{K}$

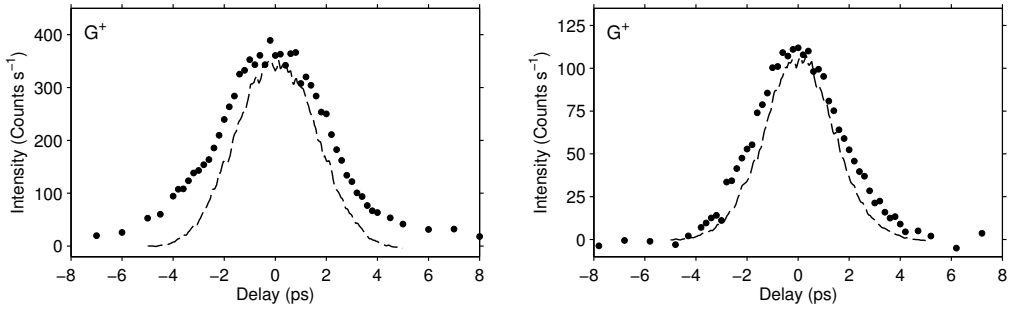

(e) $E_{\mathrm{L}} = 1.63\mathrm{eV}$ $T = 4\mathrm{K}$ (f) $E_{\mathrm{L}} = 1.63\mathrm{eV}$ $T = 500\mathrm{K}$

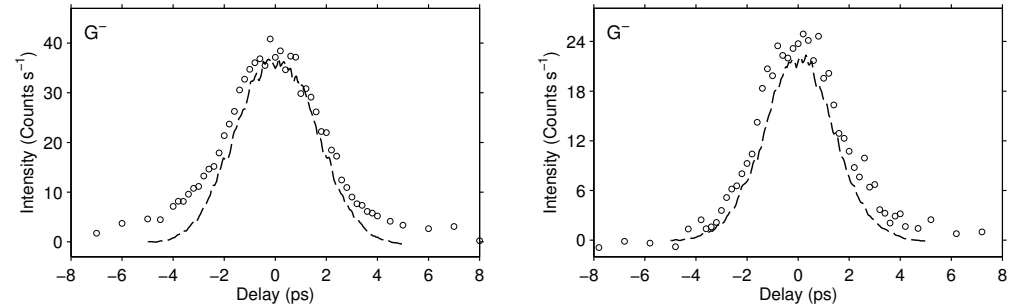

(g) $E_{\mathrm{L}} = 1.63\mathrm{eV}$ $T = 4\mathrm{K}$ (h) $E_{\mathrm{L}} = 1.63\mathrm{eV}$ $T = 500\mathrm{K}$

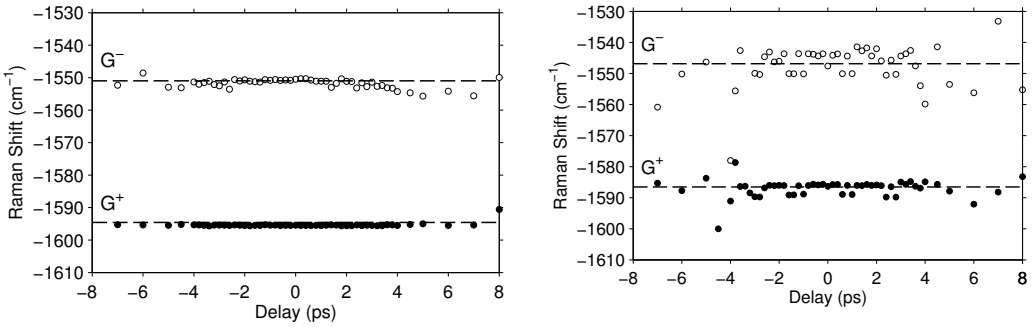

FIGURE 5.4: Representative sample of results for resolving the intensities of the G^+ and G^- bands for $E_{\mathrm{L}} = 1.63\mathrm{eV}$ TRIARS measurements. *Top row:* Example fits to the subtracted spectra for (a) $T = 4\mathrm{K}$ and (b) $T = 500\mathrm{K}$. *Middle rows:* The anti-Stokes intensity as a function of pump-probe delay for (c) the G^+ band (*closed circles*) and (d) the G^--band (*open circles*). *Bottom row:* The Raman shift as a function of pump-probe delay for (e) the G^+ band and (f) the G^--band. Intensity and shift values were obtained from fitting the spectra in (a) and (b).

time scale comparable with the cross-correlations. The G-band frequencies were found to be independent of pump-probe delay, as shown in Figures 5.4 (g) and (h), however, they were found to decrease linearly with increasing sample temperature. This frequency softening is not important to this study but can be explained by the softening of the intra- and inter-tubular bonds with increasing sample temperature [112].

5.3.2 Stability and Repeatability

There were two important issues regarding the stability and reliability of the pump-probe TRIARS experiments. One concerns the stability of the ultrafast laser source and the other concerns long-term drift of the pump and probe optical beams. To improve the stability of the Raman experiments and to ensure that the experimental data was reliable a number of procedures were put in place. Pump-probe cross-correlation measurements were made before and after every TRIARS measurement, and the data was discarded if the cross-correlation (FWHM) had varied by greater than 100fs; typical variations were < 50fs. The background spectra obtained during TRIARS experiments (taken approximately every 10 minutes) were checked to ensure that the TRIARS system was stable, and if their magnitude varied by more than 20% over the duration of an experiment, or rapidly over a short period of time, the experiment was aborted and data discarded. Figures 5.5 (a) and (b) show the intensity of the G^+ and G^- bands, obtained from fitting the background spectra from two TRIARS experiments, one where the TRIARS system was stable and one where the TRIARS system was not sufficiently stable due to long term drift, resulting in the experimental data being discarded.

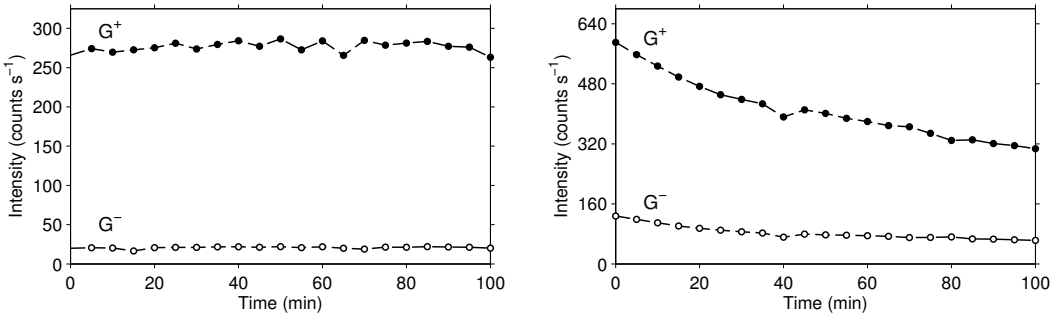

FIGURE 5.5: The intensity of the G^+ band (*solid circles*) and G^--band (*open circles*) throughout the generation of an experiment. Obtained from fitting the background spectra from two TRIARS experiments (a) one where the TRIARS system was stable and (b) one where the TRIARS system was not sufficiently stable due to long term drift, resulting in the experimental data being discarded.

For the majority of temperatures TRIARS measurements were repeated so that experimental errors could be calculated from the standard deviations of the measured phonon

population lifetimes. For some sample temperatures repeat measurements could not be obtained because of laboratory time constraints.

5.3.3 Pump-Probe Cross-Correlation Measurement

The intensity dynamics shown in Figures 5.4 (c)-(f) represent the convolution of the phonon population dynamics and the pump-probe cross-correlation (instrumental response function). Therefore, it is crucial to obtain an accurate measurement of the pump-probe cross-correlation so that the measured intensity dynamics can be deconvolved to determine the phonon dynamics. For details on how this was achieved experimentally see Section 3.3. Figure 5.6 shows a typical pump-probe cross-correlation measurement which was normalised and fitted with a Gaussian function of the form

$$f(t_{delay}, t_{offset}, b) = e^{-\frac{(t_{delay}-t_{offset})^2}{2b^2}}, \tag{5.1}$$

where t_{delay} is the pump-probe delay, t_{offset} represents small potential offset in the zero pump-probe delay position, and the cross-correlation width (FWHM) is given by $2\sqrt{2ln2}b$. This allows the pump-probe cross-correlation to be represented as a continuous Gaussian function which in turn can be used for the deconvolution the intensity dynamics.

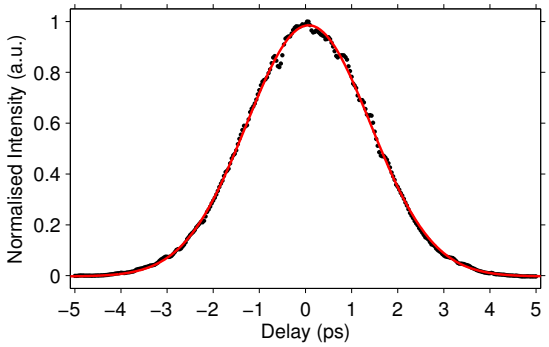

FIGURE 5.6: Normalised pump-probe cross-correlation (*black*) obtained during a TRIARS measurement with the in-situ slow scanning cross-correlator. Also shown is a Gaussian fit (Equation 5.1) (*red*) to the experimental data.

5.4 Modelling the *G*-band Phonon Dynamics

In a typical TRIARS experiment a pump laser pulse generates a non-equilibrium phonon population through the relaxation of photo-excited carriers [30, 79]. The rate at which the *G*-band phonons are generated is particularly important because it determines the rising edge in the population dynamics. Section 2.5.4 discusses the processes which are

likely to dominate the generation of G-band phonons in these particular experiments. From this discussion we can conclude that it is likely the non-equilibrium G-band phonon population dynamics rises rapidly on the 100 fs timescale and decays freely through various possible channels until the equilibrium phonon population is reached.

The TRIARS experiments reported in this thesis are based on a co-polarised degenerate pump-probe technique, which means that the measured phonon dynamics is effectively the dynamics which would be measured in a standard TRIARS experiment (where the pump and probe signals are distinguishable) added to a reflection of itself about zero delay. Since it is not possible to fully distinguish between which pulse acts as the pump and which pulse acts as the probe within the cross-correlation, it may appear that it would be impossible to determine the rising edge dynamics. However, this is not the case if reasonable assumptions and careful fitting of the dynamics are used.

A number of existing TRIARS studies have shown that the decay of a non-equilibrium population of G-band phonons can be well described by a monoexponential decay on the order of 1ps [6, 55]. For this reason it was first hypothesised that the dynamics of the G-band phonon population follows a monoexponential rise and monoexponential decay according to

$$g(t_{delay}, a_0, T_{rise}, T_1) = a_0(e^{-t_{delay}/T_1} - e^{-t_{delay}/T_{rise}}), \tag{5.2}$$

where t_{delay} is the pump-probe delay, a_0 represents an initial phonon population, T_{rise} represents the time it takes for the phonon population to increase by e times its initial value and T_1 represents the phonon population lifetime, i.e. the time it takes for the phonon population to reduce to $1/e$ times its initial value. An example of this model is shown in Figure 5.7 (a). To model the phonon population dynamics that would be measured by a co-polarised degenerate TRIARS experiment Equation 5.2 must be re-written as

$$\begin{aligned} g(t_{delay}, a_0, T_{rise}, T_1) = \; & a_0[(H(t_{delay})(e^{-t_{delay}/T_1} - e^{-t_{delay}/T_{rise}}))+ \\ & (H(-t_{delay})(e^{t_{delay}/T_1} - e^{t_{delay}/T_{rise}}))], \end{aligned} \tag{5.3}$$

where H is the Heaviside step function; $H(t_{delay}) = 1$ for $t_{delay} \geq 0$ and $H(t_{delay}) = 0$ for $t_{delay} < 0$. Figure 5.7 (b) shows normalised plots of Equation 5.3 for $T_1 = 1.2$ps and various values of T_{rise} in the range 1.0ps to 0.2ps.

Because of the finite pulse durations used in the TRIARS experiments the intensity dynamics shown in Figures 5.4 (c)-(f) represents the convolution of the phonon population dynamics and the pump-probe cross-correlation (see Appendix D). Therefore, the real phonon population dynamics are determined by calculating the convolution the functions given in Equations 5.3 and 5.1, i.e $h = (f * g)(t_{delay})$. Figure 5.7 (c) shows

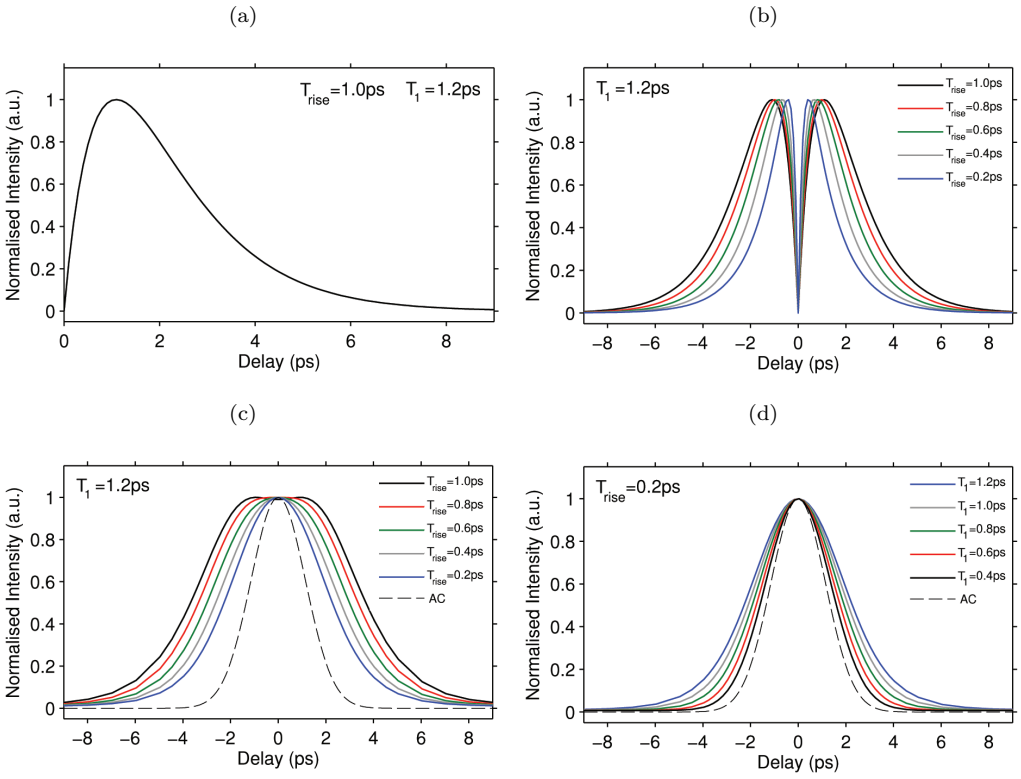

FIGURE 5.7: Modelling the phonon population dynamics. (a) Plot of Equation 5.2 for T_{rise} = 1.0ps and T_1 = 1.2ps. (b) Plot of Equation 5.3 for T_1 = 1.2ps and various values of T_{rise} in the range 1.0ps to 0.2ps. (c) shows calculated intensity dynamics for T_1 = 1.2ps and various values of T_{rise} in the range 1.0ps to 0.2ps, convoluted with a typical 1.94 ps pump-probe cross-correlation. (d) shows the same convolution calculation performed for T_{rise} = 0.2ps and various values of T_1 in the range 1.2ps to 0.4ps.

the expected intensity dynamics for T_1 = 1.2ps and various values of T_{rise} in the range 1.0ps to 0.2ps convoluted with a 1.94 ps pump-probe cross-correlation, which is typical for these experiments. The calculated pulse cross-correlation (*broken black line*) is also shown in the figure. Figure 5.7 (d) shows the same model performed for T_{rise} = 0.2ps and various values of T_1 in the range 1.2ps to 0.4ps. A quick comparison of the theoretical models for the intensity dynamics in Figures 5.7 (c) and (d) with the measure intensity dynamics in Figures 5.4 (c)-(f), particularly in the $-2 < t_{delay} < 2$ ps range, strongly suggests that the *G*-band phonon population rise time is short i.e. less than 200 fs. The same result was found for all of the *G*-band TRIARS measurements. This observation is in agreement with other TRIARS studies on the *G*-band, which all measure the rising edge dynamics to be effectively instantaneous within the resolution of experiments [6, 40, 55]. Attempts to fit the measured dynamics using Equation 5.3, without constraints on T_{rise} and T_1, also suggested that $T_{rise} \sim 0$. Therefore, it was assumed that the *G*-band phonon population was generated instantaneously, and the function used to model G-band phonon population dynamics was simplified to

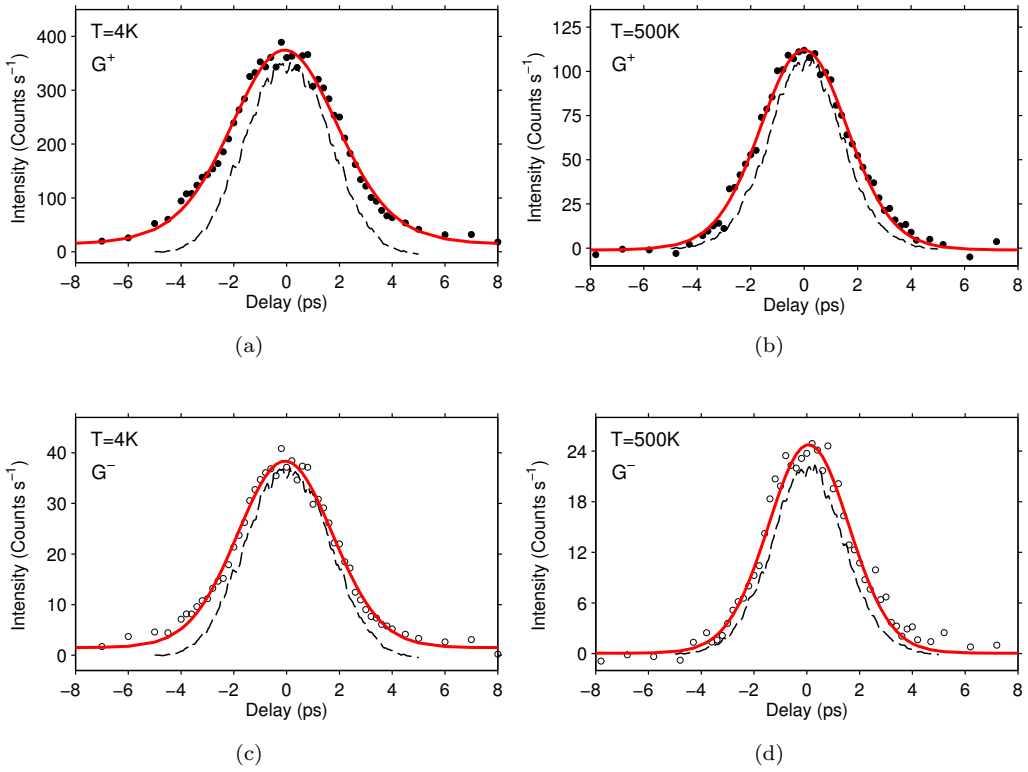

FIGURE 5.8: Fitted G^+ (*closed circles*) and G^--band (*open circles*) intensity dynamics. Obtained from low temperature ($T = 4$K) and high temperature ($T = 500$K) TRIARS experiments performed for $E_{\mathrm{L}} = 1.63$eV. The fitting function was calculated from the convolution of the functions given in Equations 5.4 and 5.1.

$$f(t_{delay}, t_{offset}, a_0, a_{offset}, T_1) = a_0[(H(t_{delay})(e^{-(t_{delay}-t_{offset})/T_1}))+ (H(-(t_{delay}-t_{offset}))(e^{(t_{delay}-t_{offset})/T_1}))]+ a_{offset}, \quad (5.4)$$

where t_{offset} and a_{offset} fitting parameters have been added to account for a small potential offset in the zero pump-probe delay position and equilibrium phonon population, which were unavoidable experimental artefacts.

To fit the measured intensity dynamics and obtain values for T_1 a linear least squares regression algorithm was used to fit the convolution of Equation 5.4 and Equation 5.1 to the measured dynamics. For completeness an example of the function which performed the convolution has been provided in Appendix A Matlab Code 4. Figure 5.8(a)-(d) show examples of the fitted G^+ and G^- band intensity dynamics obtained from low temperature ($T = 4$K) and high temperature ($T = 500$K) TRIARS experiments performed for $E_{\mathrm{L}} = 1.63$eV. The fits shown in Figure 5.8 were used to obtain low temperature $T = 4$K G-band phonon lifetimes of $T_1 = 1.27 \pm 0.17$ ps and $T_1 = 1.16 \pm 0.17$ ps for the G^+ and G^--band phonons respectively and high temperature $T = 500$K lifetimes

of $T_1 = 0.78 \pm 0.10$ ps and $T_1 = 0.59 \pm 0.20$ ps for the G^+ and G^--band phonons respectively, for an excitation of 1.63 eV. These results are consistent with previously reported measurements of the G-band phonon lifetimes [6, 40, 55].

5.5 Temperature and Diameter Dependence of the *G*-band Phonon Decay Rate

Figure 5.9, presents the results on the temperature dependence of the decay rate $(1/T_1)$ of the G^+ band phonons, (a) and (c), and G band phonons, (b) and (d), measured for two excitation energies 1.51 eV, (a) and (b), and 1.63 eV, (c) and (d). The decay rate is presented in units of ps^{-1} and cm^{-1} to show the corresponding linewidth broadening. The error bars in Figure 5.9 show the 95% confidence bounds in the fitting parameter. The reason why the confidence bounds in Figure 5.9 generally increase with temperature can be explained by the faster dynamics that are observed with increasing temperature. This reduces the difference between the measured intensity dynamics and the pulse cross-correlation function and means the fitting routine is relying on fewer data points to secure the fit. This can be clearly observed by comparing Figures 5.8 (a) and (b). In addition, the larger error bars in (b) and (d), compared with those in (a) and (c), can be explained by the intensity ratio of the G^+ and G^- band, which leads to a higher signal to noise ratio for measurements of the G^- band. Where possible, multiple independent TRIARS experiments were performed and are shown to display the significance of these errors. In each case we see no significant change in the decay rate below 200K, and an increasing decay rate between 200K and 600K. This observation is consistent with the temperature dependent results obtained by Kang and Chatzakis [6, 40].

Chatzakis showed that the temperature dependence of the G-band phonon decay rate can be well described by considering only three-phonon anharmonic processes, where the G-band phonons decay into two lower energy daughter phonons through ph-ph interactions. Section 2.5.3 provides a brief discussion of three-phonon anharmonic scattering. For the case of G-band phonons, where up-conversion processes can be ignored, it can be shown that the temperature dependence of the decay rate due to three-phonon anharmonic processes can be modelled simply as

$$\Gamma(T) = \Gamma_0[1 + n(E_1, T) + n(E_2, T)], \tag{5.5}$$

where Γ_0 is the absolute decay rate measured at $T = 0$K, E_1 and E_2 are the energies of the daughter phonons where Bose-Einstein statistics $n(E_i, T)$ is used to calculate the population of the two daughter phonons whose energies must sum to give the energy of the parent phonon, i.e. $E_2 = E_G - E_1$ where $E_G = \hbar\omega_G$. The best fits that were obtained from fitting this model are shown in Figures 5.9 (a)-(d), and the parameters obtained

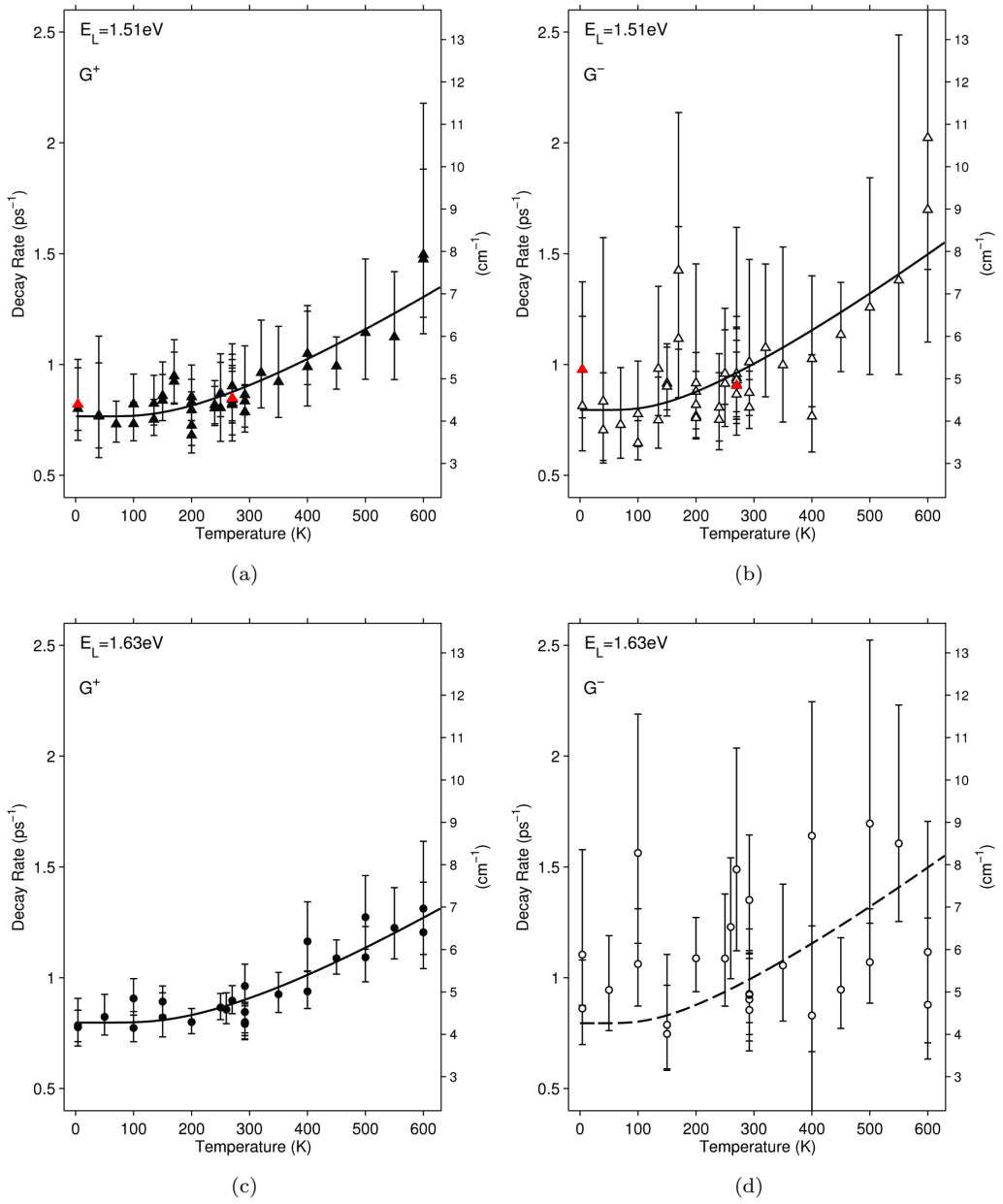

FIGURE 5.9: The decay rate ($1/T_1$) as a function of temperature for (a) the G^+ band phonons and (b) the G^- band phonons measured for an excitation of $E_{\mathrm{L}} = 1.51$ eV, and for (c) the G^+ band phonons and (d) G^- band phonons measured for an excitation of $E_{\mathrm{L}} = 1.63$ eV. The decay rate is presented in units of ps^{-1} (*left axis*) and cm^{-1} (*right axis*) to show the corresponding linewidth broadening. The experimental data (*represented as symbols*) in (a), (b), and (c) are fit to Equation 5.5 (*solid lines*). The fit from (b) is overlaid as a dashed line in (d). Each symbol corresponds to an independent measurement of the TRIARS dynamics. Red symbols represent measurements taken with pump and probe beams at half-power (2.5mW). The error bars represent the 95% confidence bounds for the fitting parameter, obtained from the fitting procedure.

from these fits are presented in Table 5.1. This model appears to describe the observed temperature dependence well, which strongly suggests that anharmonic decay is the dominant decay channel for Γ-point phonons in semiconducting SWCNTs. Because the fitting of the experimental data in Figure 5.9 (d) did not generate parameters with

sensible confidence bounds, the fit from Figure 5.9 (b) has been plotted as a dashed line in Figure 5.9 (d), and shows a reasonable correlation with the experimental data.

Band	E_i (eV)	E_1 (cm^{-1})	E_2 (cm^{-1})	Γ_0 (ps^{-1})
G^+	1.51	391 ± 59	1200 ± 59	0.77 ± 0.04
G^-	1.51	329 ± 99	1226 ± 99	0.79 ± 0.08
G^+	1.63	445 ± 72	1146 ± 72	0.80 ± 0.04

TABLE 5.1: Fitting Parameters: obtained from fitting Equation 5.5 to the temperature dependence of the G^+ and G^- band phonon decay rates.

Referring to Table 5.1, we see no measurable change in the absolute decay rate, Γ_0, for the excitation energies 1.51eV and 1.63eV, i.e. when probing SWCNT species in the diameter ranges $0.87 < d_t < 0.97$ nm and $0.99 < d_t < 1.1$ nm. We also see no measurable difference in Γ_0 for the G^+ (LO) and G^- band (TO) phonons. Furthermore, to within the experimental error, the daughter phonon energies obtained from fitting Equation 5.1 are the same in all measurements. These results provide strong evidence that the anharmonic decay branches for the LO and TO Γ-point phonons in SWCNTs are not significantly affected by the splitting of the G-band due to curvature. The results also support the notion that the decay rates do not depend critically on SWCNT diameter. This means that the observed difference in the Γ-point phonon decay rates for semiconducting and metallic SWCNTs measured in Kang's study [6] cannot be explained by anharmonic processes alone. It has been suggested that the increased e-ph coupling in metallic SWCNTs may provide an additional decay channel for the Γ-point phonons through electronic excitation, which would explain why shorter Γ-point phonon lifetimes have been observed in metallic SWCNTs compared with semiconducting SWCNTs [6, 7, 34, 55, 137].

To check whether the predicted energies of the daughter phonons (obtained from fitting Equation 5.5) make sense, we can consider the possible decay channels for the Γ-point phonons in graphene. The upper part of Figure 5.10 (a) shows a schematic of possible three-phonon anharmonic decay channels for the Γ phonons in graphene [7], which are derived from energy and momentum conservation. The lower part of Figure 5.10 (a) shows the probability of a Γ phonon decaying into two modes of frequencies ω and $\omega_0 - \omega$ for a temperature of 300K. The range of energies for the daughter phonons presented in Table 5.1 are consistent with the predicted decay channels shown in Figure 5.10 for graphene.

We know from Section 2.1.3 that the vibrational states in SWCNTs are a subset of those in graphene but also include additional modes such as the twisting mode and RBM which are unique to SWCNTs. When using a similar fit to compare the anharmonic decay in SWCNTs and graphene, Chatzakis measured an enhanced decay rate in SWCNTs and a measurable energy difference between the predicted daughter phonon pairs [40]. It was hypothesised that this was caused by the addition of decay channels from modes that are unique to SWCNTs, such as anharmonic decay with the RBM as one of the

two daughter phonons. To test this hypothesis, the model was altered to include two anharmonic decay channels; one where the two daughter phonons include an RBM, and one where the energy distribution of the daughter phonons is free to change, satisfying $E_2 = E_G - E_1$. The separate decay channels were allowed to have independent weightings given by a and b, where $a + b = 1$. The form of this model is given by

$$\begin{aligned}\Gamma(T) &= \Gamma_0[a(1 + n(E_{\mathrm{RBM}}, T) + n(E_G - E_{\mathrm{RBM}}, T)) \\ &\quad + b(1 + n(E_1, T) + n(E_2, T))],\end{aligned} \tag{5.6}$$

where E_{RBM} was obtained as a weighted average from CW Raman measurements. Figure 5.10 (b) shows the results of fitting Equation 5.6 to the temperature dependence of the G^+ band decay rate, obtained for an excitation energy of 1.63 eV. When a and b were allowed to take on any values satisfying $a + b = 1$ the best fit was obtained when the contribution from the RBM anharmonic decay channel was completely suppressed, i.e. for weighting parameters $a = 0$ and $b = 1$. To demonstrate the confidence in this result, Figure 5.10 (b) also shows the fits which were obtained for increasing contributions from the RBM decay channels. The fact that a 50% contribution from RBM decay channels results in all of the data points below 200K being above the fit and the majority of data points above 300K being below the fit, suggests that three phonon anharmonic decay involving an RBM does not provide the dominant decay channel for the G-band phonons in SWCNTs in the temperature range of these experiments.

5.6 Temperature Dependence of the *G*-band Linewidth

As discussed in Section 2.3, there are several mechanisms that can contribute to the linewidth of SWCNT Raman features. For measurements on bundled SWCNTs it is helpful to split these contributions into two groups; temperature dependence intrinsic contributions and inhomogeneous contributions which are thought to be temperature independent. We can write the intrinsic linewidth, Γ_{in}, as

$$\Gamma_{in} = \Gamma_{e-ph} + \Gamma_{ph-ph}, \tag{5.7}$$

where Γ_{e-ph} and Γ_{ph-ph} are broadening contributions resulting from e-ph and anharmonic ph-ph interactions respectively. In graphene, Bonini et al. [7] predicted that Γ_{e-ph} ($\sim 12\mathrm{cm}^{-1}$ for $T = 300K$) is much greater than Γ_{ph-ph} ($\sim 2\mathrm{cm}^{-1}$ for $T = 300K$) and that Γ_{e-ph} is expected to decrease while Γ_{ph-ph} is expected to increase with increasing sample temperature (within the temperature range of these experiments). Furthermore, this prediction has recently been confirmed experimentally [138].

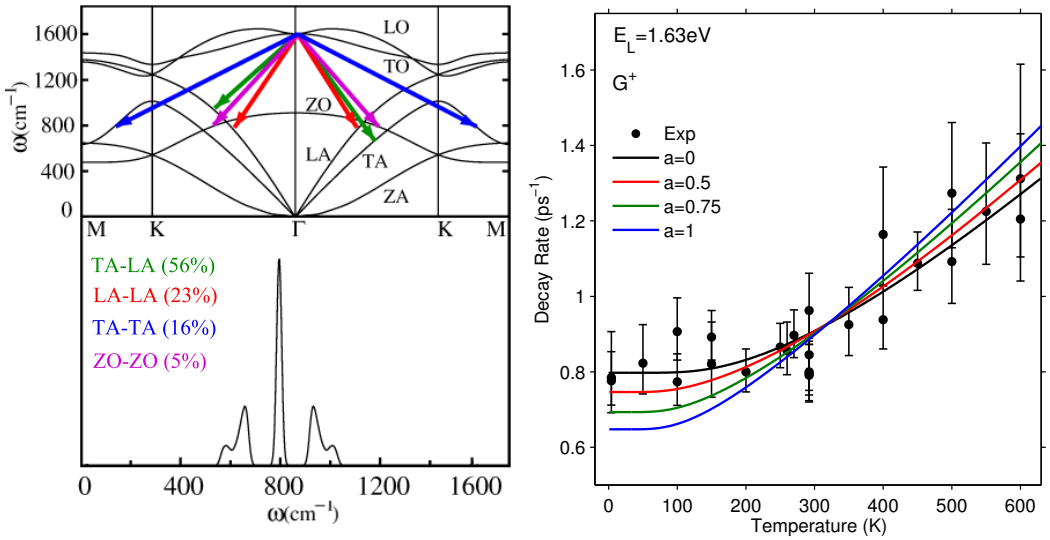

(a) (b)

FIGURE 5.10: (a) Upper part: shows a schematic of possible three-phonon anharmonic decay channels for the 1582cm^{-1} Γ-point optical phonons which are responsible for the G-band in graphene [7]. Lower part shows the probability of a Γ phonon decaying into two modes of frequencies ω and $\omega_0 - \omega$ for a temperature of 300K. Adapted from [7]. (b) The decay rate $(1/T_1)$ as a function of temperature for G^+ band phonons measured for an excitation of $E_{\rm L} = 1.63$ eV. (*Solid lines*) show fits of Equation 5.6 to the experimental data for various values of the fitting parameter a.

Figure 5.11 shows the measurements of the G^+ and G^- band linewidths as a function of temperature in the temperature range $T = 4 - 600$K for measurements performed at (a) 1.51eV and (b) 1.63eV. Each data point in the figure was obtained by averaging the linewidth fitting parameters which gave the best fits to each of the background spectra that were recorded in a single TRIARS experiment and then subtracting the instrumental response, i.e. the pulse spectral width (FWHM) as measured by the experimental system. These linewidth measurements are in good agreement with previously reported temperature dependent linewidth measurements on bundled SWCNTs [139]. In all cases the G-band linewidths increase with increasing temperature which suggests that Γ_{ph-ph} may be providing the dominant temperature dependent contribution.

To test whether the temperature dependence of the G^+ and G^- band linewidths in Figure 5.11 can be entirely explained by the same three-phonon anharmonic processes which describe the phonon population decay rates in Figure 5.9, the data points have been fit with the following function

$$\Gamma_G(T) = \Gamma_{Inhomogeneous} + \Gamma_0[1 + n(E_1, T) + n(E_2, T)]/2\pi c, \tag{5.8}$$

where $\Gamma_{Inhomogeneous}$ is the only variable fitting parameter and represents the temperature independent inhomogeneous broadening contribution. The second term represents

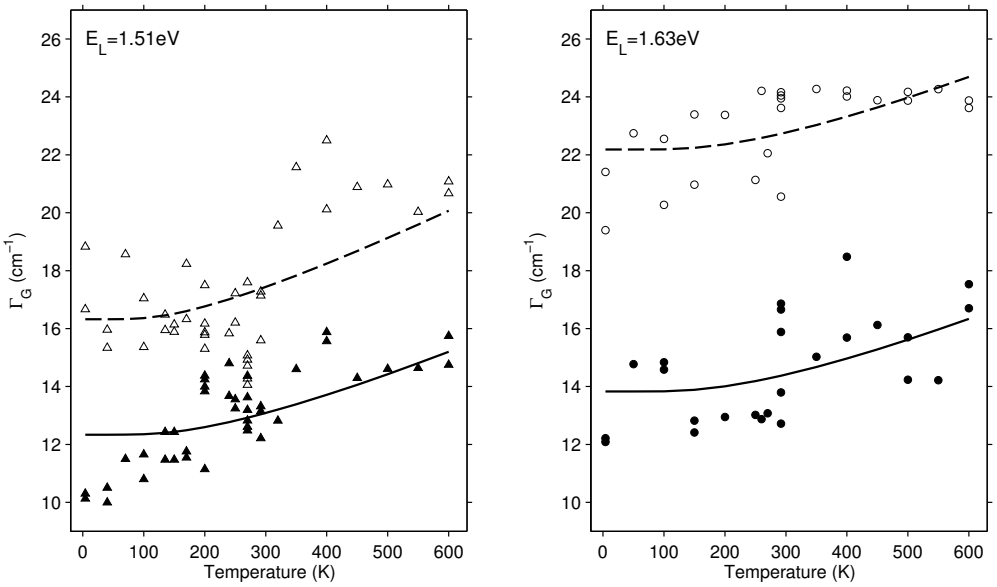

FIGURE 5.11: The G^+ band (*solid symbols*) and G^- band (*open symbols*) linewidths as a function of temperature for (a) an excitation of $E_{\mathrm{L}} = 1.51$ eV and (b) an excitation of $E_{\mathrm{L}} = 1.63$ eV. The experimental data are fit to Equation 5.8 (*solid lines*) which assumes that the temperature dependence of the linewidths can be entirely explained by the same anharmonic processes which describe the phonon population decay rates in Figure 5.9.

the phonon population decay rate (in units of cm^{-1}) due to three phonon anharmonic scattering into two lower energy phonons (Equation 5.5) where the relevant Γ_0, E_1 and E_2 values are taken from Table 5.1. It is clear that this model provides a reasonable fit to the temperature dependence of the G^+ and G^- band linewidths. If Γ_{e-ph} was significantly contributing to the measured linewidths then we would expect to see the negative temperature dependence of Γ_{e-ph} overcome the positive temperature dependence of Γ_{e-ph} for temperatures above 200K [7]; such behaviour has been observed for linewidth measurements of metallic SWCNTs [36]. Instead, the temperature dependence of the linewidths shown in Figure 5.11 are well described by the same three-phonon anharmonic processes which describe the phonon population decay rates in Figure 5.9 and a temperature independent inhomogeneous contribution. Therefore, these results support the findings from the direct measurements of the phonon population decay rates and provide evidence that e-ph interactions do not contribute significantly to the decay of a nonequilibrium G-band phonon population in semiconducting SWCNTs.

Finally, the temperature independent inhomogeneous contributions to the linewidths, as predicted from the fits, are $\Gamma_{Inhomogeneous} = 8.27 \pm 0.95\mathrm{cm}^{-1}$ and $\Gamma_{Inhomogeneous} = 12.11 \pm 0.70\mathrm{cm}^{-1}$ for the G^+ and G^- bands respectively for an excitation energy of 1.51 eV, and $\Gamma_{Inhomogeneous} = 9.60 \pm 0.62\mathrm{cm}^{-1}$ and $\Gamma_{Inhomogeneous} = 17.95 \pm 0.51\mathrm{cm}^{-1}$ for the G^+ and G^- bands respectively for an excitation energy of 1.63 eV. There are two

important observations to point out regarding the above $\Gamma_{Inhomogeneous}$ values. First, for both excitation energies the G^+ band $\Gamma_{Inhomogeneous}$ values are approximately the same. Meanwhile, both G^- band $\Gamma_{Inhomogeneous}$ values are greater than the corresponding G^+ band $\Gamma_{Inhomogeneous}$ values, with the G^- band $\Gamma_{Inhomogeneous}$ value being significantly greater for an excitation energy of 1.63 eV compared with 1.51eV. Remembering that the Raman signal comes from an ensemble of resonant SWCNTs, these observations can be explained by (1) the fact that the G^- band frequency is strongly dependent on nanotube diameter d_t, while the G^+ band frequency is not (see Figure 4.19 (a)) and (2) the fact that there are a wider range of d_t SWCNT species that are resonant for an excitation energy of 1.63 eV compared with 1.51 eV (see Section 4.2.4). In conclusion, in addition to laser line broadening and multiple mode coupling, it is likely that the temperature independent contributions to the G^+ and G^- band linewidths include contributions from different species of resonant SWCNTs, as expected.

5.7 Conclusions

In conclusion, this chapter presents TRIARS measurements of G-band (Γ-point) optical phonon lifetimes in SWCNTs as a function of sample temperature in the range $4-600$ K. The measurements have been performed for two different excitation laser energies, 1.63 eV and 1.51 eV, where the TRIARS signal is dominated by the response of semiconducting SWCNTs in two different diameter ranges, $0.87 < d_t < 0.97$ nm and $0.99 < d_t < 1.1$ nm. The G^+ band (LO) and G^- band (TO) dynamics have been separately resolved by selecting pulse durations of approximately 2ps, which strikes a sensible balance between temporal and spectral resolution.

The results provide strong evidence that the anharmonic decay branches for the LO and TO Γ-point phonons in SWCNTs are not significantly affected by the splitting of the G-band due to curvature. The results also support the notion that the decay rates do not depend critically on SWCNT diameter (excitation energy). These results are contrary to the excitation energy dependent dynamics of the D-band phonons, presented in Chapter 6. The fact that the temperature dependence of the phonon decay rates can be well fitted by a model which assumes three-phonon anharmonic decay to be the only decay mechanism, supports the hypothesis that the main decay channel for G-band phonons is three-phonon anharmonic decay, with the lower energy phonons having an energy of approximately 400 ± 100 cm^{-1}. Within experimental error, this result is consistent with the daughter phonon energy spectrum predicted by Bonini et al. [7] for graphene. Other studies [40] have shown that the G-band phonon population lifetime is shorter in SWCNTs than in graphene and this has been attributed to additional decay channels which are unique to SWCNTs, such as three-phonon anharmonic decay involving an RBM. To test this hypothesis, the model was altered to include two anharmonic decay channels; one where the two daughter phonons include an RBM, and one where

the energy distribution of the daughter phonons is free to change. The results from fitting this model suggests that three-phonon anharmonic decay involving an RBM does not provide the dominant decay channel for the G-band phonons in SWCNTs in the temperature range of these experiments, however, the experiments are unable to rule out a contribution of up to 50% of the overall decay.

These results rule out a general difference between the G^+ and G^- anharmonic decay rates being responsible for the difference between the decay rates measured for metallic and semiconducting SWCNTs by Kang et al. [6]. It has been suggested that the increased e-ph coupling in metallic SWCNTs may provide an additional decay channel for the Γ-point phonons through electronic excitation. Comparing the temperature dependence of the Raman linewidth with the temperature dependence of the anharmonic decay rate has shown that that e-ph interactions do not contribute significantly to the decay of G-band phonons in semiconducting SWCNTs. A similar study for metallic SWCNTs is likely to reveal whether additional decay channels due to increased e-ph coupling are responsible for the faster population decay rate which is observed.

Chapter 6

A TRIARS Study of the *D*- and *G*'-band Raman Features

In this chapter, the *D*- and *G*'-band Raman features of SWCNTs are studied using the same TRIARS technique that was used to study the *G*-band phonon population dynamics in Chapter 5. These features are attributed to one-phonon and two-phonon second-order DR Raman scattering processes respectively, and in both cases the scattering phonons can be represented in the vicinity of the *K*-point in the graphene Brillouin zone (see Section 2.2.5). An investigation of the *D*-band TRIARS measurements provides the first experimentally determined values for the decay rate ($1/T_1$) of a non-equilibrium population of *D*-band phonons in SWCNTs. A parallel investigation of *G*'-band TRIARS measurements, which are effectively TRIARS measurements performed on the overtone of the *D*-band, has been undertaken with the view of extending the reach of TRIARS to other overtone features in SWCNTs and graphene. The publication which covers the work in this chapter can be found in Ref [126] and in the Publications section in this thesis.

The chapter begins with a brief introduction which includes a review of the relevant literature and discusses the motivation for the study. This is followed by a TRIARS investigation of the *D*-band feature which follows a similar format to the *G*-band investigation in Chapter 5. The final section of the chapter investigates the results from the *G*'-band TRIARS measurements. As usual the chapter concludes with a summary of the findings of the experiments.

6.1 Prelude

It has been shown theoretically that Γ-point phonons and phonons near the *K*-point are important to the mobility of high-energy carriers in SWCNTs and graphene. In a

study focusing on graphene, Lazzeri et al. [34] predicted that e-ph coupling is stronger for phonons close to the K-point than for the Γ phonons. Furthermore, there have been a number of theoretical predictions and estimates which place the K phonon population lifetime, T_1, in the $4-7$ps range [7, 33, 34, 140]. If these predictions are correct, this would imply that phonons close to the K-point are more susceptible to building up a non-equilibrium population, and more importantly, that the population of phonons at K will be dominant in determining the rate at which high-energy carriers are scattered [7].

Oron-Carl et al. [36] were able to provide direct spectroscopic evidence for hot-phonon generation in electrically biased carbon nanotubes by using the Stokes to anti-Stokes Raman signal intensity ratio, I_{AS} and I_{S}, as probe to monitor the phonon temperature as a function of current bias. They observed a significant non-equilibrium population of G-band (Γ-point) phonons under high-bias ($2-3$eV), but were unable to obtain evidence for the presence of a non-equilibrium population of D-band (K-point) phonons because of a momentum mismatch between the phonons generated and the phonons probed in the experiments. There is currently a lack of direct experimental evidence to support the existing theoretical work regarding the importance of K-point phonons in determining carrier mobility. This is perhaps because of the more complex and involved nature of second-order Raman scattering. For example, the ability to approximate the phonon lifetime through Raman linewidth analysis is severely hindered for second-order Raman features (even for measurements obtained at the single nanotube level) because of the significant linewidth broadening caused by multiple mode coupling (see Section 2.2.5). It is well known that TRIARS measurements performed on first-order Raman features pose a significant experimental challenge, and it is expected that such experiments would only be made more arduous if performed on second-order Raman features, which are generally lower in intensity. Furthermore, TRIARS signals involving second-order Raman scattering processes are not necessary straight forward to interpret. For example, the D-band anti-Stokes scattering rate is proportional to the phonon population but also dependent on the rate at which electrons undergo elastic scattering from lattice defects, and the G'-band anti-Stokes scattering rate is dependent on the square of the phonon population, which significantly complicates the interpretation of the intensity dynamics.

The G-band TRIARS measurements in Chapter 5 were remarkably stable, demonstrated a high level of repeatability, and produced signals which were much stronger than those in previously reported TRIARS studies on bundled SWCNTs. This offered an ideal opportunity to extend the TRIARS experiments to measurements of the second-order D- and G'-band Raman features.

In this chapter, an investigation of D-band TRIARS measurements is undertaken in order to obtain direct measurements of the population lifetime of phonons which can be represented near the K-point in the graphene Brillouin-zone. A parallel investigation of the G'-band TRIARS measurements, which are effectively TRIARS measurements

performed on the overtone of the D-band, is carried out with the aim of developing an understanding of how to interpret TRIARS measurements of a second-order two-phonon overtone Raman feature. If successful this could extend the reach of TRIARS to other overtone features, such as the M-band, which can be found in the frequency range $1650 - 2100\text{cm}^{-1}$ in graphene and SWCNT Raman spectra [37, 141]. Such overtone features can provide access to phonons represented inside the Brillouin-zone of graphene which are not accessible though one-phonon Raman scattering processes.

6.2 Experimental Details

The TRIARS experiments reported in this chapter were performed using the same experimental setup that was used for the G-band TRIARS measurements in Chapter 5. To make sure that the experiments would remain stable, similar ($\sim$ 2ps) pulse durations were used along with an average incident laser power of 5mW for the individual pump and probe beams. A detailed description of the experimental apparatus and techniques that have been used can be found in Section 3.3.

To ensure that the conclusions reached in Section 4.4 remain valid, the experiments were performed at sampling region B on the same bundled SWCNT sample used for the RRS investigation in Chapter 4. TRIARS measurements were taken for both the D-band and G'-band, and for two laser excitation energies, 1.51 eV and 1.63 eV, so that the intensity dynamics of the second-order Raman features could be independently measured for SWCNTs in the diameter ranges $0.99 - 1.11\text{nm}$ and $0.87 - 0.97\text{nm}$ respectively. For each laser excitation energy, the TRIARS measurements were performed as a function of sample temperature in the range $T = 4 - 320$ K so that the anharmonic decay channels of the phonons could be investigated through thermal activation. Measurements were not taken for sample temperatures above $T = 320\text{K}$ because the measured dynamics are limited by the resolution of the experiment. A limited number of TRIARS measurements were performed with both pump and probe beams at half-power (2.5mW) in order to determine if there were any non-linear contributions to the phonon population dynamics.

6.3 *D*-band TRIARS Measurements

At the beginning of each TRIARS experiment anti-Stokes Raman spectra were recorded for the pump beam alone and probe beam alone by blocking each beam in turn. As was observed for the G-band in Section 5.3, the D-band anti-Stokes Raman intensity was greater than expected for thermal equilibrium when measured using a single pulsed beam. This suggests that self-scattering is occurring, and that the generation of D-band phonons is rapid while the population decay is slow enough to allow a non-equilibrium phonon population to be generated. Recalling the discussion in Section 5.3, this means

that the sum of the anti-Stokes Raman spectra obtained from the pump beam alone and probe beam alone does not represent the thermal equilibrium phonon population. To within experimental error the measurements of the D-band intensity dynamics presented in this chapter are unaffected by halving the incidence laser power of both pulses. This strongly suggests that the dynamics are linear and that the non-equilibrium phonon population generated by one laser pulse is independent of the dynamics of the non-equilibrium population generated by the other laser pulse. The background D-band intensity was again defined as the sum of the anti-Stokes Raman spectra recorded for the pump beam alone and probe beam alone.

With both pump and probe beams incident on the sample, the anti-Stokes Raman signal intensity was monitored as the pump-probe delay was increased, until the anti-Stokes Raman signal intensity was equal to that of the background phonon population. The background phonon population was reached in less than 10ps for both positive and negative delays, which meant that there was no measurable long lived signal. To be consistent with the previous TRIARS measurements, background spectra were recorded at 25ps in each experiment. Figure 6.1 (a) compares the background spectra obtained for a pump-probe delay of 25ps (*red*) with the spectra obtained by summing the pump beam alone and probe beam alone (*black*) for $T = 7$K. To obtain the temporal evolution of the anti-Stokes Raman signal, a total of 61 anti-Stokes spectra were recorded for pump-probe delays in the range 20ps to -20ps. After every third spectra was recorded, a background spectra was also recorded, so that the stability of the experiment and drift in the Raman signal could be monitored.

Figure 6.1 (c) shows a selection of anti-Stokes D-band spectra obtained for various pump-probe delays in an experiment performed at the low temperature limit ($T = 7$K) and for an excitation laser energy of $E_{\mathrm{L}} = 1.51$eV. Due to variations in the background signal, it is not entirely obvious looking at Figure 6.1 (c) that the anti-Stokes D-band intensity increases with decreasing pump-probe delay. Figure 6.1 (e) shows the spectra that were obtained by subtracting the nearest corresponding background spectra from each of the spectra shown in Figure 6.1 (c). From this figure it is clear that the anti-Stokes D-band Raman intensity increases with decreasing pump-probe delay. The subtracted spectra also exhibit a broadband background intensity which has a significant time-dependence. Section 6.4 has been dedicated to investigating this time-dependent broadband background contribution. As anticipated the second-order D-band TRIARS signal is much smaller than the TRIARS signals obtained for the first-order G-band in Chapter 5. For completeness, Figures 6.1 and 6.2 include a representative sample of results for TRIARS measurements taken at the low temperature limit and towards the high temperature limit of the D-band TRIARS experiments for excitation laser energies $E_{\mathrm{L}} = 1.51$eV and $E_{\mathrm{L}} = 1.63$eV respectively.

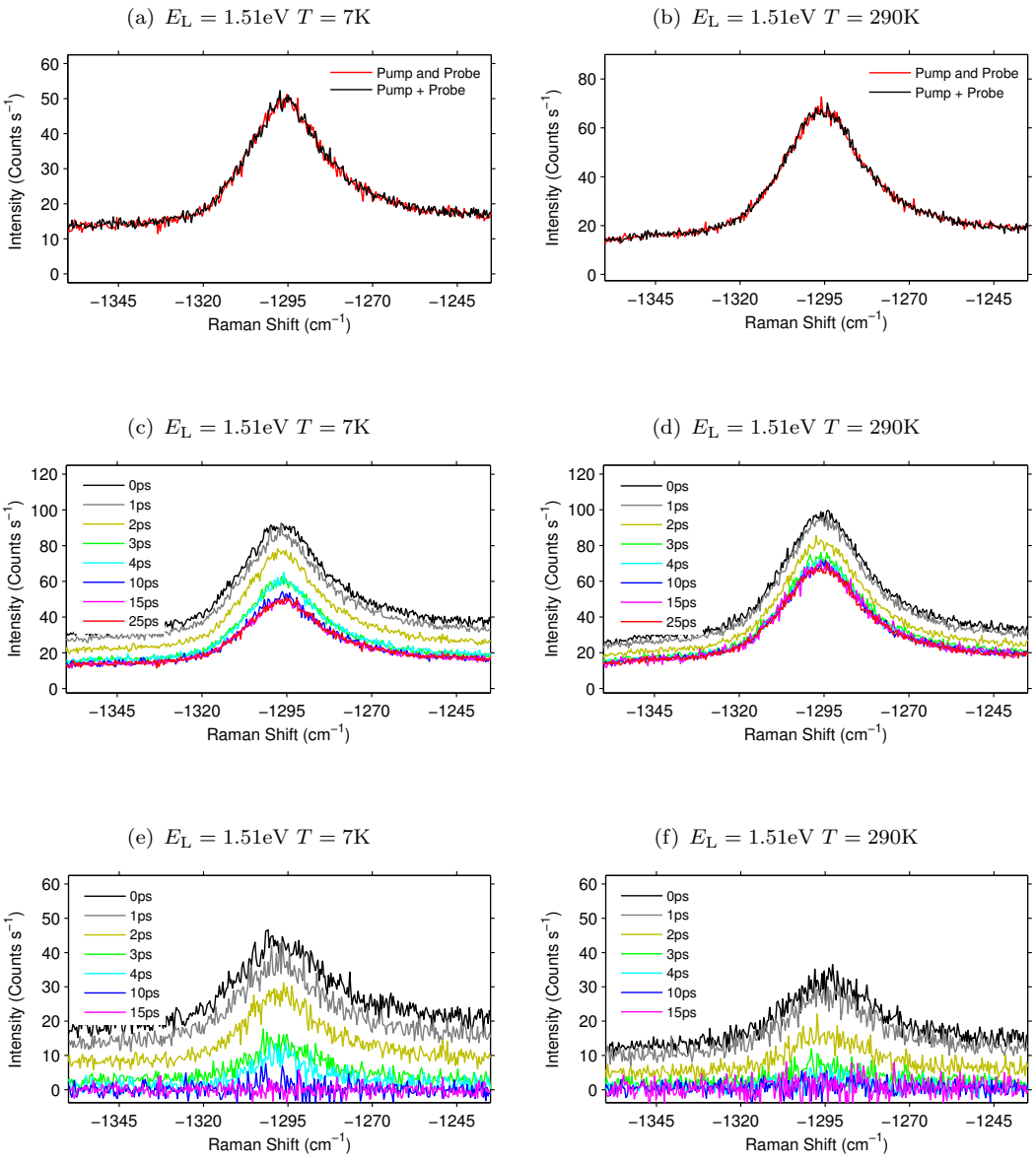

FIGURE 6.1: Representative sample of D-band TRIARS measurements obtained for $E_L = 1.51$eV. *Top row:* Plots comparing the background spectra obtained for a pump-probe delay of 25ps (*red*) with the spectra obtained by summing the pump beam alone and probe beam alone (*black*) for (a) $T = 7$K and (b) $T = 290$K. *Middle row:* Plots showing a selection of anti-Stokes D-band spectra obtained for various pump-probe delays for (c) $T = 7$K and (d) $T = 290$K. *Bottom row:* (e) and (f) show subtracted spectra that were obtained by subtracting the 25 ps background spectra from the spectra shown in (c) and (d) respectively.

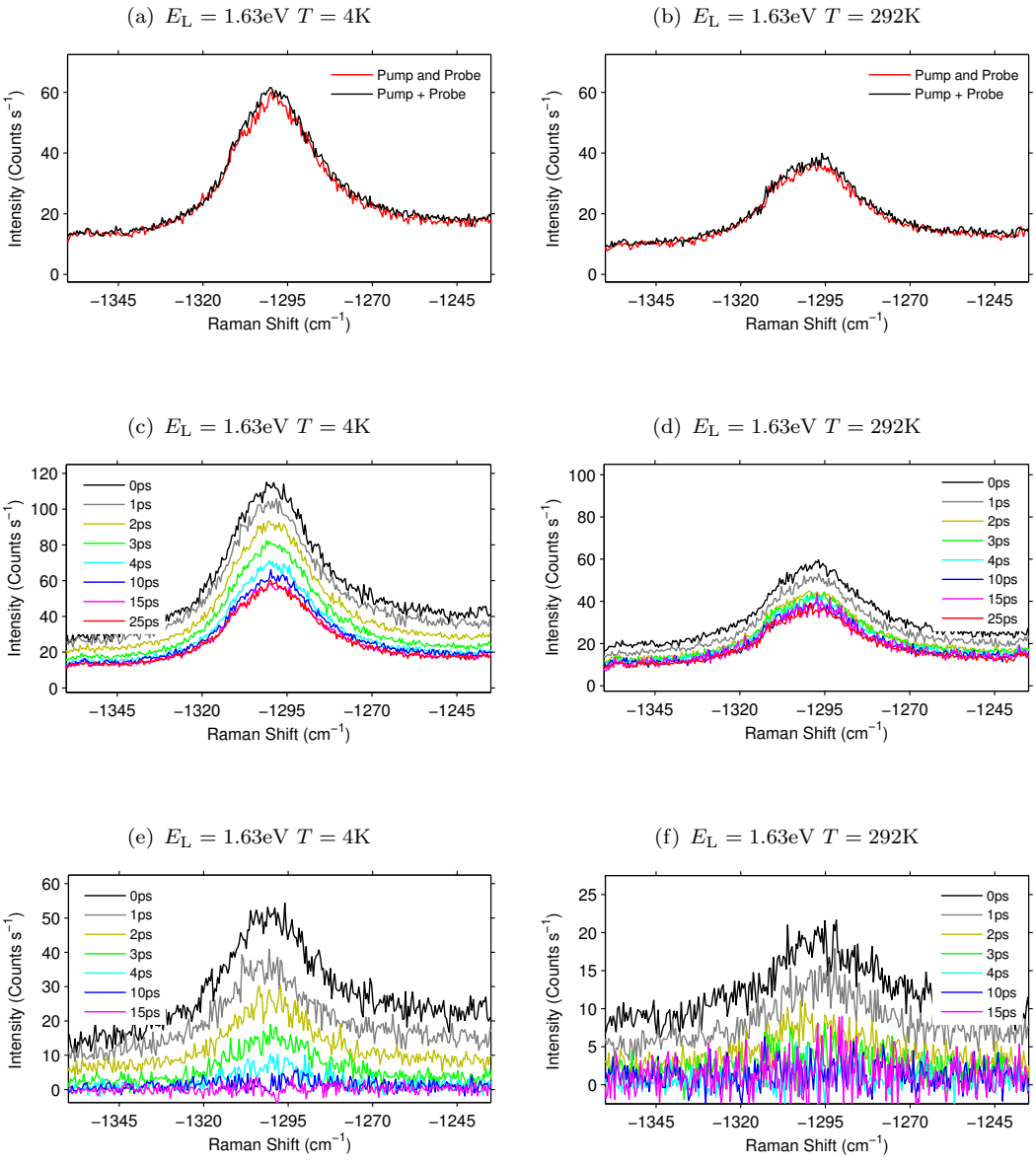

FIGURE 6.2: Representative sample of D-band TRIARS measurements obtained for $E_L = 1.63$eV. *Top row:* Plots comparing the background spectra obtained for a pump-probe delay of 25ps (*red*) with the spectra obtained by summing the pump beam alone and probe beam alone (*black*) for (a) $T = 4$K and (b) $T = 292$K. *Middle row:* Plots showing a selection of anti-Stokes D-band spectra obtained for various pump-probe delays for (c) $T = 4$K and (d) $T = 292$K. *Bottom row:* (e) and (f) show subtracted spectra that were obtained by subtracting the 25 ps background spectra from the spectra shown in (c) and (d) respectively.

6.4 Investigation of Time-Dependent Broadband Background

Before going any further, let us discuss the transient broadband background signal which is present in the subtracted spectra. In each of the *D*- *G*- and *G*'-band TRIARS measurements the background intensity shows no time dependence for large pump-probe delays, while on the order of the cross-correlation the background intensity increases with decreasing pump-probe delay. The background intensity increases by a comparable amount (in the range $5 - 20$ counts s^{-1}) in each of the TRIARS measurements, and is found to be independent of wavelength, i.e. a broadband signal, within the range covered by the anti-Stokes Raman spectra ($635 - 744$nm).

In the *G*-band subtracted spectra the time-dependent background signal is small in comparison to the time-dependent anti-Stokes Raman signal (see Figure 5.3 (e) and (f)), however, in the second-order *D*- and *G*'-band subtracted spectra the transient background signal is comparable to the much weaker time-dependent Raman intensity. Providing that the time-dependent background signal and anti-Stokes Raman signal are unrelated, the subtracted spectra consist of a linear sum of the two signals. This means that the existing procedure for fitting the subtracted spectra, i.e. fitting the sum of a linear background and a function to fit the Raman feature, can be used to separate the anti-Stokes Raman intensity dynamics from the background intensity dynamics.

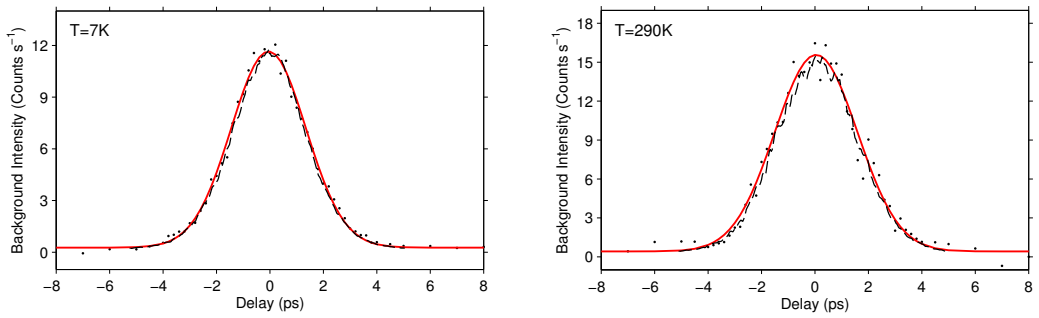

(a) (b)

FIGURE 6.3: Representative sample of results showing time-dependence of the broadband background intensity for *D*-band TRIARS measurements performed for a laser excitation energy of 1.51eV and for sample temperatures (a) $T = 4$K and (b) $T = 290$K. The values for the background intensity were obtained from the fitting the subtracted spectra using the procedure in Section 6.5 and are given as measured at 1300cm^{-1}. Also shown are the pump-probe cross-collections (*broken black line*) and de-convolved monoexponential fits (*solid red line*).

Figure 6.3 shows the time-dependence of the background intensity for *D*-band TRIARS measurements performed for a laser excitation energy of 1.51eV and for sample temperatures (a) $T = 4$K and (b) $T = 290$K. It is clear that the background signal (*black points*) follows the pump-probe cross-correlation (*broken black line*) closely. Assuming an instantaneous rise, the dynamics of the background have been fit (*solid red lines*)

with the convolution of the pulse cross-correlation and a monoexponential decay (see Section 5.4). The background dynamics were investigated for a range of TRIARS measurements, and in all cases, the background signal is measured to rise and decay on a timescale faster than 200fs.

It is possible to rule out band gap fluorescence as a source of the time-dependent background signal because the anti-Stoke spectra are higher in energy than the excitation energy [142]. One possibility may be two-photon absorption or Auger processes [79] which may lead to hot carrier PL originating from the SWCNTs [143] or the underlying Si/SiO_2 substrate. Another strong possibility is PL in the microscope objective or another optically active component in the experimental system. However, since we have shown that it is possible to successfully separate the anti-Stoke Raman intensity dynamics from the background intensity dynamics and because the background signal is not believed to be of fundamental interest to this study, no further investigation is required.

6.5 Obtaining the *D*-Band Intensity Dynamics

To obtain the D-band intensity dynamics each of the subtracted spectra were fit with a function consisting of a single Lorentzian peak and a linear background. Figures 6.4 (a) and (b) show example fits to the subtracted spectra for $T = 7$K and $T = 290$K TRIARS experiments, performed for a laser excitation energy of $E_{\mathrm{L}} = 1.51$eV. Lower limits were placed on the fitting parameters representing the Lorentzian linewidths to prevent the fitting algorithm from narrowing the linewidth to fit the experimental noise in the low signal limit. The linear term in the fits accounted for the pump-probe delay dependence of the broadband background (see Section 6.4), while the fitting parameters from the Lorentzian were used to extract the intensity, Raman shift, and linewidth (FWHM) for the D-band.

Figures 6.4 (c) and (d) show the intensity as a function of pump-probe delay, obtained from fitting each of the subtracted spectra in Figures 6.4 (a) and (b). Also shown are the pump-probe cross-correlations (*broken lines*) obtained during the TRIARS measurements. In general, the D-band intensity dynamics suffers from a smaller signal-to-noise ratio compared with the G-band intensity dynamics presented in Section 5.3. This can be explained by the lower scattering rate for second-order one-phonon Raman scattering. The difference between the intensity dynamics and the cross-correlations in these figures clearly demonstrates that the dynamics are resolvable, and suggests that there is a significant difference between the low temperature and room temperature dynamics.

Measurements of the Raman shift as a function of pump-probe delay and Raman linewidth as a function of pump-probe delay are presented in Figures 6.4 (e) and (f), and Figures

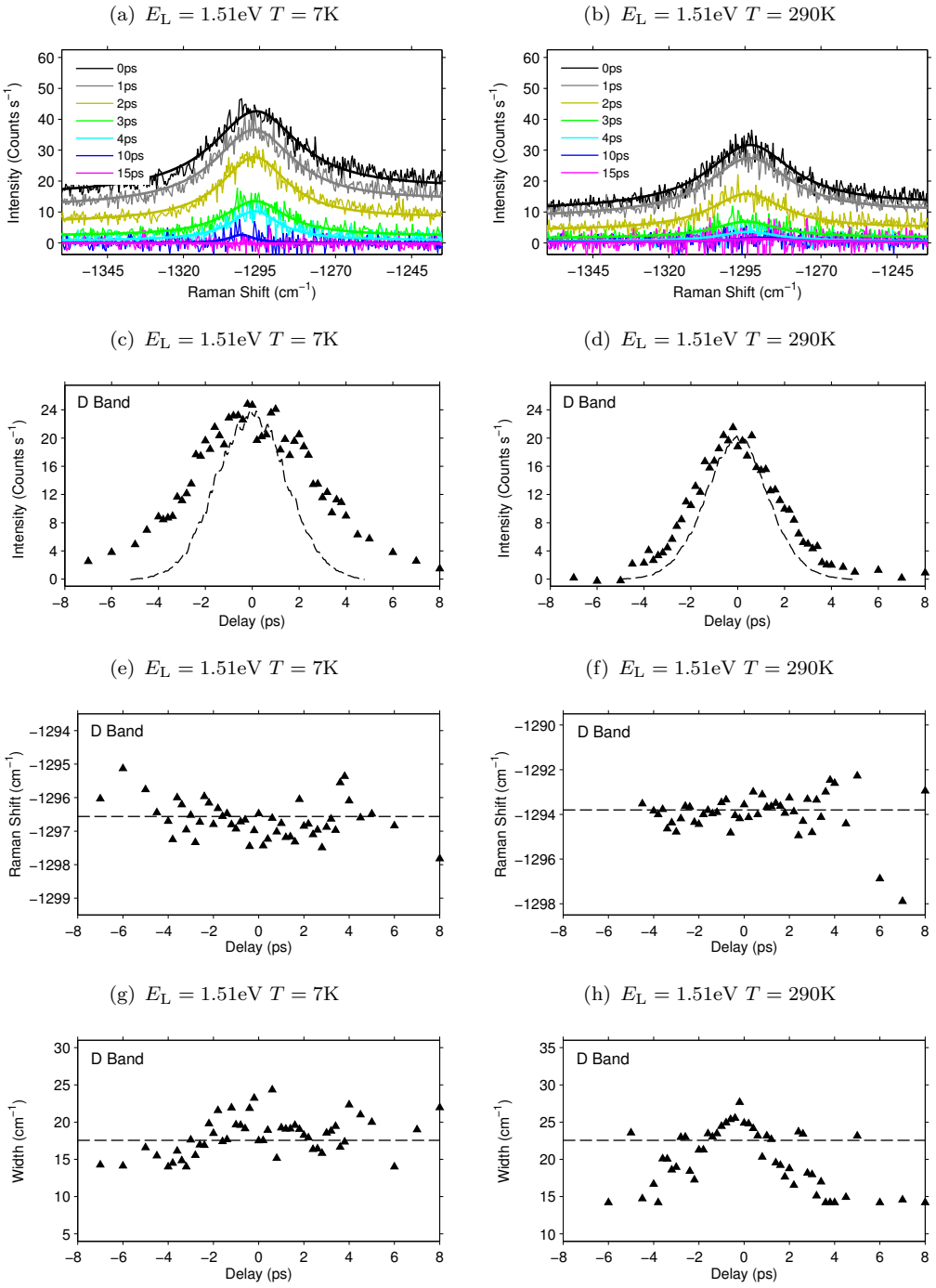

FIGURE 6.4: Representative sample of results for obtaining the intensity dynamics from D-band TRIARS experiments performed for an excitation laser energy of $E_L = 1.51$eV. (a) and (b) show example fits (single Lorentzian peak and a linear polynomial background) to the subtracted spectra for $T = 7$K and $T = 290$K respectively. The parameters from these fits were used to extract the intensity, Raman shift, and linewidth (FWHM) for the D-band. (c) and (d) show the D-band intensity as a function of pump-probe delay (intensity dynamics) for $T = 7$K and $T = 290$K. Also shown are the pump-probe cross-correlations which have been scaled for illustrative purposes. (e) and (f) show the Raman shift as a function of pump-probe delay, while (g) and (h) show the Raman linewidth as a function of pump-probe delay for $T = 7$K and $T = 290$K respectively. *Horizontal broken lines* represent average values obtained from fitting the background spectra.

(a) $E_L = 1.63$eV $T = 4$K (b) $E_L = 1.63$eV $T = 292$K

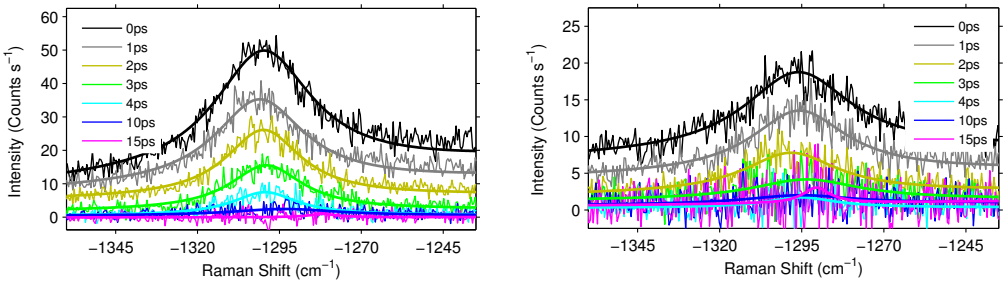

(c) $E_L = 1.63$eV $T = 4$K (d) $E_L = 1.63$eV $T = 292$K

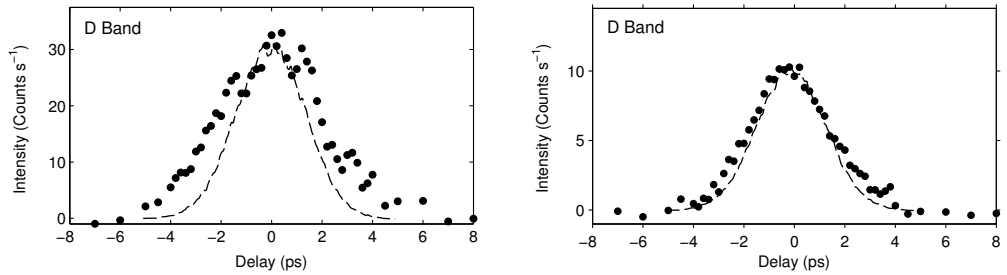

(e) $E_L = 1.63$eV $T = 4$K (f) $E_L = 1.63$eV $T = 292$K

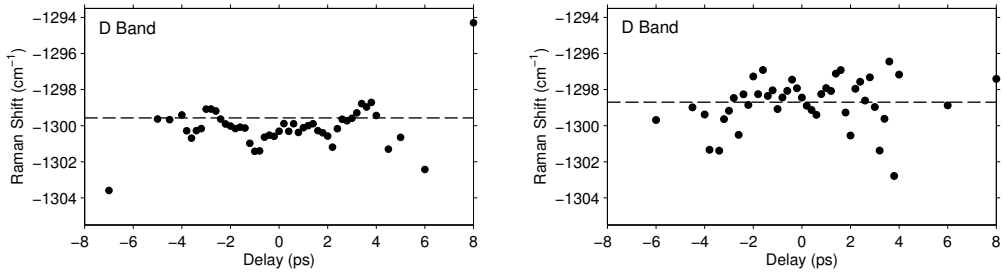

(g) $E_L = 1.63$eV $T = 4$K (h) $E_L = 1.63$eV $T = 292$K

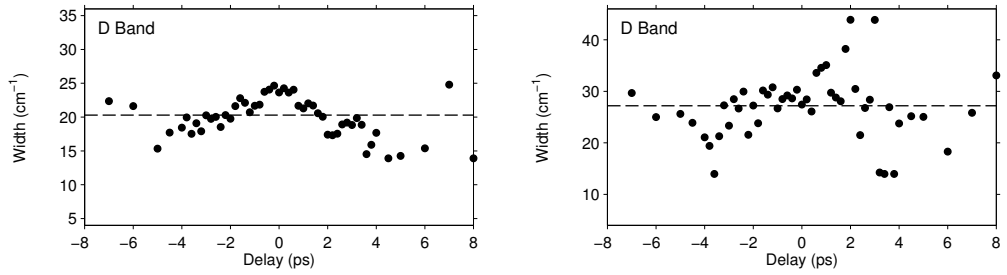

FIGURE 6.5: Representative sample of results for obtaining the intensity dynamics from D-band TRIARS experiments performed for an excitation laser energy of $E_L = 1.63$eV. (a) and (b) show example fits (single Lorentzian peak and a linear polynomial background) to the subtracted spectra for $T = 4$K and $T = 292$K respectively. The parameters from these fits were used to extract the Raman intensity, shift, and linewidth (FWHM) for the D-band. (c) and (d) show the D-band intensity as a function of pump-probe delay (intensity dynamics) for $T = 4$K and $T = 292$K. Also shown are the pump-probe cross-correlations which have been scaled for illustrative purposes. (e) and (f) show the Raman shift as a function of pump-probe delay, while (g) and (h) show the Raman linewidth as a function of pump-probe delay for $T = 4$K and $T = 292$K respectively. *Horizontal broken lines* represent average values obtained from fitting the background spectra.

6.4 (g) and (h) respectively. The D-band Raman shift was observed to be independent of pump-probe delay, while the Raman linewidth suggested a weak dependence on delay. This dependence was investigated for each TRIARS experiment by comparing the linewidths obtained from fitting the subtracted spectra with the average linewidth obtained from fitting all of the background spectra (*horizontal broken line*) in the figures). In the majority of cases, it was found that the linewidths obtained from fitting the subtracted spectra were distributed evenly about the average linewidth obtained from fitting all of the background spectra. The fits to the subtracted spectra experienced increasing uncertainty due to the decrease in intensity as the pump-probe delay increased. In some cases this caused the fitted linewidth to tend away from the correct value as the pump-probe delay increased in magnitude. Thus it was concluded that the delay dependence of the D-band linewidth in the subtracted spectra was likely to be an artefact of the fitting procedure. However, because of the statistical uncertainty in the results one cannot rule out the possibility that the linewidth in the subtracted spectra experiences a small dependence on pump-probe delay. For completeness, Figure 6.5 shows a similar representative sample of results for obtaining the intensity dynamics from D-band TRIARS experiments performed for an excitation laser energy of $E_{\mathrm{L}} = 1.63\mathrm{eV}$.

6.6 Modelling the *D*-band Phonon Dynamics

The observation of self-scattering in Section 6.3 and the form of the D-band intensity dynamics presented in Figures 6.4 and 6.5, strongly suggest that a non-equilibrium D-band phonon population is being rapidly generated before decaying on a timescale comparable to the G-band phonon population. Section 2.5.5 discusses the processes which are likely to dominate the generation of D-band phonons in these particular experiments. In this discussion it is concluded that the non-equilibrium D-band phonon population dynamics rises rapidly on the 100 fs timescale and decays freely through various possible channels until the equilibrium phonon population is reached.

It is important to consider that the D-band anti-Stokes scattering rate is proportional to the phonon population but also dependent on the rate at which electrons undergo elastic scattering from lattice defects. In this study, the rate at which the photo-excited electrons scatter from lattice defects is assumed to be independent of pump-probe delay. This means that the D-band intensity dynamics obtained from fitting the subtracted spectra is interpreted as being the phonon population dynamics convolved with the instrumental response of the pump-probe system (pulse cross-correlation), as is discussed in Appendix D. Thus it is proposed that the D-band phonon dynamics can be obtained from the intensity dynamics in the same way that the G-band phonon population dynamics were obtained in Section 5.4. Comparing the form of the D-band intensity dynamics in Figures 6.4 and 6.5 with the theoretical calculations for the intensity dynamics presented in Figures 5.7 (c) and (d), particularly in the $-2 < t_{delay} < 2$ ps

range, strongly suggests that the rise time for the D-band phonon population is short i.e. less than 200 fs. Attempts to fit the measured dynamics using Equation 5.3, without constraints on T_{rise} and T_1, also suggested that $T_{rise} \sim 0$. Fitting the dynamics with a bi-exponential decay did not improve the quality of the fit, or yield any new information. Therefore, it was assumed that the rising edge dynamics was instantaneous and that the D-band phonon dynamics could be obtained by fitting the convolution of Equation 5.4 and Equation 5.1, using the same fitting function developed for the G-band (see Appendix A Matlab Code 4).

Figure 6.6 (a)-(d) show examples of the fitted D-band intensity dynamics obtained from low temperature and high temperature TRIARS experiments performed for both laser excitation energies. The fits shown in Figure 6.6 were used to obtain a low temperature ($T = 7$K) D-band phonon population lifetime of $T_1 = 2.39 \pm 0.39$ ps and room temperature ($T = 290$K) D-band phonon lifetime of $T_1 = 0.98 \pm 0.26$ ps, for an excitation of 1.51 eV, and a low temperature ($T = 4$K) D-band phonon population lifetime of $T_1 = 1.47 \pm 0.34$ ps and room temperature ($T = 292$K) D-band lifetime of $T_1 = 0.61 \pm 0.165$ ps, for an excitation of 1.63 eV.

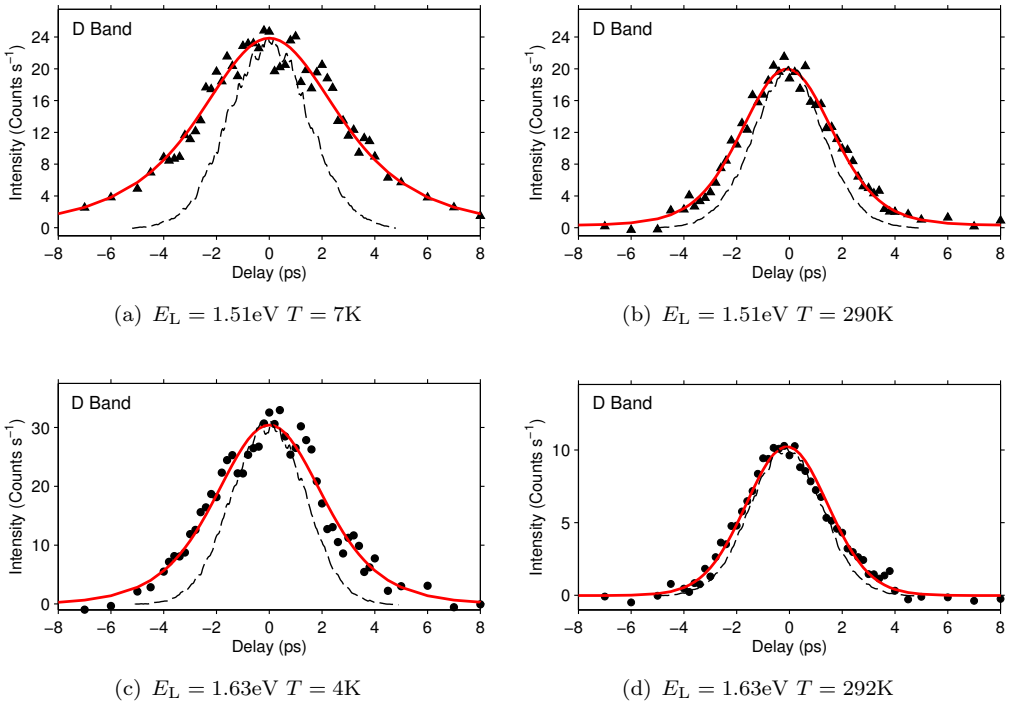

(a) $E_L = 1.51$eV $T = 7$K

(b) $E_L = 1.51$eV $T = 290$K

(c) $E_L = 1.63$eV $T = 4$K

(d) $E_L = 1.63$eV $T = 292$K

FIGURE 6.6: Representative sample of fitted D-band intensity dynamics. Obtained from low temperature and high temperature TRIARS experiments performed for $E_L = 1.51$eV and $E_L = 1.63$eV. The fitting function was calculated from the convolution of the functions given in Equations 5.4 and 5.1, which assumes the rise dynamics to be instantaneous.

6.7 Temperature and Diameter Dependence of the *D*-band Phonon Decay Rate

Figures 6.7 (a) and (b) present the results on the temperature dependence of the decay rate, $1/T_1$, of the D-band phonon population, measured for excitation energies of 1.51 eV, and 1.63 eV respectively. The decay rate has been presented in units of ps^{-1} and cm^{-1} to show the corresponding linewidth broadening. The error bars in the figures show the 95% confidence bounds in the fitting parameter. Again, the reason why the confidence bounds in Figure 5.9 generally increase with temperature can be explained by the faster dynamics that are observed with increasing temperature, which reduces the difference between the measured TRIARS dynamics and the pulse cross-correlation function, and means the fitting routine is relying on fewer data points to secure the fit. Where possible, multiple independent TRIARS experiments were performed and are shown to display the significance of these errors.

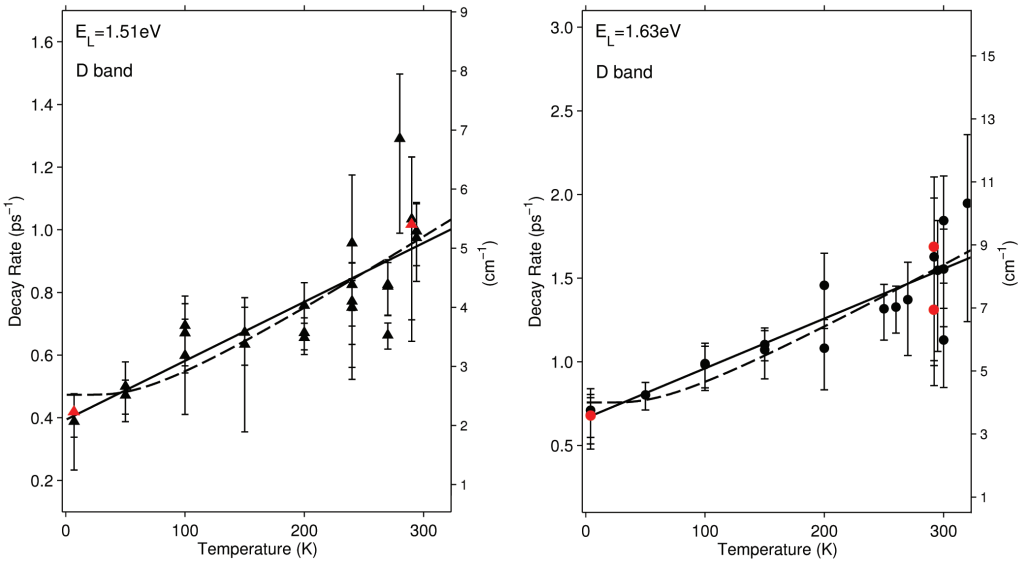

(a) (b)

FIGURE 6.7: The decay rate as a function of temperature for D-band phonon for an excitation energy of (a) $E_L = 1.51$ eV and (b) $E_L = 1.63$ eV. The experimental data (*represented as symbols*) in (a) and (b) have been fit with Equation 5.5 (*broken lines*) and Equation 6.1 (*solid lines*). Each symbol corresponds to an independent measurement of the TRIARS dynamics. The error bars represent the 95% confidence bounds. Red data points indicate results from TRIARS experiments performed at half laser power (2.5mW).

The data presented indicates that the D-band decay rate follows an approximately linear dependence on temperature in the range $T = 4-320$K for both excitation energies. Also, for any particular temperature the decay rates measured for the two excitation energies appear to be quite different. The *red data points* in Figures 6.7 (a) and (b) indicate results from TRIARS experiments performed at half laser power (2.5mW). These data

points show no indication that the D-band phonon dynamics are dependent on the phonon occupation.

Let us now examine the temperature dependence of the D-band phonon decay rate in detail. It was first assumed that three-phonon anharmonic processes dominate the decay of the D-band phonons. Thus the temperature dependence of the decay rates in Figures 6.7 (a) and (b) were fit to Equation 5.5, where Γ_0 is the absolute decay rate measured at $T = 0$K, E_1 and E_2 are the energies of the daughter phonons and Bose-Einstein statistics $n(E_i, T)$ is used to calculate the population of the two daughter phonons, whose energies must sum to give the energy of the parent phonon, i.e. $E_2 = E_D - E_1$. The best fits that were obtained from fitting this model are shown in Figures 6.7 (a) and (b) as *broken black lines*, and the fitting parameters obtained from these fits are presented in Table 6.1.

Band	E_i (eV)	E_1 (cm^{-1})	E_2 (cm^{-1})	Γ_0 (ps^{-1})
D	1.51	138 ± 51	1157 ± 51	0.5 ± 0.1
D	1.63	136 ± 46	1159 ± 46	0.8 ± 0.1

TABLE 6.1: Anharmonic Fitting Parameters: obtained from fitting Equation 5.5 to the temperature dependence of the D-band phonon decay rate.

The results from the fits suggest that one of the lower energy daughter phonons has an energy of approximately 140cm^{-1}. To check whether the predicted energies for the daughter phonons (obtained from fitting Equation 5.5) make sense, we can consider the possible decay channels for K-point phonons responsible for the D-band in graphene. Bonini et al. [7] predicted that the population lifetime of the 1300cm^{-1} optical phonons at K (responsible for the D-band in graphene), will have a strong temperature-dependence in the range of $100 - 500$ K due to a large decay channel towards low-energy (less than 150cm^{-1}) acoustic phonon modes. The upper part of Figure 6.8 shows a schematic of the possible three-phonon anharmonic decay channels for the K phonons in graphene [7], which are derived from energy and momentum conservation. The lower part of the figure shows the probability of a K-phonon decaying into two modes of frequencies ω and $\omega_0 - \omega$ for a temperature of 300K. The energies for the daughter phonons presented in Table 6.1 are consistent with the predicted decay channels shown in Figure 6.8 for graphene. This strongly suggests that three-phonon anharmonic decay processes are dominant in determining the decay rate of K phonons in SWCNTs. Unfortunately it is not possible to resolve the thermal deactivation of decay channels involving low-energy (less than 150cm^{-1}) phonons from the data points in Figures 6.7 (a) and (b), to do this one would need to obtain many more accurate data points in the $0 - 150$K temperature range.

The temperature dependence of the decay rates in Figures 6.7 (a) and (b) have also been fit with a linear function, given by

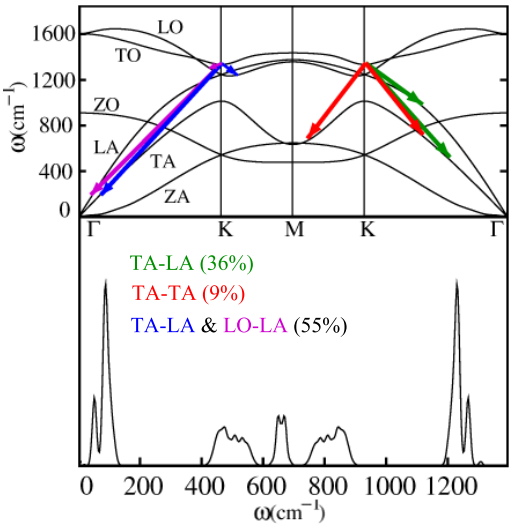

FIGURE 6.8: Upper part: shows a schematic of possible three-phonon anharmonic decay channels for the 1300cm^{-1} K-point optical phonons which are responsible for the D- and G'- bands in graphene [7]. Lower part shows the probability of a K phonon decaying into two modes of frequencies ω and $\omega_0 - \omega$ for a temperature of 300K. Adapted from [7].

$$\Gamma(T) = MT + \Gamma_0, \tag{6.1}$$

where Γ_0 is the absolute decay rate measured at $T = 0$K and M is a constant of proportionality (in units of ps^{-1}K^{-1}). The best fits that were obtained from fitting this model are shown in Figures 6.7 (a) and (b) as *solid black lines*, and the parameters obtained from these fits are presented in Table 6.2.

Band	E_i (eV)	M (ps^{-1}K^{-1})	Γ_0 (ps^{-1})
D	1.51	0.0020 ± 0.0005	0.39 ± 0.15
D	1.63	0.0029 ± 0.0007	0.66 ± 0.18

TABLE 6.2: Linear Fitting Parameters: obtained from linear fits to the temperature dependence of the D-band phonon decay rate.

The absolute decay rates, Γ_0, obtained from both fitting techniques suggest that the D-band phonons measured for different excitation energies have different decay rates. As the two excitation energies probe different SWCNT species in different diameter ranges this implies that D-band phonons in different SWCNT species have different decay rates. This is contrary to the reports of the G-band phonon decay rates which appear to be independent of SWCNT structural parameters [40, 130]. This difference can possibly be explained by the fact that while the G-band phonons in all SWCNTs are derived from the same $q \sim 0$ modes in graphene, the D-band phonons in different SWCNTs are derived from different graphene phonons. Thus these results also suggest that the decay rate of phonons near the K-point in graphene vary relatively rapidly as a function of wavevector.

6.8 An Investigation of the *G*'-band TRIARS Measurements

Let us now investigate the G'-band TRIARS measurements. As discussed in Section 2.2.5, the G'-band feature in SWCNTs is attributed to Raman scattering processes involving two opposite wavevector phonons which can be represented in the vicinity of the K-point in the graphene Brillouin zone. In this respect the G'-band can be considered an overtone of the D-band. As we have seen, the population lifetime of phonons close to K-point can be studied through D-band measurements. The aim of this 'follow up' study is to develop an understanding of how to interpret TRIARS measurements of a second-order two-phonon 'overtone' Raman feature.

At this point the reader will be familiar with the basic method used to extract the intensity dynamics from the raw spectra. For this reason, the discussions in the following two sections are intentionally short and focus only on the key points of the experimental data.

6.8.1 *G*'-band TRIARS Measurements

The G'-band anti-Stokes Raman intensity was greater than expected for thermal equilibrium when measured using a single pulsed beam, which suggests self-scattering is again occurring. Furthermore, the measurements of the G'-band phonon dynamics presented in this chapter are unaffected by halving the incident laser power, indicating that the dynamics of the non-equilibrium phonon population generated by one laser pulse is independent of the dynamics of the non-equilibrium population generated by the other laser pulse. The background G'-band intensity was again defined as the sum of the anti-Stokes Raman spectra recorded for the pump beam alone and probe beam alone. The background phonon population was reached in less than 10ps for both positive and negative delays, which meant that there is no measurable long lived signal. The background spectra were recorded at 25ps in each experiment.

Figure 6.9 (a) compares the background spectra obtained for a pump-probe delay of 25ps (*red*) with the spectra obtained by summing the pump beam alone and probe beam alone (*black*) for $T = 4$K. Figure 6.9 (c) shows a selection of anti-Stokes D-band spectra obtained for various pump-probe delays in an experiment performed at the low temperature limit ($T = 4$K) and for an excitation laser energy of $E_{\mathrm{L}} = 1.51$eV. Figure 6.9 (e) shows the spectra that were obtained by subtracting the nearest corresponding background spectra from each of the spectra shown in Figure 6.9 (c). From this figure it is clear that the anti-Stokes G'-band Raman intensity increases with decreasing pump-probe delay. The time-dependent broadband background signal (Section 6.4) is

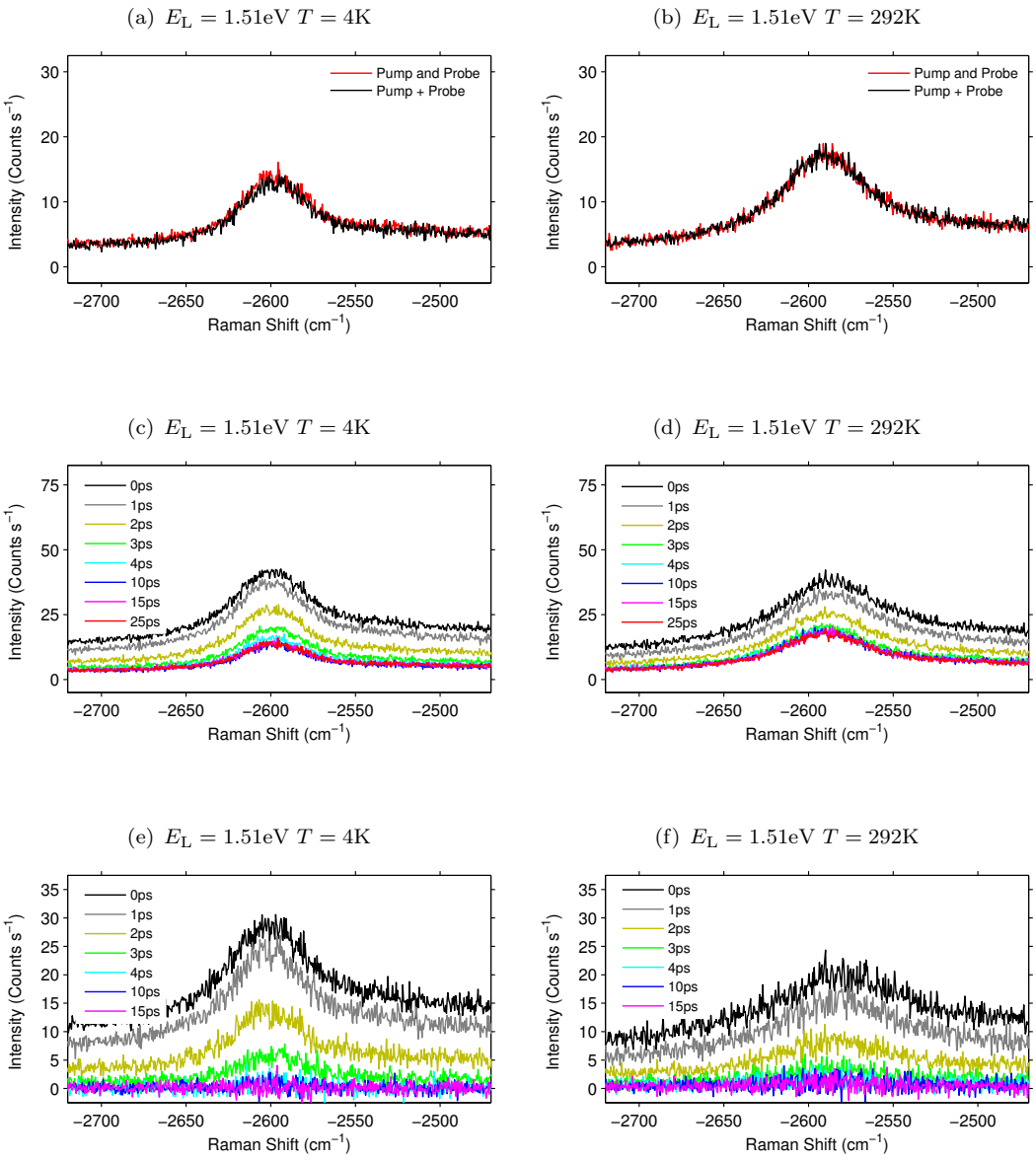

FIGURE 6.9: Representative sample of G'-band TRIARS measurements obtained for $E_L = 1.51$eV. *Top row:* Plots comparing the background spectra obtained for a pump-probe delay of 25ps (*red*) with the spectra obtained by summing the pump beam alone and probe beam alone (*black*) for (a) $T = 4$K and (b) $T = 292$K. *Middle row:* Plots showing a selection of anti-Stokes G'-band spectra obtained for various pump-probe delays for (c) $T = 4$K and (d) $T = 292$K. *Bottom row:* (e) and (f) show subtracted spectra that were obtained by subtracting the 25 ps background spectra from the spectra shown in (c) and (d) respectively.

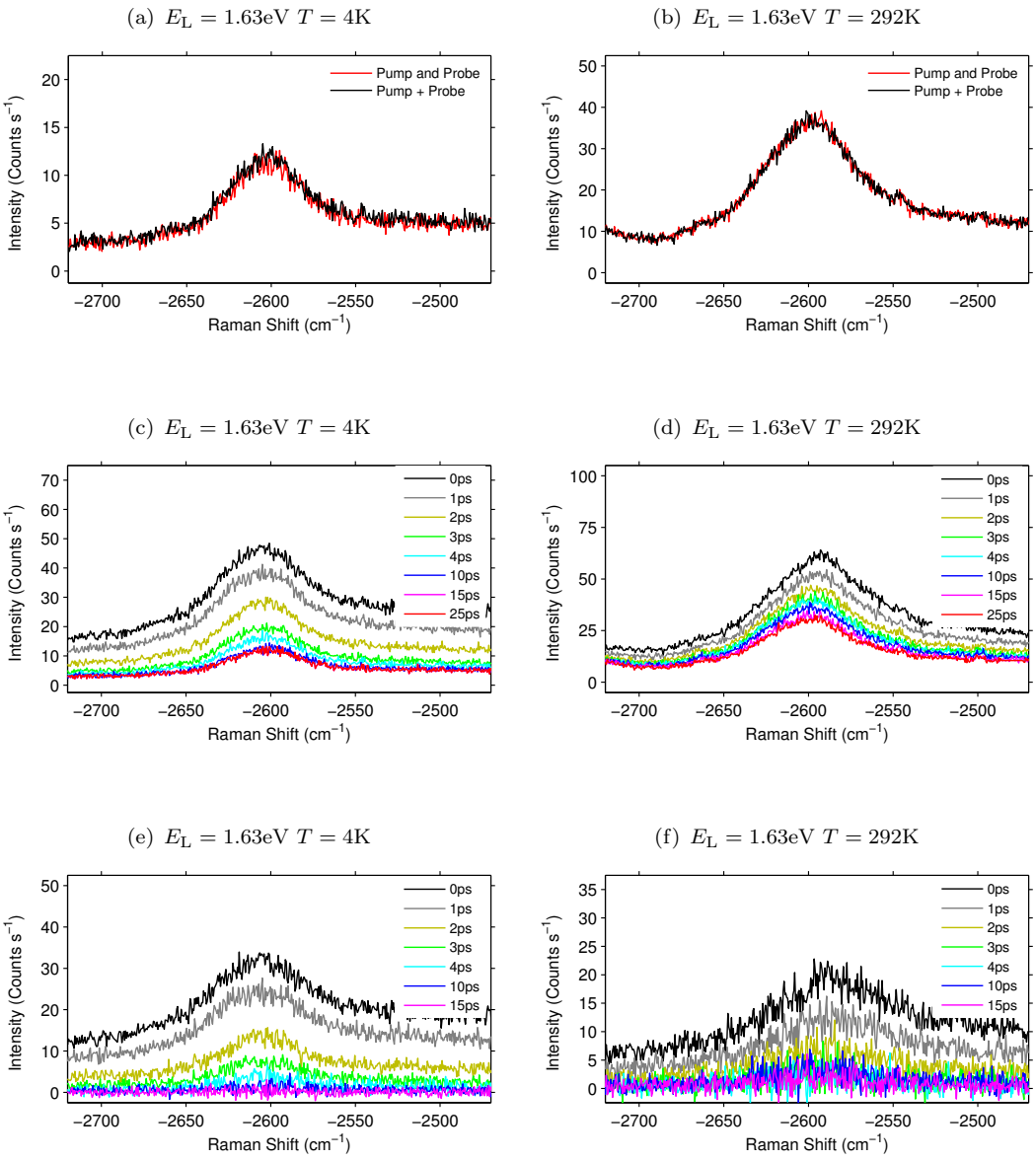

FIGURE 6.10: Representative sample of G'-band TRIARS measurements obtained for $E_L = 1.63$eV. *Top row:* Plots comparing the background spectra obtained for a pump-probe delay of 25ps (*red*) with the spectra obtained by summing the pump beam alone and probe beam alone (*black*) for (a) $T = 4$K and (b) $T = 292$K. *Middle row:* Plots showing a selection of anti-Stokes G'-band spectra obtained for various pump-probe delays for (c) $T = 4$K and (d) $T = 292$K. *Bottom row:* (e) and (f) show subtracted spectra that were obtained by subtracting the 25 ps background spectra from the spectra shown in (c) and (d) respectively.

comparable to the subtracted G'-band Raman signal because of the weak nature of two-phonon DR Raman scattering.

For completeness, Figures 6.9 and 6.10 include a representative sample of results for TRIARS measurements taken at the low temperature limit and towards the high temperature limit of the G'-band TRIARS experiments for excitation laser energies $E_{\mathrm{L}} = 1.51\mathrm{eV}$ and $E_{\mathrm{L}} = 1.63\mathrm{eV}$ respectively.

6.8.2 Obtaining the *G*'-Band Intensity Dynamics

To obtain the G'-band intensity dynamics each of the subtracted spectra were fit with a function consisting of a single Lorentzian peak and a linear background. Figures 6.11 (a) and (b) show example fits to the subtracted spectra for $T = 4\mathrm{K}$ and $T = 292\mathrm{K}$ TRIARS experiments, performed for a laser excitation energy of $E_{\mathrm{L}} = 1.51\mathrm{eV}$. Lower limits were placed on the fitting parameters representing the Lorentzian linewidths to prevent the fitting algorithm from narrowing the linewidth to fit the experimental noise in the low signal limit. The linear term in the fit accounts for the pump-probe delay dependence of the broadband background (see Section 6.4), while the fitting parameters from the Lorentzian were used to extract the Raman intensity, shift, and linewidth (FWHM) for the G'-band.

Figures 6.11 (c) and (d) show the intensity as a function of pump-probe delay, obtained from fitting each of the subtracted spectra in Figures 6.11 (a) and (b). Also shown are the pump-probe cross-correlations (*broken lines*) obtained during the TRIARS measurements. Measurements of the Raman shift as a function of pump-probe delay and Raman linewidth as a function of pump-probe delay are presented in Figures 6.11 (e) and (f), and Figures 6.11 (g) and (h) respectively.

For completeness, Figure 6.11 shows a similar representative sample of results for obtaining the intensity dynamics from G'-band TRIARS experiments performed for an excitation laser energy of $E_{\mathrm{L}} = 1.63\mathrm{eV}$.

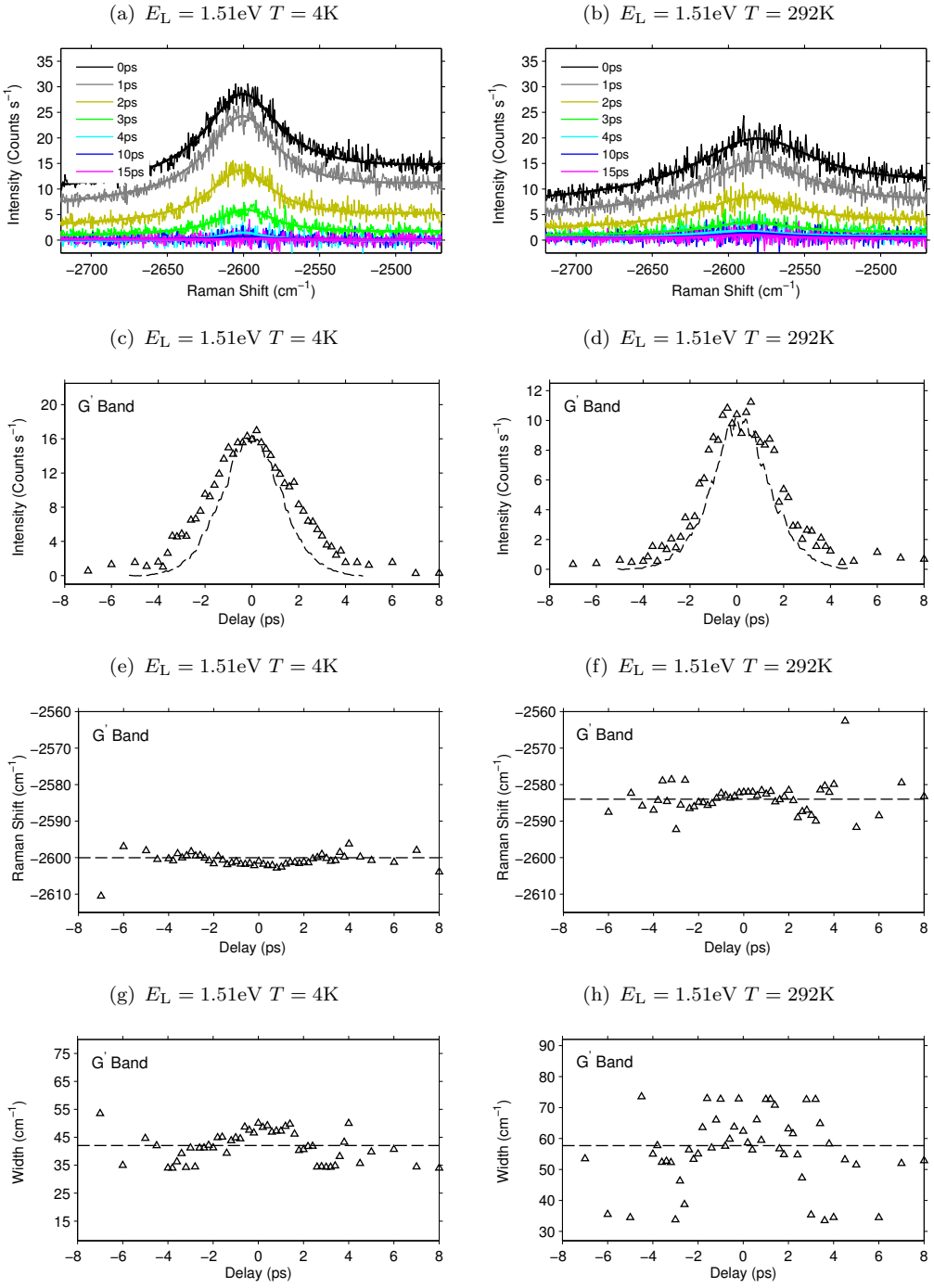

FIGURE 6.11: Representative sample of results for obtaining the intensity dynamics from G'-band TRIARS experiments performed for an excitation laser energy of $E_L = 1.51$eV. (a) and (b) show example fits (single Lorentzian peak and a linear polynomial background) to the subtracted spectra for $T = 4$K and $T = 292$K respectively. The parameters from these fits were used to extract the intensity, Raman shift, and linewidth (FWHM) for the G'-band. (c) and (d) show the G'-band intensity as a function of pump-probe delay (intensity dynamics) for $T = 4$K and $T = 292$K. Also shown are the pump-probe cross-correlations which have been scaled for illustrative purposes. (e) and (f) show the Raman shift as a function of pump-probe delay, while (g) and (h) show the Raman linewidth as a function of pump-probe delay for $T = 4$K and $T = 292$K respectively. *Horizontal broken lines* represent average values obtained from fitting the background spectra.

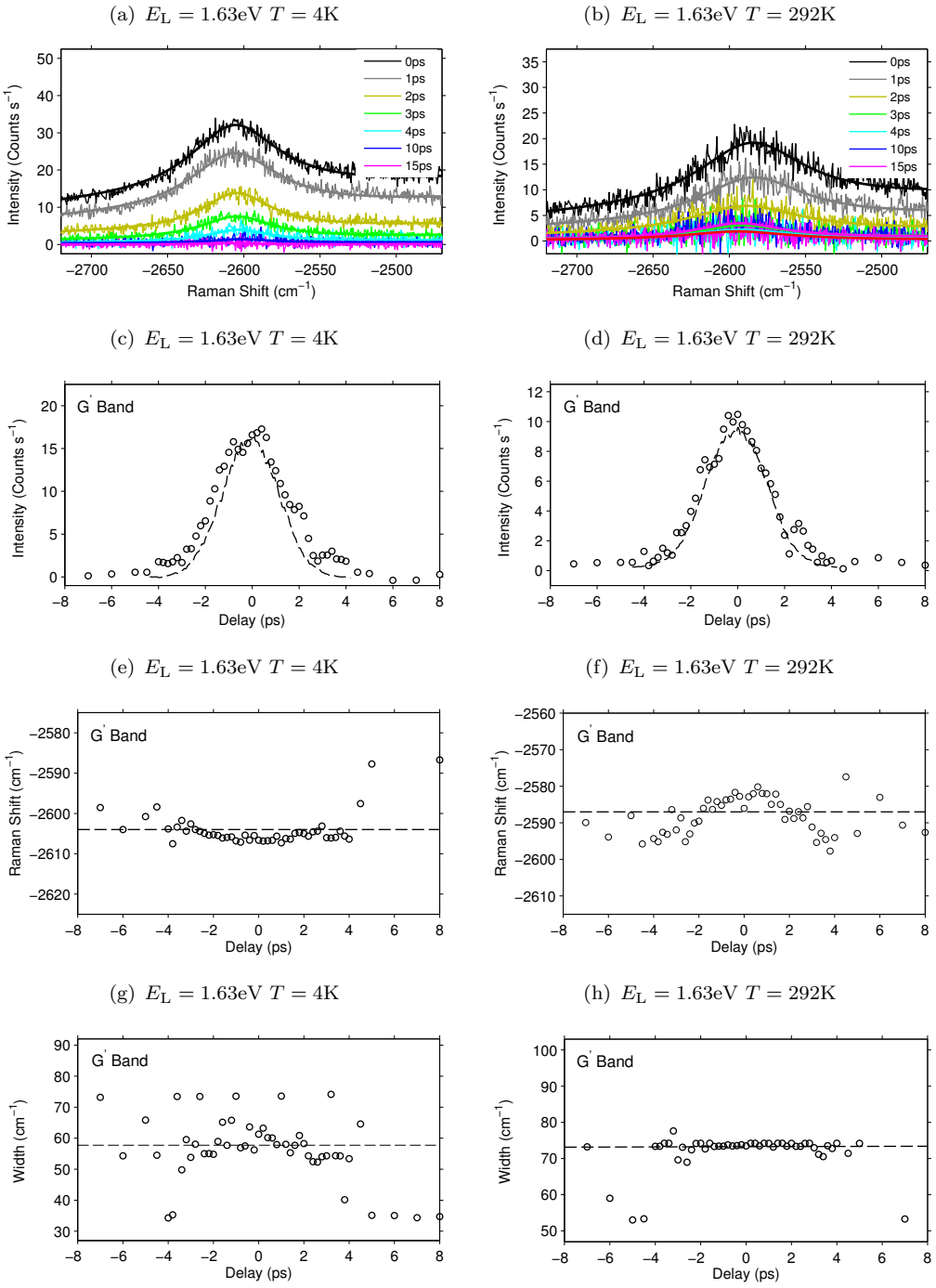

FIGURE 6.12: Representative sample of results for obtaining the intensity dynamics from G'-band TRIARS experiments performed for an excitation laser energy of $E_L = 1.63$eV. (a) and (b) show example fits (single Lorentzian peak and a linear polynomial background) to the subtracted spectra for $T = 4$K and $T = 292$K respectively. The parameters from these fits were used to extract the intensity, Raman shift, and linewidth (FWHM) for the G'-band. (c) and (d) show the G'-band intensity as a function of pump-probe delay (intensity dynamics) for $T = 4$K and $T = 292$K. Also shown are the pump-probe cross-correlations which have been scaled for illustrative purposes. (e) and (f) show the Raman shift as a function of pump-probe delay, while (g) and (h) show the Raman linewidth as a function of pump-probe delay for $T = 4$K and $T = 292$K respectively. *Horizontal broken lines* represent average values obtained from fitting the background spectra.

6.8.3 Implications for TRIARS of a Two-Phonon Raman Feature

For Raman scattering involving two phonons the anti-Stokes signal intensity is proportional to the square of the phonon population. The implications of this are discussed in detail in Appendix D. In the discussion it is shown that the G'-band subtracted spectra intensity is dependent on three terms. This leads to two possible regimes for the dynamics in the G'-band TRIARS measurements; a linear regime where the intensity dynamics are expected to be the same as for a one-phonon Raman feature and a quadratic regime where the intensity dynamics are expected to be of a different form.

As discussed in Appendix D, we are unable to determine whether the G'-band measurements presented in this chapter are in the linear or the quadratic regime. However, it seems likely that the measurements exist in the quadratic regime, or somewhere between these two regimes. It has also been shown that, regardless of the regime the measurements are in, the fitting function based on the convolution of Equation 5.4 and Equation 5.1), i.e. the same fitting function used for the D- and G band investigations, should be used to fit the G'-band dynamics in order to avoid over interpretation of the data. In this case, if the experimental measurements are in the linear regime the fitted T_1 will be a correct measurement of the phonon population lifetime. However, if the experimental measurements are in the quadratic regime the fitted T_1 will be an underestimate of the phonon population lifetime. When the measurements are believed to be in the quadratic regime, the correct phonon population lifetime T_1 values can be obtained from the conversion function which has been provided in the appendix (Equation D.9 Appendix D).

6.8.4 Modelling the *G*'-band Phonon Dynamics

The observation of self-scattering, discussed in Section 6.8.1, and the form of the G'-band intensity dynamics presented in Figures 6.11 and 6.12, suggest that a nonequilibrium G'-band phonon population is being rapidly generated before decaying on a timescale comparable to the G-band phonons. This is consistent with observations of the D-band, which is known to probe similar phonons. Section 2.5.5 discusses the processes which are likely to dominate the generation of the phonons in these particular experiments. It is concluded that the non-equilibrium G'-band phonon population dynamics rises rapidly on a 100 fs timescale and decays freely through various possible channels until the equilibrium phonon population is reached.

Assuming instantaneous rising edge dynamics the G'-band phonon dynamics were obtained by fitting the convolution of Equation 5.4 and Equation 5.1, using the same fitting function used to fit the D and G-band intensity dynamics (see Appendix A Matlab Code 4). Figure 6.13 (a)-(d) show examples of the fitted G'-band intensity dynamics obtained from low temperature and high temperature TRIARS experiments performed for both

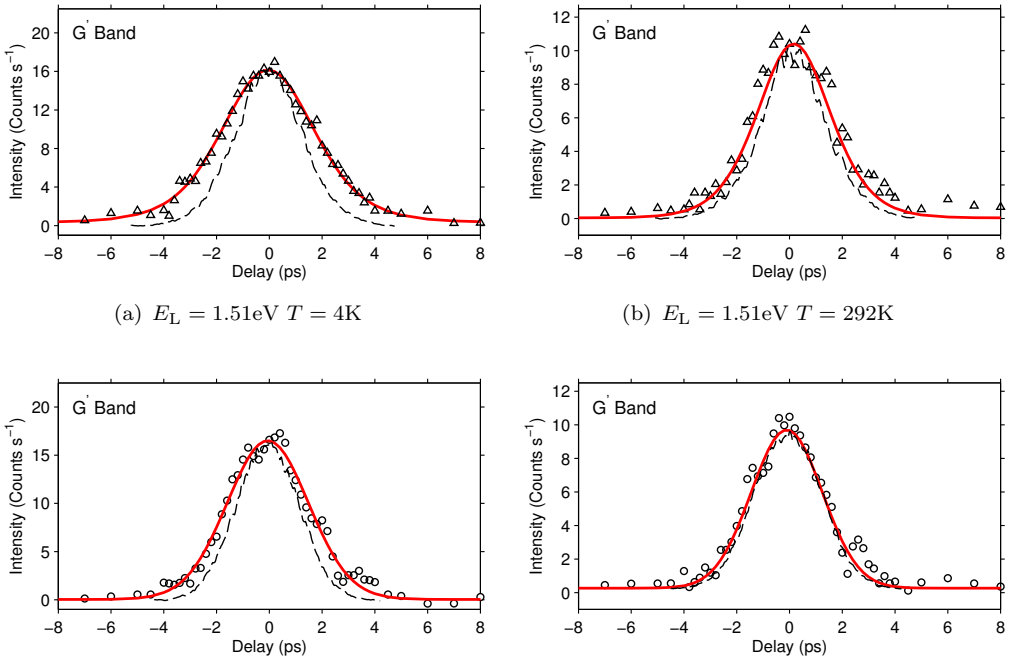

(a) $E_L = 1.51$eV $T = 4$K

(b) $E_L = 1.51$eV $T = 292$K

(c) $E_L = 1.63$eV $T = 4$K

(d) $E_L = 1.63$eV $T = 292$K

FIGURE 6.13: Representative sample of fitted G'-band intensity dynamics. Obtained from low temperature and high temperature TRIARS experiments performed for $E_L = 1.51$eV and $E_L = 1.63$eV. The fitting function was calculated from the convolution of the functions given in Equations 5.4 and 5.1, which assumes the rise dynamics to be instantaneous.

	$E_L = 1.51$ eV $T = 4$ K	$T = 292$ K	$E_L = 1.63$ eV $T = 4$ K	$T = 292$ K
T_1 *Fitted* (ps)	1.16	0.56	0.95	0.24
T_1 *Linear* (ps)	1.16	0.56	0.95	0.24
T_1 *Quadratic* (ps)	1.77	1.01	1.49	0.68

TABLE 6.3: Phonon population lifetime values, T_1, obtained from the fits in Figure 6.13. T_1 values have been calculated for the case where measurements are assumed to be dominated by the linear regime and for the case where measurements are assumed to be dominated by the quadratic regime (calculated from the conversion function, Equation D.9).

laser excitation energies. Table 6.3 shows the phonon population lifetime values T_1, obtained from fitting the intensity dynamics in Figure 6.13. T_1 values have been calculated for the case where measurements are dominated by the linear regime and for the case where measurements are dominated by the quadratic regime. It is important to remember that we do not know which regime the measurements are in, therefore it is also possible that the true phonon population lifetimes lie somewhere between the two values that are given in Table 6.3.

6.8.5 Temperature and Diameter Dependence of the *G*'-band Phonon Decay Rate

Since we cannot be sure which regime the *G*'-band TRIARS measurements are in, we will examine the *G*'-band phonon population decay rates ($1/T_1$) for the case where the measurements are dominated by the linear regime and for the case where the measurements are dominated by the quadratic regime.

Figures 6.14 (a) and (b) present the results on the temperature dependence of the decay rate, $1/T_1$, when it is assumed that the measurements are in the linear regime. The decay rate has been presented in units of ps^{-1} and cm^{-1} to show the corresponding linewidth broadening. The error bars in the figures show the 95% confidence bounds in the fitting parameter. For decay times approaching the minimum resolvable decay time the upper error bar on the decay rate will have infinite extent as the decay time could be effectively zero. The red data points in Figures 6.7 (a) and (b) indicate results from TRIARS experiments performed at half laser power (2.5mW). These data points show no indication that the *G*'-band phonon dynamics are dependent on the phonon occupation. Since the *G*'-band is expected to probe similar phonons to the *D*-band, the temperature dependence of the *D*-band phonon decay rate has been shown so that the two measurements can be compared. When the measurements are assumed to be in the linear regime the *G*'-band phonon population decay rate is measured to be much greater than the *D*-band phonon decay rate for both laser excitation energies and for all sample temperatures. One possible explanation for this result is that the *G*'-band and *D*-band probe a slightly different range of phonons for a particular excitation energy and that these phonons have different decay rates (see Section 6.7). Another possible explanation is that the *G*'-band measurements are in the quadratic regime, and that the *G*'-band decay rates presented in Figures 6.14 (a) and (b) are in fact overestimated values.

Figures 6.14 (c) and (d) present the results on the temperature dependence of the *G*'-band decay rate, $1/T_1$, when it is assumed that the measurements are in the quadratic regime. Again, the temperature dependence of the *D*-band phonon decay rate has been shown so that the two measurements can be compared. When the measurements are assumed to be in the quadratic regime the *G*'-band phonon population decay rate is measured to be comparable to the *D*-band phonon decay rate for both laser excitation energies and for all sample temperatures. Since the *G*'-band is expected to probe similar phonons to the *D*-band, this suggests that the *G*' measurements may be in the quadratic regime.

For the two possible regimes and for both excitation energies, the data presented indicates that the *G*'-band phonon decay rate follows an approximately linear dependence on temperature in the range $T = 4 - 320$K in a similar manor to the *D*-band decay rate. The decay rates measured for any particular temperature appear to be quite different

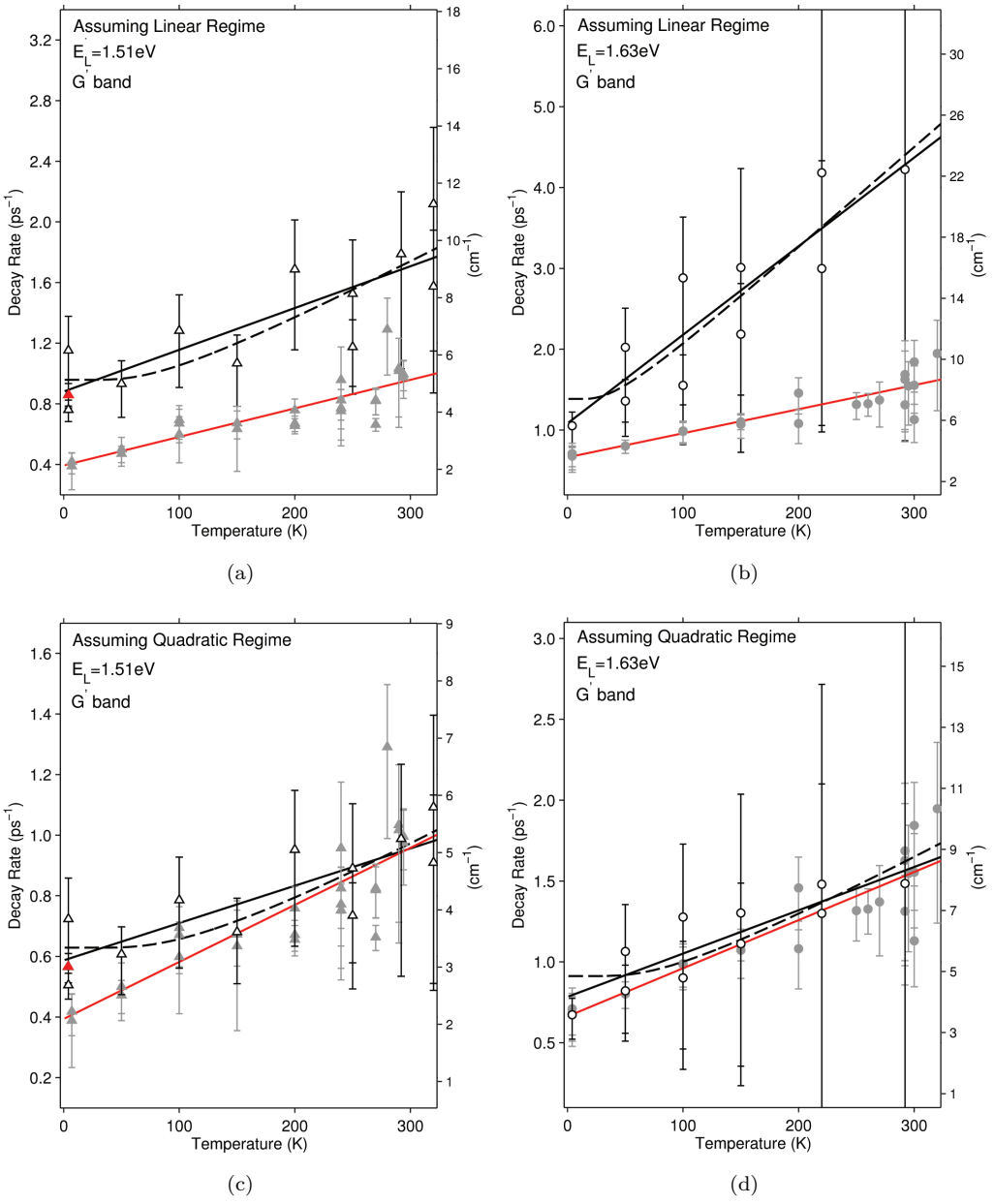

FIGURE 6.14: Figures (a) and (b) show the decay rate as a function of temperature for G'-band phonons for an excitation energy of $E_{\mathrm{L}} = 1.51$ eV and $E_{\mathrm{L}} = 1.63$ eV respectively, assuming that the measurements are in the linear regime. Figures (c) and (d) show the decay rate as a function of temperature for G'-band phonons for an excitation energy of $E_{\mathrm{L}} = 1.51$ eV and $E_{\mathrm{L}} = 1.63$ eV respectively, assuming that the measurements are in the quadratic regime. The experimental data (*represented as symbols*) have been fit with Equation 5.5 (*broken lines*) and Equation 6.1 (*solid lines*). Each symbol corresponds to an independent measurement of the TRIARS dynamics. The error bars represent the 95% confidence bounds. Red data points indicate results from TRIARS experiments performed at half laser power (2.5mW).

for the two excitation energies, however, this cannot be verified due to the uncertainty associated with each of the data points.

To examine the temperature dependence of the G'-band phonon decay rate in detail,

the temperature dependence of the decay rates were first assumed to be dominated by three-phonon anharmonic processes, and thus the decay rates in Figures 6.14 (a)-(d) are fit to Equation 5.5, using the same technique that was used to fit the temperature dependence of the *D*-band phonon decay rate in Section 6.7. The best fits that were obtained from fitting this model are shown in Figures 6.14 (a)-(d) as *broken black lines*, and the fitting parameters obtained from these fits are presented in Table 6.4. To be consistent with the *D*-band interpretation, the decay rates in Figures 6.14 (a)-(d) have also been fit with Equation 6.1 which is a simple linear function where Γ_0 is the absolute decay rate measured at $T = 0$K and M is the constant of proportionality (in units of $\mathrm{ps}^{-1}\mathrm{K}^{-1}$). The best fits that were obtained from fitting this model are shown in Figures 6.14 (a)-(d) as *solid black lines*, and the parameters obtained from these fits are presented in Table 6.5.

Regime	Band	E_i (eV)	E_1 (cm^{-1})	E_2 (cm^{-1})	Γ_0 (ps^{-1})
Linear	*G*'	1.51	167 ± 78	1128 ± 71	1.0 ± 0.2
	G'	1.63	76 ± 62	1219 ± 62	1.4 ± 0.4
Quadratic	*G*'	1.51	218 ± 105	1077 ± 51	0.6 ± 0.1
	G'	1.63	168 ± 91	1127 ± 91	0.9 ± 0.2

TABLE 6.4: Anharmonic Fitting Parameters: obtained from fitting Equation 5.5 to the temperature dependence of the *G*'-band phonon decay rates. Values are given for the case where measurements are assumed to be dominated by the linear regime and for the case where measurements are assumed to be dominated by the quadratic regime.

Regime	Band	E_i (eV)	M ($\mathrm{ps}^{-1}\mathrm{K}^{-1}$)	Γ_0 (ps^{-1})
Linear	*G*'	1.51	0.0028 ± 0.0012	0.88 ± 0.19
	G'	1.63	0.0109 ± 0.0044	1.08 ± 0.71
Quadratic	*G*'	1.51	0.0012 ± 0.0005	0.59 ± 0.11
	G'	1.63	0.0209 ± 0.0012	0.78 ± 0.19

TABLE 6.5: Linear Fitting Parameters: obtained from linear fits to the temperature dependence of the *G*'-band phonon decay rate. Values are given for the case where measurements are assumed to be dominated by the linear regime and for the case where measurements are assumed to be dominated by the quadratic regime.

Assuming that the *D*- and *G*'-band probe similar phonons we would expect to obtain similar phonon decay rates from the *D*- and *G*'-band TRIARS measurements. Let us compare the absolute decay rates Γ_0 obtained from the *G*'-band experiments in Tables 6.4 and 6.5, with the corresponding values obtained from the *D*-band experiments in Tables 6.1 and 6.2. To within experimental error the measured absolute decay rates obtained from *D*- and *G*'-band TRIARS measurements do not agree when the *G*'-band measurements are assumed to be dominated by the linear regime. However, when the *G*'-band TRIARS measurements are assumed to be dominated by the quadratic regime the measured absolute decay rates are in agreement. This provides further evidence that the measurements are likely to be dominated by the quadratic regime. To within experimental error, the anharmonic fits to the *G*'-band decay rates predict the same

energy daughter phonons as the fits to the D-band decay rates when the measurements are assumed to be dominated by the quadratic regime.

Now that we have established that the G'-band measurements are likely to be dominated by the quadratic regime, let us compare the D- and G'-band decay rates graphically. Figure 6.15 presents the temperature dependence of the D- and G'-band decay rates, assuming that the G'-band measurements are in the quadratic regime. The linear fits to the data points have also been shown. At low temperature ($T = 0$K) the absolute decay rate obtained for the D-band for a laser excitation energy of $E_{\mathrm{L}} = 1.51$eV (*blue*) is measurably lower that the absolute decay rate obtained for the G'-band for a laser excitation energy of $E_{\mathrm{L}} = 1.63$eV (*green*). This result can be explained by the fact that these measurements are expected to probe different wavevector phonons in different species of SWCNTs.

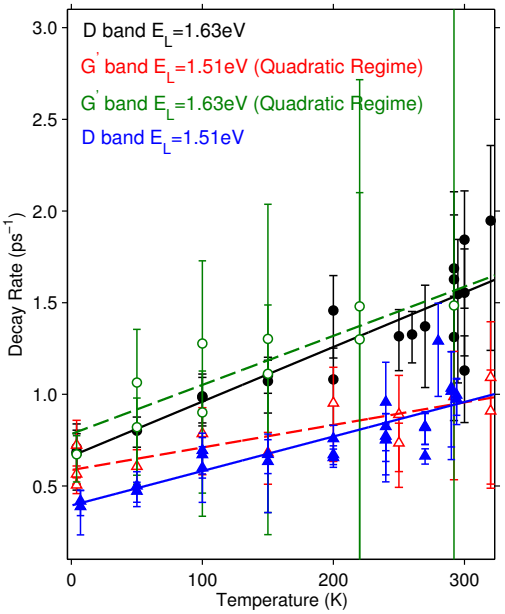

FIGURE 6.15: Comparison of the decay rates as a function of temperature, obtained from the D- and G'-band measurements for excitation energies of $E_{\mathrm{L}} = 1.51$ eV and $E_{\mathrm{L}} = 1.63$ eV. The G'-band decay rates have been obtained assuming that the G'-band measurements are in the quadratic regime (see Appendix D). The linear fits (Equation 6.1) to the data points are also shown (*solid lines*). The error bars represent the 95% confidence bounds.

Comparing the best fits in Figure 6.15 suggests that the temperature dependence of the D- and G'-band phonon decay rates are similar when measurements are performed for the same laser excitation energy, and that for measurements performed for a laser excitation energy of $E_{\mathrm{L}} = 1.63$eV the temperature dependence of the D- and G'-band phonon decay rates are more pronounced than for measurements performed for a laser excitation energy of $E_{\mathrm{L}} = 1.51$eV. This result implies that the phonons that can be represented close to the K-point in graphene may have different anharmonic decay channels

in different species of SWCNTs. This result can possibly be explained by the fact that different species of SWCNT can have significantly different vibrational structures.

6.9 Temperature Dependence of the *D*- and *G*'-band Linewidths

Figure 6.16 shows the measurements of the *D*- and *G*'-band linewidths as a function of temperature in the temperature range 4K to 320K for measurements performed for (a) 1.51eV and (b) 1.63eV. Each data point in the figure was obtained by averaging the linewidth fitting parameters which gave the best fits to each of the background spectra that were recorded in a single TRIARS experiment and then subtracting the instrumental response. These linewidth measurements are in strong agreement with previous temperature dependent linewidth measurements on bundled SWCNTs [139]. For both laser excitation energies the *D*- and *G*'-band linewidths increase with increasing temperature.

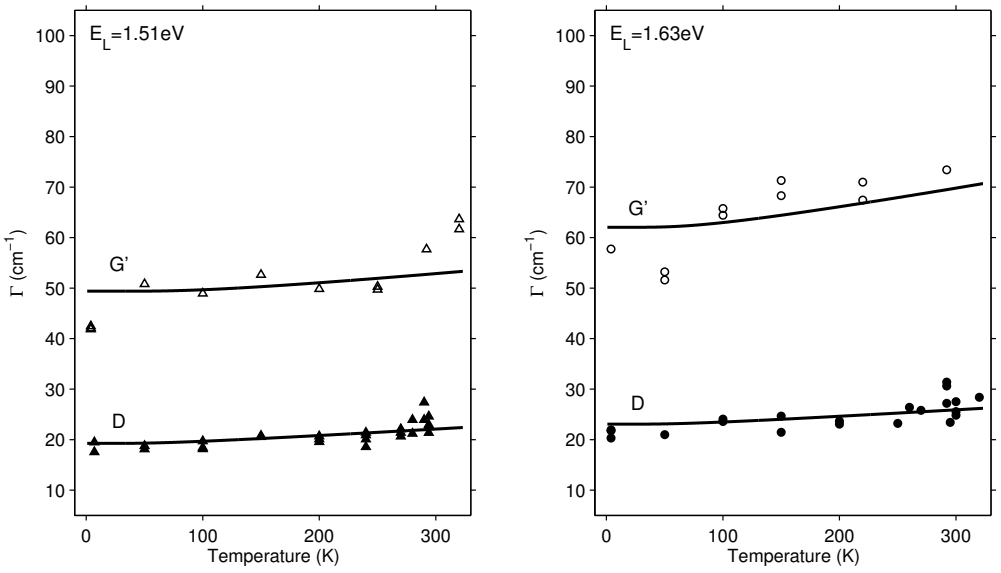

(a) (b)

FIGURE 6.16: *D*- and *G*'-band linewidths as a function of temperature in the temperature range 4K to 320K for measurements performed for (a) 1.51eV and (b) 1.63eV. The experimental data are fit to Equation 5.8 (*solid lines*) which assumes that the temperature dependence of the linewidths can be entirely explained by the anharmonic phonon population decay rates measured in the *D*- and *G*'-band TRIARS measurements.

To test whether the temperature dependence of the *D*- and *G*'-band linewidths in Figure 6.16 can be entirely explained by the anharmonic phonon population decay rates measured in the *D*- and *G*'-band TRIARS measurements, the data points in Figure 6.16 have been fit with Equation 5.8, where $\Gamma_{Inhomogeneous}$ is the only variable fitting

parameter and represents the temperature independent inhomogeneous broadening contribution. The second term represents the phonon population decay rate (in units of cm^{-1}) due to three phonon anharmonic scattering into two lower energy phonons where the relevant Γ_0, E_1 and E_2 values are taken from Tables 6.1 and 6.4. In the case of the *G'*-band the TRIARS measurements are assumed to be in the quadratic regime. Furthermore, because the *G'*-band is a two-phonon process the Lorentzian linewidth contribution, due to the phonon decay rate, must be also convolved with itself. This means that before being applied to the fit, the *G'*-band decay rate (in cm^{-1}) was divided by the deconvolution factor for a Lorentzian, 0.5.

It is clear that the models provide a reasonable fit to the temperature dependence of the *D*- and *G'*-band linewidth measurements, for both excitation laser energies. For graphene, linewidth contributions due to e-ph interactions, Γ_{e-ph}, are expected to show no significant temperature dependence in the range $4 - 320$K [7]. Assuming that this behaviour is the same for SWCNTs, this means that it would not be possible to differentiate between Γ_{e-ph} and the temperature independent inhomogeneous linewidth contributions from these experiments. The temperature independent contributions to the *D*- and *G'*-band linewidths, as predicted from the fits, are $16.61 \pm 0.63 cm^{-1}$ and $43.02 \pm 3.32 cm^{-1}$ respectively for an excitation energy of 1.51eV, and $20.42 \pm 0.71 cm^{-1}$ and $52.50 \pm 4.30 cm^{-1}$ for an excitation energy of 1.63eV.

6.10 Conclusions

In conclusion, this chapter presents TRIARS measurements of the *D*- and *G'*-band optical phonon lifetimes in SWCNTs as a function of sample temperature in the range $4-320$K. The measurements have been performed for two different laser energies, 1.63 eV and 1.51 eV, where the TRIARS signal is dominated by the response of semiconducting SWCNTs in two different diameter ranges, $0.87 < d_t < 0.97$ nm and $0.99 < d_t < 1.1$ nm. An investigation of the *D*-band measurements has led to the first experimentally determined values for the decay rate ($1/T_1$) of a non-equilibrium population of *D*-band ($\sim 1300 cm^{-1}$) phonons in SWCNTs, which can be represented close to the *K*-point in the graphene Brillouin-zone. A parallel investigation of *G'*-band TRIARS measurements, which are effectively TRIARS measurements performed on the overtone of the *D*-band, has provided valuable insight into how one should interpret TRIARS measurements of a two-phonon overtone Raman feature.

During the interpretation of the *D*-band measurements it is assumed that the rate at which the photoexcited electrons scatter from lattice defects is independent of pump-probe delay. This means the *D*-band phonon dynamics can be obtained from the intensity dynamics in the same way that the *G*-band phonon dynamics were obtained in Section 5.4. The results for the temperature dependence of the *D*-band phonon decay

rate support the existing notion that phonons which can be represented close to the K-point in graphene have a strong temperature dependence in the range $100 - 500$K due to a large decay channel towards low-energy (less than 150cm^{-1}) acoustic phonon modes [7]. The results also suggest that D-band phonons in different SWCNT species have different decay rates, which is contrary to the reports of the G-band phonon decay rates.

The interpretation of the two-phonon G'-band TRIARS measurements was more ambiguous. For Raman scattering involving two phonons the anti-Stokes signal intensity is proportional to the square of the phonon population, which leads to two possible regimes for the dynamics in the G'-band TRIARS measurements, (1) a linear regime, where the intensity dynamics are expected to be the same as for a one-phonon Raman feature, and (2) a quadratic regime, where the intensity dynamics are expected to be of a different form. Unfortunately, it is not possible to be sure which regime the G'-band measurements are in from the experiments presented in this chapter. However, it has been shown that numerical simulations of the subtracted spectra intensity dynamics can reveal the expected behaviour of the intensity dynamics in the linear and quadratic regimes. The results of these simulations have been used to predict the G'-band phonon population lifetimes in the case of each regime. The predicted phonon population lifetimes appear to be consistent with the D-band measurements when the G'-band measurements are assumed to be in the quadratic regime. This suggests that the G'-band measurements presented in this chapter are likely to be dominated by the quadratic regime. It is hoped this work will prompt others to attempt such measurements on other overtone features in SWCNTs and graphene.

Chapter 7

Conclusions and Perspectives

The aim of this thesis has been to investigate the mechanisms which control the decay of non-equilibrium Γ-point and K-point phonon populations in SWCNTs, with the view of advancing our understanding of their electronic properties. This work was primarily motivated by the strong coupling between high-energy electrons and optical phonons in SWCNTs under high electrical bias [30, 32–36]. In order to investigate the mechanisms which control the decay of non-equilibrium Γ-point and K-point phonon populations, the D- G- and G'-band phonon population dynamics have been studied as a function of sample temperature and SWCNT diameter (excitation energy), using a co-polarised degenerate pump-probe TRIARS technique. In order to allow a controlled diameter dependent study of the dynamics to be carried out, the TRIARS measurements were performed on a bundled SWCNT sample on which a detailed RRS study had been previously undertaken.

The initial RRS study involved recording a range of Stokes and anti-Stokes Raman spectra as a function of laser excitation energy and for a range of sample temperatures. Using a technique based on a graphical comparison of the relationship between experimentally determined ω_{RBM} and E_{22} and the Kataura plot, structural (n,m) assignments were made for all of the SWCNT species which were resonant in the energy range of the experimental system. Careful analysis of the RBM resonance measurements showed that for $E_{\mathrm{L}} = 1.51$eV the majority of the Raman signal was due to a response from SWCNT species in the diameter range $0.99 - 1.11$nm, while for $E_{\mathrm{L}} = 1.63$eV the majority of the Raman signal was due to SWCNTs in the diameter range $0.87 - 0.97$nm. Analysis of the D- and G-band resonance measurements, including the E_{L} dependence of the frequencies ω_D, Γ_D, and ω_{G^-} was consistent with the findings from RBM analysis. The E_{L} dependence of the D- and G-band intensity suggested that the scattering rate for outgoing resonance is lower than that for the incoming resonance for the D- and G-bands, however, this result cannot be confirmed due to the fact that the incoming and outgoing D- and G-band resonances of the individual SWCNT species cannot be separated out.

An explanation for this observation could not be found in the existing literature, however, it is likely that similar measurements performed on isolated SWCNTs would settle this matter. More, importantly, these findings indicated that TRIARS measurements performed for excitation energies $E_{\mathrm{L}} = 1.51$eV and $E_{\mathrm{L}} = 1.63$eV would predominantly probe the phonon dynamics of SWCNT species in different diameter ranges. Furthermore, RRS measurements taken at room temperature ($T = 292$K) and low temperature ($T = 4$K) suggested that there was no significant temperature dependence of the optical transition energies, E_{ii}, when compared with the energy width of the resonances. This result was important because it meant that during the TRIARS measurements it would not be necessary to tune the laser energy E_{L} when varying the sample temperature.

The G-band TRIARS experiments were performed in order to study the Γ-point optical phonon lifetimes in SWCNTs. Measurements were performed for two laser excitation energies, 1.63 eV and 1.51 eV, where the TRIARS signal was dominated by the response of semiconducting SWCNTs in two different diameter ranges, $0.87 < d_t < 0.97$ nm and $0.99 < d_t < 1.1$ nm, and as a function of sample temperature in the range $4 - 600$ K. The G^+ band (LO) and G^- band (TO) dynamics were separately resolved by selecting pulse durations of approximately 2ps, which strikes a sensible balance between temporal and spectral resolution. The results from these experiments provides strong evidence that the anharmonic decay branches for the LO and TO Γ-point phonons in SWCNTs are not significantly affected by the splitting of the G-band due to curvature. The results also support the existing notion [6, 40] that the decay rates do not depend critically on SWCNT diameter (excitation energy). The temperature dependence of the Γ-point phonon decay rate can be well fitted by a model which assumes three-phonon anharmonic decay of the Γ-point phonons in to two lower energy phonons to be the only decay mechanism. This supports the hypothesis that the main decay channel for G-band phonons is three-phonon anharmonic decay, with the lower energy phonons having an energy of approximately 400 ± 100 cm^{-1}. Within experimental error, this result is consistent with the daughter phonon energy spectrum predicted by Bonini et al. [7] for graphene. The results from fitting a model which includes two anharmonic decay channels (one where the two daughter phonons include an RBM, and one where the energy distribution of the daughter phonons is free to change), suggests that three phonon anharmonic decay involving an RBM does not provide the dominant decay channel for the G-band phonons in SWCNTs in the temperature range of these experiments, however, the experiments are unable to rule out a contribution of up to 50% of the overall decay. The results rule out a general difference between the G^+ and G^- anharmonic decay rates being responsible for the difference between the decay rates measured for metallic and semiconducting SWCNTs [6]. It has been suggested that the increased e-ph coupling in metallic SWCNTs may provide an additional decay channel for the Γ-point phonons through electronic excitation [7, 34, 55, 137]. Comparing the temperature dependence of the Raman linewidth with the temperature dependence of the anharmonic decay rate has shown that e-ph interactions do not contribute significantly to the decay of G-band

phonons in semiconducting SWCNTs. A similar study for metallic SWCNTs is likely to reveal whether additional decay channels due to increased e-ph coupling are responsible for the faster population decay rate which is observed [6].

The *D*- and *G*'-band TRIARS experiments were performed in order to study the *K*-point optical phonon lifetimes in SWCNTs. The *D*- and *G*'-band TRIARS measurements were performed for two laser excitation energies, 1.63 eV and 1.51 eV, and as a function of sample temperature in the range $4-320$ K. An investigation of the *D*-band measurements has led to the first experimentally determined values for the decay rate ($1/T_1$) of a non-equilibrium population of phonons which can be represented close to the *K*-point in the graphene Brillouin-zone, and have an energy of approximately 1300cm^{-1}. During the interpretation of the *D*-band measurements it has been assumed that the rate at which the photo-excited electrons scatter from lattice defects is independent of pump-probe delay. The implication of this assumption is that the *D*-band phonon dynamics can be obtained from the intensity dynamics in the same way that the *G*-band phonon dynamics were obtained in Chapter 5. The results for the temperature dependence of the *D*-band phonon decay rate provides the first direct experimental evidence to support the existing notion [7] that phonons, which can be represented close to the *K*-point in graphene, have a strong temperature dependence in the range $100-500$K due to a large decay channel towards low-energy (less than 150cm^{-1}) acoustic phonon modes. Similar behaviour is expected for the *K*-point phonons in graphene [7], therefore it would be valuable to perform identical measurements on a stable graphene sample.

Meanwhile, a parallel investigation of *G*'-band TRIARS measurements, which are effectively TRIARS measurements performed on the overtone of the *D*-band, has provided valuable insight into how one should interpret TRIARS measurements of a two-phonon overtone Raman feature. For Raman scattering involving two phonons the anti-Stokes signal intensity is proportional to the square of the phonon population. It has been shown that this leads to two possible regimes for the dynamics in the *G*'-band TRIARS measurements; a linear regime where the intensity dynamics are expected to be the same as for a one-phonon Raman feature and a quadratic regime where the intensity dynamics are expected to be of a different form. Unfortunately, it is not possible to determine which regime the *G*'-band measurements are in from the experiments presented in this thesis. However, it has been shown through numerical simulations that the *G*'-band measurements in this thesis are likely to be in the quadratic regime. This work opens the potential for studying the population dynamics of other overtone Raman features in SWCNTs and graphene, and possibly other materials.

Contrary to the Γ phonon decay rates which do not depend critically on SWCNT diameter, the results from the *D*- and *G*'-band TRIARS experiments suggest that the *K* phonon decay rates have a significant dependence on SWCNT diameter. Furthermore, the temperature dependence of the *K* phonon decay rate is more pronounced for measurements performed for a laser excitation energy of $E_{\mathrm{L}} = 1.51$eV, than for a laser

excitation energy of $E_{\mathrm{L}} = 1.63$eV. These results imply that the phonons that can be represented close to the K-point in graphene may have different anharmonic decay channels in different species of SWCNTs. One explanation for this is that different species of SWCNT can have significantly different vibrational structures which provide a different set of decay channels for K-point phonons. Another possible explanation is that the decay rate of phonons near the K-point in graphene vary relatively rapidly as a function of wavevector, and since the K phonons in different SWCNTs are derived from different K phonons in graphene, this leads to the behaviour observed. It is believed that an identical TRIARS experiment performed for graphene, or direct calculations of the vibrational structures of different species of SWCNTs and the resulting three-phonon anharmonic decay channels for the K phonons, may provide an explanation for these observations.

What are the implications of the work in this thesis on our understanding of the electronic properties of SWCNTs? Theoretical predictions of the effect of high-bias on SWCNT transport [33, 34, 71], indicate that both the small wavevector (Γ-point) optical phonons and large wavevector (K-point) phonons can contribute to the transport effects. The TRIARS measurements presented in this thesis, strongly suggest that, under the existing theoretical models the Γ phonon population lifetime is too short, i.e. much less than the 5 ps required, for a sufficiently large non equilibrium population to build up [33, 34], for this to be the sole reason for the transport effects in SWCNTs under high electrical bias. Meanwhile, the TRIARS study of the population lifetime of large wavevector (K) phonons, suggest that the large wavevector phonon populations have significantly shorter lifetimes ($\sim$ 1 ps) than has been theoretically predicted for graphene [7]. Therefore, the results show that a nonequilibrium population of (Γ) and (K) phonons cannot explain high-bias SWCNT transport properties on their own. A more likely explanation may be the build-up of nonequilibrium populations of both optical and low frequency phonon modes.

As discussed in Chapter 6, Oron-Carl et al. [36] were able to provide direct spectroscopic evidence for hot-phonon generation in electrically biased carbon nanotubes by using the Stokes to anti-Stokes Raman signal intensity ratio, I_{AS} and I_{S}, as a probe to monitor the phonon occupation as a function of current bias. They observed a significant non-equilibrium population of G-band (Γ-point) phonons under high-bias, but were unable to obtain evidence for the presence of a non-equilibrium population of D-band (K-point) phonons because of a momentum mismatch between the phonons generated and the phonons probed in the experiments. It would be interesting to repeat this measurement with a tunable laser system, particularly for the dispersive D-band (K-point) phonons, since it may be possible to obtain the K-point phonon occupation spectrum as a function of bias voltage.

In recent years SWCNTs have received considerable attention as novel electronic nanomaterials. The realisation of SWCNT interconnects and field effect transistors (CNFETs) [27, 28], has already proved SWCNTs to be promising materials for producing the active elements in a new generation of electronic devices. It is hoped that the work in this thesis will contribute to our understanding of the electronic properties of SWCNTs, particularly for performance optimisation of SWCNT based electronic devices. The existing and potential technological applications of SWCNTs include composite materials, energy storage, flexible electronic displays, drug delivery and electromagnetic shielding [144, 145]. It is understood that the commercialisation of SWCNT based technologies will require the controlled growth of SWCNTs, and SWCNT arrays, with specific diameter and chirality [146, 147]. However, after many years of research, it is still difficult to control the growth of SWCNT because the chirality and diameter are so weakly dependent on the variable growth parameters [115, 146, 148]. In order to solve this problem many techniques have been developed including catalyst engineering [146, 149] and post-growth purification [150–152]. With continuing efforts in the field of SWCNT synthesis, including a recent interest from the discipline of organic chemistry [153], the controlled growth of SWCNTs can be expected in the not too distant future, and such a discovery will no-doubt promote further SWCNT research.

Appendix A

Matlab Code

Matlab Code 1: Triple spectrometer efficiency matrix calculation

```
%Title: Triple spectrometer efficiency matrix import and calculation ...
    function
%Author: J M Nesbitt
%Updated: 25/08/12

%IMPORTANT: for this script to work the data files must be numbered in ...
    increments from 0 to ...
% only with an initial x character. Each file should be in 5nm steps ...
    (in this
% case from 300nm to 1200nm)
%i.e x0_1.txt....x1_1.txt.....x2_1.txt

%define directory
directoryName = 'C:\Documents and Settings\jmn205\My ...
    Documents\MATLAB\gratings\9915sub\';
fileType= '*.txt';
%file scan
fileTypeD = strcat(directoryName,fileType);
wantedFiles = dir(fileTypeD); %scan directory for txt files
numFiles = length(wantedFiles); %file count
mydata = cell(1, numFiles); %define data store file

%the following loop reads in all data found
for k = 1:numFiles, % for each file
  fullFile = strcat(directoryName,wantedFiles(k).name); %construct ...
    fileName
  mydata{k} = importdata(fullFile,',');%import data

  for j = 1:1340,
      [breakup] = strread(wantedFiles(k).name, '%s', 'delimiter','_'); ...
    %breakup filename
      x=breakup(1);
```

```
27        [token, remain] = strtok(x,'x'); %extract increment number
28        bufz=str2num(token{1}); %convert increment number to int
29        colm=(bufz+1);
30        bufwlnth=300+(bufz*5); %calculate center wavelength
31        p9915subx(j,colm)=mydata{k}(j,1); %import wavelengths
32        p9915sub(j,colm)=mydata{k}(j,3); %import intensity measured by ...
      spectrometer
33        pwavelength(j,colm)=bufwlnth; %create columns of center wavelength
34    end
35  end
36  %next generate efficiency matrices from calibration black body model
37  for k = 1:131,
38    for j = 1:1340,
39        %create calibrated wight-light for range
40        wl(j,1)=(7.856*(10^-10))*(((2*(6.62*(10^-34))* (3*(10^8))^2)/ ...
      ((p9915subx(j,k)* (10^-9))^5))* (1/(exp(((6.62*(10^-34))* ...
      (3*(10^8)))/((p9915subx(j,k)* (10^-9))* (1.38*(10^-23))* ...
      (2439)))-1)));
41        %divide calibrated white-light by measurement
42        efp9915x(j,k)=p9915subx(j,k);
43        efp9915(j,k)=wl(j,1)/p9915sub(j,k);
44    end
45  end
```

Matlab Code 2: Code to correct for triple spectrometer spectral response function using efficiency matrices produces by Matlab Code 1.

```
1  %Title: Triple spectrometer efficiency interpolation script
2  %Author: J M Nesbitt
3  %Date: 25/08/12
4
5  %Description: This code interpolates efficiency normalisation values ...
       from the existing efficiency matrices.
6  %File Format: polarization&grating_shift_laserwavelength_1.txt
7  %  (example): p151515sub_250_87600_1.txt
8  %       note: leading m in shift denotes Anti-stokes
9  %       note: wavelength is given*100
10
11 %load grating efficiency files
12 load('C:\Documents and Settings\jmn205\ My Documents\MATLAB\ ...
       gratings\gratingefficencies_28_08_12.mat');
13 %define directory of data files to be imported
14 directoryName = 'C:\Documents and Settings\jmn205\My ...
       Documents\Dropbox\Raman Data\HgTe SA RRS\';
15 fileType= '*.txt';
16 %file scan
17 fileTypeD = strcat(directoryName,fileType);
18 wantedFiles = dir(fileTypeD); %scan directory for txt files
19 numFiles = length(wantedFiles); %file count
```

```
mydata = cell(1, numFiles); %define data store file

%Used to catch and deal with correction data limit
limreached='false';

for k = 1:numFiles, %for each file
  fullFile = strcat(directoryName,wantedFiles(k).name); %construct ...
    fileName
  mydata{k} = importdata(fullFile,','); %import data
  %the following few lines contructs the variables from the filename
  [breakup] = strread(wantedFiles(k).name, '%s', 'delimiter','_'); ...
    %breakup filename
  x = breakup(1);
  y = breakup(3);
  buff =  strrep(y{1}, 'm', '-');
  centershift=str2num(buff);
  z = breakup(2);
  n = breakup(4);
  m = breakup(5);
  n1 = str2num(n{1});
  m1 = str2num(m{1});
  scaling=(n1*m1)/1000;
  laserwl=str2num(z{1});
  laserwl=laserwl/100; % shifts decimal place
  %calculate center wavelnth from laser line and wavenumber
  abswl=(1/((1/(laserwl*10^-9))-(centershift*10^2)))* 10^9;
  %the rest is dynamic on the polarization & grating, shift and wavelength
  if mod(abswl,5) ~= 0, %needs interpolation
    %rounddown to 5
    abswllow=fix(abswl);
    while mod(abswllow,5) ~= 0,
        abswllow=abswllow-1;
    end
    %calc column numbers based on 130 measurements starting at 400nm ...
    to 1050nm
    lowcol=((abswllow-300)/5)+1;
    highcol=lowcol+1;
    %perform efficiency fix interpolation
    for i=1:1339,
        if strcmp(x,'p9915sub'),
            try
                efbuff(i,1)=efp9915(i,lowcol)+ ((efp9915(i,highcol)- ...
    efp9915(i,lowcol))* ((abswl-abswllow)/5));
            catch
                if strcmp(limreached,'false'),
                warnstr=strcat('WARNING: Correction data range limit ...
    reached for: ',num2str(laserwl),'nm');
                fprintf(warnstr);
                limreached='true';
                end
            end
```

```
66              intensity(i,k)=(mydata{k}(i,3)*efbuff(i,1));
67              wavelengthwn(i,k)=(10^7/laserwl)-10000;
68              wavelength(i,k)=laserwl;
69              shift(i,k)=mydata{k}(i,1);
70          end
71      end
72    else %no interpolation
73      acol=((laserwl-300)/5)+1;
74      %perform efficiency fix
75      for i=1:1339,
76          if strcmp(x,'p9915sub')
77              try
78                  intensity(i,k)=(mydata{k}(i,3)*efp9915(i,acol));
79              catch
80                  if strcmp(limreached,'false'),
81                  warnstr=strcat('WARNING: Correction data range limit ...
       reached for: ',num2str(laserwl),'nm');
82                  fprintf(warnstr);
83                  limreached='true';
84                  end
85                  %use last possible correction
86                  intensity(i,k)=(mydata{k}(i,3)*efbuff(i,1));
87              end
88              wavelengthwn(i,k)=(10^7/laserwl)-10000;
89              wavelength(i,k)=laserwl;
90              shift(i,k)=mydata{k}(i,1);
91          end
92      end
93    end
94    intensity(:,k)=intensity(:,k)/scaling;
95  end
```

Matlab Code 3: Radial breathing mode fitting algorithm used for RRS analysis.

```
1  %Title: fitrbmrrs function
2  %Author: J M Nesbitt
3  %Updated: 10/01/13
4  function [inten] = fitrbmrrs(testx,testy)
5  % This example function controls the RBM fitting procedure. The input ...
       spectra
6  % is defined by (testx,testy). The output fitting parameters are returned.
7
8  % Apply exclusion rule
9  if length(testx)≠1339
10     error('Exclusion rule ''%s'' is incompatible with ...
       ''%s''.','test','testx');
11 end
12 ex_ = false(length(testx),1);
13 ex_([]) = 1;
14 ex_ = ex_ | (testx ≤ 150 | testx ≥ 360);
```

```
fo_ = fitoptions('method','NonlinearLeastSquares','Lower', ...
    [Lower_bound_parameters], 'Upper',[Upper_bound_parameters], ...
    'MaxFunEvals',set,'MaxIter',set);
ok_ = isfinite(testx) & isfinite(testy);
if ¬all( ok_ )
    warning( 'GenerateMFile:IgnoringNansAndInfs', ...
        'Ignoring NaNs and Infs in data' );
end
st_ = [Initial_parameter_values];
set(fo_,'Startpoint',st_);
set(fo_,'Exclude',ex_(ok_));
% Setup model
ft_ = fittype('(p2*x+p3)+a00*(b00^2)/ (((x-c00)^2)+(b00^2))+a0*(b0^2)/ ...
    (((x-c0)^2)+(b0^2))+a1*(b1^2)/ (((x-c1)^2)+(b1^2))+a2*(b2^2)/ ...
    (((x-c2)^2)+(b2^2))+a3*(b3^2)/ (((x-c3)^2)+(b3^2))+a4*(b4^2)/ ...
    (((x-c4)^2)+(b4^2))+a5*(b5^2)/ (((x-c5)^2)+(b5^2))+a6*(b6^2)/ ...
    (((x-c6)^2)+(b6^2))+a7*(b7^2)/ (((x-c7)^2)+(b7^2))+a8*(b8^2)/ ...
    (((x-c8)^2)+(b8^2))+a9*(b9^2)/ (((x-c9)^2)+(b9^2))+a10*(b10^2)/ ...
    (((x-c10)^2)+(b10^2))+a11*(b11^2)/ ...
    (((x-c11)^2)+(b11^2))+a12*(b12^2)/ ...
    (((x-c12)^2)+(b12^2))+a13*(b13^2)/ ...
    (((x-c13)^2)+(b13^2))+a14*(b14^2)/ ...
    (((x-c14)^2)+(b14^2))+a15*(b15^2)/ (((x-c15)^2)+(b15^2))',...
    'dependent',{'y'},'independent',{'x'},...
    'coefficients',{'a0', 'a00', 'a1', 'a10', 'a11', 'a12', 'a13', ...
    'a14', 'a15', 'a2', 'a3', 'a4', 'a5', 'a6', 'a7', 'a8', 'a9', ...
    'b0', 'b00', 'b1', 'b10', 'b11', 'b12', 'b13', 'b14', 'b15', 'b2', ...
    'b3', 'b4', 'b5', 'b6', 'b7', 'b8', 'b9', 'c0', 'c00', 'c1', ...
    'c10', 'c11', 'c12', 'c13', 'c14', 'c15', 'c2', 'c3', 'c4', 'c5', ...
    'c6', 'c7', 'c8', 'c9', 'p2', 'p3'});
% Fit model
if sum(¬ex_(ok_))<2
    error('Not enough data left to fit ''%s'' after applying exclusion ...
    rule ''%s''.','fit 9','test')
else
    cf_ = fit(testx(ok_),testy(ok_),ft_,fo_);
end

%store coefficients
results=coeffvalues(cf_);
inten=results;
```

Matlab Code 4: Function to calculate convolution of modelled phonon population dynamics and pump-probe cross-correlation.

```
%Title: convolution function
%Author: J M Nesbitt
%Updated:
function y = conv_ac_fit_temp( x, x0, t2,a1,y0)
```

```
%This function calculates the product of an instantaneous exponential ...
    rise and slow decay
%and convolves this back-to-back with a predefined sech^2 autocorrelation.
%Notes:
%The autocorrelation function should be obtained from the fitting tool ...
    (cftool)
%using the relevant experimental data and then imported into this script.
%First we must set the output equal to input (for Matlab).
%Input vars:
%x  -   x values (array)
%x0 -   x offset
%t1 -   rise time
%t2 -   decay time
%a1 -   scale factor
%y0 -   y offset
y = zeros(size(x));
%Set x scale from -40ps to +40ps in 0.1 increments
for i = 1:801,
    buffx(i) = (401-i)/10;
end
%Calculate the product of an exponential rise and decay over same range
for j = 1:801,
    buffy(j) =((heaviside((buffx(j)-x0))* (exp(-(buffx(j)-x0)/t2)))+ ...
    (Heaviside(-(buffx(j)-x0))* (exp((buffx(j)-x0)/t2))));
end
%Convolve this with the autocorrelation over same range

for j = 1:801,
    for k = 1:801,
        buffp(k)=1.024* exp(-(((buffx(k)-0.03756)-buffx(j))/2.279)^2) ...
    -0.02403;
    end
    count=0;
    for k = 1:801,
        count=count+ (buffy(k)*buffp(k));
    end
    buffc(j)=a1*count;
end
%Lookup y values from x input values (for cftool)
buff = size(x);
buff2=buff(1);
for i = 1:buff,
    for j = 1:801,
        if x(i)==buffx(j),
                y(i)=y0+buffc(j);
        end
    end
end
end
```

Matlab Code 5: Numerical simulations which calculate each of the three terms in equation D.8.

```
%Title: Numerical simulations
%Author: J M Nesbitt
%Updated:

%Numerical simulations of the three terms which contribute to the
%anti-Stokes signal intensity. Performed in order to determine the
%extent to which the form of the dynamics is different in each of the ...
    three regimes.

pulse_width=2; %pulse fwhm (ps)
T_1=2; %phonon population lifetime (ps)

for i = 1:801,
    %Set x scale from -40ps to +40ps in 0.1 increments
    t(i,1) = (401-i)/10;
    %Calculate I(t) based on pulse duration
    pulse_I(i,1)=exp(-((t(i,1)^2)/(2*(pulse_width/2.35482)^2)));
    %Calculate I_ac(t) based on pulse duration
    pulse_ac(i,1)=exp(-((t(i,1)^2)/ (2*(((pulse_width*sqrt(2))/ ...
    2.35482)^2))));
end

%Calculate n(t) based on pulse duration and phonon population lifetime
n(i,1)=0;
for i = 2:801,
    n(i,1)=n(i-1,1)+(pulse_I(i-1,1));
    n(i,1)=n(i,1)-((1/T_1)*n(i-1,1)/10);
end

for i = 1:801,
    %Calculate n^2(t) based on n(t)
    n2(i,1)=n(i,1)*n(i,1);
    %Calculate n(t)*pulse_I(t) based on n(t)
    n_pulse_I(i,1)=n(i,1)*pulse_I(i,1);
end

%Convolve n(t) with pulse_I(t)
for j = 1:801,
    for k = 1:801,
        ...
    buffp(k,1)=exp(-(((t(k,1)-t(j,1))^2)/(2*(pulse_width/2.35482)^2)));
    end
    count=0;
    for k = 1:801,
        count=count+(n(k,1)*buffp(k,1));
    end
    n_convolved(j,1)=count;
```

```
45 end
46 %Convolve n^2(t) with pulse_I(t)
47 for j = 1:801,
48     for k = 1:801,
49         ...
       buffp(k,1)=exp(-(((t(k,1)-t(j,1))^2)/(2*(pulse_width/2.35482)^2)));
50     end
51     count=0;
52     for k = 1:801,
53         count=count+(n2(k,1)*buffp(k,1));
54     end
55     n2_convolved(j,1)=count;
56 end
57 %Convolve n_pulse_I(t) with n(t)
58 for j = 1:801,
59     %Calculate I(t) based on pulse duration
60     for l = 1:801,
61         pulse_Ibuff(l,1)= exp(-(((t(l,1)-t(j,1))^2)/ (2*(pulse_width/ ...
       2.35482)^2)));
62     end
63     %Calculate n(t) based on pulse duration and phonon population lifetime
64     nbuff(i,1)=0;
65     for i = 2:801,
66         nbuff(i,1)=nbuff(i-1,1)+(pulse_Ibuff(i-1,1));
67         nbuff(i,1)=nbuff(i,1)-((1/T_1)*nbuff(i-1,1)/10);
68     end
69     count=0;
70     for k = 1:801,
71         count=count+(n_pulse_I(k,1)*nbuff(k,1));
72     end
73     n_pulse_I_convolved(j,1)=count;
74 end
75 %Perform reflection on convolutions
76 for i = 1:801,
77     n_convolved_r(i,1)=n_convolved(802-i,1);
78     n2_convolved_r(i,1)=n2_convolved(802-i,1);
79     n_pulse_I_convolved_r(i,1)=n_pulse_I_convolved(802-i,1);
80 end
81 for i = 1:801,
82     n_convolved_r(i,1)=n_convolved(i,1)+n_convolved_r(i,1);
83     n2_convolved_r(i,1)=n2_convolved(i,1)+n2_convolved_r(i,1);
84     n_pulse_I_convolved_r(i,1)= n_pulse_I_convolved(i,1)+ ...
       n_pulse_I_convolved_r(i,1);
85 end
86
87 %Normalise functions
88 n_convolved_r=n_convolved_r/n_convolved_r(401,1); % n(t) conv I(t)
89 n2_convolved_r=n2_convolved_r/n2_convolved_r(401,1); % n(t)^2 conv I(t)
90 n_pulse_I_convolved_r=n_pulse_I_convolved_r/ ...
       n_pulse_I_convolved_r(401,1) ; % n(t) conv n(t)*I(t)
91
```

```
92  %Plot functions
93  plot(t,pulse_ac);
94  hold;
95  plot(t,n_convolved_r);
96  plot(t,n2_convolved_r);
97  plot(t,n_pulse_I_convolved_r);
98
99  %Lookup y values from position2 values (for cftool)
100 buff = size(position2);
101 buff2=buff(1);
102 for i = 1:buff,
103     for j = 1:801,
104         if position2(i,1)==t(j,1),
105                 y(i)=n_convolved_r(j,1);
106                 y2(i)=n2_convolved_r(j,1);
107                 y3(i)=n_pulse_I_convolved_r(j,1);
108         end
109     end
110 end
```

Appendix B

Detector System Efficiency Curves

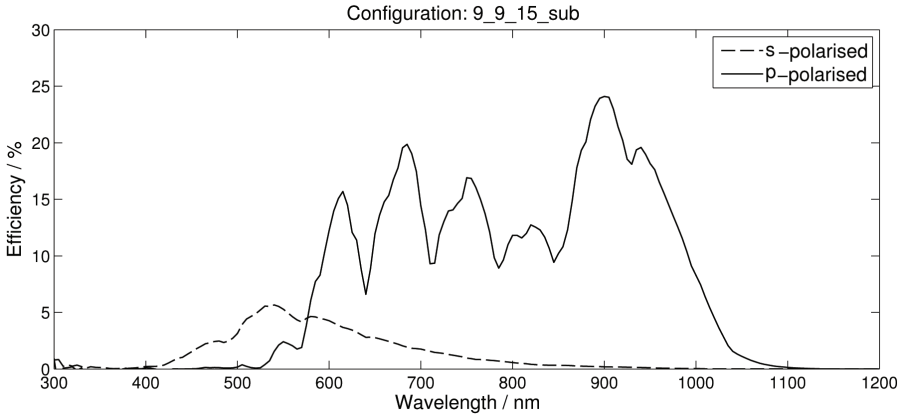

FIGURE B.1: Detector system efficiency function for 9−9−15 subtractive configuration. Calculated for both s-polarised (*dashed black line*) and p-polarised (*solid black line*) light using the technique described in Section 3.1.3.

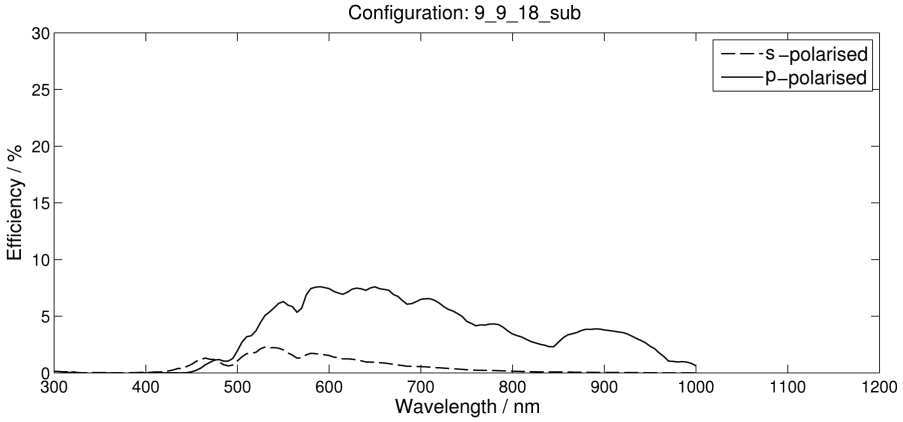

FIGURE B.2: Detector system efficiency function for 9−9−18 subtractive configuration. Calculated for both s-polarised (*dashed black line*) and p-polarised (*solid black line*) light using the technique described in Section 3.1.3.

Appendix C

Additional SWCNT Sample Details

Diameter distribution of standard purification HiPco SWCNTs provided by Carbon Nanotechnologies;

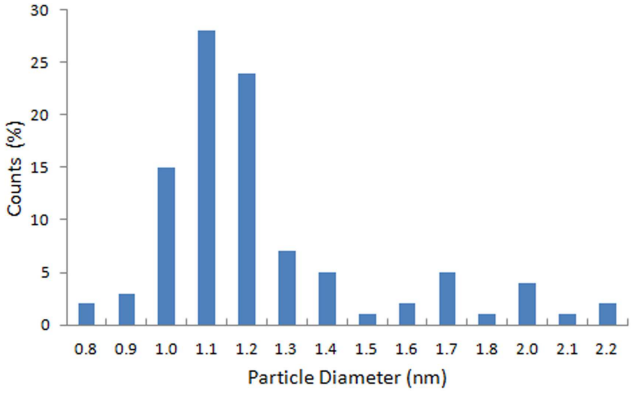

FIGURE C.1: Histogram shows data obtained from low-density dispersion AFM topographical height measurements performed for the same SWCNT batch used for the Raman measurements in this thesis. Data kindly provided by Dr G. N. Ayre.

Additional details provided by supplier;

Diameter Range	$0.8 - 2.0$ nm
Length Range	$50 - 1000$ nm
Morphology	Bundled in ropes
Catalyst Ratio	< 10 wt%
Moisture Ratio	< 5 wt%

TABLE C.1: Characterisation summary for standard purification HiPco SWCNTs.

Appendix D

Probing the Phonon Populations

Since we cannot distinguish between which pulse acts as the pump and which pulse acts as the probe in the co-polarised degenerate pump-probe TRAIRS experiment, we will label the pulses a and b. During the TRIARS experiment there are three phonon populations which exist in the SWCNTs, and which must be considered when interpreting the TRIARS measurements in this thesis,

$n_a(t)$ - the nonequilibrium phonon population generated by pulse a,

$n_b(t)$ - the nonequilibrium phonon population generated by pulse b,

$n_{\mathbf{th}}$ - the thermal population of phonons,

where the total phonon population n_T is given by

$$n_T(t) = n_a(t) + n_b(t) + n_{\mathrm{th}}. \tag{D.1}$$

All of the experimental evidence suggests that the phonon population dynamics are linear. This means that the presence of any one of the above phonon populations does not affect the dynamics of another. During a TRIARS experiment the thermal population n_{th} does not vary with time, while the nonequilibrium phonon populations follow

$$\frac{dn_{a,b}}{dt} = -\frac{1}{T_1} n_{a,b}(t) + g_{a,b}(t), \tag{D.2}$$

where T_1 is the phonon population lifetime and $g_{a,b}(t)$ is the phonon generation rate, associated with the laser pulses a and b. Thus the temporal evolution of the phonon population, $n_{a,b}(t)$, represents the phonon population dynamics convolved with the pulse intensity function, which we will define as $I_{a,b}$.

D.1 One-phonon Raman Features

During the interpretation of the one-phonon (G- and D-band) TRIARS measurements in chapters 5 and 6, the intensity dynamics obtained from fitting the anti-Stokes subtracted spectra is interpreted as "the phonon population dynamics convolved with the pulse cross-correlation.". The following is a mathematical formulation to support this assumption:

Since the phonons that are generated in a TRIARS experiment are incoherent we do not have to worry about the interference of phonons and therefore our discussion can focus on the phonon population, not amplitude. For the case of Raman scattering involving one-phonon, i.e. the G- and D-bands, the anti-Stokes signal intensity is proportional to $n_T(t)$ (Equation. 2.14). An additional complication is added because the laser pulse duration is comparable with the timescale of the phonon dynamics, i.e. $n_T(t)$ can vary within the pulse envelope. Therefore the measured anti-Stokes Raman signal intensity is given by

$$I_{AS}(t) \propto \int_{-\infty}^{+\infty} n_T(t) I_a(t)\, dt + \int_{-\infty}^{+\infty} n_T(t) I_b(t)\, dt, \tag{D.3}$$

which, substituting Eq. D.1, can be written as

$$\begin{aligned} I_{AS}(t) \propto & \int_{-\infty}^{+\infty} [n_b(t) I_a(t) + n_a(t) I_a(t) + n_{\mathrm{th}} I_a(t)]\, dt + \\ & \int_{-\infty}^{+\infty} [n_a(t) I_b(t) + n_b(t) I_b(t) + n_{\mathrm{th}} I_b(t)]\, dt. \end{aligned} \tag{D.4}$$

Note that only the first term in each integral varies with pump-probe delay. Thus the intensity in the anti-Stokes subtracted spectra simplifies to

$$I_{AS}(t) \propto \int_{-\infty}^{+\infty} [n_b(t) I_a(t) + n_a(t) I_b(t)]\, dt. \tag{D.5}$$

Equations D.2 and D.5 tell us that the time evolution of the intensity of a one-phonon Raman feature in the anti-Stokes subtracted spectra can be calculated by convolving the phonon population dynamics with the cross-correlation of pulses a and b. The two terms in equation D.5 account for the indistinguishable pump and probe pulses in the TRIARS experiments.

Additional Note: The D-band requires one inelastic scattering event (involving a phonon) and one elastic scattering event (involving a defect). Therefore, the above interpretation of the D-band phonon dynamics assumes that elastic scattering processes do not

contribute to the intensity dynamics, i.e. it assumes the rate at which the photoexcited electrons scatter from lattice defects is independent of pump-probe delay.

D.2 Two-phonon Raman Features

For Raman scattering involving two phonons the anti-Stokes signal intensity is proportional to $n_T^2(t)$. In this case the measured anti-Stokes Raman signal intensity is given by:

$$I_{AS}(t) \propto \int_{-\infty}^{+\infty} n_T^2(t) I_a(t)\, dt + \int_{-\infty}^{+\infty} n_T^2(t) I_b(t)\, dt. \tag{D.6}$$

Again, substituting Eq. D.1 this can be written as,

$$\begin{aligned} I_{AS}(t) \propto \int_{-\infty}^{+\infty} & [n_a^2(t) I_b(t) + n_b^2(t) I_b(t) + n_{\mathrm{th}}^2 I_b(t) + \\ & 2n_a(t) n_b(t) I_b(t) + 2n_a(t) n_{\mathrm{th}} I_b(t) + 2n_b(t) n_{\mathrm{th}} I_b(t)]\, dt + \\ & \int_{-\infty}^{+\infty} [n_a^2(t) I_a(t) + n_b^2(t) I_a(t) + n_{\mathrm{th}}^2 I_a(t) + \\ & 2n_a(t) n_b(t) I_a(t) + 2n_a(t) n_{\mathrm{th}} I_a(t) + 2n_b(t) n_{\mathrm{th}} I_a(t)]\, dt. \end{aligned} \tag{D.7}$$

Note that there are three terms in each integral which vary with pump-probe delay. Thus the intensity in the anti-Stokes subtracted spectra simplifies to

$$\begin{aligned} I_{AS}(t) \propto & \int_{-\infty}^{+\infty} [n_a^2(t) I_b(t) + n_b^2(t) I_a(t)]\, dt + \\ & \int_{-\infty}^{+\infty} 2[n_a(t) n_b(t) I_b(t) + n_b(t) n_a(t) I_a(t)]\, dt + \\ & \int_{-\infty}^{+\infty} 2[n_a(t) n_{\mathrm{th}} I_b(t) + n_b(t) n_{\mathrm{th}} I_a(t)]\, dt. \end{aligned} \tag{D.8}$$

Each of the three terms (for pulses a and b) contribute to the intensity dynamics in a subtly different manner. The first term is quadratic in n_a (or n_b) and is calculated by convolving the square of time evolution of the phonon population generated by pulse a (or b) with the intensity function of pulse b (or a), $n_{a,b}^2(t) * I_{b,a}$. The second term is calculated by convolving the time evolution of the phonon population generated by pulse a (or b) with the product of the intensity function of pulse b (or a) and the time evolution of the phonon population generated by pulse b (or a), $n_{a,b}(t) * n_{b,a}(t) \times I_{b,a}$. Whilst the final term

behaves in a similar manor to the linear one-phonon case described in section D.1 and is calculated by convolving the time evolution of the phonon population n_a (or n_b) with the product of the intensity function of pulse b (or a) and the time independent thermal population, $n_{a,b}(t) * n_{\mathrm{th}}(t) \times I_{b,a}$. The terms which are dominant in the measurements will govern the form of the measured intensity dynamics. As the two pulses are equal in the experiments, the contributions from $n^2_{a,b}(t) * I_{b,a}$ and $n_{a,b}(t) * n_{b,a}(t) \times I_{b,a}$ are always equal. This means that there are two possible regimes for the measurements; a linear regime where the intensity dynamics are expected to be the same as for a one-phonon Raman feature and a quadratic regime where the intensity dynamics are expected to be of a different form.

In order to determine which regime we are in we can consider the background ($t_{delay} = 25ps$) to zero delay ($t_{delay} = 0ps$) intensity ratio that would be expected for the quadratic and linear terms. If the quadratic term dominates it can be shown that this ratio will be approximately 1 : 4 while for the case that the linear terms dominate the ratio will be nearer to 1 : 1. Table D.1 shows the G'-band background to zero delay intensity ratios obtained from figures 6.9 and 6.10. In the low temperature limit the intensity ratios suggest that the measurements are somewhere between the quadratic regime and the linear regime, while in the high temperature limit the ratios suggest that the measurements are in linear regime. This effect could be caused by the linear term which is dependent on n_{th}, whose contribution is expected to increase with temperature. However, the spectra in figures 6.9 and 6.10 also contain a time-independent contribution from the thermal equilibrium phonon population, n_{th}. Furthermore, the background intensity may also contain contributions due to the outgoing resonance of SWCNT species which do not contribute to the time-dependent signal (see Section 4.3.2). This means that the high temperature ($T = 292$K) ratios given in table D.1 are likely to be an underestimate of the true intensity ratios. Thus it is also possible that the G-band TRIARS measurements are in the quadratic regime, or remain somewhere between the quadratic regime and the linear regime for all of the G'-band measurements.

$E_{\mathrm{L}} = 1.51$ eV		$E_{\mathrm{L}} = 1.63$ eV	
$T = 4$ K	$T = 292$ K	$T = 4$ K	$T = 292$ K
1 : 3.0	1 : 1.8	1 : 3.0	1 : 1.4

TABLE D.1: G'-band background to zero delay intensity ratios obtained from figures 6.9 and 6.10

Numerical simulations have been performed to allow us to understand the form each of the three terms in equation D.8. The Matlab code for these simulations is provided in Appendix A Matlab Code 5. In each case the simulations assume the phonon rise dynamics to be instantaneous and to follow a monoexponential decay on a timescale of T_1. The pulse durations are taken to be 2ps (representative of the experimental pulse durations). Figures D.1 (a)-(d) show the results from numerical simulations performed

for four values of T_1 for a range which covers the form of the measured G'-band intensity dynamics.

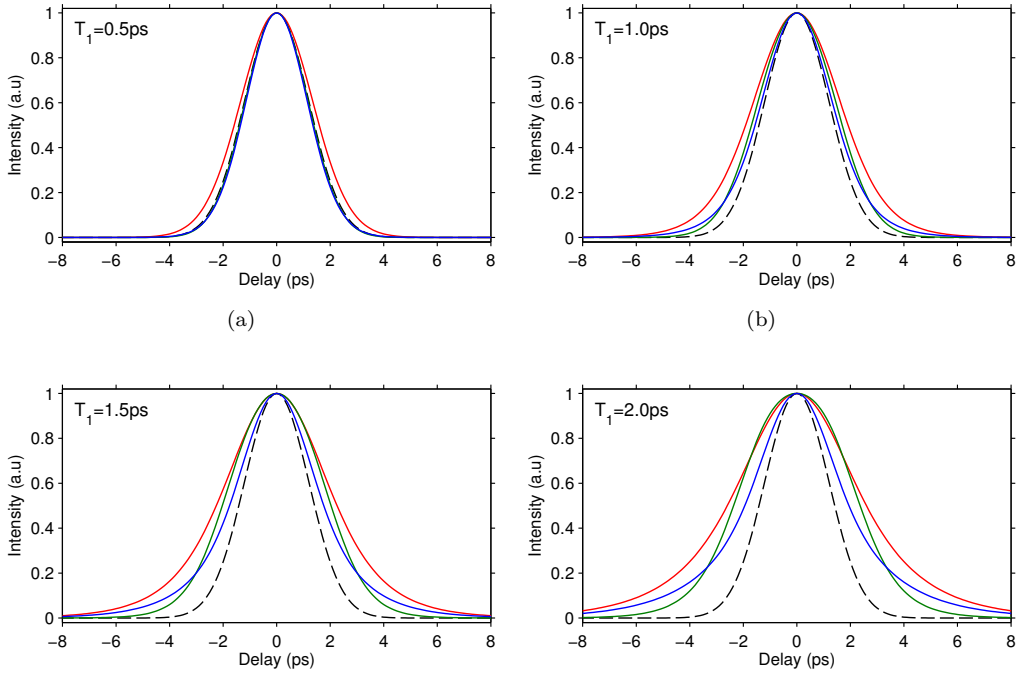

FIGURE D.1: Numerical simulations of the three terms, $n_{a,b}(t) * n_{\mathrm{th}}(t) \times I_{b,a}$ (*solid red line*), $n^2_{a,b}(t) * I_{b,a}$ (*solid green line*), and $n_{a,b}(t) * n_{b,a}(t) \times I_{b,a}$ (*solid blue line*), which contribute to the intensity of the subtracted G'-band spectra. Performed for (a) $T_1 = 0.5$ps, (b) $T_1 = 1.0$ps, (c) $T_1 = 1.5$ps and (d) $T_1 = 2.0$ps. Also shown are the cross-correlations (*broken black line*).

The results from the simulations show a significant difference in the intensity dynamics depending on which term is dominant. Let us look more closely at the case for $T_1 = 2.0$ps, where the difference in the intensity dynamics due to each of the terms is greatest. The upper plot in figure D.2 shows the intensity dynamics calculated from the simulations for $T_1 = 2.0$ps for the linear (*solid red line*) and quadratic regimes (*solid grey line*), where the quadratic regime dynamics is calculated from the mean of the $n^2_{a,b}(t) * I_{b,a}$ and $n_{a,b}(t) * n_{b,a}(t) \times I_{b,a}$ terms (because their contributions are always equal). The simulated dynamics have been fitted (*broken coloured lines*) with the same fitting function used to obtain T_1 from the G- and D-band TRIARS intensity dynamics (the convolution of the functions given in equations 5.4 and 5.1 for the case of 2ps pulses). The lower plots in figure D.2 show the residuals for the fits. In both regimes the residuals of the fits have a similar form and are less than 1% of the signal. Meanwhile, the residuals for the fits to the experimentally obtained G'-band intensity dynamics are approximately 10% of the signal and appear randomly distributed about the fit for both low and high temperature measurements. This means that it is not possible to determine which regime the measurements are in by comparing the residuals of the fits to the experimentally obtained G'-band intensity dynamics. The simplest function (based on monoexponential

decay) is used to fit the experimental intensity dynamics. However, one must be aware that the fitted lifetime T_1 may not be correct if the measurements are dominated by the quadratic regime. For example, the fits to the simulated dynamics for $T_1 = 2.0$ps, shown in figure D.2, predict $T_1 = 2.062$ps and $T_1 = 1.3675$ps for the linear and quadratic regimes respectively.

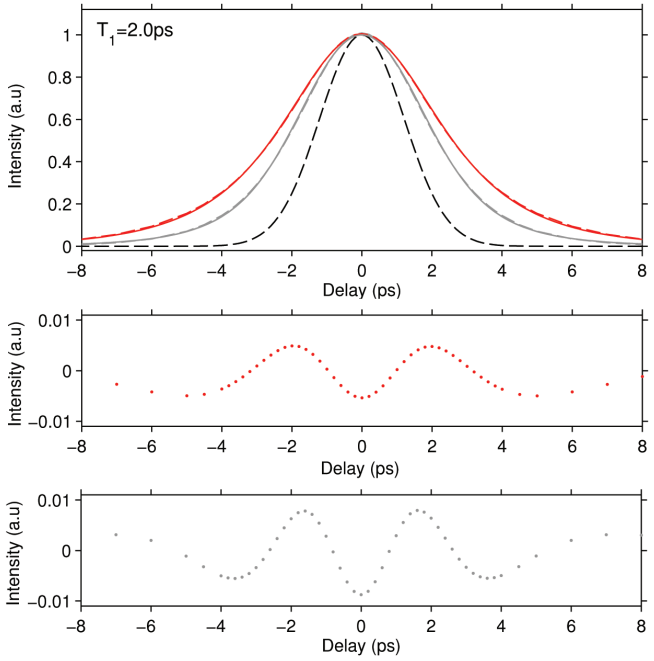

FIGURE D.2: Upper plot: shows the $T_1 = 2.0$ps intensity dynamics calculated from the simulations for the linear (*solid red line*) and quadratic regimes (*solid grey line*), where the quadratic regime dynamics is calculated from the mean of the $n^2_{a,b}(t) * I_{b,a}$ and $n_{a,b}(t) * n_{b,a}(t) \times I_{b,a}$ dynamics. The dynamics have been fitted (*broken coloured lines*) with the convolution of the functions given in equations 5.4 and 5.1). Lower plots: show the residuals for the fits.

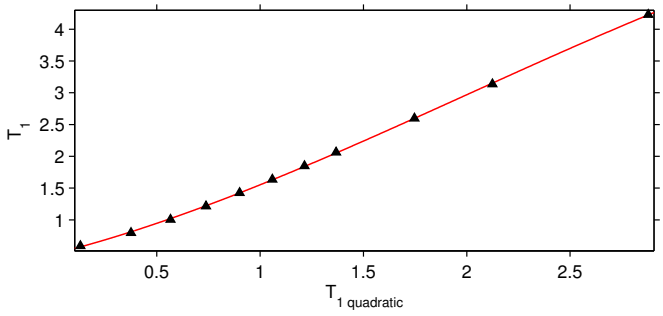

FIGURE D.3: Population lifetime values which were obtained for fitting the simulations in the quadratic regime, $T_{1quadratic}$, plotted against the phonon population lifetime T_1 which was input into the simulation. The data points have been fitted with equation D.9 which can be used to convert the underestimated $T_{1quadratic}$ into the phonon population lifetime T_1

For the case that the experimental measurements are in the linear regime the fitted T_1 will be a correct measurement of the phonon population lifetime. However, for the case that the experimental measurements in the quadratic regime the fitted T_1 will be an underestimate of the phonon population lifetime. To calculate a conversion function for the case where the measurements are in the quadratic regime the above process was repeated for various T_1 input values. Figure D.3 shows the population lifetime values which were obtained for fitting the simulations in the quadratic regime, $T_{1quadratic}$, plotted against the input phonon population lifetime T_1. The conversion function, obtained from fitting the data points in figure D.3, is provided in equation D.9. When the experimental measurements are believed to be in the quadratic regime, this function can be used to convert the underestimated $T_{1quadratic}$ into the phonon population lifetime T_1.

$$T_1 = -0.05452T_{1quadratic}^3 + 0.3274T_{1quadratic}^2 + 0.8164T_{1quadratic} + 0.4626. \quad \text{(D.9)}$$

References

[1] G. Samsonidze, R. Saito, A. Jorio, M. Pimenta, A. Souza Filho, A. Gruneis, G. Dresselhaus, and M. Dresselhaus, "The concept of cutting lines in carbon nanotube science," *Journal of Nanoscience and Nanotechnology*, vol. 3, no. 6, pp. 431–458, 2003.

[2] A. C. Ferrari, J. C. Meyer, V. Scardaci, C. Casiraghi, M. Lazzeri, F. Mauri, S. Piscanec, D. Jiang, K. S. Novoselov, S. Roth, and A. K. Geim, "Raman spectrum of graphene and graphene layers," *Phys. Rev. Lett.*, vol. 97, p. 187401, Oct 2006.

[3] V. N. Popov and P. Lambin, "Radius and chirality dependence of the radial breathing mode and the g-band phonon modes of single-walled carbon nanotubes," *Phys. Rev. B*, vol. 73, p. 085407, Feb 2006.

[4] R. B. Weisman and S. M. Bachilo, "Dependence of optical transition energies on structure for single-walled carbon nanotubes in aqueous suspension: An empirical kataura plot," *Nano Letters*, vol. 3, no. 9, pp. 1235–1238, 2003.

[5] A. Jorio, A. G. Souza Filho, G. Dresselhaus, M. S. Dresselhaus, A. K. Swan, M. S. Ünlü, B. B. Goldberg, M. A. Pimenta, J. H. Hafner, C. M. Lieber, and R. Saito, "g-band resonant raman study of 62 isolated single-wall carbon nanotubes," *Phys. Rev. B*, vol. 65, p. 155412, Mar 2002.

[6] K. Kang, T. Ozel, D. G. Cahill, and M. Shim, "Optical phonon lifetimes in single-walled carbon nanotubes by time-resolved raman scattering," *Nano Letters*, vol. 8, no. 12, pp. 4642–4647, 2008.

[7] N. Bonini, M. Lazzeri, N. Marzari, and F. Mauri, "Phonon anharmonicities in graphite and graphene," *Phys. Rev. Lett.*, vol. 99, p. 176802, Oct 2007.

[8] H. Pierson, *Handbook of carbon, graphite, diamond, and fullerenes: properties, processing, and applications*. Materials science and process technology series, William Andrew, Incorporated, 1993.

[9] H. W. Kroto, J. R. Heath, S. C. O'Brien, R. F. Curl, and R. E. Smalley, "C60: Buckminsterfullerene," *Nature*, vol. 318, pp. 162–163, Nov. 1985.

[10] S. Iijima, "Helical microtubules of graphitic carbon," *Nature*, vol. 354, pp. 56–58, Nov. 1991.

[11] A. K. Geim, K. S. Novoselov, S. V. Morozov, D. Jiang, M. I. Katsnelson, I. V. Grigorieva, S. V. Dubonos, and A. A. Firsov, "Two-dimensional gas of massless dirac fermions in graphene," *Nature*, vol. 306, pp. 197–200, 2005.

[12] M. S. Dresselhaus, G. Dresselhaus, and P. C. Eklund, *Science of Fullerenes and Carbon Nanotubes*. Academic Press, 1996.

[13] M. S. Dresselhaus and P. C. Eklund, "Phonons in carbon nanotubes," *ADVANCES IN PHYSICS*, vol. 49, pp. 705–814, 2000.

[14] W. Marx and A. Barth, *Carbon Nanotubes*, ch. I - Carbon Nanotubes, A Scientometric Study, pp. 1–19. In-Tech, 2010.

[15] M.-F. Yu, O. Lourie, M. J. Dyer, K. Moloni, T. F. Kelly, and R. S. Ruoff, "Strength and breaking mechanism of multiwalled carbon nanotubes under tensile load," *Science*, vol. 287, no. 5453, pp. 637–640, 2000.

[16] E. Pop, D. Mann, Q. Wang, K. Goodson, and H. Dai, "Thermal conductance of an individual single-wall carbon nanotube above room temperature," *Nano Letters*, vol. 6, no. 1, pp. 96–100, 2006.

[17] M. Dresselhaus, G. Dresselhaus, and P. Avouris, *Carbon Nanotubes: Synthesis, Structure, Properties, and Applications*. Topics in applied physics, v. 80, Springer-Verlag GmbH, 2001.

[18] A. Bianco, K. Kostarelos, and M. Prato, "Applications of carbon nanotubes in drug delivery," *Current Opinion in Chemical Biology*, vol. 9, no. 6, pp. 674 – 679, 2005. ¡ce:title¿Biopolymers / Model systems¡/ce:title¿.

[19] N. W. S. Kam, M. O'Connell, J. A. Wisdom, and H. Dai, "Carbon nanotubes as multifunctional biological transporters and near-infrared agents for selective cancer cell destruction," *Proceedings of the National Academy of Sciences of the United States of America*, vol. 102, no. 33, pp. 11600–11605, 2005.

[20] Z. Liu, K. Chen, C. Davis, S. Sherlock, Q. Cao, X. Chen, and H. Dai, "Drug delivery with carbon nanotubes for in vivo cancer treatment," *Cancer Research*, vol. 68, no. 16, pp. 6652–6660, 2008.

[21] J. Wang, "Carbon-Nanotube Based Electrochemical Biosensors: A Review," *Electroanalysis*, vol. 17, no. 1, pp. 7–14, 2005.

[22] M. P. Anantram and F. Leonard, "Physics of carbon nanotube electronic devices," *Reports on Progress in Physics*, vol. 69, no. 3, p. 507, 2006.

[23] A. Javey, J. Guo, Q. Wang, M. Lundstrom, and H. Dai, "Ballistic carbon nanotube field-effect transistors," *Nature*, vol. 424, no. 6949, pp. 654–657, 2003.

[24] C. T. White and T. N. Todorov, "Carbon nanotubes as long ballistic conductors," *Nature*, vol. 393, p. 241, 1998.

[25] W. Zhu, C. Bower, O. Zhou, G. Kochanski, and S. Jin, "Large current density from carbon nanotube field emitters," *Applied Physics Letters*, vol. 75, no. 6, pp. 873–875, 1999.

[26] B. Wei, R. Vajtai, and P. M. Ajayan, "Reliability and current carrying capacity of carbon nanotubes," *Applied Physics Letters*, vol. 79, no. 8, pp. 1172–1174, 2001.

[27] M. Burghard, H. Klauk, and K. Kern, "Carbon-based field-effect transistors for nanoelectronics," *Advanced Materials*, vol. 21, no. 25-26, pp. 2586–2600, 2009.

[28] R. H. Baughman, A. A. Zakhidov, and W. A. de Heer, "Carbon nanotubes–the route toward applications," *Science*, vol. 297, no. 5582, pp. 787–792, 2002.

[29] G. Pennington and N. Goldsman, "Low-field semiclassical carrier transport in semiconducting carbon nanotubes," *Phys. Rev. B*, vol. 71, p. 205318, May 2005.

[30] V. Perebeinos, J. Tersoff, and P. Avouris, "Electron-phonon interaction and transport in semiconducting carbon nanotubes," *Phys. Rev. Lett.*, vol. 94, p. 086802, Mar 2005.

[31] A. Javey, J. Guo, M. Paulsson, Q. Wang, D. Mann, M. Lundstrom, and H. Dai, "High-field quasiballistic transport in short carbon nanotubes," *Phys. Rev. Lett.*, vol. 92, p. 106804, Mar 2004.

[32] Z. Yao, C. L. Kane, and C. Dekker, "High-field electrical transport in single-wall carbon nanotubes," *Phys. Rev. Lett.*, vol. 84, pp. 2941–2944, Mar 2000.

[33] M. Lazzeri, S. Piscanec, F. Mauri, A. C. Ferrari, and J. Robertson, "Electron transport and hot phonons in carbon nanotubes," *Phys. Rev. Lett.*, vol. 95, p. 236802, Nov 2005.

[34] M. Lazzeri and F. Mauri, "Coupled dynamics of electrons and phonons in metallic nanotubes: Current saturation from hot-phonon generation," *Phys. Rev. B*, vol. 73, p. 165419, Apr 2006.

[35] J.-Y. Park, S. Rosenblatt, Y. Yaish, V. Sazonova, H. stnel, S. Braig, T. A. Arias, P. W. Brouwer, and P. L. McEuen, "Electronphonon scattering in metallic single-walled carbon nanotubes," *Nano Letters*, vol. 4, no. 3, pp. 517–520, 2004.

[36] M. Oron-Carl and R. Krupke, "Raman spectroscopic evidence for hot-phonon generation in electrically biased carbon nanotubes," *Phys. Rev. Lett.*, vol. 100, p. 127401, Mar 2008.

[37] M. Dresselhaus, G. Dresselhaus, R. Saito, and A. Jorio, "Raman spectroscopy of carbon nanotubes," *Physics Reports*, vol. 409, no. 2, pp. 47 – 99, 2005.

[38] I. Jo, I.-K. Hsu, Y. J. Lee, M. M. Sadeghi, S. Kim, S. Cronin, E. Tutuc, S. K. Banerjee, Z. Yao, and L. Shi, "Low-frequency acoustic phonon temperature distribution in electrically biased graphene," *Nano Letters*, vol. 11, no. 1, pp. 85–90, 2011.

[39] E. Pop, D. Mann, J. Cao, Q. Wang, K. Goodson, and H. Dai, "Negative differential conductance and hot phonons in suspended nanotube molecular wires," *Phys. Rev. Lett.*, vol. 95, p. 155505, Oct 2005.

[40] I. Chatzakis, H. Yan, D. Song, S. Berciaud, and T. F. Heinz, "Temperature dependence of the anharmonic decay of optical phonons in carbon nanotubes and graphite," *Phys. Rev. B*, vol. 83, p. 205411, May 2011.

[41] S. Berciaud, M. Y. Han, K. F. Mak, L. E. Brus, P. Kim, and T. F. Heinz, "Electron and optical phonon temperatures in electrically biased graphene," *Phys. Rev. Lett.*, vol. 104, p. 227401, Jun 2010.

[42] D. Mann, E. Pop, J. Cao, Q. Wang, and K. a. Goodson, "Thermally and molecularly stimulated relaxation of hot phonons in suspended carbon nanotubes," *The Journal of Physical Chemistry B*, vol. 110, no. 4, pp. 1502–1505, 2006.

[43] A. Petrov and S. Rotkin, "Energy relaxation of hot carriers in single-wall carbon nanotubes by surface optical phonons of the substrate," *JETP Letters*, vol. 84, no. 3, pp. 156–160, 2006.

[44] J. Svensson, N. Lindahl, H. Yun, M. Seo, D. Midtvedt, Y. Tarakanov, N. Lindvall, O. Nerushev, J. Kinaret, S. Lee, and E. E. B. Campbell, "Carbon nanotube field effect transistors with suspended graphene gates," *Nano Letters*, vol. 11, no. 9, pp. 3569–3575, 2011.

[45] A. Naeemi and J. D. Meindl, "Carbon nanotube interconnects," *Annual Review of Materials Research*, vol. 39, no. 1, pp. 255–275, 2009.

[46] A. A. Rashid Nizam, S. Mahdi A. Rizvi, "Calculating electronic structure of different carbon nanotubes and its affect on band gap," *International Journal of Science and Technology*, vol. 1, pp. 153–162, 2011.

[47] R. Saito, *Physical Properties of Carbon Nanotubes. R. Saito, S. Dresselhaus & M.S. Dresselhaus.* World Scientific Publishing Company, 2003.

[48] H. Kataura, Y. Kumazawa, Y. Maniwa, I. Umezu, S. Suzuki, Y. Ohtsuka, and Y. Achiba, "Optical Properties of Single-Wall Carbon Nanotubes," *Synth. Metals*, vol. 103, p. 2555, 1999.

[49] A. Jorio, A. G. Souza Filho, G. Dresselhaus, M. S. Dresselhaus, R. Saito, J. H. Hafner, C. M. Lieber, F. M. Matinaga, M. S. S. Dantas, and M. A. Pimenta, "Joint density of electronic states for one isolated single-wall carbon nanotube studied by resonant raman scattering," *Phys. Rev. B*, vol. 63, p. 245416, Jun 2001.

[50] M. Machon, S. Reich, and C. Thomsen, "Strong electron-phonon coupling of the high-energy modes of carbon nanotubes," *Physical Review B*, vol. 74, Nov. 2006.

[51] H. Myers, *Introductory Solid State Physics*. Taylor & Francis Group, 1997.

[52] A. M. Rao, E. Richter, S. Bandow, P. C. Eklund, K. A. Williams, S. Fang, K. R. Subbaswamy, M. Menon, A. Thess, R. E. Smalley, G. Dresselhaus, and M. S. Dresselhaus, "Diameter-Selective Raman Scattering from Vibrational Modes in Carbon Nanotubes ," *Science*, vol. 275, p. 187, 1997.

[53] M. S. Dresselhaus, A. Jorio, A. G. S. Filho, G. Dresselhaus, and R. Saito, "Raman Spectroscopy on One Isolated Carbon Nanotube," *Physica B*, vol. 323, p. 15, 2002.

[54] Y. J. Lee, S. H. Parekh, J. A. Fagan, and M. T. Cicerone, "Phonon dephasing and population decay dynamics of the g-band of semiconducting single-wall carbon nanotubes," *Phys. Rev. B*, vol. 82, p. 165432, Oct 2010.

[55] D. Song, F. Wang, G. Dukovic, M. Zheng, E. Semke, L. Brus, and T. Heinz, "Direct measurement of the lifetime of optical phonons in single-walled carbon nanotubes.," *Phys Rev Lett*, vol. 100, p. 225503, June 2008.

[56] M. Cardona, *Light Scattering in Solids I: Introductory Concepts*. Springer-Verlag Berlin and Heidelberg GmbH & Co. K; 2nd Revised Edition, 1983.

[57] O. E. Alon, "Number of raman- and infrared-active vibrations in single-walled carbon nanotubes," *Phys. Rev. B*, vol. 63, p. 201403, May 2001.

[58] Q. Cheng, S. Debnath, E. Gregan, and H. Byrne, "Vibrational mode assignments for bundled single-wall carbon nanotubes using raman spectroscopy at different excitation energies," *Applied Physics A*, vol. 102, no. 2, pp. 309–317, 2011.

[59] M. S. Strano, S. K. Doorn, E. H. Haroz, C. Kittrell, R. H. Hauge, and R. E. Smalley, "Assignment of (n, m) raman and optical features of metallic single-walled carbon nanotubes," *Nano Letters*, vol. 3, no. 8, pp. 1091–1096, 2003.

[60] J. Maultzsch, H. Telg, S. Reich, and C. Thomsen, "Radial breathing mode of single-walled carbon nanotubes: Optical transition energies and chiral-index assignment," *Phys. Rev. B*, vol. 72, p. 205438, Nov 2005.

[61] A. Jorio, M. A. Pimenta, A. G. S. Filho, R. Saito, G. Dresselhaus, and M. S. Dresselhaus, "Characterizing carbon nanotube samples with resonance raman scattering," *New Journal of Physics*, vol. 5, no. 1, p. 139, 2003.

[62] C. Jiang, K. Kempa, J. Zhao, U. Schlecht, U. Kolb, T. Basché, M. Burghard, and A. Mews, "Strong enhancement of the breit-wigner-fano raman line in carbon nanotube bundles caused by plasmon band formation," *Phys. Rev. B*, vol. 66, p. 161404, Oct 2002.

[63] C. Thomsen and S. Reich, "Double resonant raman scattering in graphite," *Phys. Rev. Lett.*, vol. 85, pp. 5214–5217, Dec 2000.

[64] A. Jorio, M. S. Dresselhaus, R. Saito, and G. Dresselhaus, *Raman spectroscopy in graphene related systems*. Wiley-VCH, Jan. 2011.

[65] A. Jorio, C. Fantini, M. S. S. Dantas, M. A. Pimenta, A. G. S. Filho, G. G. Samsonidze, V. W. Brar, G. Dresselhaus, M. S. Dresselhaus, A. K. Swan, M. S. Ünlü, B. B. Goldberg, and R. Saito, "Linewidth of the Raman Features of Individual Single-Wall Carbon Nanotubes," *Phys. Rev. B.*, vol. 66, p. 115411, 2002.

[66] C. Auer, F. Schürrer, and C. Ertler, "Hot phonon effects on the high-field transport in metallic carbon nanotubes," *Phys. Rev. B*, vol. 74, p. 165409, Oct 2006.

[67] K. Ikeda and K. Uosaki, "Coherent phonon dynamics in single-walled carbon nanotubes studied by time-frequency two-dimensional coherent anti-stokes raman scattering spectroscopy," *Nano Letters*, vol. 9, no. 4, pp. 1378–1381, 2009.

[68] D. Vanden Bout, L. J. Muller, and M. Berg, "Ultrafast raman echoes in liquid acetonitrile," *Phys. Rev. Lett.*, vol. 67, pp. 3700–3703, Dec 1991.

[69] R. F. Loring and S. Mukamel, "Selectivity in coherent transient raman measurements of vibrational dephasing in liquids," *The Journal of Chemical Physics*, vol. 83, no. 5, pp. 2116–2128, 1985.

[70] A. H. Castro Neto and F. Guinea, "Electron-phonon coupling and raman spectroscopy in graphene," *Phys. Rev. B*, vol. 75, p. 045404, Jan 2007.

[71] M. Lazzeri, S. Piscanec, F. Mauri, A. C. Ferrari, and J. Robertson, "Phonon linewidths and electron-phonon coupling in graphite and nanotubes," *Phys. Rev. B*, vol. 73, p. 155426, Apr 2006.

[72] J. Hone, M. Whitney, C. Piskoti, and A. Zettl, "Thermal conductivity of single-walled carbon nanotubes," *Phys. Rev. B*, vol. 59, pp. R2514–R2516, Jan 1999.

[73] B. Ridley, *Quantum Processes in Semiconductors*. Oxford science publications, OUP Oxford, 1999.

[74] S. Schmitt-Rink, D. A. B. Miller, and D. S. Chemla, "Theory of the linear and nonlinear optical properties of semiconductor microcrystallites," *Phys. Rev. B*, vol. 35, pp. 8113–8125, May 1987.

[75] J. J. Shiang, S. H. Risbud, and A. P. Alivisatos, "Resonance raman studies of the ground and lowest electronic excited state in cds nanocrystals," *The Journal of Chemical Physics*, vol. 98, no. 11, pp. 8432–8442, 1993.

[76] V. M. Fomin, V. N. Gladilin, J. T. Devreese, E. P. Pokatilov, S. N. Balaban, and S. N. Klimin, "Photoluminescence of spherical quantum dots," *Phys. Rev. B*, vol. 57, pp. 2415–2425, Jan 1998.

[77] S. Nomura and T. Kobayashi, "Exciton lo-phonon couplings in spherical semiconductor microcrystallites," *Phys. Rev. B*, vol. 45, pp. 1305–1316, Jan 1992.

[78] D. C. Smith, *Measurements of Ultrafast Dynamics in a Superconductor and a Semiconductor*. PhD thesis, University of Oxford, 1998.

[79] F. Wang, G. Dukovic, E. Knoesel, L. E. Brus, and T. F. Heinz, "Observation of rapid auger recombination in optically excited semiconducting carbon nanotubes," *Phys. Rev. B*, vol. 70, p. 241403, Dec 2004.

[80] C. H. Lui, K. F. Mak, J. Shan, and T. F. Heinz, "Ultrafast photoluminescence from graphene," *Phys. Rev. Lett.*, vol. 105, p. 127404, Sep 2010.

[81] M. Breusing, C. Ropers, and T. Elsaesser, "Ultrafast carrier dynamics in graphite," *Phys. Rev. Lett.*, vol. 102, p. 086809, Feb 2009.

[82] F. Wang, Y. Wu, M. S. Hybertsen, and T. F. Heinz, "Auger recombination of excitons in one-dimensional systems," *Phys. Rev. B*, vol. 73, p. 245424, Jun 2006.

[83] S. Berger, C. Voisin, G. Cassabois, C. Delalande, P. Roussignol, and X. Marie, "Temperature dependence of exciton recombination in semiconducting single-wall carbon nanotubes," *Nano Letters*, vol. 7, no. 2, pp. 398–402, 2007.

[84] G. Pennington, N. Goldsman, A. Akturk, and A. E. Wickenden, "Deformation potential carrier-phonon scattering in semiconducting carbon nanotube transistors," *Applied Physics Letters*, vol. 90, no. 6, p. 062110, 2007.

[85] Y.-Z. Ma, J. Stenger, J. Zimmermann, S. M. Bachilo, R. E. Smalley, R. B. Weisman, and G. R. Fleming, "Ultrafast carrier dynamics in single-walled carbon nanotubes probed by femtosecond spectroscopy," *The Journal of Chemical Physics*, vol. 120, no. 7, pp. 3368–3373, 2004.

[86] G. Srivastava, *The Physics of Phonons*. Adam Hilger, 1990.

[87] J. Menendez and M. Cardona, "Temperature dependence of the first-order raman scattering by phonons in si, ge, and α-sn: Anharmonic effects," *Phys. Rev. B*, vol. 29, pp. 2051–2059, Feb 1984.

[88] P. Aynajian, "Phonons and their interactions," in *Electron-Phonon Interaction in Conventional and Unconventional Superconductors*, Springer Theses, pp. 7–13, Springer Berlin Heidelberg, 2011.

[89] F. Wang, G. Dukovic, L. E. Brus, and T. F. Heinz, "The optical resonances in carbon nanotubes arise from excitons," *Science*, vol. 308, no. 5723, pp. 838–841, 2005.

[90] C. D. Spataru, S. Ismail-Beigi, L. X. Benedict, and S. G. Louie, "Excitonic effects and optical spectra of single-walled carbon nanotubes," *Phys. Rev. Lett.*, vol. 92, p. 077402, Feb 2004.

[91] T. G. Pedersen, "Variational approach to excitons in carbon nanotubes," *Phys. Rev. B*, vol. 67, p. 073401, Feb 2003.

[92] V. Perebeinos, J. Tersoff, and P. Avouris, "Scaling of excitons in carbon nanotubes," *Phys. Rev. Lett.*, vol. 92, p. 257402, Jun 2004.

[93] E. Chang, G. Bussi, A. Ruini, and E. Molinari, "Excitons in carbon nanotubes: An *Ab Initio* symmetry-based approach," *Phys. Rev. Lett.*, vol. 92, p. 196401, May 2004.

[94] A. Siegman, *Lasers*. Univ. Science Books, 1986.

[95] O. Svelto, *Principles of Lasers*. Springer, 2010.

[96] T. Brabec, C. Spielmann, P. F. Curley, and F. Krausz, "Kerr lens mode locking," *Opt. Lett.*, vol. 17, pp. 1292–1294, Sep 1992.

[97] J.-C. M. Diels, J. J. Fontaine, I. C. McMichael, and F. Simoni, "Control and measurement of ultrashort pulse shapes (in amplitude and phase) with femtosecond accuracy," *Appl. Opt.*, vol. 24, pp. 1270–1282, May 1985.

[98] O. Optics, *Radiometric Calibration Standards*. Ocean Optics, Inc, 2010.

[99] P. V. Huong, R. Cavagnat, P. M. Ajayan, and O. Stephan, "Temperature-dependent vibrational spectra of carbon nanotubes," *Phys. Rev. B*, vol. 51, pp. 10048–10051, Apr 1995.

[100] M. Dresselhaus, G. Dresselhaus, A. Jorio, A. S. Filho, and R. Saito, "Raman spectroscopy on isolated single wall carbon nanotubes," *Carbon*, vol. 40, no. 12, pp. 2043 – 2061, 2002.

[101] A. Romero, H. Jeschke, A. Rubio, and M. Garcia, "Atomistic simulation of the laser induced damage in single wall carbon nanotubes: Diameter and chirality dependence," *Applied Physics A*, vol. 79, no. 4-6, pp. 899–901, 2004.

[102] A. H. Romero, M. E. Garcia, F. Valencia, H. Terrones, M. Terrones, and H. O. Jeschke, "Femtosecond laser nanosurgery of defects in carbon nanotubes," *Nano Letters*, vol. 5, no. 7, pp. 1361–1365, 2005.

[103] S. Berber, Y.-K. Kwon, and D. Tománek, "Unusually high thermal conductivity of carbon nanotubes," *Phys. Rev. Lett.*, vol. 84, pp. 4613–4616, May 2000.

[104] D. von der Linde, J. Kuhl, and H. Klingenberg, "Raman scattering from nonequilibrium lo phonons with picosecond resolution," *Phys. Rev. Lett.*, vol. 44, pp. 1505–1508, Jun 1980.

[105] K. Kang, Y. K. Koh, C. Chiritescu, X. Zheng, and D. G. Cahill, "Two-tint pump-probe measurements using a femtosecond laser oscillator and sharp-edged optical filters," *Review of Scientific Instruments*, vol. 79, no. 11, p. 114901, 2008.

[106] H. Okamoto, T. Nakabayashi, and M. Tasumi, "Incoherent time-resolved pump-probe raman spectroscopy," *The Journal of Physical Chemistry*, vol. 97, no. 39, pp. 9871–9873, 1993.

[107] C. Fantini, A. Jorio, M. Souza, M. S. Strano, M. S. Dresselhaus, and M. A. Pimenta, "Optical transition energies for carbon nanotubes from resonant raman spectroscopy: Environment and temperature effects," *Phys. Rev. Lett.*, vol. 93, p. 147406, Sep 2004.

[108] S. B. Cronin, Y. Yin, A. Walsh, R. B. Capaz, A. Stolyarov, P. Tangney, M. L. Cohen, S. G. Louie, A. K. Swan, M. S. Ünlü, B. B. Goldberg, and M. Tinkham, "Temperature dependence of the optical transition energies of carbon nanotubes: The role of electron-phonon coupling and thermal expansion," *Phys. Rev. Lett.*, vol. 96, p. 127403, Mar 2006.

[109] F. Hennrich, R. Krupke, S. Lebedkin, K. Arnold, R. Fischer, D. E. Resasco, and M. M. Kappes, "Raman spectroscopy of individual single-walled carbon nanotubes from various sources," *The Journal of Physical Chemistry B*, vol. 109, no. 21, pp. 10567–10573, 2005. PMID: 16852281.

[110] A. M. Rao, E. Richter, S. Bandow, B. Chase, P. C. Eklund, K. A. Williams, S. Fang, K. R. Subbaswamy, M. Menon, A. Thess, R. E. Smalley, G. Dresselhaus, and M. S. Dresselhaus, "Diameter-selective raman scattering from vibrational modes in carbon nanotubes," *Science*, vol. 275, no. 5297, pp. 187–191, 1997.

[111] E. V. Efremov, F. Ariese, and C. Gooijer, "Achievements in resonance raman spectroscopy: Review of a technique with a distinct analytical chemistry potential," *Analytica Chimica Acta*, vol. 606, no. 2, pp. 119 – 134, 2008.

[112] N. R. Raravikar, P. Keblinski, A. M. Rao, M. S. Dresselhaus, L. S. Schadler, and P. M. Ajayan, "Temperature dependence of radial breathing mode raman frequency of single-walled carbon nanotubes," *Phys. Rev. B*, vol. 66, p. 235424, Dec 2002.

[113] V. N. Popov, L. Henrard, and P. Lambin, "Electron-phonon and electron-photon interactions and resonant raman scattering from the radial-breathing mode of single-walled carbon nanotubes," *Phys. Rev. B*, vol. 72, p. 035436, Jul 2005.

[114] V. N. Popov, L. Henrard, and P. Lambin, "Resonant raman intensity of the radial breathing mode of single-walled carbon nanotubes within a nonorthogonal tight-binding model," *Nano Letters*, vol. 4, no. 9, pp. 1795–1799, 2004.

[115] G. N. Ayre, *On the mechanism of carbon nanotube formation by means of catalytic chemical vapour deposition.* PhD thesis, University of Southampton, 2011.

[116] Y. Oyama, R. Saito, K. Sato, J. Jiang, G. G. Samsonidze, A. Grneis, Y. Miyauchi, S. Maruyama, A. Jorio, G. Dresselhaus, and M. Dresselhaus, "Photoluminescence intensity of single-wall carbon nanotubes," *Carbon*, vol. 44, no. 5, pp. 873 – 879, 2006.

[117] A. Jorio, R. Saito, J. H. Hafner, C. M. Lieber, M. Hunter, T. McClure, G. Dresselhaus, and M. S. Dresselhaus, "Structural (n, m) determination of isolated single-wall carbon nanotubes by resonant raman scattering," *Phys. Rev. Lett.*, vol. 86, pp. 1118–1121, Feb 2001.

[118] Y. Wang, X. Cao, S. Hu, Y. Liu, and G. Lan, "Graphical method for assigning raman peaks of radial breathing modes of single-wall carbon nanotubes," *Chemical Physics Letters*, vol. 336, no. 12, pp. 47 – 52, 2001.

[119] H. Telg, J. Maultzsch, S. Reich, F. Hennrich, and C. Thomsen, "Chirality distribution and transition energies of carbon nanotubes," *Phys. Rev. Lett.*, vol. 93, p. 177401, Oct 2004.

[120] Z. Yu and L. E. Brus, "(n, m) structural assignments and chirality dependence in single-wall carbon nanotube raman scattering," *The Journal of Physical Chemistry B*, vol. 105, no. 29, pp. 6831–6837, 2001.

[121] M. S. Arefin, "Empirical equation based chirality (n, m) assignment of semiconducting single wall carbon nanotubes from resonant raman scattering data," *Nanomaterials*, vol. 3, no. 1, pp. 1–21, 2012.

[122] H. Telg, M. Fouquet, J. Maultzsch, Y. Wu, B. Chandra, J. Hone, T. F. Heinz, and C. Thomsen, "G^- and g^+ in the raman spectrum of isolated nanotube: a study on resonance conditions and lineshape," *physica status solidi (b)*, vol. 245, no. 10, pp. 2189–2192, 2008.

[123] M. Souza, A. Jorio, C. Fantini, B. R. A. Neves, M. A. Pimenta, R. Saito, A. Ismach, E. Joselevich, V. W. Brar, G. G. Samsonidze, G. Dresselhaus, and M. S. Dresselhaus, "Single- and double-resonance raman g-band processes in carbon nanotubes," *Phys. Rev. B*, vol. 69, p. 241403, Jun 2004.

[124] M. A. Pimenta, A. Marucci, S. D. M. Brown, M. J. Matthews, A. M. Rao, P. C. Eklund, R. E. Smalley, G. Dresselhaus, and M. S. Dresselhaus, "Resonant raman effect in single-wall carbon nanotubes," *Journal of Materials Research*, vol. 13, pp. 2396–2404, 8 1998.

[125] L. Malard, M. Pimenta, G. Dresselhaus, and M. Dresselhaus, "Raman spectroscopy in graphene," *Physics Reports*, vol. 473, no. 56, pp. 51 – 87, 2009.

[126] J. M. Nesbitt and D. C. Smith, "Measurements of the population lifetime of d band and g' band phonons in single-walled carbon nanotubes," *Nano Letters*, vol. 13, no. 2, pp. 416–422, 2013.

[127] M. A. Pimenta, E. B. Hanlon, A. Marucci, P. Corio, S. D. M. Brown, S. A. Empedocles, M. G. Bawendi, G. Dresselhaus, and M. S. Dresselhaus, "The anomalous dispersion of the disorder-induced and the second-order Raman Bands in Carbon Nanotubes," *Brazilian Journal of Physics*, vol. 30, pp. 423 – 427, 06 2000.

[128] A. G. Souza Filho, A. Jorio, G. Dresselhaus, M. S. Dresselhaus, R. Saito, A. K. Swan, M. S. Ünlü, B. B. Goldberg, J. H. Hafner, C. M. Lieber, and M. A. Pimenta, "Effect of quantized electronic states on the dispersive raman features in individual single-wall carbon nanotubes," *Phys. Rev. B*, vol. 65, p. 035404, Dec 2001.

[129] J. Kürti, V. Zólyomi, A. Grüneis, and H. Kuzmany, "Double resonant raman phenomena enhanced by van hove singularities in single-wall carbon nanotubes," *Phys. Rev. B*, vol. 65, p. 165433, Apr 2002.

[130] J. M. Nesbitt and D. C. Smith, "Separation of G^+ and G^- phonon population dynamics in semiconducting single-walled carbon nanotubes as a function of diameter and temperature," *Phys. Rev. B*, vol. 87, p. 195446, May 2013.

[131] F. Simon, R. Pfeiffer, and H. Kuzmany, "Temperature dependence of the optical excitation lifetime and band gap in chirality assigned semiconducting single-wall carbon nanotubes," *Phys. Rev. B*, vol. 74, p. 121411, Sep 2006.

[132] R. Pfeiffer, H. Kuzmany, C. Kramberger, C. Schaman, T. Pichler, H. Kataura, Y. Achiba, J. Kürti, and V. Zólyomi, "Unusual high degree of unperturbed environment in the interior of single-wall carbon nanotubes," *Phys. Rev. Lett.*, vol. 90, p. 225501, Jun 2003.

[133] J.-H. Kim, K.-J. Yee, Y.-S. Lim, L. G. Booshehri, E. H. Hároz, and J. Kono, "Dephasing of g-band phonons in single-wall carbon nanotubes probed via impulsive stimulated raman scattering," *Phys. Rev. B*, vol. 86, p. 161415, Oct 2012.

[134] S. D. M. Brown, A. Jorio, P. Corio, M. S. Dresselhaus, G. Dresselhaus, R. Saito, and K. Kneipp, "Origin of the breit-wigner-fano lineshape of the tangential g - band feature of metallic carbon nanotubes," *Phys. Rev. B*, vol. 63, p. 155414, Mar 2001.

[135] J. S. Park, K. Sasaki, R. Saito, W. Izumida, M. Kalbac, H. Farhat, G. Dresselhaus, and M. S. Dresselhaus, "Fermi energy dependence of the g-band resonance raman spectra of single-wall carbon nanotubes," *Phys. Rev. B*, vol. 80, p. 081402, Aug 2009.

[136] E. Di Donato, M. Tommasini, C. Castiglioni, and G. Zerbi, "Assignment of the G^+ and G^- raman bands of metallic and semiconducting carbon nanotubes based on a common valence force field," *Phys. Rev. B*, vol. 74, p. 184306, Nov 2006.

[137] Y. Wu, J. Maultzsch, E. Knoesel, B. Chandra, M. Huang, M. Y. Sfeir, L. E. Brus, J. Hone, and T. F. Heinz, "Variable electron-phonon coupling in isolated metallic carbon nanotubes observed by raman scattering," *Phys. Rev. Lett.*, vol. 99, p. 027402, Jul 2007.

[138] K. T. Nguyen, D. Abdula, C.-L. Tsai, and M. Shim, "Temperature and gate voltage dependent raman spectra of single-layer graphene," *ACS Nano*, vol. 5, no. 6, pp. 5273–5279, 2011.

[139] A. Jorio, C. Fantini, M. S. S. Dantas, M. A. Pimenta, A. G. Souza Filho, G. G. Samsonidze, V. W. Brar, G. Dresselhaus, M. S. Dresselhaus, A. K. Swan, M. S. Ünlü, B. B. Goldberg, and R. Saito, "Linewidth of the raman features of individual single-wall carbon nanotubes," *Phys. Rev. B*, vol. 66, p. 115411, Sep 2002.

[140] T. Kampfrath, L. Perfetti, F. Schapper, C. Frischkorn, and M. Wolf, "Strongly coupled optical phonons in the ultrafast dynamics of the electronic energy and current relaxation in graphite," *Phys. Rev. Lett.*, vol. 95, p. 187403, Oct 2005.

[141] V. W. Brar, G. G. Samsonidze, M. S. Dresselhaus, G. Dresselhaus, R. Saito, A. K. Swan, M. S. Ünlü, B. B. Goldberg, A. G. Souza Filho, and A. Jorio, "Second-order harmonic and combination modes in graphite, single-wall carbon nanotube bundles, and isolated single-wall carbon nanotubes," *Phys. Rev. B*, vol. 66, p. 155418, Oct 2002.

[142] S. D. M. Brown, P. Corio, A. Marucci, M. S. Dresselhaus, M. A. Pimenta, and K. Kneipp, "Anti-stokes raman spectra of single-walled carbon nanotubes," *Phys. Rev. B*, vol. 61, pp. R5137–R5140, Feb 2000.

[143] M. Freitag, V. Perebeinos, J. Chen, A. Stein, J. C. Tsang, J. A. Misewich, R. Martel, and P. Avouris, "Hot carrier electroluminescence from a single carbon nanotube," *Nano Letters*, vol. 4, no. 6, pp. 1063–1066, 2004.

[144] C. Liu and H.-M. Cheng, "Carbon nanotubes: controlled growth and application," *Materials Today*, vol. 16(1-2), pp. 19–28, 2013.

[145] S. Park, M. Vosguerichian, and Z. Bao, "A review of fabrication and applications of carbon nanotube film-based flexible electronics," *Nanoscale*, vol. 5, pp. 1727–1752, 2013.

[146] Y. Kumar, M. Ando, "Chemical vapor deposition of carbon nanotubes: a review on growth mechanism and mass production," *J Nanosci Nanotechnol*, vol. 10, pp. 3739–58, 2010.

[147] C. Zhang, Y. Yan, Y. Sheng Zhao, and J. Yao, "Synthesis and applications of organic nanorods, nanowires and nanotubes," *Annu. Rep. Prog. Chem., Sect. C: Phys. Chem.*, vol. 109, pp. 211–239, 2013.

[148] C. L. Cheung, A. Kurtz, H. Park, and C. M. Lieber, "Diameter-controlled synthesis of carbon nanotubes," *The Journal of Physical Chemistry B*, vol. 106, no. 10, pp. 2429–2433, 2002.

[149] X. Zhou, F. Boey, and H. Zhang, "Controlled growth of single-walled carbon nanotubes on patterned substrates," *Chem. Soc. Rev.*, vol. 40, pp. 5221–5231, 2011.

[150] R. Haddon, J. Sippel, A. Rinzler, and F. Papadimitrakopoulos, "Purification and separation of carbon nanotubes," *MRS Bulletin*, vol. 29, pp. 252–259, 4 2004.

[151] I. W. Chiang, B. E. Brinson, A. Y. Huang, P. A. Willis, M. J. Bronikowski, J. L. Margrave, R. E. Smalley, and R. H. Hauge, "Purification and characterization of single-wall carbon nanotubes (swnts) obtained from the gas-phase decomposition of co (hipco process)," *The Journal of Physical Chemistry B*, vol. 105, no. 35, pp. 8297–8301, 2001.

[152] I. W. Chiang, B. E. Brinson, R. E. Smalley, J. L. Margrave, and R. H. Hauge, "Purification and characterization of single-wall carbon nanotubes," *The Journal of Physical Chemistry B*, vol. 105, no. 6, pp. 1157–1161, 2001.

[153] H. Omachi, T. Nakayama, E. Takahashi, Y. Segawa, and K. Itami, "Initiation of carbon nanotube growth by well-defined carbon nanorings," *Nat Chem*, vol. 5, pp. 572–576, July 2013.

Publications

NANO LETTERS

Letter

pubs.acs.org/NanoLett

Measurements of the Population Lifetime of D Band and G′ Band Phonons in Single-Walled Carbon Nanotubes

John M. Nesbitt and David C. Smith*

School of Physics and Astronomy, University of Southampton, Southampton SO17 1BJ, United Kingdom

Supporting Information

ABSTRACT: We report time-resolved incoherent anti-Stokes Raman scattering measurements of the dynamics of the D and G′ bands in single-walled carbon nanotubes at excitation energies of 1.51 and 1.63 eV over the temperature range 4–330 K. The measurements indicate that the population lifetimes (~1 ps) of the phonons responsible for the D band are dependent on nanotube type. The temperature dependencies are consistent with anharmonic decay of the phonons into one low (<190 cm^{-1}) and one high energy phonon.

KEYWORDS: *Nanotube, Raman, anharmonic, lifetime, phonon*

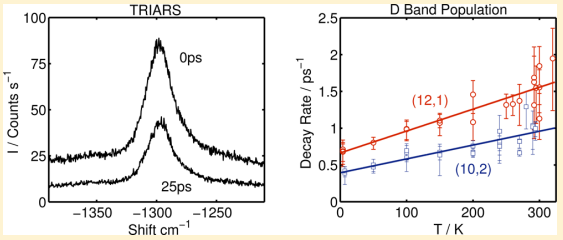

Phonons in single-walled carbon nanotubes (SWCNTs) have been extensively studied using Raman spectroscopy for a number of different reasons.[1] The radial breathing mode (RBM) provides a relatively easy method for determining the diameter and type of nanotubes,[2,3] while the relative strength of the D and G phonons provides a rapid method for estimating the relative density of Raman active lattice defects in different samples and therefore the "quality" of SWCNT samples.[4] More fundamentally, the phonons play a significant role heat and charge transport in SWCNTs.[5,6] In addition the D and G′ phonon Raman features in SWCNTs have received further attention because of the insight they give into the equivalent phonon modes in graphene.[7]

One key area of SWCNT phonon physics that is still not fully understood are the mechanisms which lead to the population and coherence lifetimes, and Raman linewidths of the various phonon modes. A number of good studies of Raman line width as a function of temperature and type have been performed.[8−10] However, as these studies discuss there are a large number of contributions to the Raman line width and separating these contributions requires care and assumptions that can be difficult to separately support. One of the main line width contributions is inhomogeneous broadening due to nanotubes in different environments, and nanotubes along whose length the environment varies. Another is the possibility of coupling to more than one phonon mode with similar frequency. This is known to occur with the D band and G′ band features which are double resonance Raman scattering features.[1,11] These line width contributions are in addition to the fundamental coherence and population decay mechanisms.

Ultrafast time-resolved spectroscopy can be used to directly measure the coherence and population lifetimes of phonons and other elementary excitations. In the case of SWCNTs there have been several time-resolved incoherent anti-Stokes Raman spectroscopy (TRIARS) measurements of the population lifetime of G band phonons reported.[12−15] These give a consistent picture that the room-temperature population lifetime of G band phonons is ~1.2 ps, and that anharmonic decay of the G band phonons into two phonons of equal energy is likely to be the predominant decay channel. Our own TRIARS measurements on the G band that were measured using the experimental system described in this paper are in full agreement with these measurements and will be published separately. As far as we are aware TRIARS measurements of population lifetimes have only been reported for the G band. In addition to the TRIARS measurements, time-resolved coherent anti-Stokes Raman (TRCARS) have also been reported.[14,16] Depending on the experimental setup and sample physics, TRCARS can be used to determine the coherence lifetime of phonon modes. However, as discussed by Lee et al. TRCARS can also measure the free induction decay, which is effectively the line width. Further modeling will be required to be sure of the interpretation of these measurements.

As just discussed there are as yet no clear measurements of the population lifetime of the intersubband phonons responsible for the D and G′ Raman features. In this paper, we set out direct time-resolved measurements of the population lifetime of these phonons using degenerate TRIARS experiments.

Continuous wave (CW) and time-resolved Raman measurements were performed with almost the same experimental system, which is shown schematically in Figure 1. The laser source was a Coherent Mira 900-P system. This was filtered using either a "Photon etc." tunable laser line filter (TLLF) for the CW experiments or a Laserspec TLLF for the time-resolved

Received: September 25, 2012
Revised: January 4, 2013

dx.doi.org/10.1021/nl303569n | *Nano Lett.* XXXX, XXX, XXX−XXX

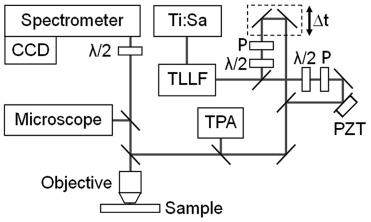

Figure 1. Schematic of the experimental apparatus used for the CW and TRIARS experiments. The TLLF is a narrow band tunable laser line filter used to remove amplified spontaneous emission from the laser beam. PZT refers to a piezo electric transducer. TPA refers to a lens and two photon absorption InGaP diode used in conjunction with the delay line to make autocorrelation measurements.

experiments to remove any fluorescence background. The laser beam was then split into two equal beams. In the case of the CW experiments, one of these beams was blocked and the other sent through a half wave plate and laser polarizer. These were adjusted to ensure a constant power at the sample as the laser wavelength was varied. The beam was then reflected from a 50:50 beamsplitter and focused onto the sample using a LMPLAN IR microscope objective. The spot size was measured to be ~1 μm and in general each laser beam had a power of 5 mW measured at the sample. The sample was mounted in an Oxford Instruments Microstat in vacuum (10^{-6} mbar) for experiments in the temperature range 4−294 K or a Linkam THMS600E hot stage purged with pure nitrogen in the temperature range 150−600 K. The back scattered Raman light was collected by the microscope objective, passed back through the 50:50 beamsplitter, and coupled into a Princeton Instruments TriVista Triple Spectrometer. The triple spectrometer was configured as a subtractive double filter (900 lines/mm) followed by a dispersive stage (1500 lines/mm). The throughput of the system was determined using an Ocean Optics LS-1 Tungsten-Halogen white light source and used to correct for the energy dependence of the throughput. The cryostat/hot stage was mounted on a high resolution (0.1 μm) translation stage. The system was equipped with a home-built microscope system that allowed observation of the sample and laser spot without disturbing the position of the laser spot. This allowed the laser spot to be repositioned on the sample with an accuracy of better than the laser spot diameter. In CW mode the system had a typical spectral resolution of 0.5 cm^{-1}.

To perform TRIARS experiments the laser was mode locked to give ~2.1 ps pulses with a spectral width of ~6.2 cm^{-1} fwhm. After the first beam splitter, the second beam was sent onto a computer controlled hollow retro-reflector variable delay line and then through a second identical set of power control optics. The two beams were recombined at a beamsplitter to form a single beam consisting of pairs of equal intensity pulses with controllable separation in time. This beam was then reflected off of the beamsplitter in to the objective-spectrometer line as before. Because of the polarization selection rules of SWCNTs the pump and probe beams were chosen to be copolarized. This has two disadvantages over a more standard cross-polarized degenerate TRIARS experiment. The first is that the collinear beams result in strong interference effects at the combining beamsplitter. These were effectively removed to within better than 98% using a piezo driven mirror in the path of one of the laser beams. This was used to rapidly vary the path length of this beam by one wavelength. Thus on the time scale of a Raman measurement the interference effects were effectively averaged to zero. The second disadvantage is that it is impossible to differentiate between pump and probe and thus the measured dynamics is effectively the dynamics which would be measured in a standard TRIARS experiment added to a reflection of itself in zero delay, that is, it is symmetric about zero time delay. While at first it might appear that this means it is not possible to determine the rising edge dynamics, this is not the case if reasonable assumptions and careful fitting of the dynamics are used. In order to enable this fitting and to measure decay dynamics faster than the pulse duration a two photon absorption autocorrelator was built just before the final beam splitter. Measurements of pulse duration were made before and after every TRIARS experiment and the data discarded if these differed by greater than the resolution of the autocorrelation (~100 fs). The pulse measurements made with the autocorrelator were checked against measurements using a two photon absorption diode (GaAsP) at the sample position that gave identical results. The major advantage of the degenerate, copolarized, colinear geometry is that both pump and probe can be tuned to the peak of the same resonance, maximizing the TRIARS signal. In addition we have found it to be more stable and simpler. All the data presented was reproducible over weeks and months and was checked to ensure that form of the dynamics was unchanged by halving the laser power.

The experiments were performed on a sample of HiPco SWCNTs bought from Carbon Nanotechnologies Inc. with only standard purification. The SWNTs were suspended in IPA and subsequently deposited onto an oxide coated (200 nm) silicon substrate to form an optically thick film. The method of preparation means that the nanotubes were in bundled form.

Before undertaking TRIARS measurements the samples were fully characterized using CW resonance Raman spectroscopy (RRS) measurements at 4 and 294 K for laser wavelengths in

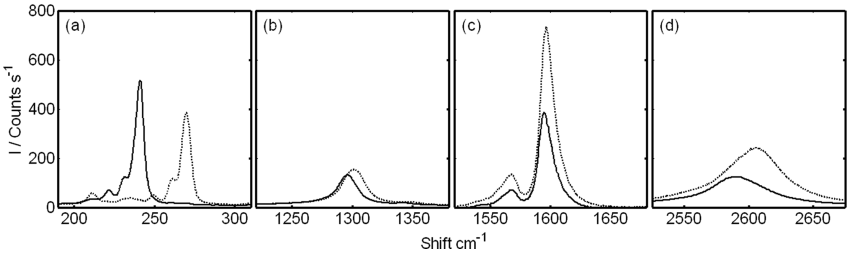

Figure 2. Stokes Raman spectra of the SWCNT sample taken at 292 K with 1.51 eV (solid line) and 1.63 eV (dashed line) laser excitation showing (a) RBM, (b) D-band, (c) G-band, and (d) G′ Band nanotube Raman features.

dx.doi.org/10.1021/nl303569n | *Nano Lett.* XXXX, XXX, XXX−XXX

the range 700–900 nm in 2 nm steps. Stokes Raman spectra measured in the spectral regions of the strongest SWCNT modes at room temperature and for both of the excitation energies used for the TRIARS experiments are shown in Figure 2. All of the standard SWCNT Raman features (RBM, D, G and G′) were observed and all the observed features were explicable as coming from SWCNTs. There was no evidence of the strong 1582 cm^{-1} G band mode seen in graphene and graphite.[17–19] The RBM, D, and G modes all demonstrated clear resonance effects. Figure 3 shows the RBM resonances

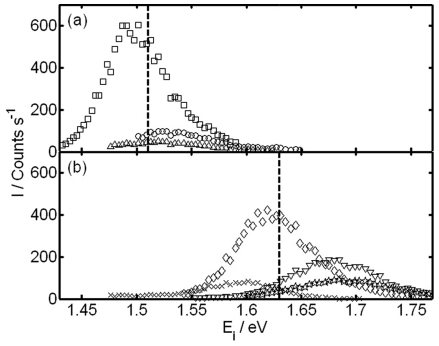

Figure 3. Room-temperature resonance curves for the RBM peaks observed with resonances near the excitation energies, 1.51 and 1.63 eV (indicated by vertical dashed lines), used in the TRIARS experiments. Squares ω_{RBM} = 238 cm^{-1}, circles ω_{RBM} = 234 cm^{-1}, triangles ω_{RBM} = 228 cm^{-1}, diamonds ω_{RBM} = 267 cm^{-1}, crosses ω_{RBM} = 211 cm^{-1}, inverted triangles ω_{RBM} = 260 cm^{-1}, stars ω_{RBM} = 249 cm^{-1}. These are separated into two panels (a,b) for clarity.

nearest to the TRIARS excitation energies that were used, along with the (n, m) indices which we have assigned. Using the method developed by Cheng et al. we have mapped our measured resonance energies and RBM Raman shifts to determine the likely chiral indices associated with each RBM mode.[2] This analysis indicates that the three nanotubes most resonant with the 1.51 eV excitation energy are (10, 5), (11, 3), (12, 1) nanotubes associated with 228, 234, and 238 cm^{-1} RBM modes whose resonance energies are 1.52, 1.53, 1.51 eV. The next nearest resonance observed in the sample was at 1.59 eV. At an excitation energy of 1.63 eV there are four close resonances in (14, 1), (8, 6), (9, 4) and (10, 2) nanotubes whose RBM shifts were 211, 249, 260, and 267 cm^{-1} and resonance energies were 1.59, 1.69, 1.68, 1.62 eV. The next nearest resonance observed in the sample was at 1.53 eV. In all cases the nanotubes are semiconducting nanotubes and the resonances are associated with E_{22} transitions.[20] The observed G band features (Figure 2c) are entirely in agreement with the semiconducting nature of the nanotubes that have been assigned.[1] Comparison of the RRS measurements at 4 and 294 K showed no significant temperature dependence on resonance, and meant that it was not necessary to tune the excitation energy when measuring the temperature dependence of the TRIARs measurements.

TRIARS measurements were performed with excitation energies of 1.51 and 1.63 eV over the temperature range 4 to 330 K at a number of different positions on the sample. The data presented in this paper is from a single location to ensure comparability, however it is entirely in agreement with measurements at other locations. Figure 4a,b shows raw

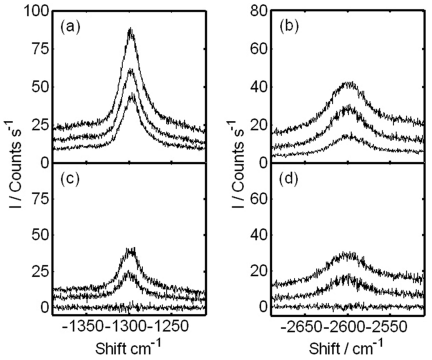

Figure 4. Raw TRIARS spectra for (a) the D band and (b) the G′ band at 292K for an excitation energy of 1.51 eV as a function of pulse delay. The raw spectra are for pulse delays of 0, 1, and 25 ps in order from top to bottom. Background subtracted TRIARS spectra for (c) the D band and (d) the G′ band for pulse delays of 0, 1, and 20 ps in order from top to bottom. Background spectra were taken at 25 ps delay.

Raman spectra of the D and G′ features taken for different time delays between the two laser pulses for an excitation energy of 1.51 eV and a temperature of 4.2 K. Clearly in both cases there is a significant increase in the Raman intensity for short time delays. In order to subtract the equilibrium Raman spectrum and obtain the dynamics of the peak we measured a background spectra every third spectra at a time delay (25 ps) sufficient that there was no measurable long-lived pump excitation. This was checked by comparing the background spectra with the sum of the spectra obtained with each of the two beams separately. The background spectra obtained during a TRIARS experiment were checked to ensure that the TRIARS system was stable. If their magnitude varied by more than 20% over the duration of an experiment the experiment was aborted and data discarded. Subtracted spectra showing the non-equilibrium Raman spectra are presented in Figure 4c,d.

The subtracted spectra were then fitted using functions that well fitted the equilibrium spectra. In both cases, this consisted of a Lorentzian peak plus a second degree polynomial background. Unlike what has been observed for the G band,[1] we could detect no significant time dependence of the central Raman shift or peak width (fwhm). The pulse delay dependence of the amplitude of the subtracted spectra for the D and G′ data presented in Figure 4 are presented in Figure 5. Also shown in Figure 5 are experimentally measured cross correlations between the two laser pulses whose amplitudes have been scaled. A comparison between these and the amplitude dynamics demonstrates that the dynamics is clearly temporally resolvable but occurs on a time scale comparable with the cross correlation.

In order to extract the phonon dynamics from the amplitude versus time data we hypothesized that the phonon dynamics is a monoexponential rise followed by either a slower monoexponential or biexponential decay. The phonon dynamics, taking into account the indistinguishability of the two laser pulses, was convolved with the measured pulse autocorrelation function and nonlinear least-squares fitting to determine the various fitting parameters. It was found in all cases that the rising edge dynamics was faster than the resolution of the experiment (~250 fs). This is in agreement with the published TRIARS measurements of the G band

dx.doi.org/10.1021/nl303569n | Nano Lett. XXXX, XXX, XXX–XXX

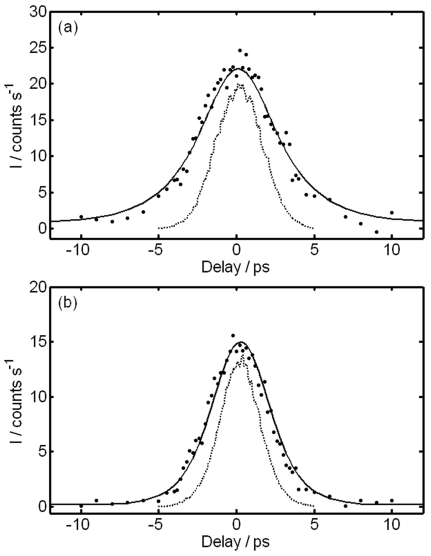

Figure 5. Amplitude (solid circles) of the background subtracted TRIARS spectra as a function of pulse delay for (a) the D band and (b) the G′ band taken at 4 K with an excitation energy of 1.51 eV. Monoexponential decay fit (solid line) and pulse intensity autocorrelation (dashed line) are shown.

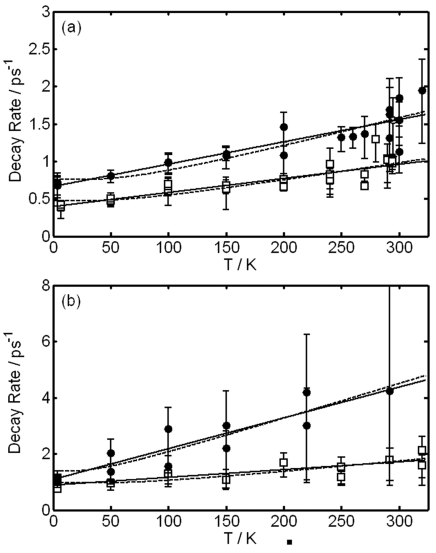

Figure 6. The decay rate of the (a) D and (b) G′ band optical phonons as a function of temperature. The experimental data, derived using a monoexponential fit as a function of temperature, are fit to eq 1 (dashed line) and eq 2 (solid line). The solid circles on each plot correspond to an excitation energy of 1.51 eV and the open squares to an excitation energy of 1.63 eV. Each symbol corresponds to an independent measurement of the TRIARS dynamics. The error bars represent the 95% confidence bounds for the fitting parameter and were obtained from the fitting procedure.

phonons.[12] Therefore the fits were repeated assuming that the phonon population had an instantaneous rise. Monoexponential decay fits are presented on Figure 5. We found that there was no significant improvement in the fits, as determined by the χ^2 and observation of the residuals when using a biexponential decay model. The phonon population decay rate as a function of temperature for both D and G′ modes for both excitation energies are presented in Figure 6. Also shown are the fits for the commonly used two phonon anharmonic decay temperature dependence described by eq 1 where we use Bose–Einstein statistics $n(E,T)$ to give the populations of the daughter phonon modes and a linear temperature dependence described by eq 2. The error bars presented in Figure 6 show 95% confidence bounds in the decay rate fitting parameter. The reason why the confidence bounds in Figure 6 generally increase with temperature can be explained by the faster dynamics at higher temperature. This reduces the difference between the measured TRIARS dynamics and the pulse cross correlation function and means the fitting routine is relying on fewer data points to secure the fit. In addition, for decay times approaching the minimum resolvable decay time the upper error bar on the decay rate will have infinite extent as the decay time could be effectively zero. Multiple independent TRIARS experiments were performed with the same temperature and excitation energy.

In order to be able to interpret the phonon dynamics, we need to consider which phonon modes we are sensitive to in the Raman measurements and how these interact with the electronic states, i.e., are generated and possibly reabsorbed. The mechanisms behind D and G′ Raman scattering are both well understood.[1] Both involve two scattering events whose net momentum is zero. In the case of the D band these are one elastic (defect induced) and one inelastic (phonon induced) scattering event. In the case of the G′ band, these involve two phonons with equal magnitude, opposite direction wavevectors. The two scattering events means that the wavevector of the phonon is not constrained to be zero as it is in single phonon Raman. However, due to the double resonance mechanism the wavevector of the phonons that can be involved in the D and G′ peaks are predominantly constrained to narrow bands about the wavevector that joins the two degenerate band minima responsible for the electronic resonance. The extent of the bands is controlled by the energy of the exciting and emitted phonons and the intermediate states relative to the electronic resonance. In the TRIARS experiments, we require the laser light to both produce strong Raman signal from our modes of interest and in addition to excite the SWCNTs. Thus we require an ingoing resonance with the SWCNTs of interest. In this case, the D band process involving elastic scattering followed by phonon scattering will be more strongly resonant than the phonon scattering followed by elastic scattering process. This will mean that the wavevector band associated with the D band will be more tightly constrained than the wavevector band associated with the G′ mode

$$\Gamma_{\mathrm{ph-ph}}(T) = \Gamma_0[1 + n(E_1, T) + n(E_2, T)] \quad (1)$$

$$\Gamma_{\mathrm{ph-ph}}(T) = MT + \Gamma_0 \quad (2)$$

Next we consider what single electron/hole scattering events could lead to generation of the D and G′ phonons. Clearly we are interested in scattering events that involve intervalley scattering of the charge carriers. As already discussed by others[21] it is simplest to discuss such scattering events if we represent the electronic and phonon states on the 2D Brillouin zone of graphite using cutting lines to apply the circumferential

dx.doi.org/10.1021/nl303569n | Nano Lett. XXXX, XXX, XXX–XXX

Table 1. Anharmonic Fitting Parameters

	E_i (eV)	E_1 (cm^{-1})	E_2 (cm^{-1})	Γ_0 (ps^{-1})
D	1.51	138 ± 51	1157 ± 51	0.5 ± 0.1
D	1.63	136 ± 46	1159 ± 46	0.8 ± 0.1
G′	1.51	167 ± 78	2433 ± 78	1.0 ± 0.2
G′	1.63	76 ± 62	2524 ± 62	1.4 ± 0.4

Table 2. Linear Fitting Parameters

	E_i (eV)	M ($ps^{-1}K^{-1}$)	Γ_0 (ps^{-1})
D	1.51	0.0020 ± 0.0005	0.39 ± 0.15
D	1.63	0.0029 ± 0.0007	0.66 ± 0.18
G′	1.51	0.0028 ± 0.0012	0.88 ± 0.19
G′	1.63	0.0109 ± 0.0044	1.08 ± 0.71

confinement. While the conclusions from such an analysis are approximate due to the possibility of mode mixing in the true SWCNT states, and electron−electron effects, this approach has proved very successful. In Figure 7, we present the initial and final electronic states and phonon modes involved in (a) scattering between the first band minima, (b) scattering between the second band minima, that is, the phonons responsible for the D band Raman signal in our experiments, and (c) scattering of carriers at the first band minima by the phonons responsible for the D band Raman signal. The cutting lines on these diagrams are calculated for a (12,1) nanotube and the states and wavevectors are indicative rather than calculated. It is obvious from the diagrams on Figure 7 that the phonons we are sensitive to do not take part in scattering between the two first band minima. In order for a carrier in the first band to absorb one of the phonons involved in scattering between the second band minima it would have to be promoted to the fourth highest band, which is not energetically possible. Thus, after the initial relaxation of the charge carriers the phonons we are sensitive to are mostly isolated from the electronic states. The same analysis means that the phonons detected in the experiments are likely to be produced by intervalley scattering within the second band. Because of the need for energy and wavevector conservation it is not possible for phonons with precisely the wavevector required to couple the two band minima to be emitted. However, slightly shorter or longer wavevector phonons could be produced by charge carriers at energies above the band minima. Charge carriers could be scattered to these energies by carrier−carrier scattering in the first stages of the relaxation after photoexcitation.[22,23] Thus it is likely that the phonons observed in the experiment are generated in the initial stages of the relaxation of the photoexcited charge carriers and then decay independent of the photoexcited charge carriers.

Let us now consider the D band TRIARS relaxation rates versus temperature set out in Figure 6. The data presented indicates that the decay rates measured at the two excitation energies are quite different. As the two excitation energies probe different SWCNTs this implies that D band phonons in the different nanotubes have different decay rates. This is contrary to the reports of room temperature G band decay rates of HiPco SWCNTs that appear to be independent of nanotube type.[12,13] This difference can be explained by the fact that while the G band phonons in all SWCNTs are derived from the same $k = 0$ mode in graphene, the D mode phonons in different nanotubes are derived from different graphene phonons. Thus these measurements imply that the decay rate of these phonons in graphene also varies relatively rapidly as a function of wavevector. Looking again at Figure 6, the best fit anharmonic model from eq 2 gives that the lower energy product phonon has an energy of 138 ± 51 cm^{-1}, which is in line with the almost linear temperature dependence observed. The fact that there is no clear difference between the quality of the fit of the two models means we cannot be sure that anharmonic decay is the main decay mechanism. Another possibility is decay of phonons into low energy single or collective excitations of the photoexcited carriers; however, the fact that the measured decay dynamics is not affected by photoexcitation intensity suggests this is unlikely. Another possibility is the decay of phonons in one nanotube into phonons in nearest neighbor nanotubes within the bundles. While some experiments have clarified that bundling of nanotubes[24] effects the shape of D and G′ peaks, it is not possible to draw conclusions about any intertube phonon energy transfer from these measurements. This is because the dependence of the shape of the D and G′ peaks can occur by a number of different mechanisms, most of which do not lead to intertube phonon transfer. For instance, bundling can shift electronic resonance energies in nanotubes, and this effect depends on the environment of the individual nanotubes, leading to inhomogeneity. This directly effects the observed peak shapes as the observed D and G′ peaks depend on the relative strength of different nanotube contributions at a particular laser energy. Furthermore, the peak shape for a specific nanotube is also dependent on the detuning of the laser and resonance energies via the double resonance mechanism.[1] While our measurements cannot be used to predict the lifetime of the equivalent modes in isolated SWCNTs they do place an

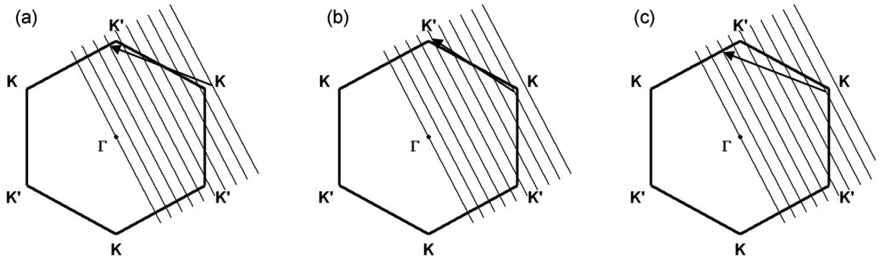

Figure 7. Representation of the wavevectors of the initial and final electronic states and phonon modes involved in (a) scattering between the first band minima, (b) scattering between the second band minima, that is, the phonons responsible for the D band Raman signal in our experiments, and (c) scattering of carriers at the first band minima by the phonons responsible for the D band Raman signal. These are plotted on the graphene Brillouin zone in the extended zone scheme. The parallel lines are the cutting lines for a (12,1) nanotube.

dx.doi.org/10.1021/nl303569n | *Nano Lett.* XXXX, XXX, XXX−XXX

upper limit on the decay rate in isolated nanotubes, since it is not possible for the same phonons in isolated nanotubes to have less decay channels. Now that we have demonstrated the utility and advantages of our degenerate TRIARS experiments on bundled nanotubes we look forward to clarifying the role of intertube phonon energy transfer in individual SWCNTs.

Interpreting the G′ band TRIARS is more difficult due to the two phonon nature of the G′ band scattering.[1,11] This means that for a small modulation of the phonon population the TRIARS decay rate is the phonon's population decay rate. However, for a large modulation of the phonon population the TRIARS decay rate is twice the population decay rate, and for an intermediate modulation we should have observed a biexponential decay with both decay rates. Determining which limit we are in is made difficult because the G′ band probes more than one phonon mode in a specific nanotube and we are possibly sensitive to more than one type of nanotube. The magnitude of the G′ peak at zero pulse duration is 50 to 100% bigger than the magnitude for a large pulse separation, that is, a fractional change of 0.5−1. However, as we cannot be sure that the fractional change in the population of all the modes to which we are sensitive is equal we cannot be sure which limit we are in. Interestingly, to within experimental error the G′ band decay rates are approximately twice the D band decay rates, independent of excitation energy and temperature. A simple explanation of this would be that the G′ band TRIARS is measuring the same phonon dynamics as the D band TRIARS but in the large modulation limit. However another possible explanation is that the G′ band and D band TRIARS are probing slightly different phonons and the strong wavevector dependence of phonon decay rates observed in the D band TRIARS measurements is responsible for the G′ band decay being faster than the D band decay. Further experimental and theoretical investigation will be required to explain this effect.

In conclusion we have presented the first published TRIARS measurements of the dynamics of the D and G′ Raman bands in SWCNTs. These measurements have been performed with two different excitations energies allowing us to probe the variation of the dynamics in different nanotubes. In addition we have measured the dynamics as a function of temperature over the range 4−330 K. The dynamics observed is consistent with a nonequilibrium population of phonons being generated within the first ∼100 fs after photoexcitation, and then decaying independently of the photoexcited carriers. The population lifetimes derived from the D band measurements indicate that the population lifetime of the D band phonons is significantly dependent on nanotube type. The temperature dependence of the population lifetimes derived from the D band measurements are well fitted by a linear temperature dependence. This observation could be consistent with a standard two phonon anharmonic decay process if one of the product phonons has an energy less than 190 cm^{-1}. The G′ band dynamics is more difficult to interpret and will require further theoretical and experimental work before it is fully understood.

These results have clear, practical applications to SWCNT and graphene devices which are limited by the carrier recombination lifetime. These include electronic devices such as p−n junctions and field effect transistors, ultrafast electronics such as terahertz devices, and optoelectronic devices such as far-infrared detectors. This is because it has been shown[25] that a key mechanism in carrier recombination in graphene and metallic nanotubes is scattering from intervalley phonons, like those probed in these experiments, and that carrier recombination lifetimes can be less than the phonon lifetimes we have measured. In this case carrier recombination will be slowed by a "phonon bottleneck"[26] and will be effectively limited to the phonon lifetimes measured in these TRIARS experiments.

■ ASSOCIATED CONTENT

Ⓢ Supporting Information

Temperature dependence of D band and G′ band decay rates. Time dependence of subtracted D band and G′ band amplitudes for both low- and high-temperate experiments. Written explanation of data supplied. This material is available free of charge via the Internet at http://pubs.acs.org.

■ AUTHOR INFORMATION

Corresponding Author

*E-mail: dcsmith@soton.ac.uk

Notes

The authors declare no competing financial interest.

■ ACKNOWLEDGMENTS

This work was supported by the EPSRC, U.K. via Grant EP/C006763/1. The manuscript was written through contributions of all authors. All authors have given approval to the final version of the manuscript.

■ REFERENCES

(1) Dresselhaus, M. S.; Dresselhaus, G.; Saito, R.; Jorio, A. *Phys. Rep* **2005**, *409* (2), 47−99.
(2) Cheng, Q.; Debnath, S.; Gregan, E.; Byrne, H. *Appl. Phys. A* **2011**, *102* (2), 309−317.
(3) Jorio, A.; Saito, R.; Hafner, J. H.; Lieber, C. M.; Hunter, M.; McClure, T.; Dresselhaus, G.; Dresselhaus, M. S. *Phys. Rev. Lett.* **2001**, *86* (6), 1118−1121.
(4) Miyata, Y.; Mizuno, K.; Kataura, H. *J. Nanomater.* **2011**, DOI: 10.1155/2011/786763.
(5) Lazzeri, M.; Piscanec, S.; Mauri, F.; Ferrari, A. C.; Robertson, J. *Phys. Rev. Lett.* **2005**, *95* (23), 236802.
(6) Lazzeri, M.; Mauri, F. *Phys. Rev. B* **2006**, *73* (16), 165419.
(7) Samsonidze, G. G.; Saito, R.; Jorio, A.; Filho, A. G. S.; Grüneis, A.; Pimenta, M. A.; Dresselhaus, G.; Dresselhaus, M. S. *Phys. Rev. Lett.* **2003**, *90* (2), 027403.
(8) Jorio, A.; Fantini, C.; Dantas, M. S. S.; Pimenta, M. A.; Souza Filho, A. G.; Samsonidze, G. G.; Brar, V. W.; Dresselhaus, G.; Dresselhaus, M. S.; Swan, A. K.; Ünlü, M. S.; Goldberg, B. B.; Saito, R. *Phys. Rev. B* **2002**, *66* (11), 115411.
(9) Lazzeri, M.; Piscanec, S.; Mauri, F.; Ferrari, A. C.; Robertson, J. *Phys. Rev. B* **2006**, *73* (15), 155426.
(10) Rao, R.; Menendez, J.; Poweleit, C. D.; Rao, A. M. *Phys. Rev. Lett.* **2007**, *99* (4), 047403.
(11) Saito, R.; Grüneis, A.; Ge, G. S.; Brar, V. W.; Dresselhaus, G.; Dresselhaus, M. S.; Jorio, A.; Cançado, L. G.; Fantini, C.; Pimenta, M. A.; Filho, A. G. S. *New J. Phys.* **2003**, *5* (1), 157.
(12) Song, D.; Wang, F.; Dukovic, G.; Zheng, M.; Semke, E. D.; Brus, L. E.; Heinz, T. F. *Phys. Rev. Lett.* **2008**, *100* (22), 225503.
(13) Kang, K.; Ozel, T.; Cahill, D. G.; Shim, M. *Nano Lett.* **2008**, *8* (12), 4642−4647.
(14) Lee, Y. J.; Parekh, S. H.; Fagan, J. A.; Cicerone, M. T. *Phys. Rev. B* **2010**, *82* (16), 165432.
(15) Chatzakis, I.; Yan, H.; Song, D.; Berciaud, S.; Heinz, T. F. *Phys. Rev. B* **2011**, *83* (20), 205411.
(16) Ikeda, K.; Uosaki, K. *Nano Lett.* **2009**, *9* (4), 1378−1381.
(17) Malard, L. M.; Pimenta, M. A.; Dresselhaus, G.; Dresselhaus, M. S. *Phys. Rep.* **2009**, *473* (5−6), 51−87.

(18) Ferrari, A. C.; Meyer, J. C.; Scardaci, V.; Casiraghi, C.; Lazzeri, M.; Mauri, F.; Piscanec, S.; Jiang, D.; Novoselov, K. S.; Roth, S.; Geim, A. K. *Phys. Rev. Lett.* **2006**, *97* (18), 187401.
(19) Nemanich, R. J.; Solin, S. A. *Phys. Rev. B* **1979**, *20* (2), 392−401.
(20) Weisman, R. B.; Bachilo, S. M. *Nano Lett.* **2003**, *3* (9), 1235−1238.
(21) Saito, R.; Dresselhaus, G.; Dresselhaus, M. S. *Phys. Rev. B* **2000**, *61* (4), 2981−2990.
(22) Hagen, A.; Moos, G.; Talalaev, V.; Hertel, T. *Appl. Phys. A* **2004**, *78* (8), 1137−1145.
(23) Hertel, T.; Fasel, R.; Moos, G. *Appl. Phys. A* **2002**, *75* (4), 449−465.
(24) Cardenas, J. F.; Gromov, A. *Nanotechnology* **2009**, *20* (46), 465703.
(25) Rana, F.; George, P. A.; Strait, J. H.; Dawlaty, J.; Shivaraman, S.; Chandrashekhar, M.; Spencer, M. G. *Phys. Rev. B* **2009**, *79* (11), 115447.
(26) Brya, W. J.; Geschwind, S.; Devlin, G. E. *Phys. Rev. Lett.* **1968**, *21* (27), 1800−1802.

Separation of G^+ and G^- phonon population dynamics in semiconducting single-walled carbon nanotubes as a function of diameter and temperature

John M. Nesbitt and David C. Smith

Department of Physics and Astronomy, University of Southampton, Southampton SO17 1BJ, United Kingdom

(Received 18 February 2013; revised manuscript received 18 April 2013; published 30 May 2013)

The paper presents time-resolved incoherent anti-Stokes Raman spectroscopy (TRIARS) measurements of the population dynamics of *G*-mode phonons in semiconducting single-walled carbon nanotubes (SWCNTs), in which the G^+ and G^- dynamics are separated. The measurements were performed as a function of temperature over the full range 4−600 K, and at two laser excitation energies, 1.51 and 1.63 eV, which give TRIARS signals from SWCNTs in two different diameter distributions, $0.99 < d < 1.05$ nm and $0.88 < d < 0.97$ nm, respectively. The population lifetimes determined from the experiments were, to within experimental error, independent of mode type and diameter. In all cases the temperature dependence of the population lifetimes was well fitted by a model that assumes that two-phonon anharmonic decay is the dominant process and that the lower-energy daughter phonon has an energy of approximately 400 ± 100 cm^{-1}.

DOI: 10.1103/PhysRevB.87.195446 PACS number(s): 63.20.K−, 78.67.Ch, 73.63.Fg, 78.47.je

I. INTRODUCTION

Single-walled carbon nanotubes (SWCNTs) are promising materials for producing the active elements for a new generation of electronic devices. This is because of their unique electronic transport properties and one-dimensional structure.[1,2] SWCNTs boast a long mean free path for low-energy carriers, ∼0.5–0.8 μm; however, it has been shown that high-energy carriers in SWCNTs couple strongly to longitudinal optical (LO) phonons with a mean free path of ∼0.3 μm.[3–6] It has been proposed that the optical phonon scattering rates are enhanced by the buildup of a significant nonequilibrium population of the phonons, comparable to a phonon temperature of $\geqslant$6000 K, leading to stimulated scattering.[5,7] These theoretical predictions suggest an optical phonon population lifetime of 5 ps.

The phonon structure in SWCNTs has been extensively studied using various Raman-scattering techniques, particularly resonance Raman spectroscopy (RRS).[8–11] The well-defined optical transition energies in SWCNTs make them ideal candidates for RRS studies.[12,13] RRS can be a useful tool, not just for providing insight into the electronic structure of SWCNTs and determining the diameter distribution in a bundled SWCNT sample,[10,14–16] but also for selectively studying SWCNTs of a particular type through resonant excitation.[17–20] In addition, studies of the effects of doping on SWCNT Raman spectra allows the strength of the interaction between phonons and charge carriers to be investigated.[21] In certain cases, studies of the temperature dependence of the Raman linewidth can indirectly probe the phonon dynamics.[19,22,23] However, direct measurements of phonon dynamics are often preferred and can be obtained by time-resolved incoherent anti-Stokes Raman spectroscopy (TRIARS) and other time-resolved Raman spectroscopy techniques.[17,18,24,25] TRIARS measurements are particularly useful for probing the mechanism of phonon population decay. With relatively high-energy phonons, such as the ones discussed in this paper, the most common decay channel is via anharmonic decay of a single high-energy phonon into a pair, or possibly more, of lower-energy phonons.[24–26] Other possible decay channels include phonons scattering charge carriers, phonons transferring energy to the environment, and phonons converting into collective electronic excitations, e.g., spin waves.[27]

The TRIARS study presented here is an extension of a number of TRIARs studies on SWCNTs. The first study was by Song *et al.*, who, using an excitation energy of 1.55 eV, measured a room-temperature *G*-mode optical phonon lifetime of 1.1 ps in isolated semiconducting (6,5) SWCNTs.[18] The SWCNTs in Song's study were suspended in D_2O with sodium dodecylbenzene sulfonate or sodium cholate as a surfactant. In a separate study by Kang *et al.*, the room-temperature *G*-mode phonon lifetimes in bundled semiconducting and bundled metallic SWCNTs were measured to be 1.2 and 0.9 ps, respectively.[24] For both semiconducting and metallic SWCNTs, Kang observed a *G*-mode phonon lifetime which was inversely proportional to temperature, scaling as ∼1/T in the 300–450 K range. In Kang *et al.*'s measurements, an excitation energy of 1.58 eV was used to excite the E_{22} transition of $0.85 < d < 1.2$ nm semiconducting SWCNTs in a bundled HiPco sample in one experiment, and excite the E_{11} transition of $1.35 < d < 1.6$ nm metallic SWCNTs in a bundled arc-discharged sample in another experiment. In both cases the bundled SWCNTs were deposited on sapphire substrates. More recently, Chatzakis *et al.* measured the *G*-mode phonon lifetime in the temperature range 6–700 K.[25] Chatzakis *et al.* obtained a room-temperature *G*-mode phonon lifetime of 1.11 ps and demonstrated that the temperature dependence of the lifetime can be well described by the anharmonic decay of the phonon into two daughter phonons. In this study, bundled HiPco SWCNTs were deposited on a fused-quartz substrate and excited with an energy of 1.55 eV. This simultaneously excited the E_{11} transition of $1.1 < d < 1.2$ nm semiconducting SWCNTs and the E_{22} transition of $d \sim 1.7$ nm metallic SWCNTs. Consequently, the *G*-mode phonon decay rates obtained in Chatzakis *et al.*'s study reflected the response from an ensemble of semiconducting and metallic SWCNTs. The good agreement of the room-temperature *G*-mode phonon lifetimes obtained from these separate studies has led to the conclusion that the *G*-mode phonon decay rate in SWCNTs does not depend critically on

the local environment or on SWCNT structural parameters.[25] However, Kang *et al.* observed a measurable difference in the decay rate of semiconducting and metallic SWCNTs under similar environmental conditions, which may indicate a significant dependence on SWCNT structural parameters. Another possible origin of this observation comes from the splitting of the G mode in SWCNTs.[11] Because of the significant bandwidth of the ultrafast pulses that are used, none of the existing G-mode TRIARS studies are able to separately resolve the G^+ and G^- phonon dynamics.[18,24,25] Instead, they make the assumption that the TRIARS signal is dominated by the G^+ mode. While it is true for semiconducting SWCNTs that the G^+ mode dominates the equilibrium Raman spectrum, this is often not the case for metallic SWCNTs and there is no guarantee that the nonequilibrium populations probed in TRIARS experiments follow the equilibrium Raman spectra in either metallic or semiconducting tubes.[11,28] Furthermore, in semiconducting SWCNTs the G^+ mode is attributed to the LO phonon, whereas in metallic SWCNTs the same mode is attributed to the transverse optical (TO) phonon.[29–31] Thus, being able to resolve the dynamics of the G^+ and G^- phonons is an important next step in understanding the dynamics of phonons in SWCNTs.

In this paper, we extend the existing G-mode TRIARS studies by using RRS to selectively excite semiconducting SWCNTs in two separate diameter ranges from a bundled HiPco SWCNT sample. We then use a TRIARS technique to measure the temperature dependence of the G-mode phonon decay rate for semiconducting SWCNTs in two separate diameter ranges, while under the same environmental conditions. In the case of semiconducting nanotubes, the G^+ mode and G^- mode are attributed to the LO and TO phonon, respectively.[29–31] By selecting pulse durations that strike a sensible balance between temporal and spectral resolution, we are able to separately resolve the G^+-mode (LO) and G^--mode (TO) phonon dynamics.

II. EXPERIMENTAL TECHNIQUE

The SWCNT sample used in our experiments was produced from commercially obtained (Carbon Nanotechnologies) nanotubes, which were synthesized by the HiPco process. The nanotubes came with only standard purification, which produced bundled semiconducting and metallic SWCNTs with 0.8–2 nm diameter. The nanotubes were suspended in isopropyl alcohol (99.9%) and subsequently deposited onto an oxide-coated (200-nm) silicon substrate to form an optically thick film of bundled HiPco SWCNTs.

Our RRS and TRIARS measurements were performed with essentially the same experimental setup, which is shown in Fig. 1. The laser source was a Ti:sapphire Coherent Mira 900-P system, which had an operational wavelength range of 700–950 nm. To remove any unwanted fluorescence produced in the laser, the output laser beam was filtered using a Photon etc laser line tunable filter (LLTF) with high out-of-band rejection for RRS measurements, and a Laserspec LLTF with low dispersion for TRIARS measurements. The laser beam was then split into two beams of equal power.

For the RRS measurements, one of these beams was blocked and the other sent through a half-wave plate followed by a vertical polarizer. As the laser wavelength was varied, only the half-wave plate was adjusted to ensure a constant power and maintain vertical polarization at the sample. The beam was then reflected from a 50:50 beam splitter into the Raman microscope, where it was focused onto the sample using a LMPLAN IR microscope objective. The laser power measured at the sample was maintained at 5.0 mW and the focal spot diameter was measured to be $\sim$1 μm. The sample was mounted in an Oxford Instruments Microstat in vacuum (10^{-6} mbar) for experiments in the temperature range 4–294 K, and a Linkam THMS600E hot stage purged with pure nitrogen in the temperature range 150–600 K. The backscattered Raman light was collected and collimated by the objective. To optimize detection, the polarization of the backscattered Raman light was rotated 90° by a second half-wave plate before entering the Princeton Instruments TriVista Triple Spectrometer. The triple spectrometer was configured as a subtractive double filter (900 gr/mm) followed by a dispersive stage (1500 gr/mm), which dispersed the spectrum onto a nitrogen-cooled PyLoN 400 BR/LN charge-coupled device (CCD) detector. The polarization and energy-dependent throughput of the system was determined and corrected for using an Ocean Optics LS-1 tungsten-halogen white light source. The sample was mounted on a high resolution (0.1-μm) translation stage for spatial Raman measurements. An *in situ* home-built microscope system allowed observation of the sample and focal spot without disturbing the position of the focus. This allowed the focal spot to be repositioned on the sample with an accuracy of better than the spot diameter. During RRS measurements the laser source was configured in cw mode to give a typical spectral resolution of 0.5 cm^{-1}.

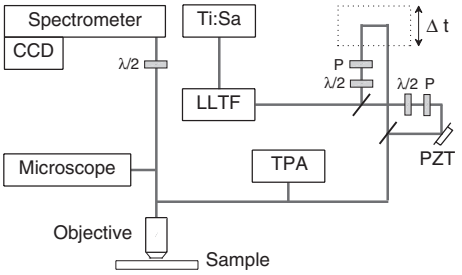

FIG. 1. Experimental apparatus used for RRS and TRIARS measurements. The laser line tunable filter, LLTF, is used to remove amplified spontaneous emission generated in the laser beam. PZT refers to a piezoelectric transducer. TPA refers to a lens and two-photon absorption GaP photodiode used to make autocorrelation measurements.

To perform TRIARS measurements the laser was mode-locked to give $\sim$2.1-ps pulses with a spectral width of $\sim$6.2 cm^{-1} full width at half maximum (FWHM). After the first beam splitter, the second beam was sent through a variable delay line and a second identical set of polarization optics. The two beams were recombined at a second beam splitter to form a single beam consisting of pairs of equal-intensity pulses with controllable delay. Because of the polarization selection rules of SWCNTs, the pump and probe beams were chosen to be copolarized. This has two disadvantages compared to a more standard cross-polarized degenerate TRIARS

experiment. The first is that the collinear beams result in strong interference effects at the combining beam splitter. These were effectively removed to within better than 98% by introducing a piezodriven mirror in one of the optical paths. The piezo was used to rapidly vary the length of one of the optical paths by a number of whole wavelengths, so that on the timescale of a Raman measurement the interference effects were effectively averaged to zero. The second disadvantage is that it is impossible to differentiate between pump and probe and, thus, the measured dynamics is effectively the dynamics which would be measured in a standard TRIARS experiment added to a reflection of itself in zero delay. At first, it might appear that this would make it impossible to determine the rising edge dynamics; however, this is not the case if reasonable assumptions and careful fitting of the dynamics are used. To make this possible, an *in situ* two-photon absorption (TPA) cross-correlator (GaP photodiode) was used to measure the cross-correlation of the pump and probe pulses before they entered the Raman microscope. The pulse-correlation measurement was made before and after every TRIARS measurement, and the data were discarded if the pulse duration had varied by greater than 100 fs. The pulse measurements made with the autocorrelator were checked against measurements using another TPA photodiode (GaP) at the sample position, which gave identical results. The major advantage of the degenerate, copolarized, collinear geometry is that both pump and probe can be tuned to the peak of the same resonance, maximizing the TRIARS signal. In addition, we found it was a stable approach and simpler to align than a two-color pump-probe system.

III. RESULTS

A. Resonance Raman scattering: Controlled excitation

Before undertaking TRIARS measurements the bundled SWCNT sample was characterized by analyzing RRS measurements. The RRS measurements were taken for laser wavelengths in the range 700–900 nm in 2-nm increments at room temperature (292 K) and 5-nm increments at low temperature (4 K). Figure 2 shows the room-temperature radial breathing mode (RBM) resonance profiles of SWCNTs which come into resonance over the energy range of the laser system. The low-temperature RBM resonance profiles are supplied in the supplemental information.[32] These measurements prove that there is no significant difference between the resonances observed at 4 K and 292 K. Thus, the TRIARS experiments performed to determine the temperature dependence of the phonon decay rates were performed without tuning the laser energy as the temperature was varied. RRS measurements obtained at random locations on the sample gave similar spectra, which confirmed that the SWCNTs were in bundled form with similar diameter distributions throughout the sample. It is clear from Fig. 2 that the SWCNTs that are out of resonance do not make significant contributions to the RBM signal for a particular excitation energy. When we compared the RBM resonance profiles in Fig. 2 with the resonance profile of the *G* mode, we found the resonance profile of the *G* mode correlated reasonably well with the sum of RBM resonance profiles. This result strongly implies that the SWCNTs, which contribute to the RBM signal for any particular excitation energy, also

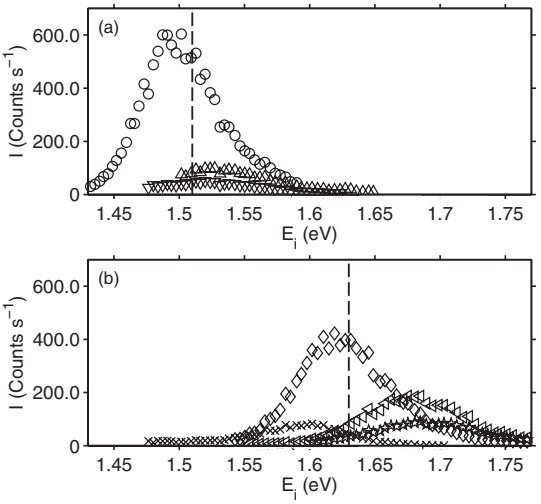

FIG. 2. Room-temperature (292 K) RBM resonance windows observed with resonances near the excitation energy (1.51 and 1.63 eV) used in the TRIARS experiments. Circles, $\omega_{\mathrm{RBM}} = 238$ cm^{-1}; triangles, $\omega_{\mathrm{RBM}} = 234$ cm^{-1}; inverted triangles, $\omega_{\mathrm{RBM}} = 228$ cm^{-1}; diamonds, $\omega_{\mathrm{RBM}} = 267$ cm^{-1}; crosses, $\omega_{\mathrm{RBM}} = 211$ cm^{-1}; rotated triangles, $\omega_{\mathrm{RBM}} = 260$ cm^{-1}; and stars, $\omega_{\mathrm{RBM}} = 249$ cm^{-1}.

contribute significantly to the *G*-mode signal. Using the method developed by Cheng *et al.*,[14] we analyzed details from our measured resonance profiles and RBM Raman shifts to determine the likely chiral indices associated with each RBM. Two TRIARS excitation energies, 1.51 and 1.63 eV, were then carefully selected so that the *G*-mode phonon dynamics could be obtained predominantly from SWCNTs in two separate diameter ranges. The three SWCNTs most resonant with the 1.51-eV excitation were (10,5), (11,3), and (12,1) and were associated with 228, 234, and 238 cm^{-1} RBM modes whose resonance energies were 1.52, 1.53, and 1.51 eV. The next-nearest resonance was at 1.59 eV, which did not contribute significantly to the Stokes or anti-Stokes Raman signal for this excitation. At an excitation of 1.63 eV there were four close resonances in (14,1), (8,6), (9,4), and (10,2) nanotubes whose RBM shifts were 211, 249, 260, and 267 cm^{-1} and resonance energies were 1.59, 1.69, 1.68, and 1.62 eV. The next-nearest resonance observed was at 1.53 eV, which similarly did not contribute significantly to the signal for this excitation. In all cases resonances were associated with the E_{22} optical transitions in semiconducting SWCNTs. Figure 3 shows the room-temperature Stokes Raman spectra of the RBM and *G*-mode features, taken at excitation energies of 1.51 and 1.63 eV. Both *G*-mode features shown in Fig. 3(b) are entirely in agreement with the semiconducting nature of the SWCNTs that are assigned to the RBMs in Fig. 3(a). All of the observed features were explicable as coming from SWCNTs, and there was no evidence of the strong 1582 cm^{-1} *G* mode seen in graphene and graphite.[33,34]

B. Resolving the G^+- and G^--mode dynamics

In our *G*-mode TRIARS experiments, a pump laser pulse generates a nonequilibrium phonon population in the

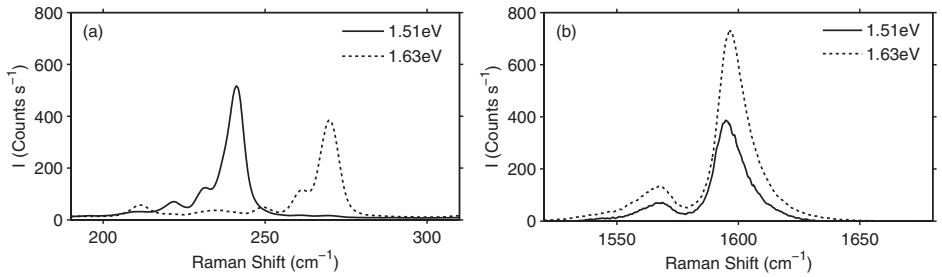

FIG. 3. Room-temperature (292 K) Stokes Raman spectra of the bundled HiPco SWCNT sample, taken with 1.51-eV (solid line) and 1.63-eV (dashed line) laser excitation showing (a) RBM and (b) G-mode Raman features.

SWCNTs through the relaxation of photoexcited carriers.[35,36] A second probe pulse then generates an anti-Stokes Raman signal which is proportional to the population of these phonons. The phonon dynamics is then observed by recording the anti-Stokes Raman signal generated by the probe pulse while varying the pump-probe delay. In Fig. 4(a), we show raw TRIARS spectra for a 0-ps pump-probe delay, where the nonequilibrium population of optical phonons was close to its maximum value, and for a 25-ps pump-probe delay, where there was no longer any measurable pump excitation. To subtract the equilibrium Raman spectrum and obtain the dynamics of the peak, we measured a background spectrum every third spectra at a time delay of 25 ps. This background subtraction technique was checked by comparing the background spectra with the sum of the spectra obtained with pump and probe beams separately. The background spectra obtained during TRIARS experiments were checked to ensure that the TRIARS system was stable, and if their magnitude varied by more than 20% over the duration of an experiment, the experiment was aborted and the data discarded.

Figure 4(b) shows nonequilibrium TRIARS spectra, obtained by background-subtracting the raw data in Fig. 4(a). To separately resolve the G^+- and G^--mode dynamics, the nonequilibrium spectra were fitted using a least-squares algorithm with a function consisting of the sum of two Lorentzian peaks (one for each G-mode phonon) and a linear background. The Lorentzian peak amplitude, peak position, and FWHM parameters were used to extract the mode intensity, Raman shift, and FWHM linewidth, respectively, for both the G^+ and G^- modes. We checked that the G^+- and G^--mode intensities could be independently determined by fixing all parameters except those controlling the Lorentzian which represented the G^- mode. In turn we altered the amplitude of the Lorentzian representing the G^+ mode to its upper and lower 95% confidence limits and reapplied the fit in each case. In doing this we observed no significant (<0.2%) variation in the fitted G^- amplitude, which confirmed that the G^+- and G^--mode intensities could be independently determined. Within the envelope of the cross-correlation we detected a small pump-probe delay dependence of the central Raman shift (<2 cm^{-1}). This blueshift has been observed in other G-band studies[24,25] and is understood to represent phonon stiffening caused by the reduced electron-phonon coupling at high electronic temperatures.[37] Figures 5(a) and 5(b) show the time dependence of the fitted peak intensities for both the G^+ and G^- modes at an excitation energy of 1.63 eV. Also shown in Fig. 5 are the corresponding pump and probe pulse cross-correlations, whose amplitudes have been scaled. To demonstrate the resolvability of the dynamics, we present the dynamics measured for $T = 4$ K and $T = 500$ K, where the decay rate is observed to be at its two extremes. The measured dynamics shown in Fig. 5 represents the convolution of the real phonon population dynamics and the pulse cross-correlation. Therefore, the real phonon dynamics are determined by fitting the convolution of two functions. The first function represents the pump and probe pulse cross-correlation, which was obtained for each measurement as discussed previously. The second function takes into account the indistinguishability of the two laser pulses and models the phonon population dynamics as an exponential rise followed by a monoexponential decay. The initial results obtained from this model indicate that the rise time was unresolvable (<200 fs); similar rise times have been observed in other TRIARS studies on the G mode.[18,24,25] Therefore, we have simplified the second function to assume an instantaneous rise followed by a monoexponential decay, in the form of Eq. (1), where x is the pump-probe delay, $H(x)$ is the Heaviside function, and t_2 is the phonon population lifetime. Fitting the room temperature dynamics gave a room-temperature lifetime of 1.2 ± 0.2 ps and 1.1 ± 0.4 ps for the G^+- and G^--mode

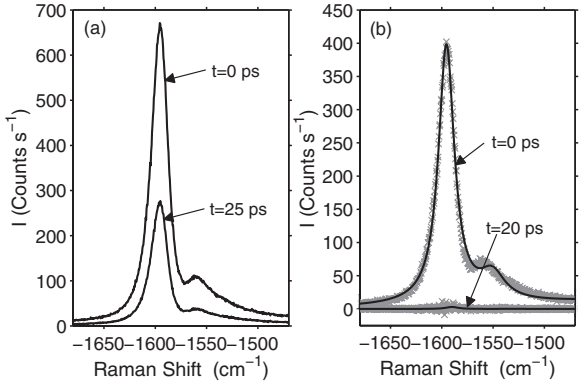

FIG. 4. (a) Raw G-mode TRIARS spectra for 25-ps and 0-ps pump-probe delay (indicated in figure), for an excitation energy of 1.63 eV and a temperature of 4 K. (b) Background-subtracted TRIARS spectra for G-mode for 0-ps and 20-ps pump-probe delay (indicated in figure), where background spectra were taken at 25-ps delay.

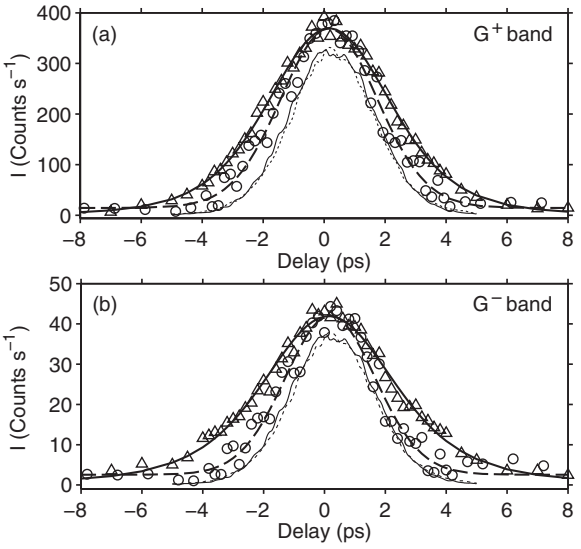

FIG. 5. Time dependence of the fitted peak intensities for both (a) G^+ and (b) G^- modes taken at 1.63 eV, showing experimental data taken at $T = 4$ K (open triangles) and $T = 500$ K (open circles). $T = 500$ K data has been scaled to the $T = 4$ K data for illusrative purposes. Also shown are monoexponential decay fits of the $T = 4$ K (thick solid line) and $T = 500$ K (thick dashed line) dynamics. Thin solid and dashed lines show the associated cross-correlations for $T = 4$ K and $T = 500$ K measurements.

phonons, respectively, for an excitation of 1.51 eV, and a room-temperature lifetime of 1.2 ± 0.2 ps and 1.0 ± 0.3 ps for the G^+- and G^--mode phonons, respectively, for an excitation of 1.63 eV:

$$f(x,t_2) = H(x)e^{-\frac{x}{t_2}} + H(-x)e^{\frac{x}{t_2}}. \quad (1)$$

C. Temperature dependence of *G*-mode phonon decay rate

In Fig. 6, we present our results on the temperature dependence of the decay rate of the G^+ [Figs. 6(a) and 6(c)] and G^- phonons [Figs. 6(b) and 6(d)], measured at two excitation energies, 1.51 eV [Figs. 6(a) and 6(b)] and 1.63 eV [Figs. 6(c) and 6(d)]. The error bars presented in Fig. 6 show 95% confidence bounds for the decay-rate fitting parameter. The reason why the confidence bounds in Fig. 6 generally increase with temperature can be explained by the faster dynamics that are observed with increasing temperature. This reduces the difference between the measured TRIARS dynamics and the pulse cross-correlation function (Fig. 5) and means the fitting routine is relying on fewer data points to secure the fit. In addition, the large error bars that are observed in Figs. 6(b) and 6(d), compared with those in Figs. 6(a) and 6(c), can be explained by the ratio of the peak intensities of the G^+ and G^- modes, seen in Fig. 4(b). Where possible, multiple independent TRIARS experiments were performed and are shown to display the significance of these errors. In each case we see no significant change in the decay rate below 200 K, and an increasing decay rate between 200 and 600 K. This observation is consistent with the temperature-dependent results obtained by Kang *et al.* and Chatzakis *et al.* To compare the anharmonic decay of these phonons, we have used the same anharmonic decay model that was used by Chatzakis *et al.* The form of this model is given by Eq. (2), where Bose-Einstein statistics $n_i(E_i,T)$ are used for the population of the two daughter phonons, whose energies must sum to give the energy of the parent phonon, i.e., $E_2 = E_G - E_1$. These fits are presented in Fig. 6, and the parameters obtained from these fits are given in Table I. It is clear that this model describes the observed temperature dependence well; however, the fitting of the experimental data in Fig. 6(d) did not generate parameters with sensible confidence bounds. Therefore, the fit from Fig. 6(b) is plotted as a dashed line in Fig. 6(d) and shows a good correlation with the experimental data. Referring to Table I, we see no measurable change in the

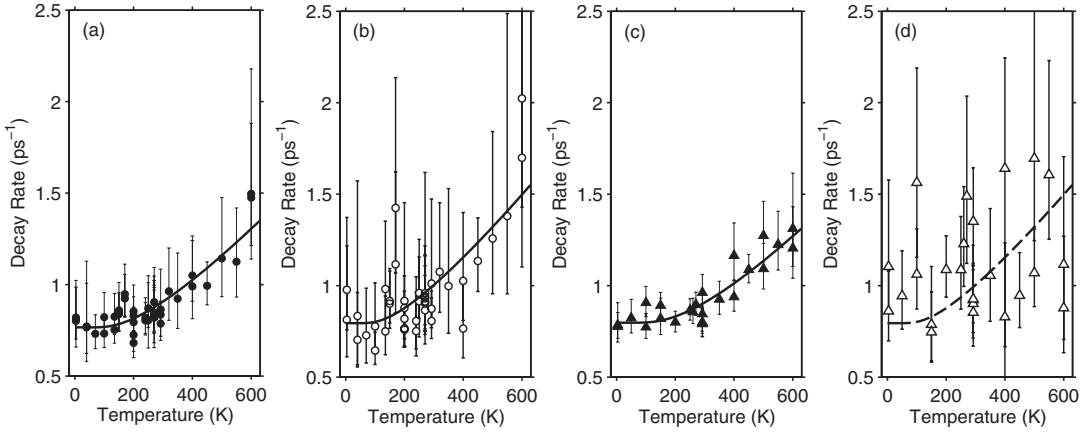

FIG. 6. The decay rate as a function of temperature for (a) G^+-mode phonon and (b) G^--mode phonon for an excitation of 1.51 eV, and for (c) G^+-mode phonon and (d) G^--mode phonon for an excitation of 1.63 eV. The experimental data (represented as symbols) in (a)–(c) are fit to Eq. (2) (solid lines). The fit from (b) is overlaid as a dashed line in (d). Each symbol corresponds to an independent measurement of the TRIARS dynamics. The error bars represent the 95% confidence bounds for the fitting parameter, obtained from the fitting procedure.

TABLE I. Fitting parameters obtained from Eq. (2).

Band	E_i (eV)	E_1 (cm^{-1})	E_2 (cm^{-1})	Γ_0 (ps^{-1})
G^+	1.51	391 ± 59	1200 ± 59	0.77 ± 0.04
G^-	1.51	329 ± 99	1226 ± 99	0.79 ± 0.08
G^+	1.63	445 ± 72	1146 ± 72	0.80 ± 0.04

absolute decay rate, Γ_0, when varying the excitation energy. We also see no measurable difference in Γ_0 for the LO and TO G-mode phonons. Similarly, to within the experimental error, the daughter phonon energies obtained from fitting Eq. (2) are the same in all of our measurements. When using a similar fit to compare the anharmonic decay in SWCNTs and graphene,[25] Chatzakis *et al.* measured a large energy difference between the predicted daughter phonon pairs. This behavior was presumed to be caused by the addition of decay channels from modes that are unique to SWCNTs, such as anharmonic decay with the RBM as one of the two daughter phonons. To determine if the RBM was significantly contributing to G-mode phonon decay, we altered Eq. (2) to include two anharmonic decay channels: one where the two daughter phonons include an RBM, and one where the energy distribution of the daughter phonons is free to change, satisfying $E_2 = E_G - E_1$. We allow these separate decay channels to have independent weightings given by a and b, where $a + b = 1$. The form of this new model is given by Eq. (3). For all of our experimental data in Fig. 6, the best fits for Eq. (3) were obtained when the contribution from the RBM anharmonic decay channel was completely suppressed, i.e., for weighting parameters $a = 0$, $b = 1$. This result suggests that the RBM does not contribute significantly to G-mode phonon decay in SWCNTs:

$$\Gamma(T) = \Gamma_0[1 + n(E_1,T) + n(E_2,T)], \tag{2}$$

$$\Gamma(T) = \Gamma_0[a(1 + n(E_{\mathrm{RBM}},T) + n(E_G - E_{\mathrm{RBM}},T)) + b(1 + n(E_1,T) + n(E_2,T))]. \tag{3}$$

IV. CONCLUSIONS

In conclusion, this paper presents TRIARS measurements of G-mode phonons in SWCNTs which separate the G^+-mode and G^--mode dynamics. These measurements have been performed over the temperature range 4–600 K and for two different laser energies, 1.63 and 1.51 eV, where the TRIARS signal is dominated by the response of SWCNTs in different diameter ranges, $0.88 < d < 0.97$ nm and $0.99 < d < 1.05$ nm. These results clearly support the hypothesis that the decay dynamics is the same for both G^+ and G^- modes and does not strongly depend on tube diameter. They also support the hypothesis that the main decay channel is two-phonon anharmonic decay with the lower-energy phonon having an energy of approximately $400 \pm 100\ cm^{-1}$. The common decay dynamics of G-mode phonons, which is contrary to the tube-dependent dynamics of the D-mode phonons,[38] is probably to be expected, as all of the G-mode phonons in all SWCNTs are derived from the same G-mode phonon in graphene.[11] However, other studies have shown that the G-mode population lifetime is shorter in SWCNTs than in graphene. This has been attributed to additional decay channels that are unique to SWCNTs, such as two-phonon anharmonic decay involving an RBM, which in principle may vary with tube type. Attempts to fit the temperature dependence of the phonon decay rate with two contributing anharmonic decay channels, with one decay channel producing an RBM, are not consistent with RBMs playing a significant role in the decay of G-mode phonons in semiconducting SWCNTs. Our data are also not consistent with a general difference between G^+ and G^- decay rates being responsible for the difference between the decay rates for metallic and semiconducting SWCNTs measured by Kang *et al.* A similar study on metallic SWCNTs may reveal whether additional decay channels are responsible for the faster decay rate observed in metallic SWCNTs compared with semiconducting SWCNTS. This work has proved that it should be possible to resolve G^+ and G^- decay rates using our experimental system and this is the subject of an ongoing study.

What are the implications of our measurements and the TRIARS measurements of others for the understanding of high-field transport in single-walled carbon nanotubes? Theoretical predictions of the effect of high-field transport[5,7] indicate that both the small-wave-vector optical phonons (G mode) and the large-wave-vector phonons (with wave vectors near the K points) can contribute to the high-field effects. The TRIARS measurements presented here and in other papers strongly suggest that the G-mode population lifetime is too short, i.e., much less than the 5 ps required for a sufficiently large nonequilibrium population to build up, for this to be the sole reason for the high-field transport effects in SWCNTs. There has only been one TRIARS study of the population lifetime of large-wave-vector phonons (D mode) and these phonons were not precisely the ones which would be responsible for the transport effects. However, TRIARS measurements of the large-wave-vector phonon suggest that, if anything, the large-wave-vector phonon populations have shorter lifetimes (~1 ps). This strongly suggests that a nonequilibrium population of optical phonons cannot explain the high-field transport properties on their own. A more likely explanation would be the buildup of nonequilibrium populations of both optical and low-frequency phonon modes. However, it is possible that another explanation will be required.

[1] M. Dresselhaus, G. Dresselhaus, and P. Avouris, *Carbon Nanotubes: Synthesis, Structure, Properties, and Applications* (Springer, Berlin, 2001).
[2] M. Dresselhaus and H. Dai, MRS Bull. **29**, 237 (2004).
[3] G. Pennington and N. Goldsman, Phys. Rev. B **71**, 205318 (2005).
[4] V. Perebeinos, J. Tersoff, and P. Avouris, Phys. Rev. Lett. **94**, 086802 (2005).
[5] M. Lazzeri and F. Mauri, Phys. Rev. B **73**, 165419 (2006).
[6] A. Javey, J. Guo, M. Paulsson, Q. Wang, D. Mann, M. Lundstrom, and H. Dai, Phys. Rev. Lett. **92**, 106804 (2004).
[7] M. Lazzeri, S. Piscanec, F. Mauri, A. C. Ferrari, and J. Robertson, Phys. Rev. Lett. **95**, 236802 (2005).
[8] A. Jorio, M. A. Pimenta, A. G. S. Filho, R. Saito, G. Dresselhaus, and M. S. Dresselhaus, New J. Phys. **5**, 139 (2003).

[9]H. Telg, J. Maultzsch, S. Reich, F. Hennrich, and C. Thomsen, Phys. Rev. Lett. **93**, 177401 (2004).
[10]C. Fantini, A. Jorio, M. Souza, M. S. Strano, M. S. Dresselhaus, and M. A. Pimenta, Phys. Rev. Lett. **93**, 147406 (2004).
[11]M. Dresselhaus, G. Dresselhaus, R. Saito, and A. Jorio, Phys. Rep. **409**, 47 (2005).
[12]M. S. Dresselhaus and P. C. Eklund, Adv. Phys. **49**, 705 (2000).
[13]H. Kataura, Y. Kumazawa, Y. Maniwa, I. Umezu, S. Suzuki, Y. Ohtsuka, and Y. Achiba, Synth. Met. **103**, 2555 (1999).
[14]Q. Cheng, S. Debnath, E. Gregan, and H. Byrne, Appl. Phys. A **102**, 309 (2011).
[15]M. S. Strano, S. K. Doorn, E. H. Haroz, C. Kittrell, R. H. Hauge, and R. E. Smalley, Appl. Phys. A **3**, 1091 (2003).
[16]F. Hennrich, R. Krupke, S. Lebedkin, K. Arnold, R. Fischer, D. E. Resasco, and M. M. Kappes, J. Phys. Chem. B **109**, 10567 (2005).
[17]Y. J. Lee, S. H. Parekh, J. A. Fagan, and M. T. Cicerone, Phys. Rev. B **82**, 165432 (2010).
[18]D. Song, F. Wang, G. Dukovic, M. Zheng, E. D. Semke, L. E. Brus, and T. F. Heinz, Phys. Rev. Lett. **100**, 225503 (2008).
[19]A. Jorio, C. Fantini, M. S. S. Dantas, M. A. Pimenta, A. G. S. Filho, G. G. Samsonidze, V. W. Brar, G. Dresselhaus, M. S. Dresselhaus, A. K. Swan, M. S. Ünlü, B. B. Goldberg, and R. Saito, Phys. Rev. B **66**, 115411 (2002).
[20]E. V. Efremov, F. Ariese, and C. Gooijer, Anal. Chim. Acta **606**, 119 (2008).
[21]A. M. Rao, P. C. Eklund, S. Bandow, A. Thess, and R. E. Smalley, Nature (London) **388**, 257 (1997).
[22]F. Simon, R. Pfeiffer, and H. Kuzmany, Phys. Rev. B **74**, 121411 (2006).
[23]R. Pfeiffer, H. Kuzmany, C. Kramberger, C. Schaman, T. Pichler, H. Kataura, Y. Achiba, J. Kürti, and V. Zólyomi, Phys. Rev. Lett. **90**, 225501 (2003).
[24]K. Kang, T. Ozel, D. G. Cahill, and M. Shim, Appl. Phys. A **8**, 4642 (2008).
[25]I. Chatzakis, H. Yan, D. Song, S. Berciaud, and T. F. Heinz, Phys. Rev. B **83**, 205411 (2011).
[26]G. Pennington, S. J. Kilpatrick, and A. E. Wickenden, Appl. Phys. Lett. **93**, 093110 (2008).
[27]H. Kuzmany, *Solid-State Spectroscopy: An Introduction* (Springer-Verlag, Berlin, 1998).
[28]S. D. M. Brown, A. Jorio, P. Corio, M. S. Dresselhaus, G. Dresselhaus, R. Saito, and K. Kneipp, Phys. Rev. B **63**, 155414 (2001).
[29]E. Di Donato, M. Tommasini, C. Castiglioni, and G. Zerbi, Phys. Rev. B **74**, 184306 (2006).
[30]M. Fouquet, H. Telg, J. Maultzsch, Y. Wu, B. Chandra, J. Hone, T. F. Heinz, and C. Thomsen, Phys. Rev. Lett. **102**, 075501 (2009).
[31]J. S. Park, K. Sasaki, R. Saito, W. Izumida, M. Kalbac, H. Farhat, G. Dresselhaus, and M. S. Dresselhaus, Phys. Rev. B **80**, 081402 (2009).
[32]See Supplemental Material at http://link.aps.org/supplemental/10.1103/PhysRevB.87.195446 for the low-temperature RBM resonance profiles.
[33]L. Malard, M. Pimenta, G. Dresselhaus, and M. Dresselhaus, Phys. Rep. **473**, 51 (2009).
[34]A. C. Ferrari, J. C. Meyer, V. Scardaci, C. Casiraghi, M. Lazzeri, F. Mauri, S. Piscanec, D. Jiang, K. S. Novoselov, S. Roth, and A. K. Geim, Phys. Rev. Lett. **97**, 187401 (2006).
[35]V. Perebeinos, J. Tersoff, and P. Avouris, Phys. Rev. Lett. **94**, 027402 (2005).
[36]F. Wang, G. Dukovic, E. Knoesel, L. E. Brus, and T. F. Heinz, Phys. Rev. B **70**, 241403 (2004).
[37]H. Yan, D. Song, K. F. Mak, I. Chatzakis, J. Maultzsch, and T. F. Heinz, Phys. Rev. B **80**, 121403 (2009).
[38]J. M. Nesbitt and D. C. Smith, Appl. Phys. A **13**, 416 (2013).

CHEMISTRY OF MATERIALS

Article

pubs.acs.org/cm

Chemical Vapor Deposition of GaP and GaAs Thin Films From [^{n}Bu$_2$Ga(μ-E^{t}Bu$_2$)$_2$Ga^{n}Bu$_2$] (*E* = P or As) and Ga(P^{t}Bu$_2$)$_3$

Fei Cheng,[†] Kathryn George,[†] Andrew L. Hector,[†] Marek Jura,[‡] Anna Kroner,[§] William Levason,[†] John Nesbitt,[#] Gillian Reid,*[,†] David C. Smith,*[,#] and James W. Wilson[#]

[†]School of Chemistry, University of Southampton, Southampton SO17 1BJ, U.K.

[‡]ISIS, STFC, Harwell Innovation Campus, Didcot, Oxfordshire, OX11 0QX, U.K.

[§]Diamond Light Source plc, Harwell Innovation Campus, Didcot, Oxfordshire OX11 0DE, U.K.

[#]School of Physics and Astronomy, University of Southampton, Southampton SO17 1BJ, U.K.

Supporting Information

ABSTRACT: Low pressure chemical vapor deposition (LPCVD) using the single-source precursors [^{n}Bu$_2$Ga(μ-E^{t}Bu$_2$)$_2$Ga^{n}Bu$_2$] (E = P or As) in the temperature range 723−823 K (0.05 mmHg), gives shiny yellow or silvery gray films of GaP and GaAs, respectively, on silica. The composition and morphology of the deposited materials have been probed via X-ray diffraction (XRD), scanning electron microscopy/energy-dispersive X-ray (SEM/EDX), X-ray photoelectron spectroscopy (XPS), atomic force microscopy (AFM), and Raman spectroscopy, revealing crystalline (cubic) GaE with 1:1 Ga/E ratios. The GaP forms nanorods growing perpendicular to the substrate surface and is rougher than the GaAs, which appears to form smaller, densely packed microcrystallites. While the GaAs films produced in this way did not exhibit any significant luminescence, the reflective GaP films obtained by LPCVD were of good electronic quality, revealing photoluminescence comparable to that of a single crystalline GaP reference. LPCVD using Ga(P^{t}Bu$_2$)$_3$ gives GaP, although this appears to be an inferior reagent compared to the dimer. Unlike the corresponding [^{n}Bu$_2$In(μ-E^{t}Bu$_2$)$_2$In^{n}Bu$_2$] dimers (see Aksomaityte et al., *Chem. Mater.* **2010**, *22*, 4246) which gave InE films and nanowires from supercritical chemical fluid deposition in sc-CO$_2$/hexane, under the same conditions (773 K, 12 MPa), the gallium dimer precursors mostly failed to give GaE. Instead significant carbon deposition occurred, indicating solvent degradation.

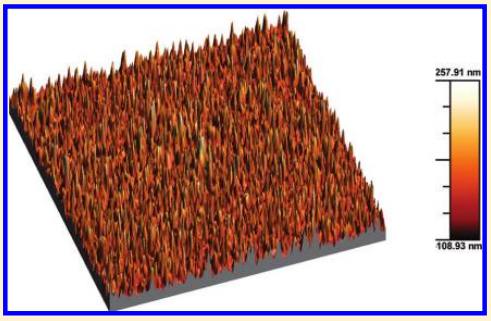

KEYWORDS: *gallium phosphide, gallium arsenide, chemical vapor deposition, luminescence*

1. INTRODUCTION

Semiconductors composed of group 13 and 15 elements (III−V materials) have huge technological significance, particularly for optoelectronic applications.[1] A key application for GaP is low cost green, orange, and red light emitting diodes, which have been produced commercially since the 1970s. GaAs is used in laser diodes and high efficiency solar cells and is also a valuable alternative to silicon for applications that require higher electron mobility, thermal stability, and resistance to radiation damage. In addition, GaAs and GaP based alloys are used in a wide range of III−V heterostructured devices.

Key deposition methods for III−V materials are vapor phase epitaxy, molecular beam epitaxy and metal−organic chemical vapor deposition (MOCVD), which have been refined to the extent that they are capable of producing high purity material with good control of film thickness. Trimethylgallium in conjunction with phosphine (PH_3) or arsine (AsH_3) have dominated CVD deposition of GaP and GaAs since the pioneering work of Manasevit and Simpson.[2] Other volatile liquid reagents, such as ^{t}BuEH$_2$, have been employed in place of the extremely toxic EH_3 gases in dual-source CVD, giving better control of composition (particularly for GaP), although these are still pyrophoric.[3] While nanowires of GaP and GaAs have been grown using ^{t}Bu$_3$Ga and E(SiMe$_3$)$_3$ (E = P or As) seeded with thiol-stabilized gold nanocrystals in supercritical hexane,[4] this is a rare example of dual-source deposition from such media. It is acknowledged that the reagents typically used in the dual-source deposition of GaE are not readily amenable to other types of deposition which may be necessary for certain applications, such as in nanoparticle formation (via high temperature solvents) or for filling high aspect ratio pores (via supercritical chemical fluid deposition (SCFD)). Single-source precursors are attractive as alternatives, as they tend to be powdered solids, rather less toxic or pyrophoric, and hence, if GaE with sufficiently high purity can be obtained, these may be much more convenient for certain applications and

Received: July 27, 2011
Revised: September 23, 2011
Published: November 15, 2011

deposition media. Previous work shows that adducts of $GaClR_2$ with tertiary phosphines or arsines such as EEt_3 generally lack volatility and surface mobility.[5] Using anionic phosphido or arsenido complexes can be advantageous, although the chloro-species $[Cl_2Ga(\mu\text{-}ER_2)]_n$ are unlikely to have sufficient volatility for CVD. $[^nBu_2Ga(\mu\text{-}P(SiMe_3)_2)]_2$ is also insufficiently volatile for CVD, but it may be pyrolyzed readily to give GaP, albeit with significant Si contamination.[6] In previous work, a series of single-source molecular species, such as of the form $[R_2^1Ga(\mu\text{-}ER_2^2)]_n$ (E = P, As; R^1, R^2 = alkyl; n = 2 or 3) or $Ga(AsR_2)_3$, have been used to good effect, and shown to be particularly effective for GaAs deposition, although studies on GaP deposition from these reagents are much more limited in the open literature.[7,8]

In another work we have shown that supercritical chemical fluid deposition (SCFD) may be used to deposit high quality CdS[9] and thin films of luminescent quality InP and InAs nanowires.[10] The III–V materials were produced from the dimeric single-source precursors $[^nBu_2In(\mu\text{-}E^tBu_2)_2In^nBu_2]$ (E = P or As) in single phase sc-CO_2/hexane at 773 K; a key feature being the high solubility of the dimers in the supercritical fluid medium and their relatively high stability compared to the reagents typically used in dual-source deposition, trialkylindium and PH_3 or AsH_3. Notably, low pressure (LP) CVD experiments also using these reagents were much less successful, leading to indium rich phases.

In this paper, we describe our efforts toward deposition of GaP and GaAs under comparable conditions from the corresponding gallium precursors $[^nBu_2Ga(\mu\text{-}E^tBu_2)_2Ga^nBu_2]$ using both LPCVD and SCFD, as well as LPCVD from the tris-phosphido gallium reagent $Ga(P^tBu_2)_3$. The preparations of these precursor compounds have been described by Cowley and co-workers,[11b,c] and they have also shown that the arsenide-reagents, $[R_2Ga(\mu\text{-}As^tBu_2)_2GaR_2]$ (R = Me, ^{i}Pr, ^{t}Bu), may be used to grow n- (Me) or p-type (^{i}Pr, ^{t}Bu) GaAs by LPCVD, including epitaxial films.[8,11] In practice, $Ga(As^tBu_2)_3$ seemed to give the highest quality GaAs, attributed in part to the absence of Ga–C bonds in the precursor.[11a] In contrast, deposition of GaP films using the molecular, single-source phosphido-reagents has been much less studied. Given our successful deposition of InE from $[^nBu_2In(\mu\text{-}E^tBu_2)_2In^nBu_2]$ via SCFD, we have now undertaken similar studies on Ga reagents using both deposition techniques, demonstrating here that while in practice the $[^nBu_2Ga(\mu\text{-}E^tBu_2)_2Ga^nBu_2]$ precursors are not well-suited to SCFD, the phosphido-species does appear to be a valuable reagent for CVD of GaP.

2. EXPERIMENTAL SECTION

All reactions were conducted using Schlenk, vacuum line, and glovebox techniques, under a dry nitrogen atmosphere. The reagents were stored and manipulated using a glovebox. $[^nBu_2Ga(E^tBu_2)_2Ga^nBu_2]$ (E = P, As) and $Ga(P^tBu_2)_3$ were prepared by the methods published by Cowley et al.[11b,c] Hexane, toluene, diethyl ether, and THF were dried by distillation over sodium/benzophenone. $GaCl_3$, ^{n}BuLi, ^{t}BuLi, $AsCl_3$ and HP^tBu_2 were obtained from Aldrich and used as received. LiP^tBu_2, HAs^tBu_2 and $LiAs^tBu_2$ were prepared according to the method of Holga et al.[12]

2.1. Characterization. X-ray diffraction (XRD) analysis was performed on a Bruker AXS D8 Discover with GADDS detector using Cu Kα_1 radiation and a 5° incident angle. Scanning electron microscopy (SEM) was performed on gold coated samples at an accelerating voltage of 20 kV using a JEOL JSM 5910, and energy-dispersive X-ray (EDX) data on carbon coated samples were obtained with an Oxford INCA300 detector. Raman measurements were taken at an excitation energy of 3.09 eV, which was produced by a Coherent Inc. mode locked Mira 900 Ti:Sapphire laser and second harmonic generator (SHG). The bandwidth of the pulses was 0.30 nm; the pulses were produced at a repetition rate of 80 MHz. The Raman microscope was set up in a colinear alignment, where an Olympus LMPlan 50× IR objective was used to focus an 8 mW beam to a spot size $\approx$ 1 μm^2 on the sample and subsequently collect the scattered Raman light. The Raman signal was detected with a Princeton Instruments Pi-Action TriVista triple spectrometer fitted with a Roper Scientific ST133B nitrogen cooled charge-coupled device (CCD). Photoluminescence measurements were made with a 405 nm excitation from a Diode laser (Sanyo, DL-3146-151). A power density of 8.7 W cm^{-2} was used. The emission was collected and collimated by 0.25 NA lens, passed through a 45° laser line mirror (CVI TLM1-400-45P-2037) to remove the intense laser light, and then focused into an optical fiber and analyzed using a UV–visible spectrometer (Ocean Optics, HR4000). The throughput of the system was corrected for using a fiber coupled tungsten–halogen white light source placed at the position of the sample. Atomic force microscopy (AFM) was conducted using a Veeco Dimension 3100 in tapping mode. Absorption spectra were recorded using the diffuse reflectance attachment of a Perkin-Elmer Lambda 19 spectrometer.

X-ray photoelectron spectroscopy (XPS) data were obtained using a Scienta ESCA300 photoelectron spectrometer with a rotating anode Al Kα (hν = 1486.7 eV) X-ray source at the National Centre for Electron Spectroscopy and Surface Analysis (NCESS), Daresbury Laboratory, U.K. Samples were etched using argon ion bombardment for 300 s at 3 keV. Where necessary, sample charging was eliminated by use of an electron flood gun delivering 5 eV electrons. The Ga 2p and 3p, As 2p and 3p, P 2s and 2p, C 1s, and O 1s spectra were collected. The CasaXPS package was used for data analysis. Data were referenced to the C 1s peak, which was assigned a binding energy of 284.8 eV.

2.2. LPCVD from $[^nBu_2Ga(E^tBu_2)_2Ga^nBu_2]$ (E = P, As). In a typical experiment, 0.100 g of reagent and silica substrates were loaded into a closed-end silica tube in a glovebox (precursor at the closed end, followed by substrates positioned end-to-end through the heated region). The tube was set in a furnace such that the precursor was outside the heated zone, the tube was evacuated, then heated to the target deposition temperature (773 K) under 0.05 mmHg (66 Pa) and the furnace was allowed to stabilize. The tube position was then adjusted so that the precursor was moved gradually toward the hot zone until slow sublimation was observed (approximately 573 K based on temperature profiling carried out after deposition). At this point the sample position was maintained until sublimation and deposition were complete. The tube was then cooled to room temperature and transferred to the glovebox where the tiles were removed and stored under an N_2 atmosphere prior to analysis. Typically, the best films were found just outside the furnace hot zone and 50–100 mm from the precursor, where the temperature was ca. 30 K below the set temperature, and these were the films selected for further study. Similar experiments were conducted at 623, 673, 723, and 823 K.

2.3. LPCVD from $Ga(P^tBu_2)_3$. In a typical experiment, 0.100 g of reagent and silica substrates were loaded into a quartz tube in a glovebox. The tube was set in a furnace and evacuated; then, it was heated to achieve deposition at 773 K under 0.05 mmHg (66 Pa), using the method described above.

Samples deposited at lower temperatures tended to have a more matte appearance, whereas higher temperatures gave reflective films, and EDX measurements revealed Ga:E ratios closer to 1:1 from the higher temperature depositions. GaAs films obtained were gray, shiny, and reflective, with powdery regions on the substrates closest to the precursor. The majority of the GaP films were yellow or grayish and powdery; however, films deposited at higher temperatures (773 K) were yellow, shiny, and reflective, and these were the ones subjected to more detailed analysis, including photoluminescence measurements. Samples were generally very well adhered to the tiles, as evidenced by the fact they remained intact even when removed from an SEM stub to which they had been attached by carbon tape. Excellent reproducibility was obtained and films were visually very similar between depositions

conducted at the same temperature. Similar characterization data were obtained from several different samples.

3. RESULTS AND DISCUSSION

The air-sensitive, white dimeric compounds [^{n}Bu$_2$Ga(μ-E^{t}Bu$_2$)$_2$Ga^{n}Bu$_2$] (E = P or As) were obtained in good yield using the method developed by Cowley and co-workers.[11b,c] The tris-phosphido gallium reagent, Ga(P^{t}Bu$_2$)$_3$, was isolated as an extremely moisture and oxygen sensitive red solid by reaction of GaCl$_3$ with LiP^{t}Bu$_2$ in THF.[11b,c] The solids were stored and manipulated in an N$_2$ purged, dry (<1 ppm H$_2$O) glovebox and were characterized by ^{1}H and ^{31}P{^{1}H} NMR spectroscopy and microanalysis as appropriate.

3.1. LPCVD of GaP and GaAs. LPCVD from [^{n}Bu$_2$Ga(μ-E^{t}Bu$_2$)$_2$Ga^{n}Bu$_2$] was undertaken as described previously[8] at a range of temperatures (50 degree intervals) between 623 and 823 K, leading to clean sublimation of the precursor compound (no residue) and deposition of yellow films (E = P) and shiny silvery films (E = As) onto the silica substrate. The tiles closest to the precursor tended to produce a powdery deposit, whereas in the hotter region of the furnace much more reflective films were produced, and in general, the arsenide reagents yielded more reflective deposits than the phosphide reagent. The films that were selected for further characterization were typically those deposited at approximately at 723 K. These films were selected by visual inspection, choosing either yellow films (E = P) or shiny silvery films (E = As).

By analogy with the GaAs work,[11a] we also studied Ga(P^{t}Bu$_2$)$_3$ as a reagent for deposition of GaP via LPCVD under similar conditions. It was anticipated that the increased P/Ga ratio in the precursor might have a favorable effect on the composition of the deposited films and this reagent has been used successfully to make GaP nanoparticles and quantum dots.[13] These experiments resulted in the deposition of thin shiny yellow films on the slides closest to the precursor, and a significant amount of yellow powdery material remained where the reagent had been positioned originally. The films were shown to be crystalline GaP by X-ray diffraction (XRD) and SEM analysis, with EDX showing Ga/P ratios of 1:1.0. There was some minor variation in composition across the tiles (< ± 0.1 in ratio of Ga/P by EDX). The remaining yellow powder also contained mainly GaP, along with GaPO$_4$ and other impurities. On the basis that a significant amount of GaP was produced where the precursor complex had been positioned originally, indicating that the sublimation and deposition temperatures for this reagent are very similar, it was concluded that this was an inferior reagent for LPCVD of GaP, and therefore, the discussion below focuses on the materials deposited from the dimeric reagents [^{n}Bu$_2$Ga(μ-E^{t}Bu$_2$)$_2$Ga^{n}Bu$_2$].

XRD measurements on the materials deposited from [^{n}Bu$_2$Ga(μ-E^{t}Bu$_2$)$_2$Ga^{n}Bu$_2$] at 773 K confirmed them to be cubic GaP (a = 5.465(4) − 5.503(9) Å) (Figure 1) and cubic GaAs (a = 5.465(4) − 5.496(5) Å) (Figure 2), respectively (literature values for bulk GaP and GaAs are 5.358 − 5.473 Å and 5.508 − 5.750 Å),[14] with no evidence of other phases. There is no significant variation with temperature and no evidence from the X-ray patterns for preferred orientation of the crystallites.

Raman spectra recorded from the same thin film samples each show two bands (Figure 3), GaP (at 367 and 402 cm^{-1}) and GaAs (at 270 and 291 cm^{-1}), which are entirely in agreement with literature values for the TO and LO phonons in each material, respectively.[15,16] Raman measurements taken at several locations on the sample showed variations in the relative amplitudes of the TO and LO peaks, as well as small shifts in the peak frequencies, which can easily be explained by the microcrystallinity of the sample.

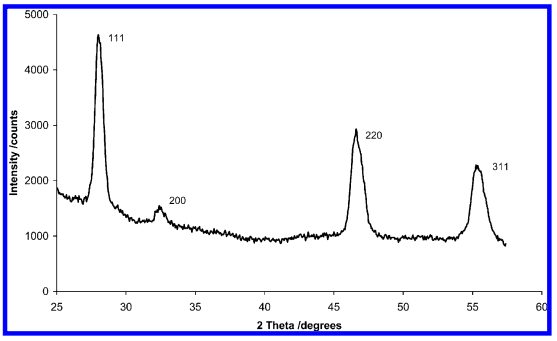

Figure 1. XRD pattern obtained from a GaP thin film grown on silica at 773 K by LPCVD from [^{n}Bu$_2$Ga(μ-P^{t}Bu$_2$)$_2$Ga^{n}Bu$_2$].

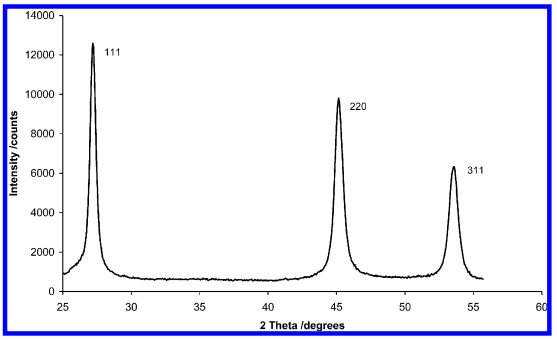

Figure 2. XRD pattern obtained from a GaAs thin film grown on silica at 773 K by LPCVD from [^{n}Bu$_2$Ga(μ-As^{t}Bu$_2$)$_2$Ga^{n}Bu$_2$].

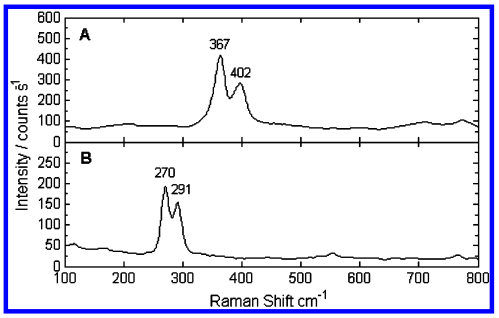

Figure 3. Raman spectra of GaP (a) and GaAs (b) thin films grown by LPCVD at 773 K from [^{n}Bu$_2$Ga(μ-E^{t}Bu$_2$)$_2$Ga^{n}Bu$_2$].

SEM analysis on the more reflective GaP films showed a regular morphology formed of a dense mat of columnar nanorods with a growth direction approximately perpendicular to the substrate surface (Figure 4), and typical GaP films grown at 773 K using 0.10 g of precursor were ~1 μm thick. The GaAs film morphology was much denser and smoother than that of the GaP (Figure 4). AFM measurements (Figure 5) were consistent with the SEM data, revealing that the GaP film surfaces are considerably rougher than the GaAs films produced

dx.doi.org/10.1021/cm202158a | Chem. Mater. 2011, 23, 5217–5222

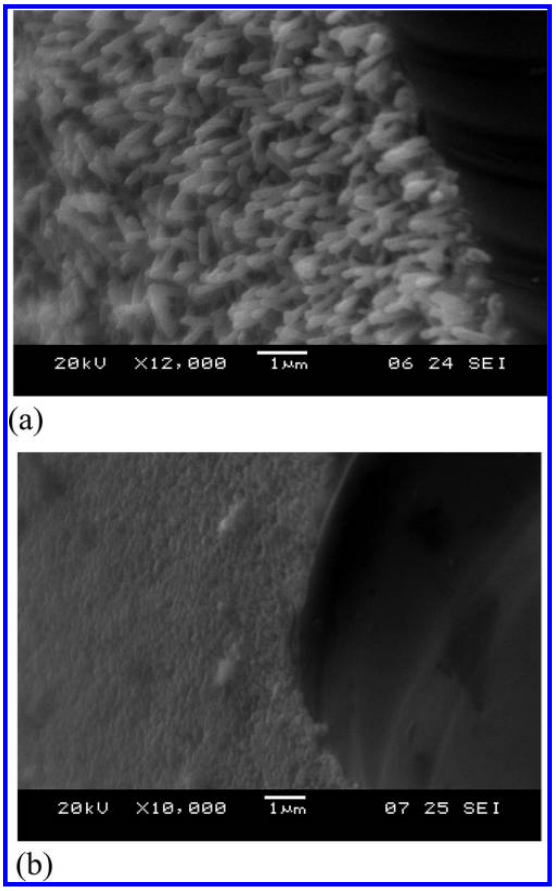

Figure 4. SEM cross-sectional images of (a) cubic GaP film and (b) GaAs films deposited on silica at 773 K by LPCVD from [$^{n}Bu_2Ga(\mu\text{-}E^{t}Bu_2)_2Ga^{n}Bu_2$]. Tiles were fractured through the films and the darker regions on the right-hand side of the images are the fractured tile edges.

under the same experimental conditions (GaAs rms roughness = 8.0 nm (2 × 2 μm scan)). The obvious columnar morphology of the GaP surface precluded accurate determination of its rms roughness.

The elemental composition of these deposited materials was probed by EDX analysis, which showed Ga/P and Ga/As ratios closest to 1:1.0 for samples deposited at higher temperature (773 K; see the Supporting Information). XPS measurements on unetched films showed P- or As-deficient compositions. Only one Ga, P, and As environment was observed in these GaE films. For GaAs, both O (15.9 wt %) and C (4.6 wt %) were also evident. With the expectation that the oxygen presence and the pnictogen deficiency were due to reactions of the surface with air (XPS only samples the top few nm of the sample), the samples were Ar ion etched. This resulted in significant reductions in the oxygen and carbon signals (to 10% and 1.8 wt %, respectively). The rod-like morphology of the GaP samples is likely to lead to inherently higher C and O levels pre-etching, as observed, and this also precluded effective etching of the whole of their surfaces; hence, the % C and % O

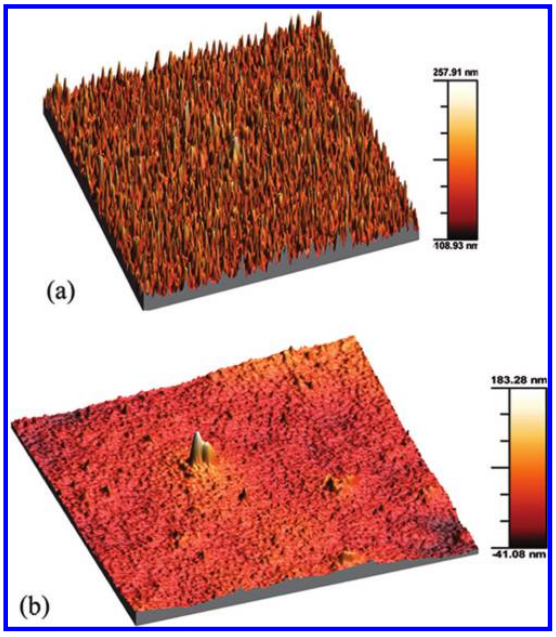

Figure 5. 3-D AFM images (20 μm × 20 μm) of films grown at 773 K by LPCVD from [$^{n}Bu_2Ga(\mu\text{-}E^{t}Bu_2)_2Ga^{n}Bu_2$], E = P (a) and E = As (b).

determinations from the GaP samples were not possible by XPS.

To probe the electronic quality of the GaP films, photoluminescence measurements were also undertaken on a number of the GaP and GaAs thin film samples. The GaP samples gave photoluminescence whose magnitude and form was comparable with that from a single crystalline sample (99.99%, Aldrich) (Figure 6), suggesting the deposited material has good

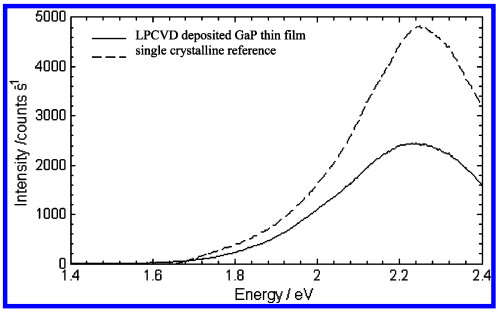

Figure 6. Luminescence spectrum of GaP film grown at 773 K by LPCVD from [$^{n}Bu_2Ga(\mu\text{-}P^{t}Bu_2)_2Ga^{n}Bu_2$].

electronic quality. However, the GaAs samples gave no measurable luminescence. One likely explanation for this is that the GaAs is formed from nanocrystallites whose surfaces act as nonradiative recombination sites. For this reason we repeated the photoluminescence measurements with samples that had been freshly etched with 12 mol dm^{-3} HCl (for GaAs) or 12 mol dm^{-3} H_2SO_4 (for GaP) for 6 and 10 s, respectively, to try to remove the nonradiative recombination sites.[17,18] The

dx.doi.org/10.1021/cm202158a | *Chem. Mater.* 2011, 23, 5217–5222

etching had little effect for the GaP samples and references. In the case of GaAs, the etching increased the intensity of the luminescence from the single crystal reference by approximately a factor of 6; however, the GaAs samples still produced no luminescence. While this may indicate these samples consist of defective GaAs, it is also possible that the dense nature of the films means that the etchant was unable to reach most of the crystallite interfaces.

An optical transmission measurement from a shiny GaAs film is presented in Figure 7a. While a precise determination of the onset of absorption in the film is difficult, the onset has certainly occurred by 1.46 eV, the accepted band gap of bulk GaAs. This suggests there may be sub-band gap absorption which would agree with the conclusion from the photoluminescence measurements that the GaAs films are not of high optical quality. The GaP films are scattery, and so, for these films, we performed absorbance measurements using an integrating sphere based system. A result from these measurements is shown in Figure 7b. While these measurements do not show a clear onset of absorption at 2.27 eV, the GaP direct band gap E_g, there is a clear feature at approximately 2.78 eV, the GaP zone center band gap E_o. This, combined with the PL measurements that show emission at E_g, leaves no doubt that the optical properties of these films are in agreement with the accepted band structure of GaP.

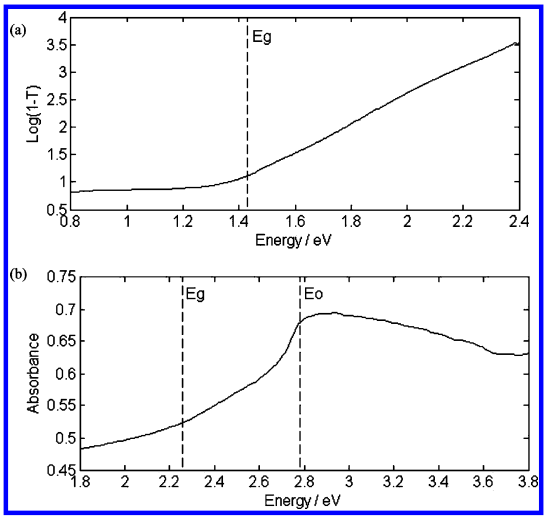

Figure 7. (a) Transmission spectrum of GaAs film grown at 773 K and (b) diffuse reflectance spectrum of GaP film grown at 773 K.

3.2. Attempted SCFD of GaP and GaAs. Our earlier work has demonstrated that reflective films of InP and InAs nanowires, showing good band-edge luminescence in the former case, could be deposited from the analogous [^{n}Bu$_2$In-(μ-E^{t}Bu$_2$)$_2$In^{n}Bu$_2$] precursors by SCFD from single phase sc-CO$_2$/hexane at 773 K (12 MPa).[10] The Ga dimers also exhibit good solubility in hydrocarbons, and hence, similar experiments were performed using these reagents, in an attempt to deposit GaP and GaAs. Under these conditions, shiny green films were often obtained with phosphide and gray, scattering films were obtained with arsenide. However, the films were always amorphous and contained high levels of carbon, with highly variable Ga/P ratios and no As detected by EDX. It has been shown that Lewis acidic metals can promote the decomposition of hydrocarbons to carbon (including multiwalled nanotubes) under supercritical conditions;[19] hence, the solvent was changed to benzene, which has been used in solvothermal conditions at temperatures up to 823 K to produce transition metal nitrides.[20] However, this was also unsuccessful, leading to significant carbon deposits, but not GaP (or GaAs). These results contrast with the successful InE deposition by SCFD, and probably arise as a consequence of the greater reactivity of Ga(III) over In(III) under the supercritical fluid conditions employed. A crystalline film was produced only in one deposition, when a toluene solution of [^{n}Bu$_2$Ga(μ-E^{t}Bu$_2$)$_2$Ga^{n}Bu$_2$] was piped directly into the reactor at 823 K, in very close proximity to the substrate. A small patch of tan-colored, scattering film was found to consist of GaP contaminated with Ga$_2$O$_3$.

4. CONCLUSIONS

This work has demonstrated that the [^{n}Bu$_2$Ga(E^{t}Bu$_2$)$_2$Ga^{n}Bu$_2$] (E = P, As) dimers are effective single-source precursors for the deposition of crystalline GaE films via LPCVD, although in practice, unlike the indium analogs, they are not well-suited for SCFD under the experimental conditions employed. This is the reverse of the observations we made previously in the indium systems for which SCFD gave good quality InE films of nanowires.[10] Importantly, while the GaP is produced via LPCVD as nanorods and appears to form a rougher surface than the GaAs, the material is of good electronic quality, revealing band-edge luminescence comparable to single crystalline GaP. This is very encouraging given the relative simplicity of the CVD rig employed, indicating that [^{n}Bu$_2$Ga-(P^{t}Bu$_2$)$_2$Ga^{n}Bu$_2$] may be a viable single-source CVD reagent for GaP deposition and suggesting that, in a fully optimized system, with mass flow control and UHV conditions, even better quality GaP may be obtainable.

■ ASSOCIATED CONTENT

Ⓢ Supporting Information

Representative XRD patterns, SEM images, and EDX data for GaP and GaAs deposited from [^{n}Bu$_2$Ga(E^{t}Bu$_2$)$_2$Ga^{n}Bu$_2$] (E = P, As) by LPCVD at different temperatures. This material is available free of charge via the Internet at http://pubs.acs.org.

■ AUTHOR INFORMATION

Corresponding Authors

*E-mail: G.Reid@soton.ac.uk.
*E-mail: D.C.Smith@soton.ac.uk.

■ ACKNOWLEDGMENTS

We thank RCUK (EP/C006763/1 and EP/H007369/1) and the CMSD at STFC for funding and Dr M. E. Light for assistance with the XRD measurements. We also thank STFC for access to NCESS under RG696 and Bob Bilsborrow, Danny Law, and Ben Gray for assistance with collecting and analyzing the XPS data.

■ REFERENCES

(1) (a) Grant, I. R. In *Group 13 Metals Aluminium, Gallium, Indium, and Thallium*, 1st ed.; Downs, A. J., Ed.; Wiley: London, 1993; (b) Malik, M. A.; O'Brien, P. In *Group 13 Metals Aluminium, Gallium, Indium and Thallium*, 2nd ed;Aldridge, S., Downs, A. J., Eds.; Wiley; London, 2011, p 612.

(2) Manasevit, H. M.; Simpson, W. I. *J. Electrochem. Soc.* **1969**, *116*, 1725.
(3) Malik, M. A.; Afzaal, M.; O'Brien, P. *Chem. Rev.* **2010**, *110*, 4417.
(4) (a) Davidson, F. M.,; Wiacek, R.; Korgel, B. A. *Chem. Mater.* **2005**, *17*, 230. (b) Davidson, F. M.,; Schricker, A. D.; Wiacek, R.; Korgel, B. A. *Adv. Mater.* **2004**, *16*, 647.
(5) Zaouk, A.; Constant, G. *J. Phys. (Paris), Colloq.* **1982**, *43*, C5.
(6) Janik, J. F.; Baldwin, R. A.; Wells, R. L.; Pennington, W. T.; Schimek, G. L.; Rheingold, A. L.; Liable-Sands, L. M. *Organometallics* **1996**, *15*, 5385.
(7) Jones, A. C.; O'Brien, P. *CVD of Compound Semiconductors: Precursor Synthesis, Development, and Applications*; Wiley-VCH: Weinheim, Germany, 1997.
(8) Cowley, A. H.; Jones, R. A. *Angew. Chem., Int. Ed. Engl.* **1989**, *28*, 1208.
(9) Yang., J.; Hyde, J. R.; Wilson, J. W.; Mallik, K.; Sazio, P. J. A.; O'Brien, P.; Malik, M. A.; Afzaal, M.; Nguyen, C. Q.; George, M. W.; Howdle, S. M.; Smith, D. C. *Adv. Mater.* **2009**, *21*, 4115.
(10) Aksomaityte, G.; Cheng, F.; Hector, A. L.; Hyde, J. R.; Levason, W.; Reid, G.; Smith, D. C.; Wilson, J. W.; Zhang, W. *Chem. Mater.* **2010**, *22*, 4246.
(11) (a) Cowley, A. H.; Jones, R. A. *Polyhedron* **1994**, *13*, 1149. (b) Arif, A. M.; Benac, B. L.; Cowley, A. H.; Geerts, R.; Jones, R. A.; Kidd, K. B.; Power, J. M.; Schwab, S. T. *J. Chem. Soc., Chem. Commun.* **1986**, 1543. (c) Arif, A. M.; Benac, B. L.; Cowley, A. H.; Jones, R. A.; Kidd, K. B.; Nunn, C. M. *New J. Chem.* **1988**, *12*, 553. (d) Miller, J. E.; Kidd, K. B.; Cowley, A. H.; Jones, R. A.; Ekerdt, J. G.; Gysling, H. J.; Wernberg, A. A.; Blanton, T. N. *Chem. Mater.* **1990**, *2*, 589. (e) Atwood, D. A.; Atwood, V. O.; Cowley, A. H.; Gobran, H. R.; Jones, R. A. *Organometallics* **1993**, *12*, 3517. (f) Atwood, D. A.; Cowley, A. H.; Harris, P. R.; Jones, R. A.; Koschmieder, S. U.; Nunn, C. M. *J. Organomet. Chem.* **1993**, *449*, 61. (g) Cowley, A. H.; Corbelin, S.; Jones, R. A.; Lagow, R. L.; Nail, J. W. *J. Organomet. Chem.* **1994**, *464*, C1. (h) Lakhotia, V.; Heitzinger, J. M.; Cowley, A. H.; Jones, R. A.; Ekerdt, J. G. *Chem. Mater.* **1994**, *6*, 871.
(12) Holga, K. T.; George, C. *Organometallics* **1990**, *9*, 275.
(13) Green, M; O'Brien, P. *J. Mater. Chem.* **2004**, *14*, 629.
(14) Inorganic Crystal Structure Database (ICSD) Fachinformationszentrum Karlsruhe (FIZ), accessed via the United Kingdom Chemical Database Service Fletcher, D. A.; McMeeking, R. F.; Parkin, D. *J. Chem. Inf. Comput. Sci.* **1996**, *36*, 746.
(15) Fu, L.-T.; Chen, Z.-G.; Zou, J.; Cong, H.-T.; Lu, G.-Q. *J. Appl. Phys.* **2010**, *107*, 124321.
(16) Campos, C. E. M.; Pizani, P. S. *Appl. Surf. Sci.* **2002**, *200*, 111.
(17) Adachi, S; Oe, K. *J. Electrochem. Soc.* **1983**, *130*, 2427.
(18) Tjerkstra, R. W. *Electrochem. Solid-State Lett.* **2006**, *9*, C81−C84.
(19) Smith, D. K.; Lee, D. C.; Korgel, B. A. *Chem. Mater.* **2006**, *18*, 3356.
(20) Mazumder, B.; Chirico, P.; Hector, A. L. *Inorg. Chem.* **2008**, *47*, 9684.